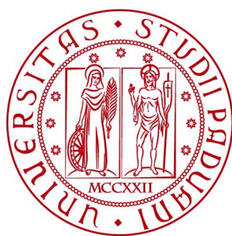

UNIVERSITÀ
DEGLI STUDI
DI PADOVA

Administrative office:
Università degli Studi di Padova

Department:
Scienze Chimiche

PhD course in:
Scienza e Ingegneria dei Materiali e delle Nanostrutture
Series: XXXII

Innovative Methods for Germanium Doping

Coordinator:
Ch.mo Prof. GIOVANNI MATTEI

Supervisor:
Prof. DAVIDE DE SALVADOR

PhD Candidate
FRANCESCO SGARBOSSA

PhD Thesis
Innovative Methods for Germanium Doping

Francesco Sgarbossa

Dep. of Chemical Sciences
and
Dep. of Physics and Astronomy
University of Padova
September 2019

"Nothing in life is to be feared, it is only to be understood.
Now is the time to understand more, so that we may fear less."

Marie Curie

Abstract

The semiconductor research is focused on the production of shallow junctions conformal to the surface of the device. This request emerges from the increasing importance of nano-structured devices made by semiconductor materials like multi-gate transistors. The non-planar geometry of these devices implies the capability to dope semiconductor materials with a nanoscale control and in a non-planar geometry, which is still a difficult task nowadays. One of the most promising techniques for the deposition and diffusion of a well-defined amount of dopant is based on the use of self-limiting chemical adsorption on semiconductor surfaces. This technique is called *monolayer doping* (MLD). This particular technique consists in the adsorption of molecular precursors by a self-limited surface interaction, which leads to a chemisorbed or physisorbed mono- or multilayer. This molecular precursor may act as a source of atomic species that are released and diffuse into the underlaying material after thermal induced decomposition. This interesting technique, invented and applied for silicon, is still largely unexplored with others substrates, such as germanium. Due to relatively low cost with respect to ion implantation, the technique may also be interesting for large area junction production, needed for photovoltaic or detector applications.
Germanium is actually a very interesting semiconductor: small band-gap and high mobility of charge carriers have recently made it more and more interesting in several application fields, from nano-electronics to photovoltaics, from optics to radiation detectors . Indeed, during last years, germanium has been reconsidered as a photonics material due to the possibility to obtain a direct band gap by the controlled use of strain (also induced by the presence of a heavily doped region). As a consequence, the scientific and academic research efforts are focused on the creation of a doping protocol able to conformally dope nanostructured surfaces through the creation of shallow and high doped layer.
We investigated the MLD process starting from different P containing molecular precursors and Sb self-limiting evaporation. A detailed analysis of the layer formation as a function of precursor and process parameters was performed. In

particular, we investigated the doping species amount, the chemical structure and the modification (oxidation) of the substrate under different processing conditions. In this study, we determined the best conditions to obtain homogeneous and well controlled monolayers. In this thesis, a full characterisation of the layers chemical state is presented. Diffusion experiments were also performed both with standard equilibrium annealing techniques and with Pulsed Laser Melting (PLM).
Overall results demonstrate that oxidation is a relevant aspect of the entire process. The oxidation of the precursor and of the Ge surface can be limited under proper conditions, choosing the right precursor for P or the process temperature for Sb. Unfortunately, it can not be avoided completely, lacking an easy chemical deoxidation process in inert atmosphere for Ge surface. In every considered case we observed that the doping atoms bond to Ge through an oxygen bridge. In case of P, this kind of bonding is dominant for most of the precursors, while in the case of Sb we saw that a fraction of Sb is incorporated in the surface in a metallic state.
Under thermal equilibrium annealing, we observed that the investigated P MLs don't allow the P injection into the bulk. This is because of the strong P-O bond that can not be broken at the relatively low annealing temperature allowed by Ge crystals. Many of the same investigated precursor molecules are effective for Si doping thanks to the fact that higher temperatures can be reached due to the higher melting temperature ($1412°$C for silicon $937°$C for germanium). In the case of Sb under thermal equilibrium annealing, we observed that only the Sb fraction in metallic oxidation state is available for diffusion and effectively produce a doped junction.
On the other hand, PLM which is an out equilibrium process, is effective to promote P and Sb diffusion and form a junction. During this process, Ge melts for a very short time (ns time scale). Apparently, the overall thermal budget is not much higher than in the previous case, indicating that direct interaction of the ML with UV light may promote the Oxygen-doping atom bond breaking. In case of P MLs, P availability is lower and high concentration can be reached only after multi-pulse annealing. In the case of Sb, the full monolayer diffuses in Ge with a single pulse denoting that the Sb-O-Ge surface phase is less stable under UV irradiation than the surface phosphates.

Contents

Introduction **iii**

1 Interdisciplinary Background **1**
1.1 Germanium in our times 1
1.1.1 Germanium at the end of Moore's Law 2
1.1.2 Germanium doping applications 5
1.2 Diffusion in germanium: the n-type case 11
1.2.1 Fick's law for diffusion 12
1.2.2 Lattice point-defects 13
1.2.3 The dopant diffusion in Ge 15
1.3 Monolayer Doping Technique 19
1.3.1 Monolayer Doping on Si 20
1.3.2 Monolayer Doping on Ge 28
1.4 Germanium surface 30

2 Methods **33**
2.1 Processing techniques 34
2.1.1 Thermal processing 34
2.1.2 Pulsed Laser Melting technique 36
2.2 Characterisation techniques 39
2.2.1 Rutherford Backscattering Spectrometry 39
2.2.2 Nuclear Reaction Analysis 43
2.2.3 X-Ray Photoelectron Spectroscopy 50
2.2.4 X-Ray Absorption Spectroscopy 56
2.2.5 Electrical Measurements 62
2.2.6 Secondary Ion Mass Spectrometry 65
2.2.7 Infrared Spectroscopy 66

3 Phosphorus Monolayer Doping **69**
3.1 Phosphorus Precursor Adsorptions 69
3.1.1 Surface preparation 69

3.1.2 Adsorption processes 72
3.1.3 AFM surface topography 75
3.2 Characterisation of Phosphorous functionalized Ge surfaces 77
3.2.1 Phosphorus and Germanium oxidation states 77
3.2.2 Germanium oxide interlayer quantifications 84
3.2.3 Phosphorus quantifications in adsorbed layers 91
3.2.4 Structural modification of adsorbed molecules 94
3.3 Phosphorus Diffusion Tests 111
3.3.1 Thermal Diffusion 111
3.3.2 Pulsed Laser Melting 117
3.4 Conclusions 124

4 Antimony Monolayer Doping 129
4.1 Deposition Method 129
4.2 Sb Monolayer Formation 134
4.2.1 Gas phase deposition: time and temperature deposition parameters study. 134
4.2.2 Monolayer areal homogeneity analysis. 137
4.3 Sb Monolayer Surface Characterisation 139
4.3.1 AR-XPS surface analysis 140
4.3.2 Chemical Adsorption suggested reaction 146
4.4 Sb Monolayer Diffusion 149
4.4.1 Sb thermal diffusion 150
4.4.2 Sb diffusion by PLM 155
4.5 Conclusions 159

Conclusions 161

Bibliography 164

Acknowledgments 181

Introduction

One of the main goals in semiconductor research is the production of shallow junctions conformal to the surface of a device. This request emerges from the increasing importance of nanostructured devices made of semiconductor materials like multi-gate transistors. The 3D geometry of these devices implies the capability to dope the semiconductor material in a nanostructured, non-planar geometry, which is still a difficult task.
In the field industry research, new doping techniques are being studied and tested, in order to find a replacement technique for the ion implantation, which is more and more inappropiate as the device scaling brought us in the nanoscale doping regime. One of the most promising techniques for the deposition and diffusion of a well-defined amount of dopant is based on the use of self-limiting chemical deposition on semiconductor surfaces: that is the key point of the *monolayer doping technique* (MLD).
This particular technique consists in adsorbing a monolayer of a molecular precursor by a self-limited surface adsorption interaction, which leads to a chemi- or physisorbed mono- or multilayer structure. This layer(s) acts as a source of dopant for the substrate in-diffusion. This new technique allows to dope not only 3D nano-structured materials with an intrinsically conformal method, but also flat semiconductor surfaces by avoiding ion implantation and its consequent damage of the crystal lattice. Indeed, the damage induced by the high energy ion bombardment step implies a subsequent high temperature damage recovering process that can broaden the formed shallow junction. Moreover, a huge statistical variability of dopant is expected for ion implanted nano-scaled devices due to the extremely low number of atoms that are at stake: this problem is in principle avoidable using a conformal molecular precursor layer (MLD). Finally, the doping of non-planar geometry is challenging too, due to several problems related with the tilted ion-implantation process.
Thanks to the low cost of process and precursors, the MLD technique is perfectly compatible for large areal scale doping, being a good alternative to ion implanta-

tion also for non nanostructured materials.

Nowadays, MLD is well studied in silicon substrates for n and p type doping, but applications to other semiconductor materials, such as germanium or III–V semiconductors, are still largely unexplored. The rising of germanium based devices and nano-structures makes these studies more and more appealing.
Furthermore, germanium is actually a very interesting semiconductor: small band-gap and high charge carrier mobilities have recently made it more and more appealing in several application fields, from nano-electronics to photovoltaics, from optics to radiation detectors. In fact, during the last years, germanium has been re-considered as photonics material due to the possibility of obtaining a direct band gap by the controlled use of strain (also induced by a heavily doped region).

This work is focused on the challenging n-type doping of Ge by using new doping methods based on the surface interaction between molecular precursors and germanium (001) surface. For the first time, a complete study on phosphorus monolayer doping technique on germanium is presented, using surface molecular precursor, and also a new antimony self-limiting deposition via gas phase has been discovered and tested as a new technique to obtain a surface monolayer that can be used as a source for Ge doping.
This work highlights how the germanium surface influences the adsorption reactions, mainly because of its strong tendency to oxidise and generates a mixed Ge oxide. To explain the chemistry and the physics of germanium surface, this study used different adsorption processes and different surface investigation techniques, in order to verify structural changes induced by the surface adsorption process and correlate it with the ML role as a dopant source. Thanks to this work, it is increasingly clear that the study of monolayer doping must be approached in a multidisciplinary manner, combining the use of surface chemistry and chemical surface characterisation, with more physical techniques such as Ion Beam Analysis and XAS analysis, that are fundamental to correctly understand the ML composition and behaviour with thermal annealing and diffusion tests.
In this work P and Sb dopants are investigated: phosphorus presents a large variety of chemical compounds that are normally non-toxic, not expensive and readily available on the market. On the contrary, arsenic does not presents the same advantages and especially for its chemical hazards (that characterise almost the whole family of As compounds) it will not be treated. Antimony presents some chemical hazards but in general it is more manageable than As compounds and,

thanks to a new gas phase monolayer deposition, this dopant is tested on Ge in this work.

The P and Sb ML sources are synthesised in completely different ways: the phosphorus precursors depositions are done via wet chemistry, using a reflux method (called standard procedure) or by using a dry procedure in a dry-box ambient (dry N_2 ambient) both near $160°$C, while the antimony monolayer is deposited via gas phase in a N_2 flux at high temperature (about $600°$C $< T < 790°$C). These two deposition methods are analysed by means of different surface characterisations: they allow us to deeply understand the role of germanium oxide in Ge MLD and correlate it with crucial aspect of this technique. In both cases, the germanium oxide plays a crucial role: in the P case the oxide plays a fundamental role in the adsorption mechanism, while in the Sb case it contributes to oxidise the incoming antimony gas. In both cases the new chemical bond between the precursor and the substrate is a Ge-O- based bond: Ge-O-P or Ge-O-Sb. The presence of the Ge-O- bond seems to be the cause of the high surface stability of monolayers, thus limiting in diffusion with standard thermal in-diffusion processes. Indeed, the presence of highly stable chemical bonds act as a diffusion barrier, since P or Sb atoms release from the chemisorbed ML is possible only after a thermal bond disruption, as will be further discussed.

A completely different scenario is presented with the use of pulsed laser melting technique (PLM): it has been used on monolayer molecular sources on Ge (001) and thanks to its out-of-equilibrium nature, the molecular precursor act as a doping source, being effective also for Ge doping.
Phosphorus monolayers act as a source of dopant during PLM technique, releasing P and generating a doped layer: the use of more than one pulse ensures that most of the P atoms diffuse in germanium. In the antimony oxide ML case, the entire surface ML is available for diffusion (with no Sb loss) with only one PLM pulse, even if all the surface ML is in an initial oxidised state. The PLM technique promotes its reduction and atomic Sb diffuses and dopes the surface of the Ge substrate. The creation of a fully active Sb layer with a surface concentration over $10^{20} cm^{-3}$ is the clear demonstration of the feasibility of the use of Sb ML as a source of dopant, using a perfectly self-limiting process that generates a stable layer that can be fully diffused in Ge only with one PLM pulse technique.

This work is divided in four chapters: in the first, an interdisciplinary background introduces the reader to recent research problems related with nanoelectronics and doping procedures, highlighting the role of germanium in differ-

ent recent research fields. In the same chapter an overview on Monolayer Doping Technique is also given, especially focused on silicon MLD, due to the lack of literature referring MLD technique on Ge, with only some exceptions. The second chapter is focused on the experimental methods, describing the techniques used in this work and their related analysis procedures. Chapter three and four are focused on experimental results on phosphorus MLD and antimony MLD respectively. In these chapters, results and discussion are presented, starting from the ML synthesis procedure description, to thermal diffusion and junction characterisations. Finally, an overall conclusion on this work is presented.

Chapter 1

Interdisciplinary Background

1.1 Germanium in our times

Germanium was discovered as an element of the periodic table only in 1886 by Winkler [1], as predicted by an unfilled space at 72 uma atomic weight in the IVth column of the original Mendeleev's periodic table.

During the 40s and 50s, germanium was the most used and studied semiconductor material, since it was the material with the best crystalline lattice available at that period and today it still remains one of the best. Moreover, germanium is the most pure available semiconductor material, with an atomic electrically active impurities concentration level $< 10^{10}\ cm^{-2}$. Germanium history was completely

Reihen	Gruppo I. — R^2O	Gruppo II. — RO	Gruppo III. — R^2O^3	Gruppe IV. RH^4 RO^2	Gruppe V. RH^3 R^2O^5	Gruppo VI. RH^2 RO^3	Gruppo VII. RH R^2O^7	Gruppo VIII. — RO^4
1	H=1							
2	Li=7	Be=9,4	B=11	C=12	N=14	O=16	F=19	
3	Na=23	Mg=24	Al=27,3	Si=28	P=31	S=32	Cl=35,5	
4	K=39	Ca=40	—=44	Ti=48	V=51	Cr=52	Mn=55	Fe=56, Co=59, Ni=59, Cu=63.
5	(Cu=63)	Zn=65	—=68	—=72	As=75	Se=78	Br=80	
6	Rb=85	Sr=87	?Yt=88	Zr=90	Nb=94	Mo=96	—=100	Ru=104, Rh=104, Pd=106, Ag=108.
7	(Ag=108)	Cd=112	In=113	Sn=118	Sb=122	Te=125	J=127	
8	Cs=133	Ba=137	?Di=138	?Ce=140	—	—	—	— — — —
9	(—)	—	—	—	—	—	—	
10	—	—	?Er=178	?La=180	Ta=182	W=184	—	Os=195, Ir=197, Pt=198, Au=199.
11	(Au=199)	Hg=200	Tl=204	Pb=207	Bi=208	—	—	
12	—	—	—	Th=231	—	U=240	—	— — — —

Figure 1.1. Mendeleev's periodic table, 1869.

upset when Bardeen and Brattain, in the Shockley research group at Bell Laboratories, accidentally invented the first transistor on 1948 [2] while on the search for the field-effect device with germanium. The transistor invention paved the way to the most important technological and industrial revolution of the last century, radically changing the economical and social world. Germanium has been

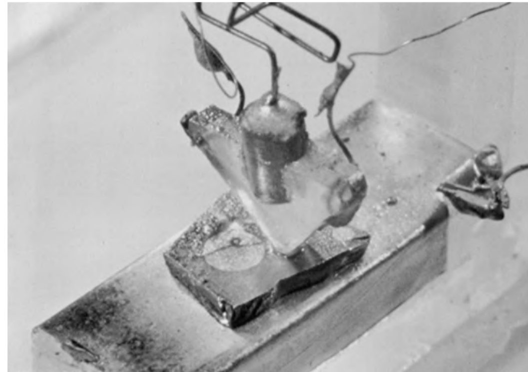

Figure 1.2. First point contact transistor, by Bell Labs, 1948.

the material of choice for the development of semiconductor electronics, such as bipolar transistors, for more than a decade, being the material that permits the development of a several theories on semiconductor physics. In the late sixties and in the seventies, silicon dethroned germanium, becoming the main microelectronics material. This occurred basically because germanium surface presents a low quality oxide [3] that if compared with Si, which has a very good Si/SiO_2 interface [4]. For field-effect devices, this Ge surface characteristic creates a lot of problem in the surface passivation and dielectric integration. Moreover, Si has a lower cost and even if it can be produced with a lower purity than Ge, it still remain a perfect material for microelectronics devices [5]. These two main reasons prevailed in the material change decision more than other reasons, such as the intrinsically better conduction performances on germanium (Ge mobility is two times higher than Si for electrons, three times for holes). So the planar metal-oxide-semiconductor field effect transistor MOSFET process has been developed for silicon substrates, which took over as the dominant industry material [6]. This is basically the reason why nowadays all of us know a valley near San Francisco as *Silicon Valley* instead of *Germanium Valley*, that would have been its name if germanium surface passivation problems had been overcome in the seventies.

1.1.1 Germanium at the end of Moore's Law

The rule of thumb that described the development of semiconductor industries growth, called Moore's Law, today is nearing the end [7]. Moore's Law, that stated that the increasing number of transistors on a microprocessor chip would double every two years or so [8], has been observed until these years. The reason why this technological evolution begins to slow down is the basilar fact that it is

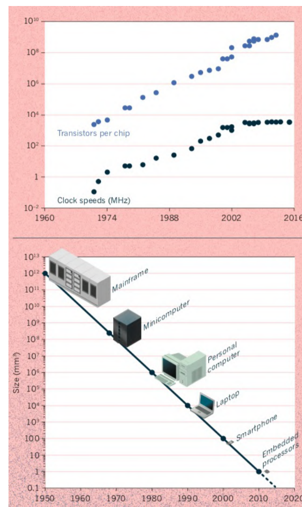

Figure 1.3. Moore's law graph and related new technologies [7].

impossible to put more and more transistors in the same area, or, in other terms, to infinitely scale down the dimension of transistors. Nowadays the dimension of commercial transistor is in the order of few nanometers, and the *scaling* problems become more and more challenging.
As Paolo Gargini [1] said:

> *Even with super-aggressive efforts, we'll get to the 2-3 nm limit (on 2020s), where features are just 10 atoms across. Is that a device at all?*

Probably the answer is no, if only because the electron at this scale are dominated by quantum uncertainties that will make transistors unreliable [7]. Unfortunately this is not the only problem, because other correlated issues are equally unsolved and important, such as the heat that is unavoidably generated by transistors, that increases through their scaling. So, how will the microelectronics industry meet the incessant demand for the increase in computing power?
As Daniel Reed [2] said: *A Boeing 787 does not go any faster than a 707 did in the 1950s, but they are very different airplanes* [7]. So, the innovation in this field will continue for sure, but in a different and more complicated way.

During last years, several proposals have been put forward, starting from the use of high-k oxides, multi gate transistors, or strained channel silicon materials, that are already implemented in devices. But the most important point is the realisation of millivolt switches, that should allow to generate much less heat:

[1] Chair of the road-mapping organization
[2] Computer scientist and vice-president for research at the University of Iowa in Iowa City

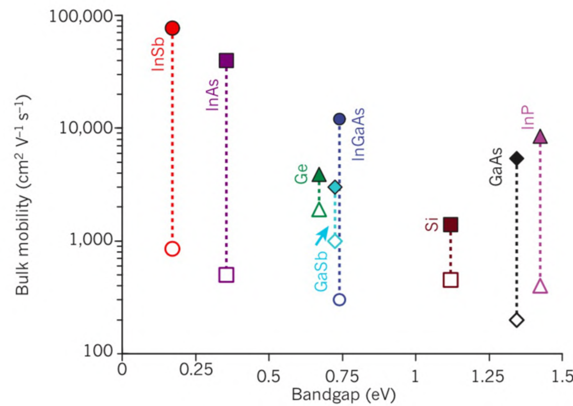

Figure 1.4. The bulk mobilities as a function of bandgap for different semiconductor materials [6].

unfortunately, they haven't been realised yet and the industry is now exploring different paths. The most popular option is to use 3D geometry architecture, especially for memories that do not have heat dissipation problems, but again, this will not resolve the main problem.
The use of different materials seems to be one of the possible solutions, using less resistant materials with a higher carrier mobility, especially for the channel region in MOSFETs. For this reason, III-V semiconductors, 1D nanotubes and germanium are good candidates as new channel materials, although they present different problems and advantages [6, 9]. It is clear that any new technologies based on a different material must be integrated on silicon substrate, for economic reasons and material availabilities. The materials integration on Si substrate is one of the most interesting technological challenges, since the lattice constants of other semiconductors are in principle different from that of silicon: for example, Ge lattice parameter is 4% larger than that of silicon. This difference causes the creation of an extremely high number of defects inside Ge grown directly on Si substrate, causing the degradation of carrier mobilities and an increased junction leakage. To accommodate different lattice parameters, several ploys have been studied. The creation of buffer layers is one of the most used techniques for germanium, because the use of a Si_xGe_{1-x} (buffer) layer seems to drastically reduce the defect density in the active Ge layer [10].
But what about the germanium surface passivation for microelectronics devices? As described before, the main disadvantage coming from the use of Ge as an active material for MOSFET technology is the creation of a surface passivation layer; unlike silicon, germanium has a very low germanium oxide quality and its thermal oxidation does not form a good passivation layer. A lot of research has

been conducted in these years, and different solutions have been discovered. The thermal growth of a $GeON$ layer in an ozone-oxidizing atmosphere has proved to exhibit a minimal degradation of carrier mobility in germanium MOSFET [11, 12]. Moreover, the use of high-k gate-dieletric materials have been successfully tested with a germanium based gate, demonstrating that the actual HfO_2 oxide, used for Si MOSFET, can be adopted also for germanium [13, 14].

1.1.2 Germanium doping applications

In this section, a brief overview of germanium applications will be presented, underlining the most important applications besides nanoelectronics, that was discussed in the previous paragraph.

Optoelectronics

Nowadays, probably one of the most interest fields for germanium doping application is the photonics and in particular optoelectronics: the communication and information technologies start to request new innovations and thanks to new scientific results on Ge such as its band engineering, new applications in these fields are also very appealing for Ge.

Indirect semiconductor materials, like Si and Ge, are intrinsically not suitable for light emission, since the radiative recombination process that generates a photon by hole-electron recombination has to be mediated by a phonon to balance the crystal momentum and is therefore usually less probable than non radiative processes. In order to make Ge suitable for light emission it is mandatory to modify its band structure.
germanium has an indirect gap of 0.66 eV, and a pseudo direct gap of 0.8 eV at room temperature. The indirect transition is a $L \rightarrow \Gamma$ transition, since the lowest conduction band is placed in L valley, while the maximum of the valence band is in the Γ point. The energy difference between direct and indirect transition is only 136 meV, and it was demonstrated [15, 16] that is possible to obtain a direct band gap germanium by applying in-plane tensile strain (1.9% [15]). The distance variation between bands is well described by the linear relation $E_g(\Gamma) = 0.89 - 20\epsilon_{||}\ (eV)$. A side effect of this treatment is that the energy gap of the material decreases, and Ge direct band gap becomes 0.5 eV [17], which is far from the commonly used telecommunications and optical band.
In particular, devices in the 800-1600 nm (1.55-0.77 eV) range are requested, since this is the preferred wavelength for optical fiber transmissions and Si based de-

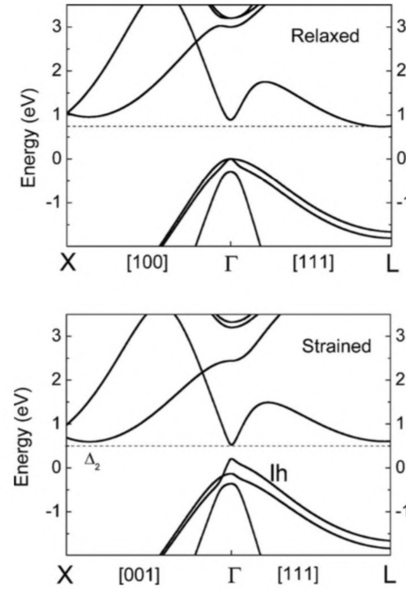

Figure 1.5. On top, unstrained low temperature germanium band structure, compare with 3% in-plane tensile-strained germanium (bottom) [15].

vices are not able to cover this band. Nowadays III-V semiconductor based solutions are in the market, but they are currently not integrated on silicon substrates. The III-V materials integration on Si substrate seems more promising for its low-cost and high-yield fabrication for direct hetero-epitaxial growth [18]. However, Germanium (Ge)-on-Si laser is also competitive for large-scale monolithic integration in the future. Compared with a III-V-based Si laser, the biggest potential advantage of a Ge-on-Si laser lies in its material and processing compatibility with Si technology, as reported by Zhou and co-workers [18]. Additionally, the versatility of Ge facilitates photon emission, modulation, and detection simultaneously with a simple process complexity and low cost [18]. But how is it possible to obtain direct transitions in Ge without changing its energy gap?

A different approach is the application of a smaller tensile strain in combination with a high germanium doping ($> 7\ 10^{19}\ cm^{-3}$) as proposed by Liu et. al. [17]. Thanks to this approach, the L valley is populated with a high electron concentration, thus raising the Fermi Energy level. The population of L valley is now sufficient to populate also the Γ valley, and so these electrons can recombine with holes via direct transition, emitting light at 1550 nm (0.8 eV). Liu and co-workers [17] demonstrated that a 0.25% tensile-strain in combination with an active n doping of $7.6\ 10^{19}\ cm^{-3}$ is sufficient to obtain a direct gap light emission.

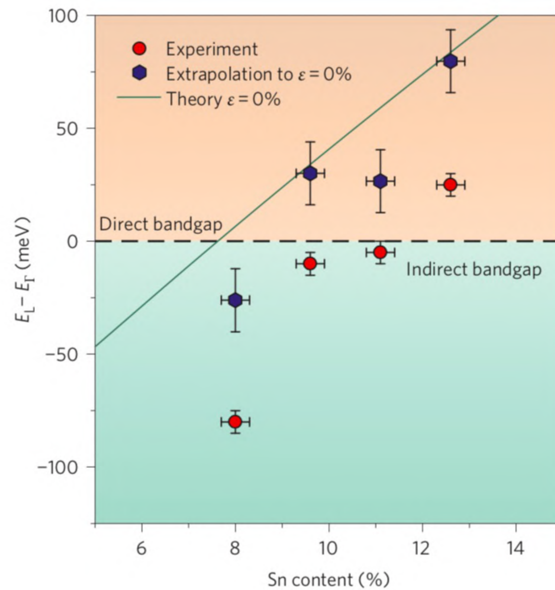

Figure 1.6. Energy difference between Γ and L valley in GeSn conduction band as a function of Sn content. Indirect-Direct transition is found at about 9% Sn for unstrained layers using an extrapolation [19].

Another interesting technique to obtain direct transitions in Ge is the introduction of Sn in Ge crystal, inducing a strain without any mechanical action. Thanks to this approach, Wirths and co-workers [19] demonstrate that a 6.5-11% of Sn in Ge is sufficient to induce a direct transition, and lasing in GeSn alloy was demonstrated at low temperature. Moreover, in that work the GeSn alloy is integrated on Si substrate using a Ge buffer layer, demonstrating that a perfect Si integration is possible.
In last years a lot of research has focused on this field, generating GeSn/SiGeSn Heterostructure and Multi Quantum Well Lasers [20], direct band-gap $Ge_{1-x}Sn_x$ nanowires [21] and many others interesting materials and devices.

Solar Energy

The simplest solar cell consists in a p-n junction in which solar photons are absorbed, generating electron-holes pairs. These carriers are separated by an electrical field (normally generated by the built-in potential) and collected by an external circuit, so providing electrical power. The photons are properly absorbed if their energy is greater than the semiconductor energy gap ($h\nu > E_g$), otherwise photons can not be absorbed correctly and their energy is lost. On the contrary, if the energy of photons is very high with respect to the semiconductor gap, the

carriers need to thermalise after their creation and so a lot of energy is dissipated throug phonon generation. The ideal semiconductor family for solar cells is direct band gap materials, since no phonon assisted mechanism should be involved. As a matter of fact, GaAs solar cells exist, but Si solar cells are the most commercially used, basically for their cost.
A smart approach to improve solar cell efficiency is the multi-junction approach, that consists in the creation of different layers in which each layer has a different energy gap, in order to absorb different parts of the solar spectrum in each layer. These devices are called multi-junction solar cells. They are made with the widest band gap material on top, in order to absorb the most energetic part of the spectrum and transmit the lower energetic fraction to lower layers, presenting smaller band gap materials. This technique is also known as *spectrum splitting*.
It is clear that thanks, to the 0.66 eV band gap, germanium can play an important role in the multi-junction solar cell since it can absorb a wide low energy portion of the sun spectrum that others conventional cells based on other semiconductors normally lose. [22]
As an example, figure 1.7 shows a multi-junction cell with 3 different layers,

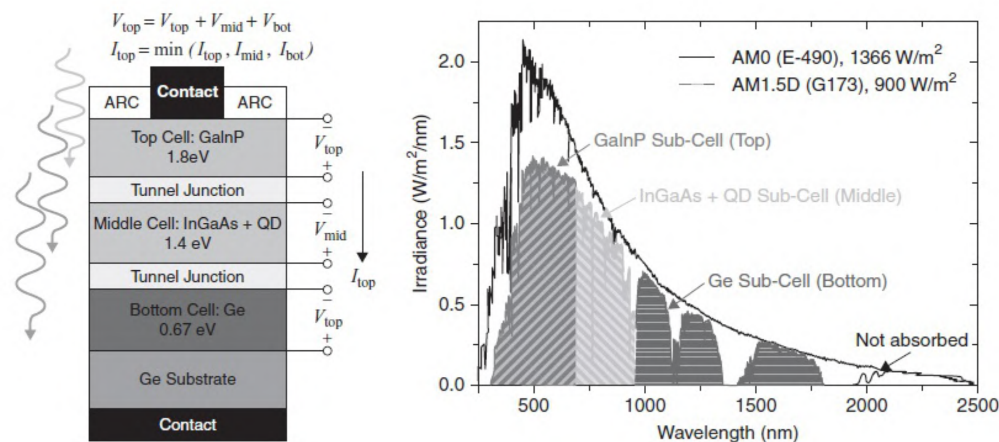

Figure 1.7. Structure of a multi-junction solar cell with the portions of the spectrum that are covered by each material. Spectrolab Inc. Copyright (2011) Spectrolab.

having 1.8 eV($Ga_{1-x}In_xP$), 1.4 eV($InGaAs$) and 0.67 eV (Ge) band gaps: these are clearly reflected into the absorption of solar spectrum, presented on the right. The theoretical efficiency of these cells is very high (experimental efficiency around 40% [23–25]), thanks to the very similar lattice parameter of Ge and GaAs, that allows to grow these two materials one on the other without major problems. The efficiency of these cells can be theoretically increased over 60% using a larger

number of layers, but the costs of these devices are in general not sustainable for standard low cost applications. [22]
Multi-junction solar cells based on Ge are now used for space applications, where

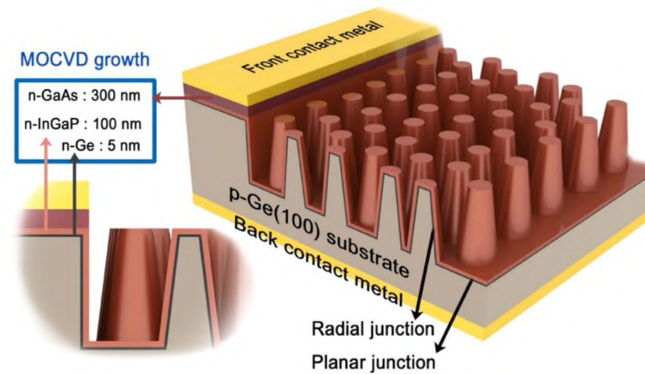

Figure 1.8. Germanium nanopillar solar cell schematic diagram [26].

the combination of high-efficiency and low-weight is mandatory, and the cella cost is justified.
Another interesting work is focused on a different approach: Kim and co-workers [26] focused to generate a Ge nanopillar solar cell (see figure 1.8) using a nanospheres lithography and ion etching technique, in order to improve the power conversion efficiency. Nanopillar is reported to decrease the reflectance at the top of Ge NP solar cell with respect to similar planar solar cell.

Much research is present in literature regarding Ge solar cells, mostly focused on alloying Ge with Si [27, 28] to tune the material bandgap, and several patents on pure Germanium solar cell have been issued [29, 30] and Si and Ge multilayer solar cell [31–33].

Thermophotovoltaic

The thermophotovoltaic (TPV) energy conversion is a quite new research field in which the heat is captured by cells and converted into electrical power. These cells are basically the same that are normally used in conventional photovoltaics, but in this case the absorbed photons are in the infrared spectral region instead of the visible region. The thermophotovoltaic cells are designed to work in near infrared region in which lots of industrial machines emit thermal radiation as a simple consequence of their high temperature working conditions. The thermophotovoltaic cells can recover this thermal dispersion and so improve the global efficiency of several industrial processes.

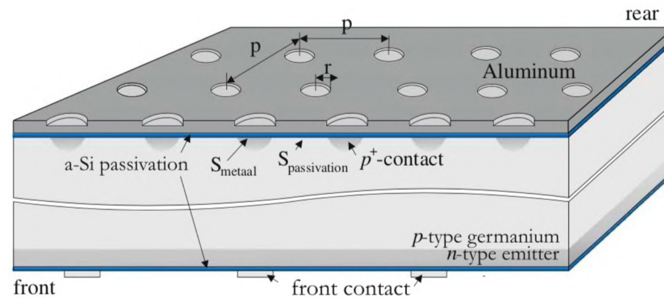

Figure 1.9. Schematic representation of the structure of a germanium based thermophotovoltaic cell presenting a passivated highly reflective rear structure contacts, created by laser fired contacts (LFC) where point contacts are formed by local laser heating [34].

The TPV cells are based on small energy gap materials like gallium antimonide ($GaSb$) and germanium (Ge). An important feature that characterise some TPV cells is the presence of a highly reflective rear contact to apply an optical confinement of the radiation, increasing their efficiency up to 20% [34]. Different works are present in literature regarding these TPV technology [34–37] and a general increasing interest is present in the scientific community.

High Purity Germanium gamma ray detectors

The study of gamma radiations emitted by radioactive sources or after nuclear reactions is one of the applications in which germanium is the most proper material [38]. In this field, the use of Hyper Pure Ge (HPGe) is mandatory, since the working principle of these gamma ray detectors requires a hyper-pure semiconductor material. The γ photons are revealed detectors by collecting and analysing electron and hole carriers generated from the interaction between a γ photon and Ge material. Since the interaction of a γ photon with the active material would generate a number of electron-hole pairs much lower than the free charge carriers of common Ge (Ge or Si in microelectronic grades), the use of HPGe is mandatory. In fact, the HPGe detector presents a charge active impurity concentration lower than $10^{10}\ cm^{-3}$, while a 1 MeV γ photon generates $3.5\ 10^{5}$ electron-hole pairs. Nowadays, no other semiconductor presents a mass production with a lower electrical contaminants concentration respect to HPGe. The use of gamma ray detectors require also a cooling system down to 200K, since also thermal generated carriers must be suppressed: as a matter of fact, Ge presents a thermal carrier concentration of about $2\ 10^{13}\ cm^{-3}$ at room temperature, that would generate the same problem mentioned above.

After the generation of electron-hole pairs by a γ photon, the carriers must be collected for their analysis: this is possible since the active area of the device is a depleted region, polarised by an applied external potential that generates a built in potential in the depleted zone. This potential induces a motion in generated charges, attracting them into n and p region of Ge, and then into metal electrodes applied on Ge-n and Ge-p zones.

Considering the working principle [38], the material requirements and also the production procedures, there is still room for improvements [39]. In fact, the Ge-n layer present in gamma ray detectors is doped with Li, and there is no possibility with this technology to implement a fine segmentation [40]. Moreover, during the damage recovering annealing step, the entire Li doped zone is heated over $100°$C for several hours, but this causes Li diffusion that damages the contacts and decreases the active zone of the Ge detector. Some literature studies on alternative Ge n-type doped layer is present [39, 41, 42], but the actual technology is still focused on Li based contacts. The p-type contact is a B doped Ge layer, made by ion implantation, that is an expensive technique, especially for the large area to process.

The implementation of MLD technique in this Ge application could bring some improvements, exploiting MLD low cost process and large scale implementability. Also the MLD conformal behaviour could play a role, since the macroscopical geometry of a Ge detector presents a non planar geometry, as in the coaxial gamma ray detector.

The use of PLM technique is perfectly compatible with HPGe material, as demonstrated by literature works [43], and the use of PLM technique in combination with ML molecular source should be effective for gamma ray detector production in the future.

1.2 Diffusion in germanium: the n-type case

The solid state diffusion is a migration process of atoms inside a crystalline or an amorphous matrix. Diffusion is a key process for semiconductors research and industries, since semiconductors doping is based on the diffusion of doping atoms inside a semiconductor crystal. The description and the modelling of these processes are present in literature, both for Si and Ge [44–48][49–52], since the diffusion step process is present in any device construction industrial process. Normally, diffusion processes are described as thermally activated processes, that are well described with an Arrhenius or an activation type law. In this section,

a global introduction on this semiconductor research field will be given, and the most important impurity diffusion mechanism in germanium crystal will be presented.

1.2.1 Fick's law for diffusion

The basics laws that describe the diffusion process are *Fick's laws*: they describes the flux of matter in a macroscopic scale. The first Fick law describe the flux of atoms (J that is also the diffusion current) as the gradient of the concentration (C expressed as atoms per unit volume) multiplied by a coefficient D, that is called diffusion coefficient [44].

$$J = \; - \; D \cdot grad(C) \tag{1.1}$$

The diffusion coefficient is, in general, a second rank tensor, but for the high symmetric cases of Si, Ge and other semiconductors presenting a diamond structure, the diffusion coefficient is reduced to a scalar number.
The second Fick law can be derived writing a continuity equation within a material, considering a generation rate G and a loss rate R; considering the infinitesimal volumes, we can write the differential (or local form) equation:

$$\frac{\partial C}{\partial t} = -div(J) \; + G \; - R \tag{1.2}$$

By neglecting the sources and sinks, equation 1.2 can be written as:

$$\frac{\partial C}{\partial t} = \; div\Big(D \; \cdot grad(C)\Big) \tag{1.3}$$

This equation is called Second Fick law [44]. This formula expresses the relation between the variation in concentration of a certain species with the diffusion coefficient and the atoms concentration.

Fick's second law has some simple solutions, especially for two remarkable cases.
The *infinite source* case, that corresponds to a constant surface concentration of diffusing atoms, presents an error function based solution [44]:

$$C = C_{x=0} + (C_{t=0,\, x>0} - C_{x=0}) \, erf\left(\frac{x}{\sqrt{4Dt}}\right) \tag{1.4}$$

If the initial concentration is null ($C(0,x) = 0$), it can be written as follow :

$$C = C_{x=0} \cdot \left(1 - erf\left(\frac{x}{\sqrt{4Dt}}\right)\right) \; = \; C_{x=0} \cdot erfc\left(\frac{x}{\sqrt{4Dt}}\right) \tag{1.5}$$

The other remarkable case is the deposited thin layer, that can also be called *finite source*: it is basically the case in which a fixed amount of atoms are redistributed, starting form a delta function at a depth x equal to zero. In this case, the solution is a Gaussian based function:

$$C = \frac{N}{\sqrt{\pi D t}} \cdot exp\bigg(-\frac{x^2}{4Dt}\bigg) \tag{1.6}$$

where N is the total amount of atoms, which is fixed. They diffuse inside a matrix with a diffusion coefficient D, in a time t, for a distance from the surface x (depth) [44].
The *diffusion length* is defined as the σ of the gaussian distribution function, representing a characteristic diffusion depth; it is defined as:

$$L_{diff} = \sigma(t_f) = \sqrt{2Dt_f} \tag{1.7}$$

Regarding the diffusion coefficient, since the diffusion process is thermally activated, the most important dependance of the diffusion coefficient with thermodynamic variables is the temperature dependance. The diffusion coefficient is normally expressed as a function of temperature by the Arrhenius law:

$$D = D_0 \cdot exp\bigg(-\frac{E_a}{k_b T}\bigg) \tag{1.8}$$

in which D_0 is known as diffusion pre-factor, and E_a is the activation energy for the diffusion process, also called activation enthalpy [44].

1.2.2 Lattice point-defects

Lattice point-defects play a fundamental role in the diffusion processes in semiconductors [5]. As it was shown before, the diffusion process can be modelled with Fick's law as a motion of atoms, and it can be considered as a thermodynamic equilibrium of two zones with a different atomic concentration. In some materials, the diffusion mechanism can be mediated by lattice point-defects, that influence the dynamic and the activation energy of this motion, and in particular the diffusion pre-factor.

Germanium is a crystalline material and its structure presents point defects, as any real crystals, thanks to its finite size and entropic effects at non-zero temperature. Crystal defects are in general terms translation symmetry breaking. Point defects are the simplest one and the most common are self-interstitial atoms and

vacancies. Point defects can be neutral or they can be charged, depending on several parameters, such as the material lattice structure [44].
Points-defects can be intrinsic defects or induced defects. Induced defects can be generated by external factors, such as irradiation with particles, ion implantation, mechanical stress and others. Intrinsic defects have a thermodynamic origin, and they have a thermodynamic equilibrium concentration with generation and annihilation processes. There are two processes for intrinsic point defects generation called *Frenkel and Schottky processes* [48, 53]. The former occurs when an atom leaves a lattice position, moving to an interstitial lattice position. Thanks to this process, a self-interstitial defect and a vacancy are generated which are called Frenkel pairs.

$$0 \longleftrightarrow V \; + \; I \tag{1.9}$$

The latter process happens when an interstitial atom is generated by its diffusion from a surface site into the bulk. Similarly, a vacancy can be generated from the bulk, when an atom moves towards the surface leaving a missing site in the bulk. Point-defects can also undergoe annihilation: indeed, the Frenkel reaction 1.9 is a reaction that can go in both directions, but the equilibrium point-defects concentrations are normally not fully restored with damage recovering processes. It is possible to define a variation of the *Gibbs energy* of the system during this last process, that can be expressed as follow for neutral point defect vacancies.

$$\Delta G_V = N_V(-\Delta S_V^f T + \Delta H_V^f) - k_b T \; ln\left(\frac{N_L!}{N_V!(N_L - N_V)!}\right) \tag{1.10}$$

with N_V the vacancy population in the lattice and N_L the number of lattice sites. The Schottky process generates vacancies or interstitial defects independently, and their concentration can be expressed as follows [44]:

$$C_V^* = C_L \; exp\left(\frac{\Delta S_V^f}{k_b}\right) \; exp\left(\frac{-\Delta H_V^f}{k_b T}\right) \tag{1.11}$$

$$C_I^* = C_L \; exp\left(\frac{\Delta S_I^f}{k_b}\right) \; exp\left(\frac{-\Delta H_I^f}{k_b T}\right) \tag{1.12}$$

for vacancies and interstitials equilibrium population respectively. ΔS_I^f and ΔH_I^f are the variations of entropy and enthalpy of formation for vacancies and interstitial point defects.
For the Frenkel process, the generation of a vacancy creates also a self-interstitial,

and vice-versa. So the population of vacancies and interstitials generated from this process must be equal this can be expressed as follows [44]:

$$C_I^* = C_V^* = C_L \, exp\left(\frac{\Delta S_I^f + \Delta S_V^f}{2k_b}\right) exp\left(-\frac{\Delta H_I^f + \Delta H_V^f}{2k_b T}\right) \tag{1.13}$$

In the event of the population of point-defects exceeding the equilibrium one, point-defects can condensate to form an extended defect, such as dislocations, clusters, stacking faults and others.
In germanium, the interstitials population is lower than the vacancies one [54], and this fact can be easily justified by their formation energies, which are equal to $2.35 \pm 0.1eV$ for vacancies (obtained by Ge self-diffusion experiments [51]) as opposed to the interstitial formation energy, which is estimated to be between $3 - 4eV$ [51, 55].

1.2.3 The dopant diffusion in Ge

Diffusion mechanisms in semiconductor materials can be different for different crystalline materials, but also for different impurities diffusing in the same crystalline matrix. This fact is related to different parameters, such as the dimension of the impurities, their nature (n-type, p-type, homovalent) and other properties, such as the charge of point-defects.
The most simple diffusion processes are the *direct diffusion mechanisms*, that are point-defects independent processes, consisting in the diffusion of an impurity through a crystalline lattice without the interaction with point-defects. The *direct interstitial mechanism* is a typical diffusion mechanism for small impurities in Ge, such as H and Fe atoms. This diffusion mechanism describe the migration of an atom between two interstitial lattice position in a crystalline lattice. Finally, there is another direct mechanism, the *direct substitutional mechanism*, which consists in a direct exchange between two first neighbouring atoms in a lattice position: one is the impurity atom, the other is a lattice atom (Ge atom in a germanium crystal). This process is rare because it requires a high activation energy. The most common diffusion mechanisms are mediated by point-defects: P, B, Ga, As and Sb, that are the most common doping atoms, diffuse in the Ge matrix with these diffusion mechanisms [50–52]. As a consequence, the population of vacancies in Ge is much higher than the interstitial population.

The most common diffusion mechanisms via point defects are the *pair diffusion reactions*: they are two different mechanisms involving a substitutional impurity

A_s paring with a vacancy V or an interstitial I defect, to form a mobile pair.

$$V + A_s \rightleftharpoons AV \tag{1.14}$$

$$I + A_s \rightleftharpoons AI \tag{1.15}$$

Another important mechanism is the *kick-out mechanism*: kick-out reaction can be written as:

$$I + A_s \rightleftharpoons A_i \tag{1.16}$$

where A_i is an impurity in an interstitial position. The opposite reaction is called *Watkins replacement mechanism*. Formally, the kick-out mechanism involves the creation of a mobile pair through kick-out reaction, while the dissolution of the pair, with the inverse reaction, is called Watkins replacement.
Lastly, the *Frank-Turnbull* mechanism is expressed as:

$$A_i + V \rightleftharpoons A_s \tag{1.17}$$

The reverse reaction is called dissociative reaction.
Vacancies interactions dominate most of the dopant diffusion processes in germanium, with the important exception of boron [55]. Indeed, the n-type doping atoms diffuse via vacancy mediated mechanism, while boron atoms diffuse via kick-out mechanism. Cu atoms in a substitutional site normally diffuse via Frank-Turnbull mechanisms, while in interstitial position diffuse via direct interstitial mechanisms.

As previously discussed, boron diffuses with an interstitial interaction, since the formation of BV pairs is not energetically favoured, and so its diffusivity is proportional with the interstitial population, while others dopant are population sensitive to vacancy. As discussed before, the population of interstitial point defects in Ge is much lower than the vacancies one; as a consequence, boron diffuses slower than other n- or p- type dopants in germanium, as shown in figure 1.10.
In the same graph, it is clearly represented another important trend: p- type dopant atoms (like aluminum) diffuse slower than n- type dopant atoms, though the diffusion mechanism is the same. This could be counterintuitive, but a clear explanation was given by Chroneos and Bracht [51]. Equation 1.14, ($V + A_s \rightleftharpoons AV$) represents the diffusion mechanism in general, but for n-type dopant atoms this reaction must be modified. Indeed, Chroneos at al [51] demonstrate that the vacancy charge status in germanium can differ, depending on the position of the Fermi level in the material, which in turn depends on the active dopant present in the material. In the n-type dopant case, the vacancy has a V^{2-} charge status,

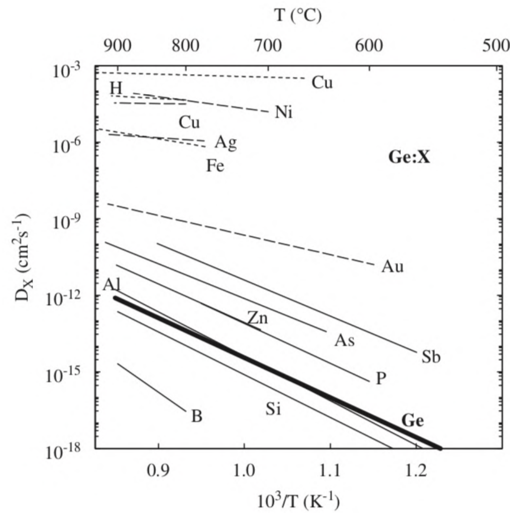

Figure 1.10. Impurities diffusivities in germanium as a function of temperature. Ge self-diffusion is reported in thick line. Long-dashed lines are reported for atoms normally dissolved in substitutional sites, but diffused in interstitial configuration via dissociative mechanism. The short-dash lines indicate the diffusion of mainly interstitial dissolved elements. [49].

while in p-type dopant case they are neutral V^0, as it can be seen in figure 1.11. As a consequence, for n-type dopant the diffusion mechanism presented in equation 1.14 must be modified as follows:

$$A_s^+ + V^{2-} \rightleftharpoons AV^- \tag{1.18}$$

On the contrary, for p-type dopant equation 1.14 becomes:

$$A_s^- + V^0 \rightleftharpoons AV^- \tag{1.19}$$

The charge state of the defects allows to qualitatively explain the higher diffusivity of n-type dopant with respect to p-type. Charged negative vacancies are electrostatically attracted by the positive ionised donors. Therefore the mobile AV^- complex is more stable and travels for a long path before dissociating by inverse reaction. A longer diffusion path means a higher diffusion coefficient. The same does not hold true for p-type dopant, that repels the charged vacancy and has no colombian attraction with the neutral one.
Another fundamental phenomenon is related to defects charge and is peculiar of n-type dopants.
The diffusion coefficient for n-type dopant is [50, 51]:

$$D_A(n) = D_A(n_{in}) \cdot \left(\frac{n}{n_{in}}\right)^2 \tag{1.20}$$

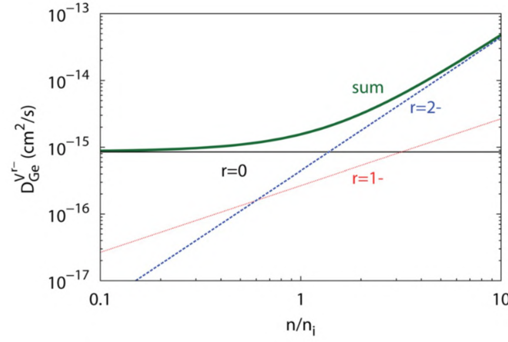

Figure 1.11. Individual contribution of vacancies to Ge self-diffusion for different doping level concentrations. Different vacancies charge lines are reported (charge r equal to 0, -1, -2) and the global contribution, denoted as sum, is reported with a green line. Reported data for T=700°C. [51].

where n_{in} is the intrinsic carrier concentration, or in other words, the carrier concentration under low doping regime. For germanium n_{in} can be expressed as [50]:

$$n_{in} = 7.3^{+5.4}_{-3.1} \times 10^{20}\ exp\bigg(- \frac{(0.44 \pm 0.05)\ eV}{k_b T}\bigg) cm^{-3} \tag{1.21}$$

The quadratic term that appears into equation 1.20 is related to the fact that the introduction of donor injects electrons into the material, which favours the generation of V^{2-} through the $V^0 + 2e^- \rightarrow V^{2-}$ reaction.
At low doping regimes ($c < n_{in}$), when the electron population is dominated by thermally generated electron hole pairs ($n = n_{in}$, intrinsic regime), the diffusion coefficient does not depend on dopant concentration and the usual diffusion shape can be seen (see ref. [50]) . As an example, diffusion profiles below $2\ 10^{18}\ cm^{-3}$ (the right side of in figure 1.12) are in this regime being n_{in} of the order of $1\ 10^{19}$ at the annealing temperatures for that experiment (in figure 1.12, on the left side) . Such profile can be fitted with the usual erf function as described in the previous paragraph.
The diffusion length and shape remarkably change for the profile at higher concentration. In this case the $(n/n_{in})^2$ term plays a strong role over most of the profile causing the evident diffusion length increase. Only in the deep part of the profile, the concentration drops causing a reduction of the diffusivity and inducing a box-like shape of the profile. This trend can only be reproduced by solving the non linear diffusion equation that results combining eq. 1.20 with eq. 1.3.

The intrinsic carrier concentration temperature dependence for n-type

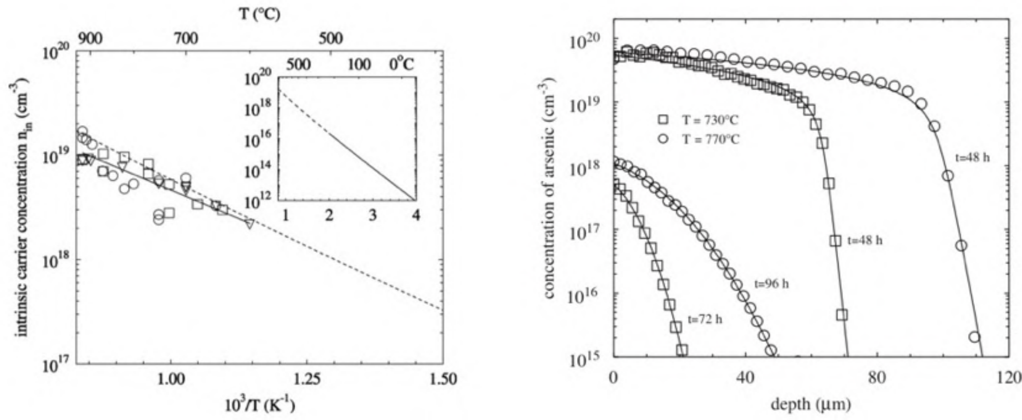

Figure 1.12. On the left, intrinsic carrier concentration n_{in} vs the inverse of temperature obtained from the modelling: P, As and Sb data are reported respectively in circles, squares and triangles [50]. On the right, concentration profiles of As in Ge obtained by diffusion at 730°C and 770°C. The two profiles that exceed 10^{19} cm^{-3} show a typical extrinsic diffusion behaviour, with a box-like shape [49].

dopants was calculated by Brotzmann and co-workers [50], and they are:

$$D_P(in) = 9.1^{+5.3}_{-3.4}\, exp\biggl(-\frac{(2.85 \pm 0.04)\ eV}{k_b T}\biggr) cm^2 s^{-1} \tag{1.22}$$

for P in Ge, while

$$D_{As}(in) = 32^{+21}_{-13}\, exp\biggl(-\frac{(2.71 \pm 0.06)\ eV}{k_b T}\biggr) cm^2 s^{-1} \tag{1.23}$$

for As in Ge, and finally

$$D_{Sb}(in) = 16.7^{+6.6}_{-4.7}\, exp\biggl(-\frac{(2.55 \pm 0.03)\ eV}{k_b T}\biggr) cm^2 s^{-1} \tag{1.24}$$

for Sb in Ge.

1.3 Monolayer Doping Technique

The Monolayer Doping (MLD) is a doping technique that was conceived in 2008 by C. Ho and co-workers [56] and then developed and expanded to other materials until today. MLD is based on the use of a molecular precursor adsorbed on a semiconductor surface as a source of dopant. The basic concept is to promote an interaction between the precursor and the semiconductor surface to form a monolayer (ML) with a fixed amount of dopant [57]. The ML can be adsorbed

with a physisorption or a chemisorption interaction, as long as it shows a self-limited adsorption behaviour that is mandatory for the dopant amount control. Normally a self-assembled monolayer [58] is preferred, but it is not necessary as it will be further described. This ML will act as a controlled dopant source which is injected into the semiconductor bulk by means of thermal treatments, inducing a dopant release from the molecular source and then a dopant diffusion and an electrical activation.
This technique is based on different materials science fields, starting from surface chemistry and surface analysis, to matter physics, regarding solid state diffusion and thin film doping characterisation. In fact, the first step of this technique normally requires a surface preparation in order to functionalise the semiconductor surface for the subsequent adsorption reaction. The molecular precursor is then adsorbed on the semiconductor surface by different reactions showed in the next sections, depending on the substrate nature, and normally requires a thermal or UV activated reaction. The thermal release of dopant and the diffusion process are normally conducted with standard or Rapid Thermal Annealing (see the technique section) treatments.

In the following sections, a brief introduction and a literature summaries on MLD technique on Si and Ge will be given, underline the most important results both in semiconductor surface chemistry and in semiconductor doping activations.

1.3.1 Monolayer Doping on Si

It is clear that the surface chemistry plays a crucial role in MLD technique, and for this reason it is mandatory to present an overview of Si surface chemistry.
The main contribution on Si surface chemistry is due to J.M. Buriak, that presented a *Chemical Review* on Si and Ge surface chemistry [59] in 2002, summarising different routes to Si chemisorption. Silicon presents on its surface its native oxide, a SiO_2 layer. For MLD technique on Si, two different surfaces are used for molecule adsorption: SiO_2 surfaces or oxideless surfaces. Different adsorption and diffusivity behaviour are shown for these surfaces: in particular, silicon oxide presents lower dopant diffusivity coefficients than a free Si surface [60, 61], that modifies not only the adsorption, but also the thermal treatments needed to diffuse and dope the semiconductor.
The most interesting surface group on Si surfaces is the Si-H because it can react with different functional groups, making Si surfaces available for several reac-

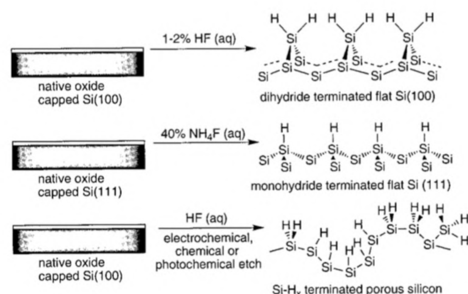

Figure 1.13. Silicon oxide removal and Si-H surface functionalization [59].

tions. Moreover, as it will be clearer below, this functionality is similar to the one studied in this work for Ge surface, and for this reason it is important to report its reactivity in this section.

To synthesise the Si-H functional group, the silicon oxide must be removed from the surface. This can be easily obtained with an acid etching, as showed in figure 1.13. The stability of Si-H group is reported to be more than tens minutes in air, since no degradation of Si-H functionalization within this period. Further reactions must be water-free, in order to avoid any oxidation of Si surface.

Thanks to Si-H functionalization, different reactions can be performed, as reported in figure 1.14 [62]. The Si-H group undergoes *Hydrosilylation* reaction, reacting with an allyl- group (1-alkenes) to form a new C-C bond (Si–C–C–R), with 1-alkynes forms Si–C–C–R on Si(100). This reaction requires a thermal or UV activation, so they can be divided into *thermal hydrosilylation* or *photochemical hydrosilylation* [62]. Others reactions are possible on Si-H terminated surfaces: Si-H can react with an alcohol molecule or an aldehyde to form a new Si-O-R bond, or by the application of an electrical potential 1-alkenes and 1-alkynes can react with the Si-H functional group. This last reaction is called *electrografting* reaction. Other less common techniques involve the chlorination of Si surfaces by the use of PCl_5 or chlorine gas, and the use of Si-Cl group as a gripping site for alkyl Grignard reagents (R-Mg-Cl) or alkyl lithium reagents (R-Li). The Si-Cl group can be also used for primary amines chemisorption, or thermal induced reaction of alcohol molecules, as reported in figure 1.14.

The idea of using these reactions to adsorb molecular precursors as a source of dopant for semiconductor doping was proposed the first time by a Berkeley University group in the USA in 2008. Historically, the MLD technique was proposed to dope flat silicon substrates and for the first paper was published on *Nature Materials* in 2008 [56]. They report that p- and n- molecular precursors were

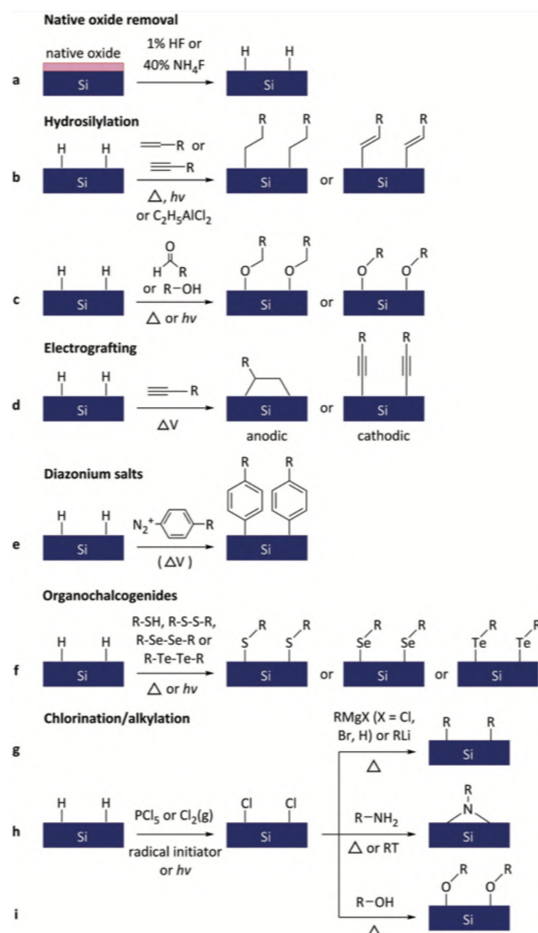

Figure 1.14. Surface chemical reactions with Si-H functionalization [62].

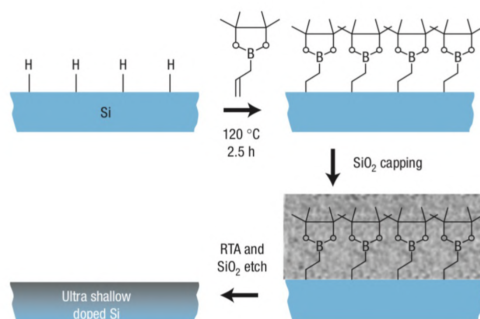

Figure 1.15. Schematic representation of monolayer doping technique as proposed by Ho and co-workers with ABAPE boron precursor [56].

successfully chemically adsorbed on Si substrate via surface chemistry, and after a subsequent annealing, doping atoms diffused inside Si and doped the semiconductor. They used allylboronicacid pinacol ester (ABAPE) as a B-containing reagent and diethyl 1-propylphosphonate (DPP) as a P-containing reagent. The deposition of both precursors was made in a solution of mesitylene, by heating the solution in the presence of a Si-H surface, prepared via HF etching. After the ML deposition, the monolayer was capped with a SiO_2 layer deposited with an electron beam evaporator. The diffusion in Si was promoted by rapid thermal annealing procedure between $950°$C and $1100°$C: B and P diffusion in Si is demonstrated by SIMS analysis. Moreover, they performed MLD not only on a flat Si, but also on a Si nanowire (NW), demonstrating probably the most important MLD feature: its *conformal behaviour to surfaces*.

A second work from the same group was published on *Nano letters* the follow-

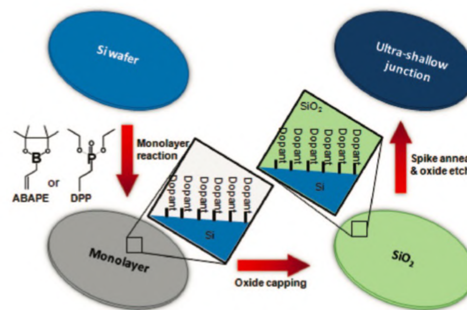

Figure 1.16. Schematic representation of wafer scale monolayer doping technique as reported in [63] .

ing year [63], demonstrating the possibility to form an *ultra-shallow junction* (USJ) starting with a MLD technique on Si substrate. Also in this paper, they used ABAPE and DPP precursors for p- and n- type doping. The paper reports that the process was carried out on an entire wafer, obtaining about 70% activation of the incorporated dopant.

A new version of MLD technique has been proposed in literature: the *Monolayer Contact Doping* (MLCD) in which the dopant-containing monolayer is not necessarily adsorbed directly on the target semiconductor surfaces, but it is deposited on another substrate called donor substrate [64, 65]. By putting in contact the donor substrate with an acceptor substrate, after an annealing process, also the latter is doped. The MLCD technique does not require any capping layer, because the upper part of the ML is covered by another target material. Thanks to this strategy, two samples are doped with the same source. Hazut and coworkers[64] use phosphine oxides molecules (di- and tri- phenylphosphine oxide

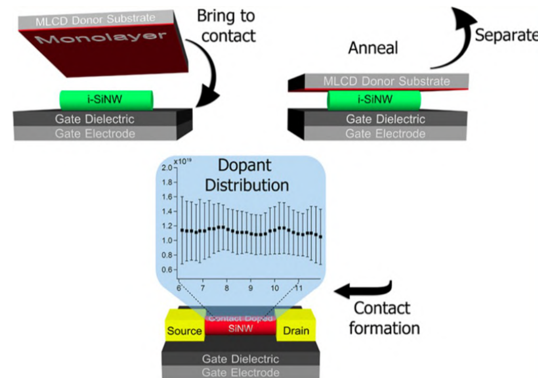

Figure 1.17. Monolayer Contact Doping applied on intrinsic Si nanowire as a channel material for FinFET [64].

and tetraethylmethylenediphosphonate) adsorbed on SiO_2 substrates as a source not only for flat Si wafers, but also for Si nanostructures. In particular, they doped a Si nanowire with MLCD technique, with the procedure described in figure 1.17, demonstrating the effectiveness of this technique at the nanoscale, also with non planar structures.

Figure 1.18 is reported the scheme of the creation of a p-n junction via MLCD

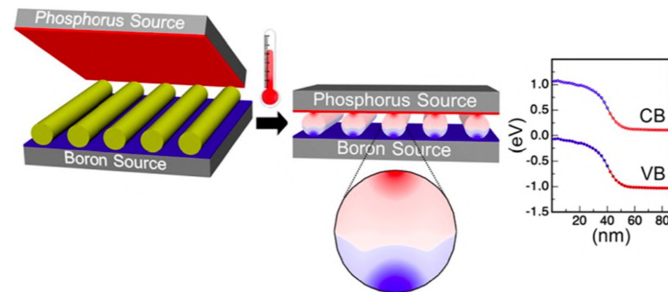

Figure 1.18. Monolayer Contact Doping applied on intrinsic Si nanowire, generating a p-n junction from two different monolayers [57, 64].

technique, starting from an i-Si NW with the diffusion of p- and n- type dopant from two different ML used as two different sources of dopant, in a one step doping procedure.
An interesting work by Veerbeek at al [66] presented an interesting comparison of MLD and MLCD on Si NW doping with boron and phosphorus contained molecules, evaluating also the use and the effects of capping layers on dopant amount.

The interaction of phosphine oxide monolayers with SiO_2 surfaces, used by Ho and co-workers, has been studied by Yerushalmi et al [67] in an interest-

ing *Angewandte Chemie* paper, in which the interaction between phosphine oxide molecules and silicon oxide surface is experimentally and theoretically investigated. Since the adsorption on Si-H functionalities of other molecular functional groups are well known, as previously reported, the phosphine oxides can interact in different ways with silicon oxidised surfaces.

Yerushalmi and co-workers propose that $P = O$ group undergoes H-bond inter-

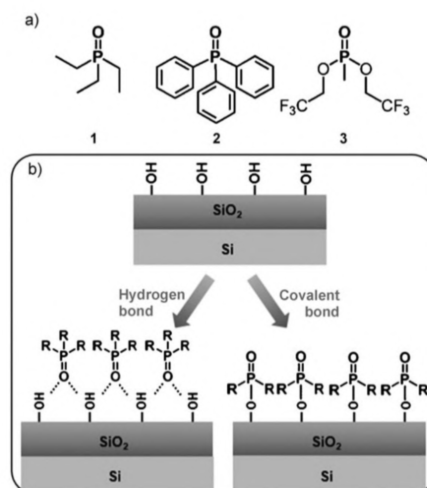

Figure 1.19. The three different molecular precursors studied by Yerushalmi et al. In the lower section, the two different interactions that phosphine oxide monolayer can perform on SiO_2 surfaces [67].

action with SiO_2 if there are phenyl- like substituent groups, otherwise, in presence of $R-O-$ like substituent, the adsorption could be involving the creation of a chemical bond. This behaviour is clearly due to the $P = O$ substituent electron-withdrawing effect that can interact in different ways with hydroxyl terminating surfaces, like SiO_2. The self-limiting behaviour in these systems is normally guaranteed, thanks to the relative short range nature of H-bond interactions: in fact, not only a chemisorption process can in principle show a self-limiting behaviour, but also a physisorption process can show it. As proposed by Yerushalmi and co-workers, a chemical rinsing with a solvent presenting a strong H-bond capability should remove physisorbed molecules, but not chemisorbed molecules, suggesting a practical method to verify the nature of the adsorption.

More recently, Arduca and co-workers [68] studied quantitatively the adsorption of phosphine oxide on SiO_2, and the diffusion from these molecule is well characterised.

Longo and co-workers [69] extended the MLD technique by studying the adsorption of $-OH$ containing molecules on $Si - H$ functionalized surfaces. They

study with DFT simulations and experimentally verify the chemisorption of octadecylphosphonic acid (ODPA) on $Si - H$ surfaces by the creation of a new $Si - O - P$ bond, with the elimination of H_2 molecule. Moreover, thanks to DFT calculations, they evaluate the energy barriers of physisorption and chemisorption, showing that not only both mono- and bi- dentate chemisorption are possible, but also tri- dentate chemisorption is reachable, involving the $P = O$ group. The Longo team demonstrates that ODPA contains a $P - CH_2 - CH_2-$ chain that can be thermally removed over $500°$C, highlighting for the first time a crucial step for the molecule degradation with quantitative calculations.

One of the characteristics of MLD technique is to cover all the Si surfaces, with a self-limiting behaviour determined by the active surface sites and by the steric hindrance of molecules. So, how is it possible to dope selectively some regions, and to chemisorb a different amount of dopant on silicon surfaces?
The possible solutions to the first question were analysed and solved by Voorthuijzen and co-workers [70], by combining the MLD technique with a lithography procedure. The idea is to use a standard thermal hydrosilylation chemistry to

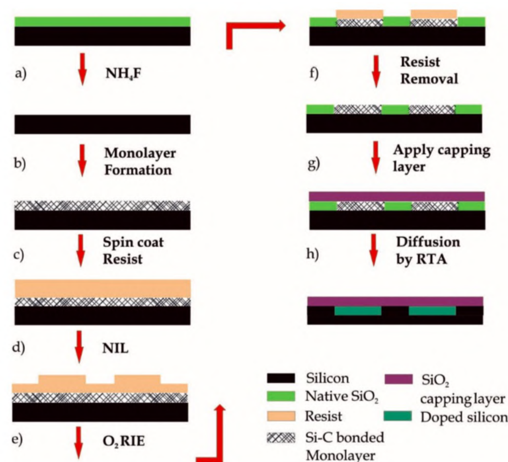

Figure 1.20. The Monolayer Doping tecnique (monolayer deposition a,b, and diffusion g,h) with the Nanoimprinting Lithography (c,d) and Reactive Ion Etching (e) steps to pattern the ML deposition. [70].

form a ML, a then patterning the ML with a *Nanoimprinting Lithography* step, creating a micro-patterning. Using a *Reactive Ion Etching* step, the residual layer exposed is removed, creating a patterned ML deposition on Si surface, as reported in figure 1.20. Thanks to this process, phosphorus ML is patterned in $100\ \mu m$ wide regions, that generate, after a capping and a diffusion process, a phosphorus doped region with a $200\ \mu m$ period. This paper [70] demonstrate not only the possibility of directly patterning a monolayer dopant source, but also that it is

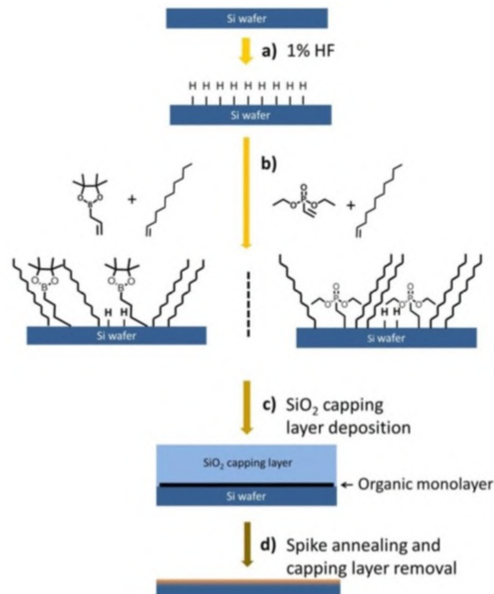

Figure 1.21. Mixed MLD process for n- and p-type doping [71].

possible to maintain this patterning after the diffusion process, with only a small lateral doping spread due to the unavoidable lateral diffusion.

Ye and co-workers [71] propose an interesting approach to control the amount of dopant by using a mixed-monolayer deposition on Si surface. By mixing dopant-containing alkenes with structurally analogous alkenes that not contain any dopant atoms (only carbon and hydrogen atoms), it is possible to tune the amount of dopant deposited on Si surface. Indeed, these two molecules are pre-mixed in a desired ratio, and then they are grafted during the same deposition process, as reported in figure 1.21. Thanks to the initial molecules ratio and the steric hindrance, the adsorbed amount of dopant can be arbitrary reduced from a maximum value (that corresponds to the deposition without any mixing with other alkenes) down to a desired one. The residual carbon fraction coming from to the undoped molecules fraction does not create any issue, since it was demonstrated that C segregates at Si surfaces after the thermal degradation of ML molecules, and so it is removed during the capping removal step.

Finally, a MLD application on a Si photovoltaic cell is reported in literature [72], where MLD is applied on Si nanowires grown on p-doped Si substrate by metal catalysed CVD.

Other works are present in literature on MLD technique, such as arsenic Si doping

[73], or silica nanostructures doped via MLD [74]; other publications can be found in these reviews on MLD [57, 62, 75].

1.3.2 Monolayer Doping on Ge

The Monolayer Doping technique was discovered and applied on Si substrate, as described above, while MLD on Ge substrate still remains quite unexplored. Here, the results present in literature will be reported.

The first literature on Ge MLD dates back to an *Ion Implantation Technology Proceeding* by Long and co-workers [76] in 2014, in which preliminary results on As based molecules on Ge (100) were shown. Long at. al. deposited the triallylarsine (TAA) molecule on Ge, after a HF (10% water solution) oxide removal step and the formation of $Ge - H$ group. The reaction was conducted in an inert atmosphere by using a UV lamp at 254 nm for 3 hours. Then, after a rinsing procedure, a SiO_2 capping layer was deposited by sputtering and, after that, samples were thermally treated at $650°$C for 1, 10, 100s. In figure 1.22, an

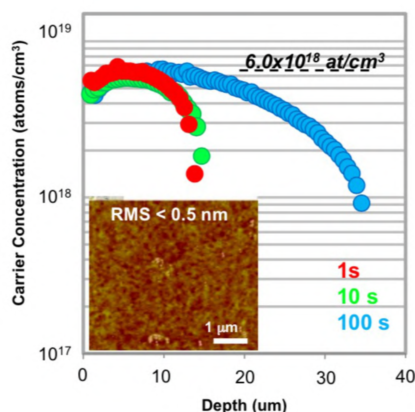

Figure 1.22. Active carrier concentration obtained by extracting a depth profile from Electrochemical Capacitance-Voltage (ECV) of As doped Ge. A 6 10^{18} $atoms\ cm^{-3}$ active carrier concentration is obtained. [76]

Electrochemical Capacitance-Voltage (ECV) measure is shown, demonstrating that a $6\ 10^{18}$ $atoms\ cm^{-3}$ active carrier concentration is obtained by As MLD on Ge.

A recent paper by Long and co-workers [77] in 2017 highlight and expand the triallylarsine MLD study on Ge. In particular, TAA molecule is deposited on 2D structures (as shown in figure 1.23), simulating a Ge Fin doping process. Long at al studied the effect of a SiO_2 capping layer on Ge MLD technique, showing

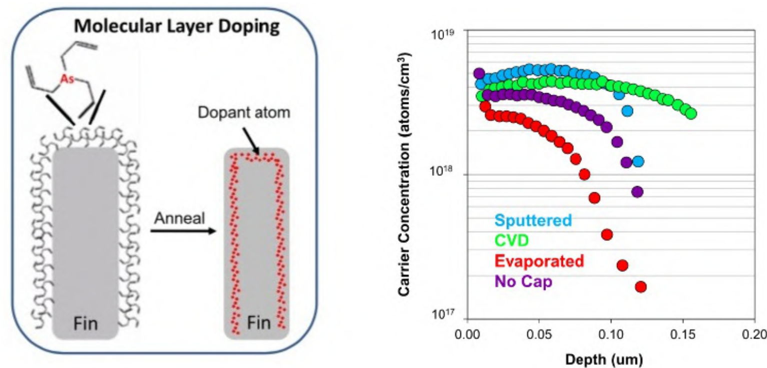

Figure 1.23. Description of MLD process on Ge FIN structure (on left), active carrier concentration obtained by extracting depth profile from ECV measurement for different capped samples annealed at 650°C *for 60s via RTA (on right) [77].*

the different effects of the capping nature: in particular, by looking at the graph trend (figure 1.23, right graph), the density of SiO_2 capping layer seems to be the most important parameter for As diffusion in Ge. Moreover, the evaporated SiO_2, that should be the less dense material this comparison, appears to be worst than the no capping case. In conclusion, these two studies by Long and co-workers demonstrate the effectiveness of As-based MLD on Ge, reaching $6\ 10^{18}\ electrons\ cm^{-3}$ active carrier concentration, even in a non-planar geometry.

Alphazan and co-workers published a paper on antimony MLD on Ge [78] in 2017, expanding the MLD technique also to Sb based molecules. The Sb precursor used in this work is a non commercial silsesquioxane (Hepta-isobutyl polyhedral oligomeric silsesquioxane, POSS) with a tri-ester antimony functionalization (POSS-Sb), which contains Sb atoms in a $Si - O - Sb$ site in the POSS cage. The precursor deposition was done by a reflux in acetonitrile solution of POSS-Sb overnight after a complicated Ge cleaning procedure with several acetone and methanol cleaning steps, followed by a re-oxidation with H_2O_2, and a final rinsing in citric acid (1M) that should remove germanium oxide (a strong GeO XPS component still clearly remains in XPS spectrum). The POSS-Sb functionalized surface is then capped with a SiO_2 capping layer and annealed at 550°C for 5 min and then at 600°C for 10s with a RTA machine. The Sb diffusion in Ge was tested via SIMS and electrical measurements, but several doubts raised from these measurements:

- the SIMS depth profiles show only a surface signal peak (below 10 nm) and some tails that are not totally compatible with an equilibrium Sb diffusion

profile in Ge.

- Moreover, the electrical measurements were done with 4 AFM tips, with probe spacing in the range of some μm, as reported in the work. This fact means that the detected electrical activation is an extremely localised information, while normally the electrical measurements are a mean value over several mm or cm square area.
- These data are more compatible with localised doped regions, since no larger scale electrical activation data are given.

1.4 Germanium surface

The germanium presents a particular surface behaviour, that strongly differs from the silicon one. First of all, germanium presents a mixed native oxide formed by GeO and GeO_2, instead of silicon that present only SiO_2. The formation of GeO_x is spontaneous and it forms as a simple consequence to air exposure. The two different components of germanium oxide present different behaviours: the GeO_2 component is water soluble (warm water [3]), while GeO can be removed only by the use of strong acid, such as HF 10% [3, 79]. Germanium oxide removal normally generates Ge-H surface terminations, especially if the oxide removal is intercalated by H_2O rinsing [79]. The Ge-H termination is stable for some minutes in air exposure, and the re-oxidation was studied in literature by Park and co-workers [80]. The surface oxidation occurs either in air and in water: in this last case, it is normally enhanced, especially if it is heated. The oxidation forms as a first product the GeO component, while the GeO_2 component is predominant after a long air / water exposure [80].
Germanium can be oxidised by H_2O_2, HNO_3 and their mixture also if diluted in water, and the main product is the GeO oxide form. Unfortunately, there is no method to form only one oxide component: the GeO is oxidised to GeO_2 during time, while a perfect GeO_2 has not been synthesised yet [3].
An interesting paper written by William and co-workers [81] study the equilibrium of the reaction $Ge + GeO_2 \longleftrightarrow GeO$ for the first time. Pauleau and co-workers [82] continued the results, presenting some interesting studies on Ge oxidation mechanisms and extracting them some thermodynamics properties that will be used also in this work. In particular, germanium oxide sublimation occurs as a consequence of the following reactions. First of all the GeO_2 is transformed

in GeO and then the GeO sublimates [82]:

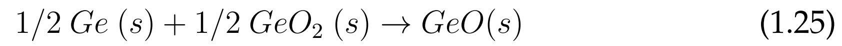

$$1/2\ Ge\ (s) + 1/2\ GeO_2\ (s) \rightarrow GeO(s) \tag{1.25}$$

$$GeO(s) \rightarrow GeO(g) \tag{1.26}$$

This process is thermally activated and obey Arrhenius' law:

$$K \ = \ K_0\ exp - \frac{E}{RT} \tag{1.27}$$

with $E = 60\ kcal/mol$ and $K_0 = 4.5\ 10^{11}\ mg\ mm^{-1}$.

Chapter 2

Methods

In this chapter, experimental methods adopted in this work will be described. The specific chemical and physical processes used to produce phosphorus and antimony monolayer will be described at the beginning of the related chapters (chapter 3 and 4 respectively). Here in section 2.1 we describe the annealing steps that are used to study diffusion processes for both the precursors kinds. Furnace and Rapid Thermal Processing will be described first, while pulsed laser melting (PLM) is described below. The former are equilibrium standard thermal processes, the latter is an out of equilibrium process.
Different surface and bulk analysis are adopted in order to characterised the precursor adsorption and diffusion: they will be presented in section 2.2.
Rutherford Backscattering Spectrometry (RBS) and *Nuclear Reaction Analysis* (NRA) were used to determine the total amount of dopant adsorbed on semiconductor's surfaces and will be described in Section 2.2.1 and 2.2.2.
X-ray Photoelectron Spettroscopy (XPS) was adopted to investigate the surface chemical state; thanks to the possibility to vary the photoemission angle (called take-off angle) by varying the sample orientation, also a quantitative estimations can be done by modelling and fitting the angular dependence of XPS peak intensity with a multi-layer simulation tool. This technique is called *Angle Resolved XPS* (ARXPS) and will be described in Section 2.2.3.
X-Ray Absorption Spectroscopy (XAS) in grazing incidence condition is describe in Section 2.2.4. This powerful technique were adopted to detect EXAFS oscillation at phosphorus K-edge, in order to determine the first shell structure around the P.
Secondary Ion Mass Spectrometry were adopted to study the diffusivity of doping species diffusing on Ge bulk, and *Van der Pauw - Hall* electrical measurements were adopted to test the electrical activation. These technique are described in

section 2.2.6 and 2.2.5 respectively. Finally, Infrared Spectroscopy is described in section 2.2.7: in this work, it was used to analyse the molecular precursor structures before and after the adsorption process. In particular, the Diffuse Reflectance Infrared Fourier Transform Spectroscopy was used to study the IR adsorption on adsorbed molecular layers on Ge powder, in order to characterise the adsorbed layer also after the deposition process by increasing the ML signal using a higher Ge surface to volume ratio.

2.1 Processing techniques

2.1.1 Thermal processing

Tubular furnace

The most common treatment used in this work is a tubular furnace, equipped with a quartz tube and a transfer system as can be seen in figure 2.1. This furnace was designed in order to permit a full control of the inner quartz tube atmosphere: for this scope, a vacuum system and flow-meters are connected with the tube, allows us to evacuate and refill the tube with the desired gas. In this furnace,

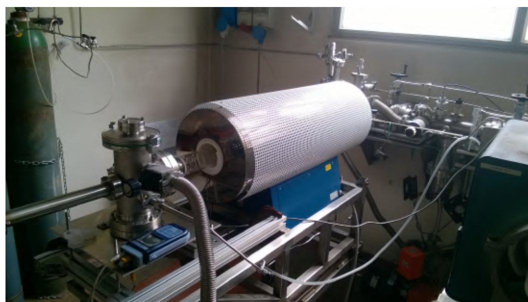

Figure 2.1. Tubolar Furnace with a fast entry system at Legnaro National Laboratories.

it is present a fast entry chamber that gives access to a quartz vessel connected to a transfer system, that allows the sample handling by a magnetic coupling with the inner rod. Before any thermal process, the sample is positioned on the vessel and 5 vacuum/gas cleaning cycles are always done to remove any contaminants from the inner atmosphere. The furnace can reach temperature over 1000°C, and ramps ranging from $50°$ to 150°C/min, depending the set point values.

Rapid Thermal Processing

The Rapid Thermal Processing (RTP) machine, also known as Rapid Thermal Annealing (RTA) machine, is a particular apparatus that allows to thermally treated samples with a rapid thermal ramps. The RTP is an equipment widely used in semiconductor applications and is designed for semiconductor wafers process. The machine used in this work is the commercial *RTP Jipelec Jetfirst 150* reported

Figure 2.2. RTP Jipelec jetfirst 150 machine.

in figure 2.2. This apparatus is a cold wall furnace, which allows to process wafer up to 6″, to reach a temperature up to $1200°$C, with ramps up to $150°$C/s. The machine present an isolated process chamber that is connected to a vacuum pump and with flow-meters (N_2 and O_2 gases). The heating is guaranteed by 18 halogen

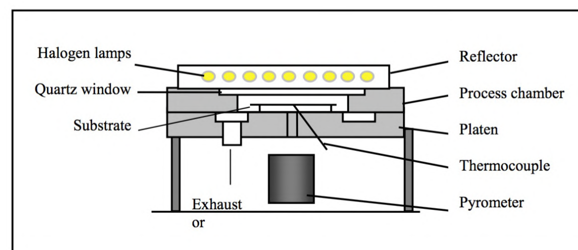

Figure 2.3. RTP chamber scheme.

laps, separated from the chamber by a quartz window. The power control of the lamps is driven by a feedback system connected to a thermocouple or a pyrometer that measure the Si wafer temperature. The system allows to upload recipes in which several parameters, like the thermal ramps, the plateaux temperatures, pumping, venting and the gas fluxes programmed as a function of time allowing to perform complex thermal processes.

This machine allow to strictly control thermal processes on semiconductor materials, that is a fundamental tasks to study impurities diffusion, even in seconds time regimes. The use of pyrometer as a temperature reading device, periodically calibrated with a thermocouple embedded on a Silicon wafer, involves a maximum error of 3°C.
Typically our experiments are performed on 10x10mm pieces of wafer that are placed on top of the reference wafer. This is not an issues for temperature control when silicon samples are used, since the sample has the same emittivity of the wafer and adsorb light power at the same way. The use of Ge samples has to be more carefully considered. Being the pyrometer calibrated with a Si wafer, the supporting wafer has to be made of Silicon. Ge emissivity is slightly different and a different thermal power exchange has to be considered. By setting a 2D model of the RTA by finite element thermal calculations, we have analysed the errors induced by the use of Ge sample in RTA. It turns out that the setting temperature is reached inside 5°-10°C error in the temperature ranges used in this thesis (550°-800°C). This is mainly due to the thermal exchange between the Si wafer and the sample that compensates the emissivity difference. The different Ge emissivity with respect to Si induces a delay of the order of few seconds while reaching the setting.

2.1.2 Pulsed Laser Melting technique

Pulsed Laser Melting (PLM) is a technique used for thermal treatments based on a surface localised heating of materials induced by an UV pulsed laser beam. The localised heating induced a surface melting. It occurs until a certain depth that is defined as maximum melt depth. At the end of the pulse, the liquid starts to cool down mainly by heat transfer to the bulk and a re-solidification process occurs, as soon as the solid liquid interface reach back the melting temperature. A typical time scale for temperature exchange between liquid and bulk and regrowth is on the order of 100 ns, therefore shorter laser pulse duration are used to have an impulsive melting process (for example the laser used in this thesis has a 7 ns laser pulse duration).
The materials treated with PLM technique are normally mono-crystalline materials and the re-solidification process is an epitaxial regrowth that starts from the solid-liquid interface and the regrow tread towards the surface, disposing atoms with the same crystalline structure of the bulk material. During this process, impurities are englobed in the crystalline lattice, in a strongly out-of-equilibrium

process. As a consequence, the solid solubility limits are normally exceeded.
The PLM technique requires a pulsed laser source with a specific energy density that allows to melt the surface of the sample: this means that the wavelength of the laser must be absorbed by the target material in a shallow depth. UV light is suitable to this aim since it is absorbed with an absorbed length of the order of few nanometers in semiconductors. More in detail, the Laser we used, with a 355 nm wavelength, has an absorption depth in Ge of about 10 nm at room temperature for undoped crystals. Such depth decreases by increasing temperature, doping and in liquid Ge. Therefore, most of the power is absorbed inside such length and the heating can be considered very superficial. Ge thermal conductivity redistribute such heat in the sample and melt depth is the portion of sample that reach the melting point. Such value strongly depends on the total energy density released on the sample, and of course there will be a minimal energy over which melting occurs. The duration of the laser beam is in the nano-second scale since the absorption of UV photons by materials (normally is used semiconductor materials like Si and Ge) is due to the excitation of electron in the conduction band and a subsequent de-excitation in a ps time range, causing an efficient heating of the material. As an example, for Si and Ge, the minimum energy density of laser beam is in the order of one - two hounder of $mJ\ cm^{-2}$.

The most important consequence of a PLM material processing are based on the following key points:

- The liquid phase epitaxial regrow induced by PLM can efficiently suppress defects present on the treated area if they are present on the melted zone. In literature, this technique were successfully used to suppress ion implantation damage (such as ion induce amorphization) and also to improve the electrical activation of dopant implanted with ion implantation technique [83].

- Since the diffusivities in liquid ($10^{-5} - 10^{-4}\ cm^2/s$) are normally order of magnitude higher than solid state diffusivities ($10^{-12}\ cm^2/s$), the PLM technique is a very good doping technique to create box-like doping profile. The interface between liquid and solid material acts as a diffusion stopper, since the difference of diffusivities are so huge that doping species penetration into the crystal can be neglected [83, 84].

- By tuning the energy of the incoming beam, the maximum melt depth can be easily tuned: thanks to this, also ultra shallow junction (USJ) can be created [84, 85].

- As reported by several measure and modelling [86, 87], the liquid-solid interface is characterised by a very strong thermal gradient (10^8 C/cm) and this is the cause of two important fact: the first is that the regrow is very rapid, and this gives to PLM technique the properties of out- of equilibrium technique since the incorporation of heteroatom (dopant atoms or atoms to form alloys) on the matrix can exceed orders of magnitude the equilibrium segregation coefficient [87]. The second consequence is that the bulk sample remains at almost room temperature: this has an important consequence for pure materials like high purity Ge (HPGe), since no bulk contamination is induced during PLM processes. As demonstrated in literature, this is a technique that allows high concentration of doping and at the same time no bulk contamination [43].

In this work a Nd:YAG laser was used to perform PLM on functionalized Ge to degrade and diffuse the surface source of dopant. The threefold frequency (wavelength equal to 355nm) of a Quantel YG981 Nd:YAG laser was used, presenting a 7 ns pulse and a 7mm circular beam. The energy density of laser was around $400\ mJ\ cm^{-2}$ even if the circular beam presents a gaussian distribution of the energy on its section, as reported in figure 2.4 [1]. The fixed energy, the lim-

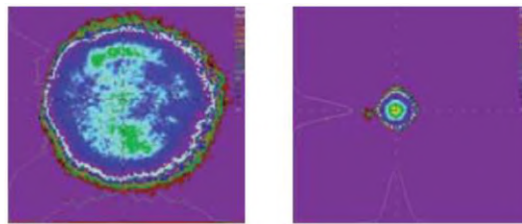

Figure 2.4. Quantel YG981 near (left) and far (right) field spatial energy profile; 1.6J at 1064nm, 10Hz.

ited stability and a non perfect homogeneity make this instrument not suitable for process optimisation but it was successfully used in this thesis to make some proof of concept of PLM doping feasibility, starting from MLD sources. Actually, under the SENSITISE project, a more suitable facility is operative at DFA and process optimisation will be performed in future work. This laser is installed at Italian National Institute of Nuclear Physics (INFN), Legnaro National Laboratories, at Legnaro Padova.

[1] Laser characterisation presented on Maximilian Linser's Master Thesis, title: Germanium Doping by Aluminium Ion Implantation and Laser Thermal Annealing, 2015/2016, University of Padova.

Others information on PLM technique can be find in [84, 85, 87–91] and the textbook [83]. On Ge doping with PLM techniques there are a lots of works: n-type doping [41, 92–94], p-type doping [95], and oxygen contamination [96].

2.2 Characterisation techniques

2.2.1 Rutherford Backscattering Spectrometry

In this thesis, the Rutherford Backscattering Spectrometry (RBS) technique is used to characterise functionalized semiconductor surfaces and to quantify the amount of adsorbed precursor. In this work, I will not treat in detail the fundamentals of the technique, but I will only report basic concepts and no-standard measure conditions.

Basic concepts

The RBS technique is based on the study of collisions between an accelerated ion beam and the atoms of the target. The number of ion particles interacting with nuclea and revealed by the ion detector (called Y) can be expressed as:

$$\frac{Y}{Q} = N_s \frac{d\sigma(\theta)}{d\Omega}\Omega \tag{2.1}$$

where θ is the scattering angle, Y is normalised to Q, the total incoming ion, N_s is the atomic density of a specific atomic species, Ω is the detector solid angle, and $\frac{d\sigma(\theta)}{d\Omega}$ is the differential cross section. If the collision can be treated as a pure Coulomb and elastic interaction, the technique is properly called Rutherford Backscattering Spectrometry, otherwise it is named Resonant/Non-Rutherford Backscattering Spectrometry or Nuclear Reaction Analysis (see 2.2.2), indicating a elastic non Coulomb iteration or the presence of a nuclear reaction induced by the incoming beam.
The Rutherford cross section in the center of mass can be expressed as:

$$\frac{d\sigma(\theta)}{d\Omega} = \Big(\frac{Z_1 Z_2 e^2}{8\pi\epsilon_0 E}\Big)\frac{1}{sin^4(\frac{\theta}{2})} \tag{2.2}$$

Under the elastic interaction assumption, that imply the energy and the momentum conservation, the out-coming ion energy E_1 after a scattering event can be simply correlated with the incoming energy E by a factor K, as follow:

$$E_1 = K[M_1, M_2, \theta]E \tag{2.3}$$

$$\frac{E_1}{E} = \Big[\frac{\sqrt{M_2^2 - M_1^2 sin^2(\theta)} + M_1 cos(\theta)}{M_1 + M_2}\Big] \tag{2.4}$$

Equations 2.3 and 2.4 demonstrate that the out-coming energy of the beam depends on the target atom mass M_2 once the ion mass M_1 the scattering angle and the incoming energy are experimentally fixed. If the atoms at the surface of a sample are considered, E is simply the beam energy, but if we want to describe the scattering on inner atoms the incoming ion energy loss has to be considered.
Energy loss phenomenon at MeV energy regime is mainly due to the interaction of ions with material's electrons. Depending on the type of the atomic masses presented on a target, the energy loss changes. Energy loss is described by stopping power functions $dE(E)/dx$ that quantify the infinitesimal energy loss when crossing a dx sample thickness. They are empirically determined over large database sets [2].
The energy of an ion before a scattering phenomenon E can be expressed as the energy of a beam E_0 subtracted by the energy loss between the surface and the depth x at which the scattering event happened:

$$E = E_0 - \Delta E = E_0 - \int_0^x \left(\frac{dE}{dx}\right) dx \tag{2.5}$$

After the event of elastic scattering, the ions escape from the sample. The energy loss during this path is brings to a final energy of the particles E_2 that can be described by:

$$E_2 = KE - \Delta E_2 = KE - \int_0^{\frac{x}{cos\theta}} \left(\frac{dE}{dx}\right) dx \tag{2.6}$$

E_2 is measured by the detector for each particles and a spectrum represents the number of particles measured at each out-coming energy.
The stopping power factor for a specific atomic species is defined as:

$$\epsilon = \frac{1}{N}\left(\frac{dE}{dx}\right) = \frac{dE}{dD} \tag{2.7}$$

where N is the atomic density of the material and ϵ is typically expressed as an energy unit of areal density and where D is the crossed areal density of the material.

[2]Database available online at http://www.srim.org

In the case of a generic alloy/material A_xB_y, the stopping power factor can be estimated with the Bragg rule:

$$\epsilon_{A_xB_y} = x\epsilon_A + y\epsilon_B \tag{2.8}$$

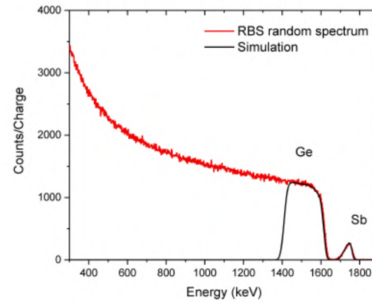

Figure 2.5. In red, a RBS spectrum of a Ge sample with a Sb diffused in the first 100 nm. The spectrum is acquired in random incidence beam condition, with a 2 MeV α beam. In black, a RBS spectrum simulation for Sb quantification, truncated about 300 nm below the Ge surface.

Main physical informations

The main physical quantities that can be derived from an RBS spectrum are:

- *The mass of the elements presents in the sample*. The mass of all the element present between the surface and the maximum probed depth. The maximum probed depth is the most deeper region of the sample from which particles, after the scattering event, can exit the sample and reach the detector. This depth is strictly correlated to the composition of the target and its stopping power, as reported before.

- *The total amount of species*. Any species in the sample can be deduced by equation 2.1, where Y is the total yield coming from a given species obtained by integration of particular spectrum portions. Equation is strictly valid if particles have a single energy value while crossing the region of the element. If this does not occur, spectrum simulation is performed to get precise results. Simulation is performed numerically solving the above equations on the basis of a trail sample chemical profile and using experimental parameters such as total number of injected ions, scattering angle, solid angle energy calibration. Moreover tabulated stopping powers are used.

- *The thickness of layers*. The thickness of a layer is determined by considering the energy distribution of layer species inside the spectrum. There are approximated formula to ΔE_2 energy interval to the thickness but generally simulation is performed.
- *The crystallinity of a material*. The crystallinity of a material can be evaluated by using the channeling phenomenon, described in the next paragraph.

In this work, the RBS analysis are conducted at AN2000 accelerator at INFN *Legnaro National Laboratories* in Legnaro (PD), with a $^{4}He^{+}$ ion beam accelerated up to 2 MeV. In the light of all sample compositions and ion energy ranges, all the RBS measurements can be treated as purely elastic collision based experiment.

Channeling phenomenon

The channeling is a phenomenon, that occurs when a collimated ion beam interacts with a high quality crystalline materials: the charged particles trajectory are confined by the periodic potential generated by the ordered atoms. Positive particles are repelled by atomic row or lattice planes and this changes the probability of interaction between beam ions and the atom's nuclei and decrease the backscattering yield when the ion beam is aligned to crystalline planes or axes. In other words, Rutherford (but also nuclear) cross section may strongly varies with the orientation of the beam with respect to the crystal orientation. This phenomenon open the possibility to evaluate structural properties of samples such as lattice location of impurities atoms, defect characterisation and strain measurements in multilayer samples [97]. On the other hand, the angle dependent interaction probability variation is a source of systematic error when standard RBS analysis is applied. RBS cross section (but also energy loss) are strictly valid only for isotropic means as amorphous or polycrystalline materials and may strongly strongly vary for single crystals. The trick to restore isotropy without destroying the sample is to collect the RBS spectrum as an average of many spectrum taken ad different angle smoothing the channeling effects. This strategy is called "Rotating Random". As an example, in figure 2.7 a comparison between a rotating random spectrum and channeling spectra is shown.
Another indirect advantage for which channeling phenomenon is to exploit the overall decrease of yield from crystalline bulk when the beam is aligned with an axis or a plane. Thanks to the decrease of yield, also the unwanted pileup signal is minimised and the overload of acquisition electronic system is avoided. Since

Figure 2.6. Measurement chamber with channeling goniometer at AN 2000 accelerator, 60 deg. beamline.

the pileup signal is generated by a missing recognise of two separated pulses come too close together in time, this phenomena create a background noise in RBS spectra in high energy range and so it can be minimised by decreasing the total RBS yield. Thanks to this method, also an extremely low signal coming form a ML can be detected, thanks to the possibility to measure samples with a high ion beam current and a low pileup background in the ML signal region.

References for this section [98] [99] [97], channeling [100] [101].

2.2.2 Nuclear Reaction Analysis

In this work, the Nuclear Reaction Analysis is used to detect the phosphorus amount present on Ge samples. The use of this technique is necessary due to the lower mass of phosphorus compared to the germanium one; that would produce a too small P signal superimposed to a much bigger Ge background, even if channeling would be used. After nuclear reaction, the reaction products gets energy by the mass excess and therefore easily emerges from the background. The nuclear reaction exploited in this work is:

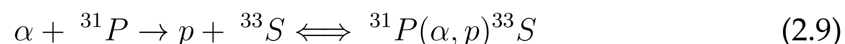

$$\alpha + {}^{31}P \rightarrow p + {}^{33}S \iff {}^{31}P(\alpha, p)^{33}S \tag{2.9}$$

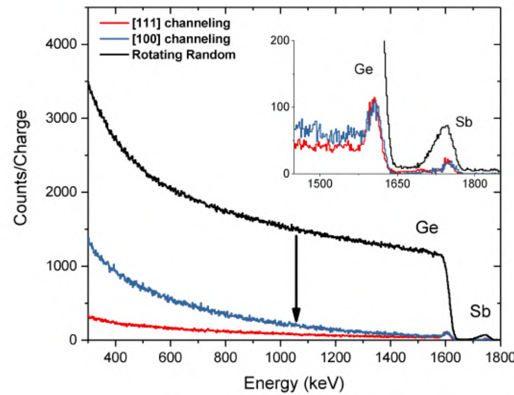

Figure 2.7. RBS spectra of a mono-crystalline Ge sample with a high concentration of Sb diffuse in the first 100 nm. Red and blue lines are spectra acquired in axial channeling conditions, compared with the black one, that is a rotating random spectra. The red curve is a 111 axial channeling, and the second is a 100 axial channeling. The yield decrease of Ge signal is highlighted with the black arrow in the graph. In the in-box, a zoom in the Sb region of the spectra is shown. As can be clearly seen, the Sb yield changes with Ge axial channeling conditions, since Sb is distributed in Ge matrix, almost placed in a substitutional lattice position, i.e. at the same place of a Ge atom.

In our case, the alpha particles are generated by a Van de Graaff accelerator as a continuous beam and the ^{31}P atoms are all the P atoms present in the adsorbed molecules on Ge [3]. If the ^{31}P is hit by a sufficient energetically α particle, an unstable atomic nucleus is created and its decay products the emission of energetic protons with the creation of a ^{33}S atoms. Since the mass of the products is higher than the mass of the reagent, energy is released in the reaction that is transferred or to ^{33}S or to the proton. The reaction can product ^{33}S nucleus at different energies, causing the emission of protons with different energies. When ^{33}S nucleus is at the ground state, the most energetic proton is emitted, called p_0 [102].

By counting the proton emitted from the sample with an appropriate detector (see figure 2.8), it is possible to correlate this number with a P atomic dose on sample. The probability (or better the cross section) that connects the proton yield to the target atom areal density has many sharp resonances as a function of the beam energy: the $^{31}P(\alpha, p_0)^{33}S$ reaction cross section is reported in Figure 2.9. The most high and sharp resonance peak present in this spectra is positioned at 4.96 MeV α particle energy; this peak ensures the most high probability of the event.

[3]The phosphorus is a mono isotopic element and this imply that all P is present as ^{31}P; for this reason, is not necessary to take in account the isotopic abundance during the data analysis.

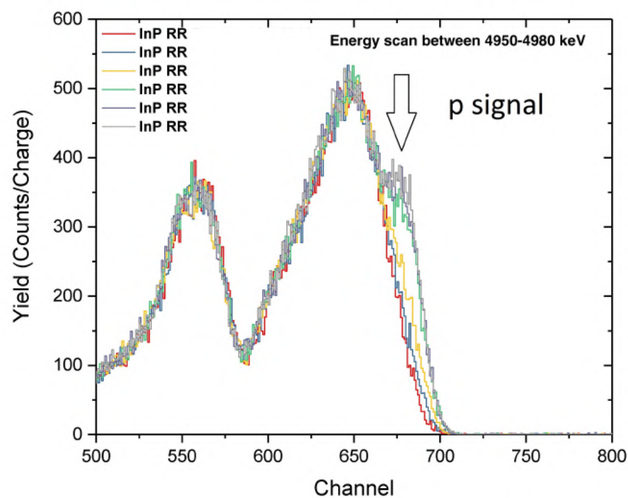

Figure 2.8. Raw signal coming from the detector during NRA analysis: different signal are reported by varying the beam energy near the nuclear resonance. The sample is a InP crystal and the proton p_0 emitted from the nuclear reaction $^{31}P(\alpha, p_0)^{33}S$ generates a signal indicated in the figure.

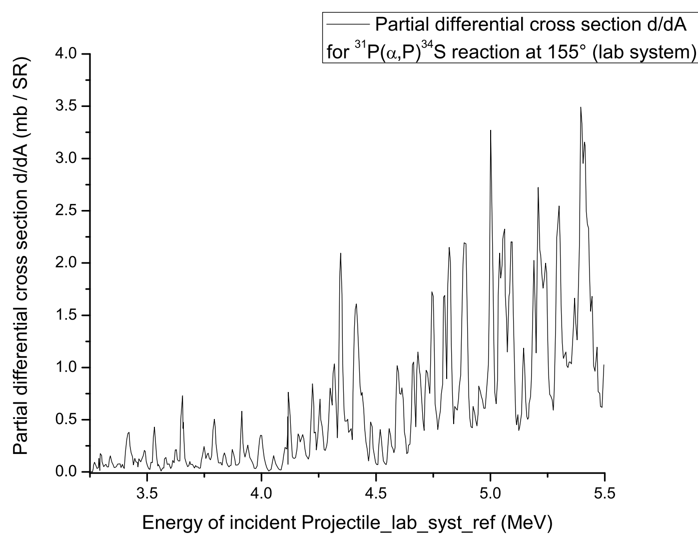

Figure 2.9. Differential cross section of $^{31}P(\alpha, p_0)^{33}S$ reaction. [103]

The high energy required for this reaction, needs to have an ion beam accelerator able to reach a α acceleration of 6 MeV or more; for this reason, the NRA experiments are conducted at the CN accelerator placed at INFN Legnaro National Laboratories.

Let's start explaining the measurements strategy for a thin P deposit on a substrate as in the case of our MLs. If we use beam energies close to the 4.96 MeV resonance a single resonance cross model can be used. Generally the cross section trend is described as a Lorentzian distribution function as a function of the energy and therefore the signal (yield normalised to the total charge $\frac{Y}{Q}$) can be written as follow:

$$\frac{Y}{Q} = \Omega\sigma_c\mathcal{L}(E)D_p = \Omega\sigma_c\frac{\omega}{\omega^2 + 4(E - E_c)^2}D_p \tag{2.10}$$

where σ_c is the reaction cross section, Ω is the solid angle and D_p is the amount of P in therms of dose [cm^{-2}] and the $\mathcal{L}$ is the Lorentzian shape of the peak as a function of the energy E, with a maximum in E_c, and ω is the full with half maximum of the resonance.

The function 2.10 can be used to obtain D_p by collecting some value of Y at different energies around the resonance (once σ_c and Ω are calibrated). To this aim, a InP crystal is used as reference sample since it is intrinsically made by 50% of P atoms. The crystal has a constant amount of P from the surface into the bulk, and for this reason the signal coming from InP can be written as:

$$\frac{Y}{Q} = \Omega\sigma_c\int_0^\infty \mathcal{L}(E)dD_p \tag{2.11}$$

In order to explicitly solve the 2.11 integral the dependence of the interaction energy E on the depth has to be considered exploiting the stopping power factor defined in equation 2.7. The equation 2.11 becomes:

$$\frac{Y}{Q} = \Omega\sigma_c\int_0^\infty \frac{\omega}{\omega^2 + 4(E - E_c)^2}dE\frac{dD_p}{dE} \tag{2.12}$$

remembering that dE/dD_p is the ϵ_{InP} and its variation is less than 0.5% in 5ω, it can be derived:

$$\frac{Y}{Q} = \frac{\Omega\sigma_c}{2\epsilon_{InP}}arctan\left(\frac{2(E - E_c)}{w}\right) + c \tag{2.13}$$

As can be noted once determined the ϵ_{InP} function calibration parameters ($\Omega\sigma_c$ and ω) can be deduced by the standard and applied to the sample to obtain

D_p.

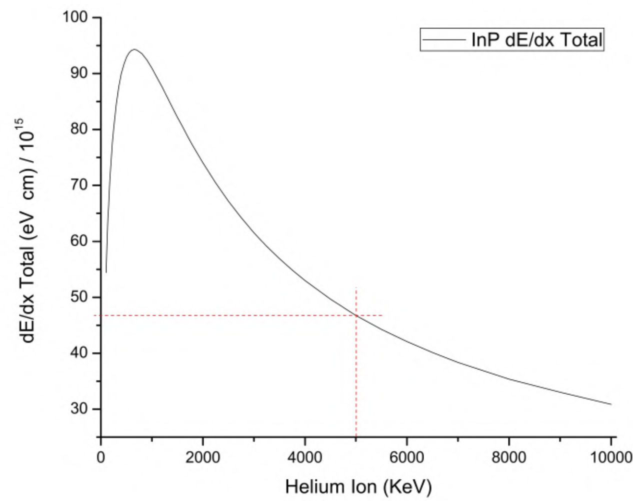

Figure 2.10. InP energy loss in a wide range of ion energy. Dashed red lines are referred to the nearest ϵ value to nuclear peak resonance.

In order to improve the analyses reliability simultaneous fitting of InP and samples data are performed as shown in figure 2.11. The data are taken at different beam energy around the resonance. In the figure 2.11, a further peak is visible at lower beam energy: this is due to a further small resonance at lower energies that is simply summed to the analysis to improve accuracy.

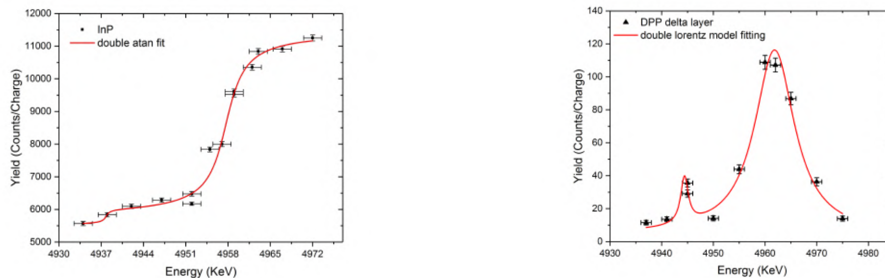

Figure 2.11. On the left, InP data fitting with double Lorentzian model; on the right side, a phosphorus δ layer data fitting with the same model. The fit of InP as samples are always a global fitting with shared parameters.

In some cases the NRA analysis was used to detect P atoms not at the surface of the sample for example we characterised P ML after SiO_2 capping before and

after annealing. In this case, further physical phenomenon has to be taken into account to properly analyse the data. We know that the particle energy at a certain depth will be reduced by stopping power so the resonance peak will be shifted by the energy loss into the cap. Moreover, being the energy loss a stochastically process, not all the particles at a given depth will have the same energy. Energy will be distributed according to a nearly Gaussian distribution with an FWHM given by the following equation:

$$\Omega_{Bohr} = \sqrt{0.26\ Z_1^2\ Z_2\ N\ t\ 10^{18}}\ [KeV] \tag{2.14}$$

where N is the volumetric density expressed in $\frac{atoms}{cm^3}$ and t is the sample thickness.

In our energy range, the Bohr's theory is the most appropriate and equation 2.14 describe the energy variance of the collision between the ion beam and a material.

For a superficial phosphorus deposition this therm is negligible, while a NRA evaluation of P under a capping layer, this therm must be taken into account.

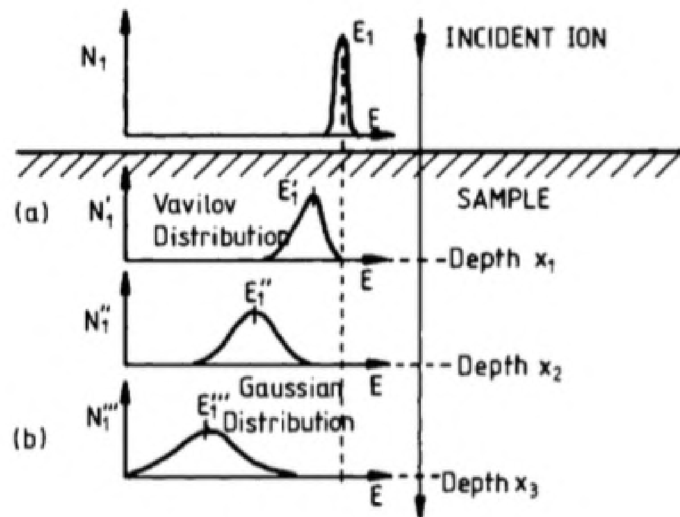

Figure 2.12. Straggling effect on the energy distribution of an ion beam in a material. [104]

Energy straggling cause a broadening of the experimental resonance bell, as schematically shown in figure 2.12. In order to properly analyse the data, ad hoc simulation code making the convolution between the resonance shape, the energy straggling an an eventual in-depth distribution of P was used.

Experimental considerations Experimentally, the signal coming form a reaction are normally detected as a peak with a certain width by the particle detector: the proton signal reported as a point on NRA plots is basically the sum (integral) of the intensities of each channel presenting a signal of the proton peak (see figure 2.8). This value can be affected by some systematic experimental error: here the two main source of systematic error are described and a data correction is proposed.
The beam energy at CN accelerator is chosen by variating the magnetic field of the so called *analysis magnet* coupled with a set of silts; thanks to this system, the energy of the beam can be easily varied near a pre-defined value at which all the accelerator and lens parameters were optimised. Unfortunately, the heat of the magnet and lens, the magnet hysteresis and others secondary experimental factors contributes to generate some *energy shifts of the beam*, that becomes systematic errors to be taken into account during the data analysis. In order to monitor these

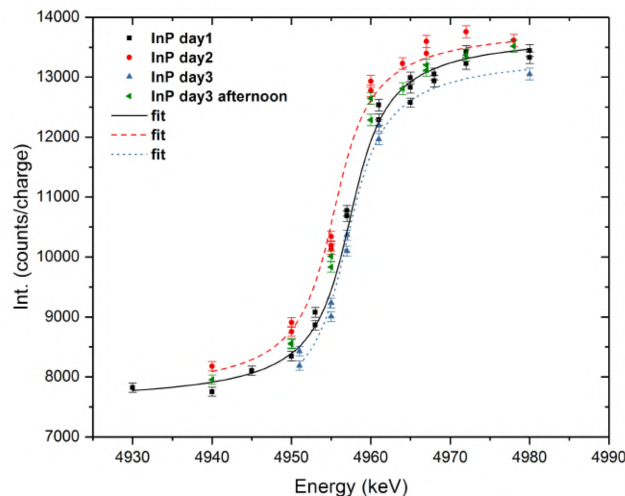

Figure 2.13. InP energy scan around the nuclear resonance at the surface: the data are the integral of the raw proton signal. Different data are reported for different scan during a 3 day measurement shift. The data are fitted with the single Lorentzian model. The beam energy shift between different days are clearly present.

shifts, InP energy scan around the nuclear resonance help us to verify the energy shifts and to correct (or minimise) this energy error. Normally, the beam energy oscillation is between 1.5-2.5 keV during the same half day. In figure 2.13 the shift between different days, and also during the same day, are clearly shown. This energy beam uncertainty will be shown by horizontal bar error in the fitting result

plots.
Another systematic error is the electronic shift of the particle signal due to the electronic acquisition and amplification system instability. This error affects the integrals of the signal, i.e. the value of the integrals used for NRA fitting. This deviation can be corrected by shifting the whole spectra or by shift the integral boundaries (ROI), compensating the shift. This is possible tanks to the presence of a digital pulser, that is an artificial stable signal injected into the electronics, which act as a reference signal: any pulser signal shift can be only caused from an electronic shift. I developed a C++ code that integrate the proton signal produced by the nuclear reaction (detected by the detector and amplified by the electronics) and automatically identify the pulser peak: in the presence of a pulser shift, the integral boundaries (ROI) are modified, compensating the electronic shift. Thanks to this software, this source of systematic errors are avoided.

Reference for the NRA section [102–105]

2.2.3 X-Ray Photoelectron Spectroscopy

The X-Ray Photoelectron Spectroscopy is a chemical analysis of solid materials based on the energy analysis of secondary electrons that are emitted after absorption of photons in the X-Ray range. The main features of this technique are the possibility to detect all elements (except H and He) and their chemical bonding states on the surface of a sample. Under special geometrical condition there is the possibility to detect the relative positions of elements in case of ordered structures (XPD, X-ray Photoelectron Diffraction) or the depth distribution of the elements sorted by chemical status (AR-XPS, angle resolved XPS). The latter can also be to disordered system and allows to analyse depth of few nm from the surface.

Basic Concepts

In XPS analysis, the surface of a sample is irradiated with a monochromatic X-Ray beam, having a $h\nu$ energy. This beam can be generated by a X-Ray source that could be a *conventional source* (typically Mg or Al anodes that are filtered in order to obtain only the K_α radiation at 1253.6 eV or 1486.6 eV respectively) or by a *synchrotron source*, that allows to tune the X-Ray energy and present an extremely high beam brightness and energy resolution. These photons interact with sample's material and a core electron is emitted from an absorber atom as

a consequence of a photon absorption in the soft X-Ray energy range, which is typically used for these experiments. Ionised states are created as a consequence of photoelectron emission from the surface of the sample. These photoelectrons are detected by an electron analyzer in an ultra-high vacuum chamber and an energy spectrum is collected. The photoelectron are counted and sorted by kinetic energy. The revealed kinetic energy is converted into the binding energy scale that directly quantifies the original bounded electron state into an atom of the investigated sample. The basic relation for this conversion is:

$$E_b = h\nu - E_{kin} - \Phi_A \tag{2.15}$$

The analyzer working function Φ_A is a setup characteristic and in our case it is determine by the use of a standard sample: an Au film sample is measured to calibrate the binding energy scale by acquire the Au 4f peak.

One of the most important XPS information is the *chemical shift*: the binding energy of a core electron in a pure element is modified when the atom forms a chemical bond. This change is called chemical shift. The energy shift of a core electron peak is caused by a charge transfer induced by a new chemical bond that modify the atomic potential felt also by core electrons. As a consequence, the electron energy level is shifted and so also the binding energy is modified. Local charge modification can be correlated to the electronegativity of binding species and by oxidation state of a species. For example, if a first neighbouring has a higher electronegativity respect to excited atom (absorber atom that emits a photoelectron), a charge transfer occurs and the charge of the former become partially positive, thus increasing the binding energy. So, an atom with higher electronegativity shows a reduced binding energy.

Another important XPS spectra characteristic is the *spin-orbit splitting*, always present in all peaks with $l \neq 0$, i.e. for p, d, f and not for s orbitals. These peaks present a doublet structure caused by the fact that unpaired electrons left after a photoemission event can present a parallel or anti-parallel orientation: since there is an energy difference between them, the resulting photoelectrons present a energy difference. The binding energy difference can vary from few decimal of eV to several eV, depending on the type of atom and orbital, but the relative intensities between the two peaks are fixed from a quantum-mechanical relation. The relative intensity is the ratio between their degeneracy, and so it is equal to $2j + 1$; in other words, for p is 2, d is 1.5 and d is 0.75.

In a XPS spectra not only photoelectron peaks can appear, but also other peaks can be present; for example, Plasmon Loss Peaks appears into XPS spectra, gener-

ated by bulk or 2D collective electron oscillations, or Auger peak can also appears, produced by Auger de-excitation of ionised atoms.

In order to modelled and resolve different peaks, the peaks must be fitted with a proper peak analysis, also called deconvolution process. The basic line shape of photoelectron peaks is a Lorentzian function that is the natural shape given by the pure physical emission process that contribute to the line width with ΔE_0 contribution, that is determined by the lifetime τ of the core-hole state left by photoemission. The uncertainty principle define it by $\Delta E_0 \tau = h$ relation. The peak shape used for the fitting is not a Lorentzian function but a Voigt function since the Lorentzian shape is modified by a gaussian broadening caused by several reasons like thermal vibrations, analyzer resolution and others contributions. A more complicated peak shape can be used for XPS signal coming from conductor materials (like Au 4f peak, the standard target used for XPS calibrations); the *Doniach-Sunjic* line shape is used in these cases in order to take into account the asymmetry of XPS peaks originated by many-body interactions of the photoelectrons with free electrons at the Fermi edge.
In general, the peak width is subjected to of several contributions:

$$\Delta E = (\Delta E_0^2 + \Delta E_{is}^2 + \Delta E_p^2 + \Delta E_{WA}^2)^{1/2} \tag{2.16}$$

where ΔE_0^2 is the natural width of the core-level, ΔE_{is}^2 due to the screening effects of phonon and local configuration interactions, ΔE_p^2 is the line width of the source, ΔE_{WA}^2 is the analyzer resolution. In this work XPS spectra will be shown, some coming form XPS analysis using a conventional X-Ray source and from synchrotron one: for these reason, the FWHM of peaks will be differ, due to different terms ΔE_p^2 and ΔE_{WA}^2, remembering that also the electron analyser is different.
For a correct peak fitting, not only the model of a peak must be specified and fitted with care, but also a correct background subtraction is mandatory. The background model is normally chosen by the user, depending on the aspect of XPS spectrum. The linear background is the most simple (and also unrealistic) background that can be used, but sometime it is extremely similar to the more accurate *Shirley* background. This types of background is normally used in this work and it's in general the most used. It takes into account that the background at lower energy side of a peak is usually higher than at the higher kinetic energy side. This fact comes from inelastically scattered photoelectrons that subtract electron to the elastic peak and distribute at lower energy. In more detail, Shirley background is build solving the constraint that the background at a given kinetic energy in the peak spectrum should be proportional to the total number of electrons above this

energy.
The fitting and deconvolution process of XPS spectra are made by a commercial software called *KolXPD* [4].

Quantitative and Angle Resolved Analysis

In this work, the XPS technique allows to determine the binding energy of elements present in the investigated samples, giving informations on the nature of chemical bonds. By comparing our results with literature data, the molecular oxidation states of adsorbed precursors can be determined. A more quantitive approach is also possible: the analysis of the XPS peaks intensity as a function of angles allowing to quantify the element sorted by their chemical bonding as a function of depth. For this purpose, a specific simulation software will be presented in this section. Finally, the obtained value will be compared with Nuclear Reaction Analysis results, for a cross check evaluation on P amount estimations.
This aspect is not trivial. Quantitive analyses of doping species in the ML are generally missing in the literature of MLD process. This could appear surprising, being maybe the most important parameter of a source layer. The reason is that XPS seems to be the only technique to face this aim but generally the quantification is quite slow due to long time of vacuum and acquisition. Moreover, quantification (as we will see) go through a long analyses where systematic errors are difficult to be checked. In this thesis, we solved these problems by a double approach. Most of the preliminary quantifications necessary to define the processes were done by NRA analysis to which our team has continuous and relatively frequent access. This technique is less affected by systematic errors being essentially based on a well known standard and give also access to deep layers. Then, after the set up of the processes, we accessed to XPS synchrotron source with a dense beam acquisition run where 337 spectra were collected over 15 samples produced by optimised processes.
We will see that cross check of NRA and XPS quantification is satisfactory giving strength to the accuracy of our approach.

In this work will be used a code developed specifically for quantitative XPS and in this section some theoretically background is shown; more details are published in literature [106].

The *Brixias Code Package* is based on the calculation of the *Depth Distribution Function* (DDF) via Monte Carlo simulation or Analytical calculations, a complete

[4]More info: https://www.kolibrik.net/kolxpd/

Photo-Ionisation Cross Section database, an automatic transmission function calculations. All these feature are implemented with a core computational engine that allows to fit (or predict) a XPS spectra, starting from a given layer by layer input model. In this code, there is also a fitting mode, that allows us to fit the angular dependence trend of peak intensities: the thickness of different input layers (i.e. the amount of the species) is obtained after an initial composition guess. This modality allows us to quantify not only the dopant amount on the surface, but also the oxidation of Ge surface before and after the adsorption chemical treatments. This analysis is called *Angle Resolved XPS* (AR-XPS).

The *Depth Distribution Function* (DDF) is the probability that a photoelectron generated at a certain depth z, emerges from the material with a given angle θ. The *Brixias Code Package* is able to evaluate the DDF of a multi-layer material, considering the properties of each layer and calculating the global DDF value. The purpose of a material database is to provide the necessary parameter in order to simulate the inelastic and transport mean free paths (IMFP and TMFP) which determine the trajectories of photoelectrons. The IMFP describes the average distance travelled by an electron before performing an inelastic scattering (i.e., before losing energy) while TMFP describes the average distance before an elastic scattering (thus a change in direction with no energy loss).
Brixias Code Package takes into account both elastic and inelastic scattering of electrons, for a better data description and analysis. The electron transfer to the surface, that gives the XPS surface sensitivity, is commonly described by the electron Inelastic Mean Free Path (IMFP), i.e. the average travel length of an electron in the matter before an inelastic (energy loss) event. This parameter allows a simple description of the probability of an electron to escape the substrate P, starting from a depth z (i.e. the simplest DDF function).

$$P(z) = \frac{e^{-\frac{z}{\lambda(E)\cos(\theta)}}}{\int_0^\infty e^{-\frac{z}{\lambda(E)\cos(\theta)}}dz} \tag{2.17}$$

Where θ is the angle between the normal to the sample, λ is the IMFP and the analyzer and the denominator presents an integral that takes care of the normalisation. This model is quite simple because electrons may perform inelastic as well elastic scattering before escaping the sample. So IMFP is not a complete description of the photo-emitted electron travel to the surface: an elastic scattering mean free path must also be considered (TMFP). The simplest implementation

possible is to modify only the λ as follow:

$$\lambda_{average} = \lambda_{IMFP} \frac{\lambda_{TMFP}}{\lambda_{IMFP} + \lambda_{TMFP}} \tag{2.18}$$

This model leading to the so called Effective Attenuation Length (EAL), that is a not accurate evaluation, even if it is used sometimes in literature.
In order to include the elastic scattering effect, angle-dependent elastic scattering length should be included. With the knowledge of IMFP and TMFP, it is possible to analytically calculate the exact DDF function for a single, homogeneous material. The resulting formula, due to Tilin et al. [107], is extremely complex and relies on numerical integration and a special H Chandrasekar function. This model, called analytic in the software, is the standard method used in this work to analyse e modelled AR-XPS spectra. This calculation is implemented for each layer given in the input model into the software, finally calculating the the DDF function of a multi-layer system.
Brixias Code Package provides also a suitable Monte Carlo code (based on Werner at al. [108]), which simulates the electron trajectories for a generic multi layered sample: the DDF function for each AR-XPS simulation is compared with analytical result by default, and normally no significant differences are detected.

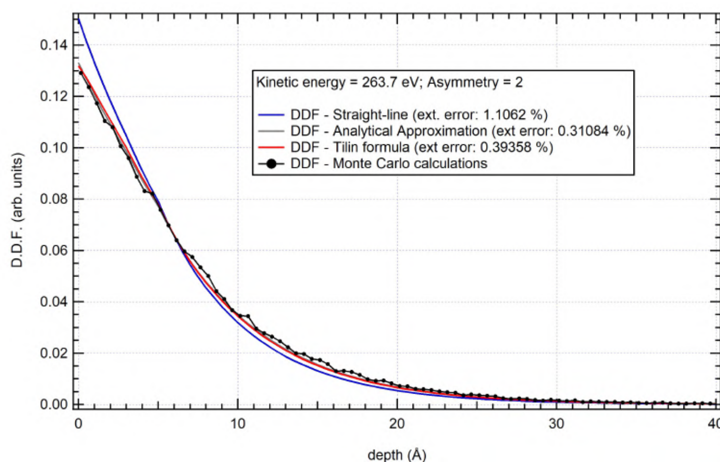

Figure 2.14. Comparison between different DDF estimations based on different theories implemented in Brixias code package.This graph shows DDF function calculations for a phosphorus based monolayer on top of Ge bulk sample.

In this work, XPS spectra were acquire in two different facilities. Some XPS spectra were acquired with a custom designed UHV system equipped with an EA 125 Omicron electron analyser, working at a base pressure of $10^{-10} mbar$. This system has a standard $Al\ K\alpha$ x-ray source (1486.6 eV) and the spectra are acquired

with a pass energy equal to 20 eV. The binding energies (BE) were referenced to the C 1s peak at 284.6 eV for these set of measurements.

A second batch of measurements were collected with a Synchrotron radiation source, at ELETTRA synchrotron in Basovizza, Bach beamline [109]. The synchrotron worked at 2.0 GeV beam energy, in a top-up injection mode regime, and the x-ray beam was generated by an APPLE-II elliptical undulator insert into the electron ring. The Bach beamline presents a VG Scienta R3000 electron analyser placed at $60°$ from the beam direction is used for this experiment: the sample holder can be rotated along the vertical rotation axis allowing to varying the take-off angle and allows to measure up to 5-6 samples with the same vacuum procedure.
The x-ray beam is monochromatized by a variable angle spherical grating monochromator coupled with a set of motorised slits. The grating resolving powers is 20 000–6000 in the energy range of 158–597 eV (SG2 grating). The reported spectra were collected in a normal emission geometry with 50 eV pass energy, at room temperature. These spectra were calibrated with Au 4f 7/2 peak.

2.2.4 X-Ray Absorption Spectroscopy

The X-Ray Absorption Spectroscopy (XAS) is a measure of the energy dependence of the absorption coefficient μ with photon energy close to a core electron absorption edge (i.e. with the photon energy close to the binding energy). XAS is a powerful technique to investigate the neighbourhood of a specific atom, since it was demonstrated that the oscillations of the absorption coefficient μ near the absorption edge contains informations about the surrounding atoms of a central absorbing atom. The absorption of X-Ray photons is based on the well known photoelectric effect, with the emission of a core electron from an absorbing atoms. The oscillation of the absorption coefficient can be obtained by tuning a monochromatic X-Ray energy of an incoming beam near an atomic adsorption edge and looking the oscillation of absorption coefficient in function of the energy beam. The absorption coefficient can be measured in a transmission geometry (i.e. by measuring the incident and the transmitted intensity of the beam), or by looking the fluorescence photons coming from the de-excitation after the X-Ray absorption.
The oscillation of the absorption spectra were discovered in the ’20s, but the correct interpretation of this phenomena was given in the ’70s. The discovering and the correct explanation of this phenomenon is correlated with the quality and the

number of available XAS spectra, which was strongly increased with the use of X-Ray beam from synchrotron. Its continuous tunable X-Ray source and its high X-Ray flux are the reason why this technique is considered a synchrotron technique.
The first explanation of the oscillation of the absorption probability phenomenon were based on the long range oscillation of the Density of States (DOS) in crystalline materials, but nowadays we know that this explanation is wrong. As a matter of fact, the X-Ray Absorption Fine Structure (XAFS), that is the specific structure of a X-Ray Adsorption Spectra (XAS), is observed basically in all materials, with the only exception of the mono-atomic gases, and this experimental evidence falsify the previous explanation.
The XAFS oscillations is due to the interference of the emitted photo-electrons wave function with itself, i.e. with the same wave function scattered by surrounding atoms. This interference changes the probability of the absorption of the central atom (the absorbing atom, so the photoelectrons emitter atom) and generates the variation of the absorption probability. This theory was proposed for the first time by Stern in 1971 [110], by assuming that the atoms are point scatterers and demonstrating that via Fourier Transform data analysis, the oscillation of absorption probability are related with interatomic distances. In 1974 Stern proposed an upgrade of the theory, by adding a more formal treatment of interference effect involving the final-state wave function, in which it is clear that the modulation in the matrix element is important, instead of the DOS as previously proposed. In particular the absorption coefficient can be written as:

$$\mu = n\sigma = n\frac{\pi e^2\omega}{\epsilon_0 c}\mid\langle\psi_f|\,H\,|\psi_i\rangle\mid^2\,S_0^2\,\rho(\epsilon_f) \tag{2.19}$$

Stern underline that the most important factor for XAS oscillation is the matrix element $\mid\langle\psi_f|\,H\,|\psi_i\rangle\mid^2$ therm instead of $\rho(\epsilon_f)$ DOS therm.

There are not so much experimental technique able to detect a local molecule changes using a very low amount of analyte. The XAS technique is a very powerful tool able to detect local structures, but in our situation also this technique presents some major challenges. First of all, the molecule atoms used in this work presents very light scattering atoms, making it difficult to detect an absorption fine structures (XAFS signal for EXAFS analysis). Others challenges are related to the low amount of P atoms present in a monolayer and another problem is related to the P K-edge energy near 2 KeV: it is very difficult to experimentally generates a monochromatic X-Ray beam with a high photon flux in this energy range, mainly due to a technological monochromator problems. The monochromator

installed at SIRIUS beamline is based on a multilayer grating system that allows to cover this desired energy range. This prototype presents a variable line spaced holographic diffraction grating with line density = 2400 lines/mm over which a multilayer with 35 periods of $Cr(2.5nm)/B_4C(4.1nm)$ has been deposited, and two matched multilayer mirrors as second optical elements. This ensure a 50% efficiency at 4 keV and allow to access down to 1.4 keV. This characteristic allows to have a sufficient photon flux in an intermediate X-Ray energy region: in fact, classical double crystal monochromator and grating monochromator usually work in the hard and soft X-Ray respectively, leaving this intermediate region hardly covered.
One of the few beamline in the world that present a proper monochromator to generate high photon flux ($> 10^{13}\ photons\ s^{-1}$) and the possibility to work in a very low incidence angle geometry is the *Sirius Beamline* at SOLEIL synchrotron, Paris metropolitan city [111] [112]. Some functionalized Ge (001) sample were analysed at *Sirius beamline* at the phosphorus K-edge, in order to collect XAFS phosphorus absorption signal, containing neighbouring atom informations. To perform it, the samples are analysed in a total reflection configuration, with the X-Ray beam below the critical angle, in order to maximise the surface signal and minimise the bulk Ge fluorescence background. This technique is generally called Grazing incidence-EXAFS, or in some case Refl-EXAFS, and it will be further explained.

Grazing incidence-EXAFS The analysis of the acquired XAS data is a quite complicated task, since it is necessary to numerically treat the data also with Fourier Transform based model; nowadays there are more than one software developed for this scope, and the Demeter package (Athena and Arthemis software) will be used in this work to analyse XAS data. In particular, the XAS data can be divided in two range: the XANES and the EXAFS region. The former is the absorption spectra near the absorption edge (also called NEXAFS): it contains multiple-scattering informations and it is normally defined from the edge to 50-100 eV above the edge. The EXAFS region start from 100-200 eV above the edge and it ends thousand eV after the edge (can be 35000 eV). The EXAFS region is the most simple to analyse since it is well described with single scattering theory [113], instead of a full scattering theory needed for XANES region.
In this paragraph only the most important formulas will be reported and more attention will be given to EXAFS region [114].

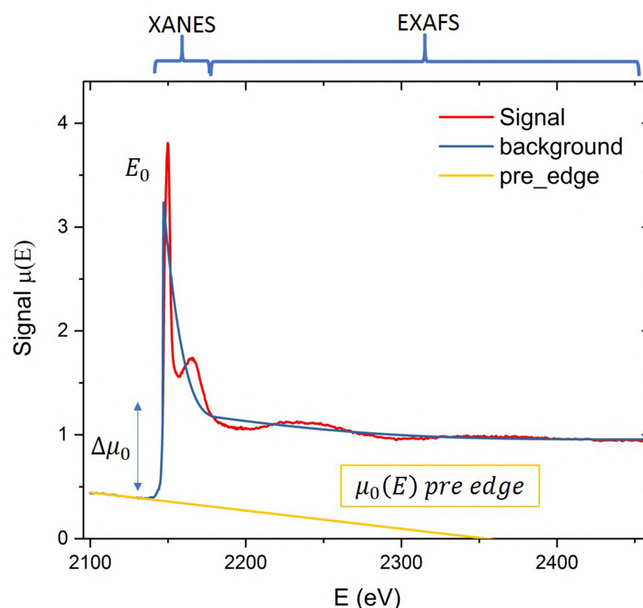

Figure 2.15. Example of an absorption spectra at phosphorus K-edge. The signal (red curve) is analysed and the E_0 edge position is identified. The pre-edge background is calculated (yellow curve) and the single atom contribution is plotted (blue curve).

The main steps of data analysis will be:

1. Extraction of oscillation data, i.e. the subtraction of background and single atom contribution.
2. Fourier filtering of data. The Fourier transform of data produce a spectrum in the so called R space. In this step it is possible to evidence different shells contributions.
3. A modelling step: calculation of the signals connected to any absorber - scatterer atom couple are calculated (paths). Paths are generated starting from a given structural model via FEFF simulations [115].
4. A EXAFS region fitting procedure that adjust physical parameters of the starting structure (number of atom contributing to each path (multiplicity), interatomic distance and distance distribution) in order to match simulation to the experimental datum.

The basic relation used as a first step during the data analysis is the relation between the wave vector **k** and the energy of the beam E:

$$k = \sqrt{\frac{2m(E - E_0)}{\hbar^2}} \tag{2.20}$$

As mentioned in the first point, the single atoms contribution must be subtracted to the collected absorption spectra, in order to isolate the oscillation function χ. So the function χ is defined as:

$$\chi(k) = \frac{\mu - \mu_0}{\mu_0} \tag{2.21}$$

where μ is the collected absorption spectra and μ_0 is the hypothetical single atom contribution to the absorption.

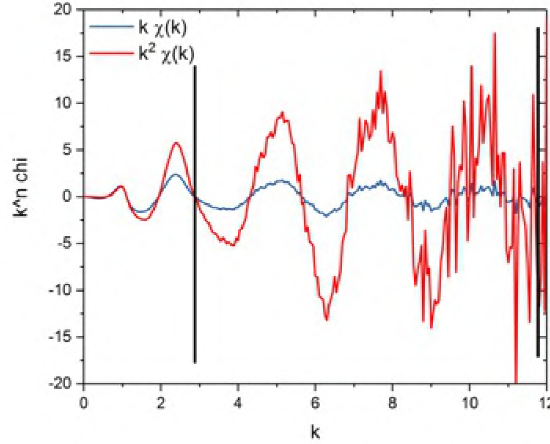

Figure 2.16. Data in K-space: blue curve is $k\chi(k)$ and red curve is $k^2\chi(k)$.

μ_0 is fitted by a non oscillating function as blu line in figure 2.15.

The $\chi(k)$ signal in EXAFS region is well described by:

$$\chi(k) \approx S_0^2 \sum_j N_j \frac{f_j(k)}{kR_j^2} \sin\Big(2kR_j + \delta_j(k) + 2\delta_c(k)\Big) e^{-2R_j/\lambda(k)} e^{-2k^2\sigma_j^2} \tag{2.22}$$

where the sum is over all surrounding atoms, the $f_j(k)$ is the scattering amplitude of the wave at j-th atom, N_j is the number of j-th atom, the $2kr_j$ is the phase shift due to the distance of the neighbouring atom, the $\delta_j(k)$ and $\delta_c(k)$ are two phase

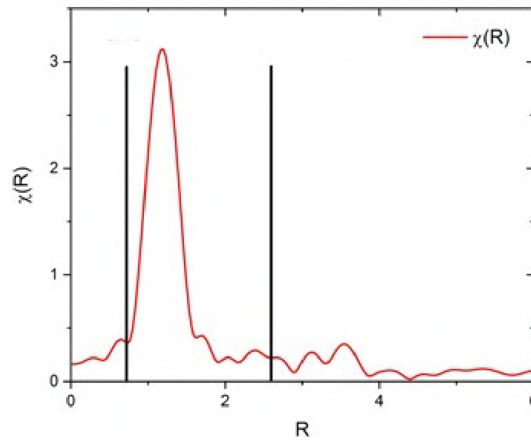

Figure 2.17. Data in R-space: red curve is $\chi(R)$ function.

shift contribution coming from the wave scattered by the j-th scatterer atom and from the central atom respectively. The $e^{-2R/\lambda(k)}$ term is the dumping term of the wave function due to the inelastic scattering of the electron, where λ is normally the λ_{IMFP}. The last term $e^{-2k^2\sigma_j^2}$ is the disorder factor, that takes in to account the static (or structural) and the thermal displacement of the atom shell with respect to the average R_j position. σ is the standard deviation of such distribution.
The first term S_0^2 is the Amplitude Reduction Term, that takes in to account that the core-hole has a finite lifetime: so it considered the effect of the relaxation of N-1 electrons present on the atom (technically an ion after the photoelectron emission) and it can be expressed as:

$$S_0^2 \approx \sum_f |\langle\psi_f^{N-1}|\psi_i^{N-1}\rangle|^2 \approx 0.7 < S_0^2 < 1 \tag{2.23}$$

The $\delta_j(k)$ and $f_j(k)$ are calculated by FEFF software with an ab-initio self-consistent calculation.
At this point, equation 2.22 can be used to fit the experimental data, adjusting R_j, σ, S_0^2 and N_j free parameters to experimental data. Since S_0^2 and N_j are strongly correlated parameters, as a first assumption, S_0^2 is fixed to 1, and only N_j is used. This parameter is also called path multiplicity. An estimation of S_0^2 will be given at the end of EXAFS analysis, in the phosphorus chapter, number 3.
In our case, the EXAFS signals do not allow us to fit the data with such a high number of free parameters. For this reason, the σ parameters are estimated with

a model, called *Einstein model* [116].

$$\sigma^2(\omega_E, T) = \frac{\hbar}{2\mu\omega_E} coth\left(\frac{\hbar\omega_E}{2k_BT}\right) \tag{2.24}$$

This model considers the pair of absorber and backscattered atoms as an independent oscillator with a frequency ω_E, and correlates this frequency with symmetrical molecular stretching frequencies ν_{sym}. As reported in the model, the symmetrical vibrational frequency can be considered a measure of the effective bond-stretching force constant, and its value can be utilised to estimate and compare the strength of different bonds, placing $\omega_E = \nu_{sym}$. Thanks to this model, a σ value can be estimated for each given path, knowing its symmetrical stretching frequency.
The used path in the fitting models are based on P=O, P-O and P-C bonds: for each of this paths, a σ value is estimated, starting from literature or measured symmetrical stretching mode frequency vibration. For this reason, their estimation is expressed in the EXAFS analysis section, after the Infrared Spectroscopy results. Also experimental fitting analysis will be properly discussed and showed in the phosphorus chapter 3.

2.2.5 Electrical Measurements

The electrical measurements presented in this work are based on a four point probe electrical measurements system, called Van der Pauw-Hall measurements. This system is design to test a doped semiconductor material by electrical measurements with the use of a source-meter connected to 4 Au point tips in contact with the semiconductor surface. The system allows to apply a current between two tips (the user can select two of the four) and to measure the potential between the other two.
The use of 4 probes, instead of 2, allows to perform the measure of the sample resistivity independently of leads and contact resistivities; moreover, the four probes placed in a square geometry permit to measure the carrier concentration by the application of an external constant magnetic field, inducing the formation of a Hall voltage contribution.
The Van der Pauw method is based on two papers [117] [118] published by Van der Pauw in which he described the method to measure a flat sample starting from the following assumptions:

- The contact area between tips and the sample is small

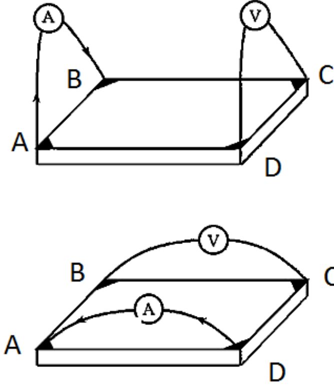

Figure 2.18. Van der Pauw sheet resistance measurement configuration.

- The tips are at the perimeter of the sample
- The sample (in particular the doped area) is continuous and homogeneous

The relation expressed in the work is:

$$exp\Big(-\frac{\pi t}{\rho}R_{AB,CD}\Big)+exp\Big(-\frac{\pi t}{\rho}R_{BC,DA}\Big)=1 \tag{2.25}$$

where t is the thickness of the sample (or of the doped layer), ρ is the resistivity of the material and $R_{AB,CD}$ and $R_{BC,DA}$ are defined as follow:

$$R_{AB,CD}=\frac{V_D-V_C}{I_{AB}} \tag{2.26}$$

$$R_{DA,CB}=\frac{V_B-V_C}{I_{DA}} \tag{2.27}$$

with V_D, V_C, V_B are voltages measured at the apex labelled in figure 2.18. While I_{AB} and I_{AD} are currents generated by a current generator connected to AB and BC respectively.

By measuring the resistances $R_{AB,CD}$ and $R_{DA,CB}$, the resistivity ρ can be calculated by eq. 2.25. The sheet resistance R_s is related to the resistivity by $\rho = tR_s$. The sheet resistance R_s can be expressed as a function of the properties of a doped semiconductor as follow:

$$R_s=\frac{1}{q\,N_d\,\mu\,t} \tag{2.28}$$

where the N_d is the active donor dose that we consider equal to the carriers concentration under saturation regime and μ is the carrier mobility.

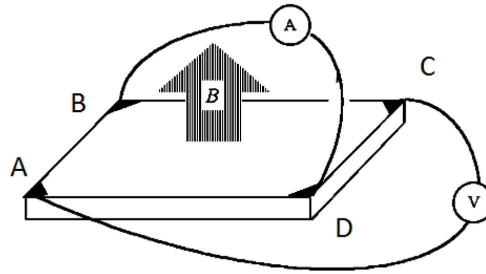

Figure 2.19. Van der Pauw Hall measurement configuration.

Figure 2.20. Van der Pauw-Hall chamber.

Regarding the Hall effect, Van der Pauw showed that a Hall measurements can be performed in a flat geometry simply by applying a magnetic field (perpendicular to the sample surface) and delivering current between B and D contacts and measuring the voltage between A and C. The Hall coefficient can be calculated as follow:

$$R_H = \frac{t}{B}\frac{(V_C - V_A)}{I_{BD}} \tag{2.29}$$

The Hall coefficient can also be expressed as a function of materials properties as follow:

$$R_H = \frac{1}{eN_D} \tag{2.30}$$

Defining $R_{HS} = R_H t^{-1}$, i.e. the thickness independent Hall factor, we can express

the active carrier dose n_s and the carrier mobility μ as a function of R_{HS}.

$$n_s = \frac{1}{e\, R_{HS}} \tag{2.31}$$

and the mobility:

$$\mu = \frac{R_{HS}}{R_s} \tag{2.32}$$

2.2.6 Secondary Ion Mass Spectrometry

The Secondary Ion Mass Spectrometry (SIMS) is a technique devoted to analyse chemical concentration profiles in solid state materials with a sensitivity down to part per billion or part per million (ppb or ppm) range, depending on experimental conditions. In our case, SIMS spectra are devoted to detect the chemical profiles of impurities (doping atoms) in semiconductor matrix (germanium) in order to characterise the diffusion of dopant after thermal or laser processes.
The SIMS technique is a destructive technique, since the sample is excavated by an ion beam (called primary ion beam) in ultra high vacuum chamber, focused by a complex electrostatic lens system. The ejected sputtered material are generated from a specific area of the sample were the focalised primary ion beam is rastered. The secondary beam composition is a mixture of sample's atoms and a combination of sample's atoms and primary ion: they can be charged or neutral. The ionised fraction of the expelled materials (about 2-3% of the total amount of sputtered material) are accelerated by an electric field and sent to the mass spectrometry. Thanks to an electrostatic sector analyzer (ESA) coupled with a system of slits and a magnetic sector analyses (MSA) coupled to others slits, a specific ion with a known mass is selected and finally counted by detectors (photomultiplier or Faraday cup).
The raw data are expressed in ion yield (counts) as a function of time of sputtering (s). In order to obtained a concentration profile as a function of depth, there are two calibration steps: the dose calibration is done by the quantitative comparison between an ion-implanted standard sample SIMS profile area and samples areas, and a depth calibration done with a profilometer evaluation of the depth of SIMS crater.

The SIMS used in this work is a dynamic SIMS *CAMECA IMS 4f* located at the Physics and Astronomy Department of the University of Padova. This machine can use two different primary ion beam: O_2^+ and $^{133}Cs^+$ ion beam. The choice of the primary ion beam is based on the maximisation of secondary ion yield, and

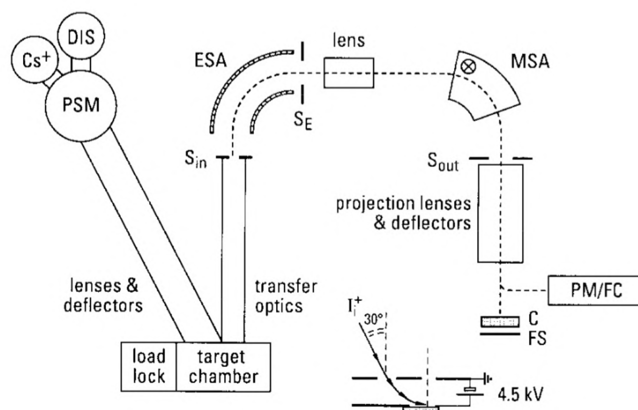

Figure 2.21. Cameca IMS 4f Secondary Ion Mass Spectrometry general scheme.

at the same time, on avoiding unwanted matrix effects.
The dynamic SIMSs are not suitable for surface analysis since the first 10-15 nm are normally affected by the so called surface peak. This peak is an artefact and is due to an initial variation in sputtering yield that has not yet reached a sputtering steady state.
Finally, the final chemical profiles are characterised by an uncertainty that is less than 10% for the dose (i.e. the area of the chemical profile), and with an uncertainty around 2% regarding the depth of the profiles.

2.2.7 Infrared Spectroscopy

The Infrared Spectroscopy is a standard characterisation technique for materials, liquids and gases, normally used in each chemistry and solid state physics areas. This technique involves the interaction between an infrared beam and matter, studying the absorption of IR radiation. Infrared spectroscopy is based on the fact that molecules absorb photons with frequencies that are characteristic of their structure, or in other words, there is an absorption in resonance conditions between the vibration frequencies of molecules and the radiation frequencies. Thanks to this basic fact, the infrared spectroscopy gives access to information related with chemical bonds in a material, for example. In a simple molecule case, it is possible to evaluate the the normal modes of vibration of a given molecule, and in some simple cases, it is possible to calculate the characteristic vibrational frequency for each specific mode. It is important to remember that a harmonic oscillator based theory is not sufficient to completely described all IR phenom-

ena, but a more complete description has to take into account an an-harmonic interatomic potential, such as overtones signals. The formal description and interpretation of IR interaction with matter is very wide and it is not the scope of this section. Nevertheless, it is important to underline that the intensity of a particular IR band is related to the concentration of the observed species and with the molar extinction coefficient involved. The first is correlated with the amount of a particular surface functionalization (as will be described further in this work), but the molar extinction coefficient of an IR band is proportional to the square of the dipole moment changes over the normal coordinates of the specific normal mode vibration. These considerations underlines the intrinsically difficulty to use IR Spectroscopy as a quantitative technique; for these reasons, only qualitative evaluations will be further presented.

In this work, the IR spectroscopy is used to characterise the molecular precursors and the molecular monolayer adsorbed on Ge surfaces. In the former case, an IR transmission geometry is used for molecular precursor, using a tablet with a mixture of KBr and molecular precursor powder. In the liquid molecular precursor case, a transmission cell is used to obtain a IR spectrum. The case of surface adsorbed molecules is more complicated, since the surface signal is very low for a standard IR transmission spectra. In fact, we decide to use a different technique called *Diffuse Reflectance Infrared Fourier Transform Spectroscopy* (DRIFTS), in which the analyte is a solid state powder, a germanium powder in our case. Thanks to this ploy, the Ge surface area (and consequently the global amount of molecular precursor adsorbed on Ge surface) are strongly increased. The Ge powder were synthesised by Ball Milling technique (Retsch, PM100, stainless steel jar), and a micro-metric powder were obtained and measured with SEM technique.

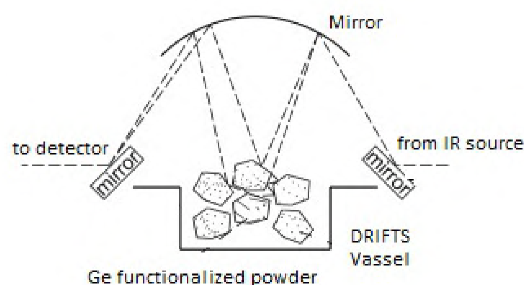

Figure 2.22. DRIFTS experimental setup scheme. The IR beam passes through the powder and is reflected multiple times. During this process, it interact with the surface molecular monolayer and consequently the IR beam is absorbed also by it. The emerging radiation is collected by a converging mirror and sent to the detector.

It is interesting to underline that DRIFTS techniques requires a particular attention during the data processing, since the light propagation in powder sample differs from the propagation of light in a homogeneous material, since of many scatters off points in its path. This different propagation was treated in the famous Kubelka-Munk model paper [119] and others following papers [120] [121] that allows to predict the fraction of light reflected from a surface exposed to radiation from all directions in a hemisphere. By an approximate descriptions Kubelka-Munk (K-M) model has a particularly simple solution in the case of semi-infinite samples.
The diffuse reflectance R_∞ (infinite thick sample approximation) is:

$$R_\infty = 1 + \frac{k}{s} - \sqrt{\frac{k}{s}\left(2 + \frac{k}{s}\right)} \tag{2.33}$$

where s is the semi-empirical scattering coefficient containing all the geometric peculiarities of inhomogeneous samples (mainly the particle size and refractive index of the sample), k is the absorption coefficient ($k = 4\pi k/\lambda$), and λ is the wavelength.
By solving equation 2.33 for k/s, the K-M transformation is obtained.

$$\frac{k}{s} = \frac{(1 - R_\infty)^2}{2R_\infty} \tag{2.34}$$

The K-M transformation relation 2.34 allows to transform the measured spectroscopic observable into a so called K-M units, proportional to the absorption coefficient, so approximately proportional to the concentration.

Finally, the IR spectra and DRIFTS data were both collected with a Jasco 660 Plus spectrometer: the interferometer and the sample cell were evacuated to remove the atmospheric gases signals and its resolution was about $4\ cm^{-1}$.

Chapter 3

Phosphorus Monolayer Doping

In this chapter, *Phosphorus Monolayer Doping* experimental details, analysis and results will be described, starting form the germanium surface preparation, the adsorption procedures and several surface characterisations. Afterwards, procedures and results on thermal diffusion and Pulsed Laser Melting techniques will be shown and discussed.

3.1 Phosphorus Precursor Adsorptions

In this section, the MLD technique that we optimised and applied to Ge is described. In particular, the Ge (001) sample surface preparation together with its experimental characterisation are reported in details. Afterwards, the ML deposition process is described.
The Ge powder preparation and their functionalization are reported, in order to verify the molecules adsorption via infrared spectroscopy. The Ge powder is used in this work to enhance the surface to volume ratio of germanium, and so to maximise the monolayer surface signal. This ploy permit to detect infrared absorption by monolayer functional group adsorbed on Ge powder.

3.1.1 Surface preparation

A Ge (001) wafer (supplied by Umicore) was cut in $1x1\ cm^2$ samples and subsequently rinsed with 2-propanol (electronic grade) in order to remove Ge cutting powder accidentally deposited on the Ge surface.
The untreated germanium surface presents a germanium native oxide, that is a

GeO and GeO_2 mixed oxide [3, 122]. For this reason, the germanium oxide is normally indicated with the generic stoichiometry GeO_x. This two oxides present different chemical properties, first of all, a very different solubility: germanium dioxide is water soluble, while germanium monoxide is soluble only in strong acids, such as hydrofluoric acid HF [79].

In order to prepare a free oxide surface, an oxide removal protocol has been

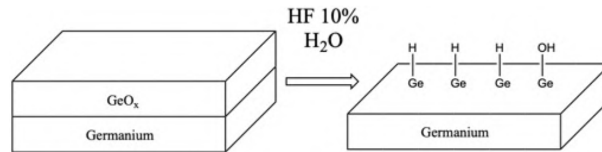

Figure 3.1. Germanium oxide removal and germanium surface functionalization: Ge-H termination.

adopted to minimise the germanium oxide and to maximise the Ge-H termination. A deep study on this procedures have been conducted by our team and published in literature [79], demonstrating that a pre-etching with hot water (60°C - 80°C) followed by 5 cycles with 10% HF alternated with distillated water rinsing, removes almost all germanium oxide, and generates Ge-H functionalities. This procedure is schematised in figure 3.1.
The oxide removal process was studied also in this work, analysing an untreated Ge (001) surface, and a Ge sample after the germanium oxide removal procedure. In figure 3.2 is reported a synchrotron XPS signal of Ge 3d region of these two samples, demonstrating the oxide removal, with a minimum GeO_x residual signal in the Ge-H sample.
A similar study on Ge oxide removal has been published by our group [79], and similar results were obtained. Moreover, analysing the XPS published data, we obtain that about 0.5 ML of GeO_x is present after the germanium oxide removal procedure.

The Ge-H surface functionalization can be clearly seen by Infrared Spectroscopy, since the Ge-H group presents an absorption near $2000\ cm^{-1}$. To obtain a sufficient signal from Ge-H functional group, a large functionalized area is necessary. To this aim, Ge powder was produced by a planetary ball milling process with grain size in the μm range (Retsch, PM100, stainless steel jar), starting from few grams of Ge pieces. After that, the powder was treated with HF and water cycles and after a drying procedure in vacuum oven, a DRIFT spectrum of Ge powder is collected. To achieve a surface oxidation, a pre-treated HF powder was heated at 50°C for 4 days in air. DRIFTS data are reported in figure 3.4: the black spectrum clearly shows a GeH_x peak [123, 124] near $2000\ cm^{-1}$, while an ox-

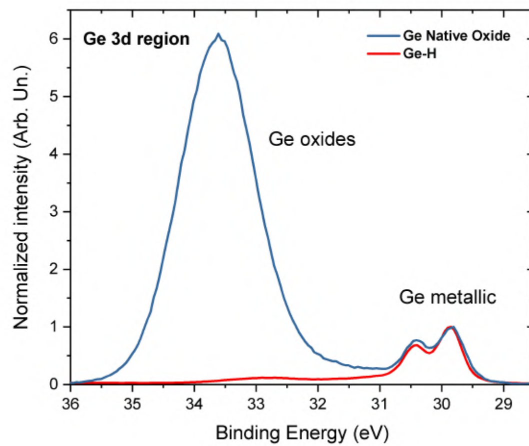

Figure 3.2. XPS Ge3d region of untreated germanium surface (called germanium native oxide, blue spectrum) and a germanium after Ge oxide removal procedure (red spectrum), as described in the text. The spectra are normalised to Ge metallic peaks. The energy of the X-Ray beam is 350 eV.

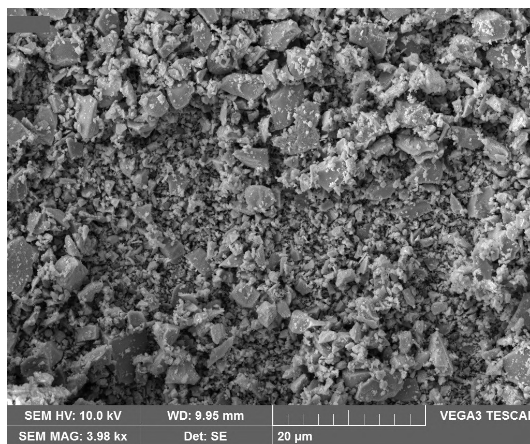

Figure 3.3. SEM image of Ge powder.

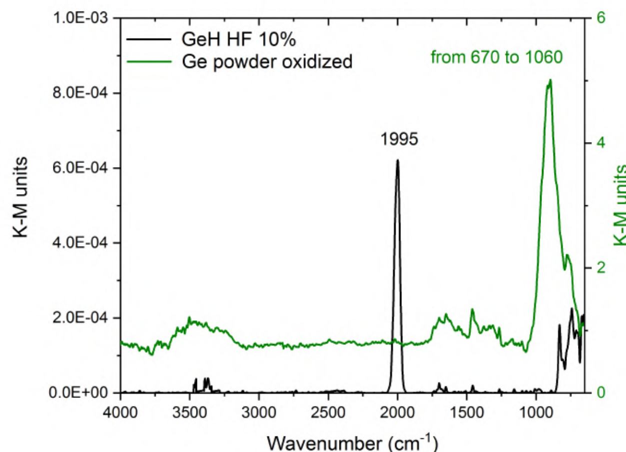

Figure 3.4. DRIFTS data of Ge-H functionalized Ge powder (reported in black) presenting a Ge-H peak near $2000\ cm^{-1}$*, and oxidized powder reported in green (shifted up) presenting absorption in the* $1060 - 670\ cm^{-1}$ *region.*

idized Ge powder presents absorption peaks in the $1060 - 670\ cm^{-1}$ region, where classically germanium oxide absorption is found. Moreover, a broad absorption band centered at around $3450\ cm^{-1}$ normally attributed to O–H stretching is also present (green line, figure 3.4), though with low intensity. This can be related either to the formation of Ge–O–H surface bonds, by reaction of Ge–H with humidity, or to water surface adsorption.

Finally, combining our and previously cited literature results, the Ge surface obtained after the removal process is a partially Ge-H functionalized surface (in the order of 50%), with also some Ge-OH and Ge-O-Ge residual functionalization.

3.1.2 Adsorption processes

The precursors were adsorbed on Ge (001) and powder samples with the same wet chemical procedure: the substrate was immersed in a solution containing the precursor and the entire system was heated with a reflux apparatus at the solution boiling point (about $164°$C). The precursors used in this work are: diethyl 1-propylphosphonate (DPP) from Alfa Aesar, purity 97.56%, and Sigma Aldrich, purity 95%; octadecylphosphonic acid (ODPA) from PCI, purity 99%; allyldiphenylphosphine (ADPP) from Sigma Aldrich, purity 95%. These precursors were chosen for different reasons: DPP and ODPA are two precursor that were successfully applied to Si substrates in literature with two different expected

chemisorption behaviour, while ADPP was chosen as a reduced P precursor, expecting a different chemisorption reaction with Ge surfaces. The reflux system

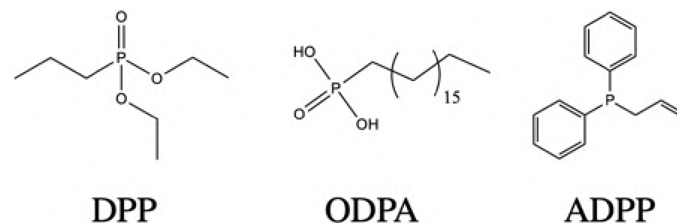

Figure 3.5. Chemical structures of phosphorus precursors used in this work: Diethyl 1-propylphosphonate (DPP), octadecylphosphonic acid (ODPA) and allyldiphenylphosphine (ADPP) chemical structures.

was filled with argon, in order to minimise the humidity presents in the glassware and to minimise water and oxygen content in the reaction flask thus preventing the degradation of molecules during the deposition (see figure 3.6 A). The solution was formed by mixing 25 ml of 1,3,5-trimetylbenzene (also called mesitylene 98+%, Sigma Aldrich) and a fixed amount of solute, depending on the used type of precursor: DPP 2 ml, ODPA 2-3 mg and ADPP 200 μl. After 30 min - 2.5 h, the sample was extracted from the solution and rinsed with hot mesitylene. The temperature was monitored during the depositions, to confirm the temperature stability guaranteed by reflux conditions (see figure 3.6 B). Ge (001) samples were dried using argon flux after removal from the bath, while powders were filtered and dried for 1 h at $50°$C in a vacuum oven.
During a temperature study, the reflux system was heated with a sand bath (see figure 3.6 C), in order to perform the process at lower temperatures (temperatures below the solution boiling point).

This process is the so called standard process, that can be simply performed with a standard chemical lab glassware under a fume hood. A different protocol, called dry process, has been developed, and will be described below.
The main difference between standard and dry process is the use of a chemical dry box in the latter: the adsorption procedure is conducted in an extremely controlled ambient, with water and humidity content constantly monitored below 1 ppm, and in between 40-50 ppm respectively. New reagents are used for these process, and they are open and kept inside the dry box, in order to prevent air exposure. The dry process is intrinsically not compatible with the Ge acid oxide removal, since the HF chemical attack is based on a water solution treatment: for this reason, the germanium oxide removal is the only process done without the use of dry box. After this step, the sample presenting the Ge-H functionalization is kept in mesitylene and put inside the dry box, for the adsorption procedures

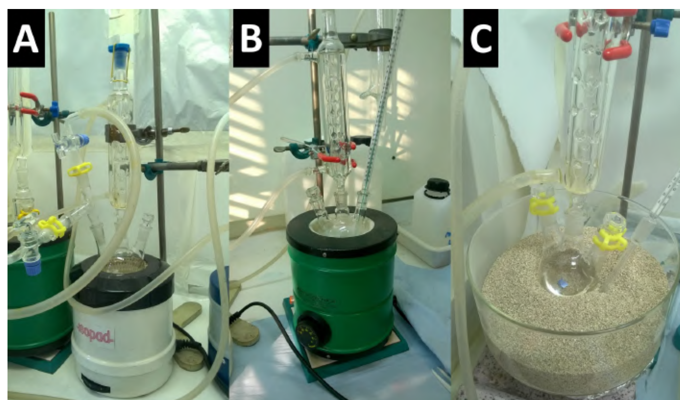

Figure 3.6. Reflux system for adsorption. ***A*** *Argon line connected with a triple neck round-bottom flask.* ***B*** *Thermometer inserted in the flask to control the boiling temperature.* ***C*** *Reflux system in sand bath for adsorption tests below the solution boiling point.*

in 10-20 minutes. Only in the case of sample measured by XPS (figure 3.2) the permanence time in mesitylene vessel was longer (3-4 hours) due to transfer to synchrotron measurements chamber. Also a reflux system cannot be used inside the dry box, and for this reason the adsorption procedures are done within an ace glass tube. The solution inside the pressure tube is heated with a sand bath, by controlling the temperature with a thermometer: the vapour creation inside the tube indicates that the reaction temperature is reached. After these temperature pre-tests, the sand temperature for the adsorption reaction is chosen.

Figure 3.7. Dry box located at DISC, Applied Organometallic Chemistry group.

The functionalized samples were stored in a closed vessel filled with argon until the next procedure step or surfaces analysis. In some cases, samples are also rinsed with methanol (electronic grade) in order to remove the physisorbed fraction of the adsorbed molecules, as suggested in literature [67].

In case of a diffusion test, the functionalized surface is covered with a capping layer, which consists in the deposition of 70-100 nm silicon dioxide capping layer via RF sputtering deposition acting as an out-diffusion barrier for the dopant and preventing Ge evaporation. This coating is reported to behave as the best SiO_2 capping from ML source in Ge [76]. Other tests were performed by using SiO_2 from e-beam evaporation, but similar results were obtained.

3.1.3 AFM surface topography

The Ge samples are characterised before and after the chemical surface functionalization, in order to record its topological evolution. The images were acquired with DI Cp-II AFM instrument using a commercial silicon nitride cantilever. The images were collected as larger as possible, in order to verify the surface topology in a large area. The image shown in this section are 100 x 100 μm^2.

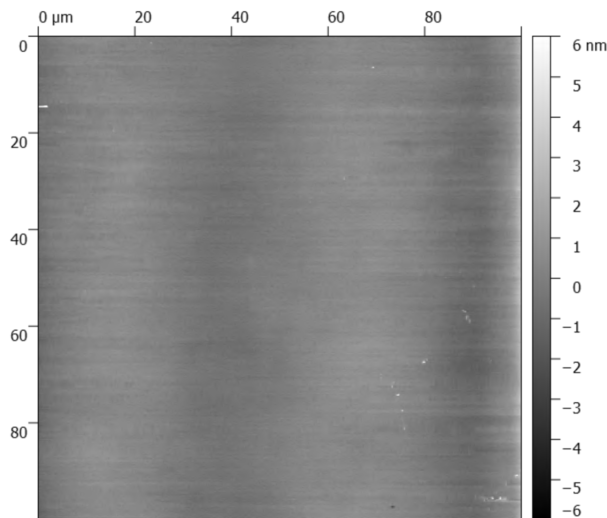

Figure 3.8. AFM image of untreated Ge (001) surface. The collected area is 100 x 100 μm^2.

A Ge untreated image (shown in figure 3.8) is acquired as reference, while a ODPA dry functionalized sample is reported in figure 3.9.

As can be seen, ODPA functionalized sample show no macroscopical surface modification, revealing that no macroscopical surface damage is induced as a consequence of the treatment.

Also a DPP std functionalized sample is shown in figure 3.10. As can be seen, there is some dirt on the sample, due to the fact that it was mounted, measured and transported at the synchrotron facility. Neglecting this features, the surface

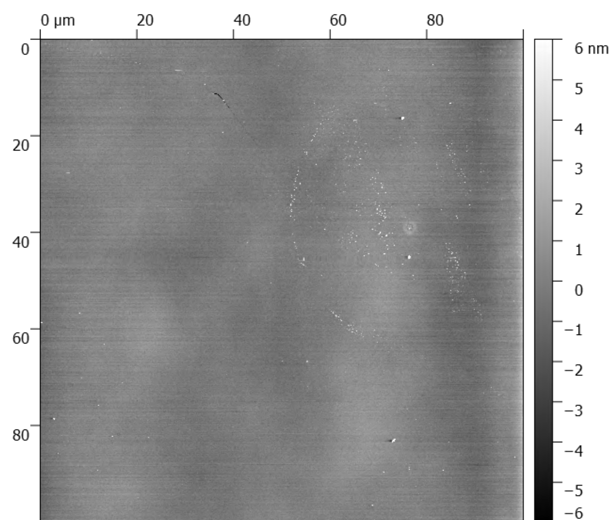

Figure 3.9. AFM image of a Ge (001) surface functionalized with ODPA molecule with a dry process. The collected area is 100 x 100 μm^2.

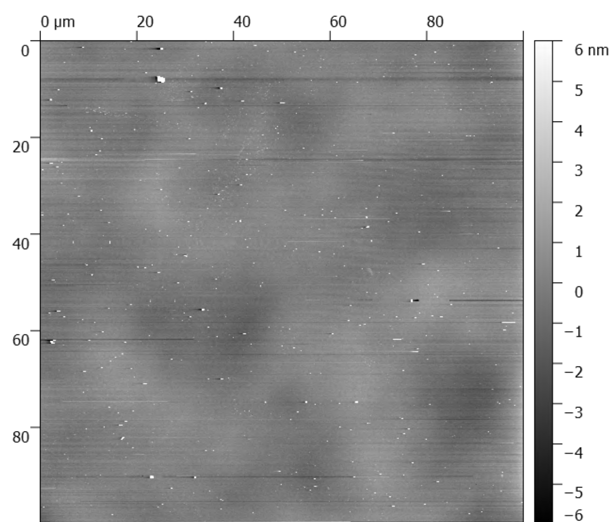

Figure 3.10. AFM image of a Ge (001) surface functionalized with DPP molecule with a standard process. The collected area is 100 x 100 μm^2.

appears flat and defect free also in this case.
In order to quantitatively compare these figures, some statistical analyses can be performed on these images, such as the calculation of the surface roughness. This analysis can be performed with a free software, on the entire image or in a portion if it, simply by selecting the desired area. The roughness calculation over the whole area returns a value of 3.0 Å for the untreated Ge, a value of 6.7 Å for ODPA dry sample, and a value of 17 Å for DPP std. Unfortunately this estimation is extremely sensitive to dirt, and the DPP and ODPA value are mainly affected by this. Selecting a portion of the image (around 15 x 15 μm^2) that is cleaner than others, the roughness estimation gives: for the untreated Ge a value of 2.8 Å, for ODPA dry 2.9 Å, and for DPP 3.9 Å. This confirms that no visible surface modification is present on a 15x15 scale. Eventual modulation of the precursor deposition amount over a bigger scale is not detectable with these measurements.

3.2 Characterisation of Phosphorous functionalized Ge surfaces

In this section, surface analysis on adsorbed precursors are reported, comparing XPS, AR-XPS, NRA, Grazing incidence-EXAFS and DRIFTS analysis. The DRIFTS analysis were conducted on Ge powder while all the others are conducted on Ge (001) surfaces: for this reason, a careful comparison between experimental results will be presented and discussed in details.

3.2.1 Phosphorus and Germanium oxidation states

The first analysis presented in this work is a comparison of XPS signal from precursors adsorbed on Ge (001) surface. As shown in figure 3.11, P 2p (peaks at about 134 eV) and Ge 3p (peaks in 120-130 eV region) signals of ODPA, DPP and ADPP precursors deposited with dry and standard process are reported.
The first clear result is the adsorption on Ge (001) of all molecules, using both standard and dry processes, thought some differences are present. The first difference between standard and wet process is the amount of precursor adsorbed to the surface which is higher in standard for DPP and ODPA, while it is about the same for ADPP. These facts will be discussed in detail in the next section with an accurate quantification analysis.
The second difference is the phosphorus binding energy for ODPA and DPP molecules. For both molecules, the phosphorus binding energy is equal to 133.9

eV for dry process and 134.5 eV for standard process, outside the error of each spectrum equal to ± 0.1 eV. These values can be easily compared with literature data of Branch and co-workers [125] that report ODPA (free, not chemisorbed) and ODPA adsorbed on HfO_2 XPS spectra analysis.

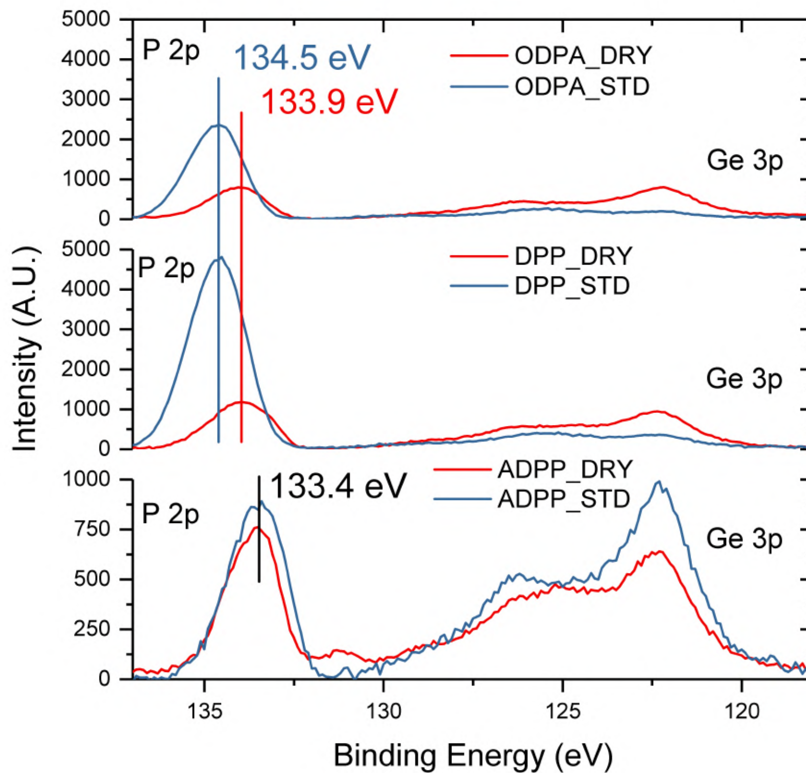

Figure 3.11. Synchrotron XPS spectra of ODPA, DPP and ADPP precursors adsorbed on Ge (001) surface on P 2p and Ge 3p region. For each molecule, dry and standard process spectra are reported in red and blue respectively. Blue, red and black vertical lines are reported to compare different peaks binding energies. The X-Ray beam energy is 350 eV.

P 2p binding energy is between 134.7-135 eV for ODPA molecule [125], shifting to 133.5-134 eV in the ML case after adsorption. These values are clearly compatible with our data. In particular, the ODPA deposited via dry process presents a P 2p peak at 133.9 eV, a value comparable with Branch et al. ODPA ML value. The ODPA deposited via standard process presents a binding energy of 134.5 eV, that is more similar to the Branch at al. not adsorbed ODPA value. This fact will be clearly interpreted after the quantitative analyses of P content, and here we can

Formal oxidation number	Compound	P 2p 3/2 BE eV
-III	$P(C_4H_9)$	130.5
-III	$P(C_6H_5)_3$	130.7-131.3
I	$(C_4H_9)_2P(O)OH$	133.1
I	$(C_6H_5)_2HPO_2$	133.3
III	$P(OC_3H_7)_3$	133.8
III	$CH_3P(O)(OH)_2$	134.3
III	H_3PO_3	134.3
III	$H_2(C_6H_5CH_2PO_3)$	134.6
III	$C_{18}H_{39}O_3P$ ODPA	134.7-135
V	P_2O_5	135.1-135.6
V	H_3PO_4	135.2

Table 3.1. Different binding energies of P based molecules reported in the NIST online XPS binding energy database srdata.nist.gov .

anticipate that it is related to the fact that ODPA std peak has a chemisorbed and a physisorbed component too. In this case the physisorbed component presents the ODPA molecule binding energy, while the chemisorbed shows a binding energy shift due to the new surface interaction between the ODPA and the new bond(s). The 134.5 eV value is also compatible with the common P (III) molecule H_3PO_3 that has a P 2p peak at 134.3 eV, as reported in the on-line NIST binding energy database [1].

In the DPP precursor case, the P 2p peaks show the same BE of the ODPA molecule ones. Formally, DPP and ODPA precursors (see figure 3.5) have the same P oxidation state equal to (III), but in principle the absorption behaviour should bring to different BE. Also in DPP case, the P 2p presents a shifted binding energy for dry process compared to the standard adsorption process, and also the std process presents a higher amount of P respect to the dry process. These facts suggests that the two molecules should undergo similar adsorption processes.

A completing different phosphorus precursor is the phosphine ADPP molecule (see figure 3.5 for the precursor molecular structure), that was also adsorbed on Ge (001) surface. This precursor has an initial oxidation state formally equal to (-III), since it is a phosphine. Its structure presents two phenyl groups directly bonded to the central P and an alkyl chain presenting an allyl- functional group. The XPS P 2p signal shown in figure 3.5 evidences a phosphorus binding

[1] online NIST binding energy database http://srdata.nist.gov/xps

energy equal to 133.4 eV both for standard and dry procedures. These data are quite surprising since the initial binding energy for ADPP molecule should be much lower. As an example, the common triphenylphosphine presents a binding energy ranging between 130.7-131.3 eV (by looking at different BEs reported in NIST database and in table 3.1), while in ADPP case, it presents 2 phenyl groups and an aliphatic chain, so one electron withdrawing group less than triphenylphosphine. This means that ADPP BE should be in the same binding energy range or slightly less than the triphenylphosphine BE.
Yerushalmi and co-workers [67] reported a BE range that is between 133-133.5 eV for phosphine oxide molecules (bulk, not adsorbed to any surfaces), a values compatible with our data. This fact is another confirmation that an oxidation of ADPP molecule occurs.

By looking the ADPP XPS spectra in figure 3.5, a small P 2p peak can be seen, at 131 eV position that should correspond to native ADPP. It is important to stress that this peak is not present when short measurements are done in a pristine spot area but this peak has been seen growing during the measurements, and so it is caused by the X ray beam: this fact is not so strange and shows a vacuum reduction of oxidised ADPP phosphorus under the X-Ray beam.

In figure 3.12, the P 2p are fitted, and the peak asymmetry is clearly due to the 3/2 and 1/2 components. The ADPP DRY spectrum is interesting due to the fact that a P 2p reduced component can be seen, and thanks to this deconvolution binding energy is estimated to be about 131 eV.
P 2p, Ge 3p regions are deconvoluted to analyse Ge 3p peaks, that clearly shows different contributions. In figure 3.12, the ADPP Ge 3p P 2p region is fitted with two components, that can be connected to metallic and oxidised contributions. The Ge 3p 3/2 metallic is normally present at 122.2-122.4 eV and the oxidised at 124.4-124.7 eV, as reported in literature [126] [127].

Ge 3d peaks were also acquired during the synchrotron measurements session for all samples, as reported in figure 3.13. Thanks to their high XPS cross section, higher signal vs background ratio was obtained. Moreover, Ge 3d region can give good information on germanium oxidation and sensitivity to oxidised state is which is higher than P 2p Ge 3p region, because it has different and more pronounced chemical shifts. From the simple comparison of data, it is difficult to evaluate the binding energy of each peak, and it is clear that several components are present. As an example, in figure 3.14 a Ge 3d region of Ge-H ADPP functionalized surface with a DRY process is shown. Thanks to the high quality of the signal, the XPS spectrum can be deconvoluted with different components:

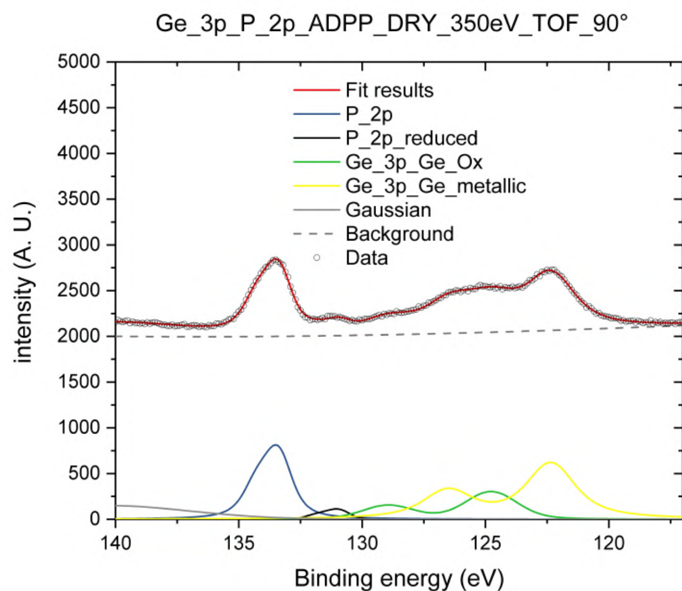

Figure 3.12. Synchrotron XPS spectrum of ADPP precursors adsorbed on Ge, P 2p and Ge 3p region, 350 eV X-Ray energy beam at 90° take-off angle.

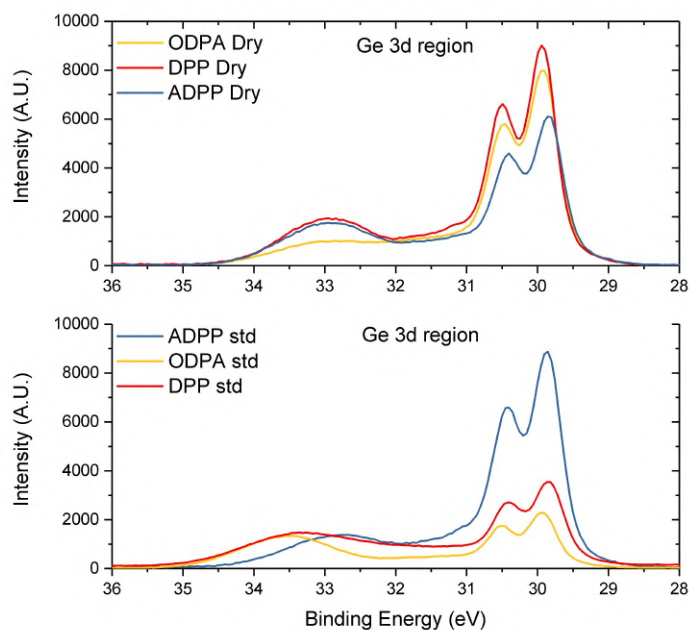

Figure 3.13. Synchrotron Ge 3d XPS spectra of DPP, ODPA and ADPP for standard and dry deposition procedures. The data are collected at 90° take-off angle with a 350 eV X-Ray energy beam.

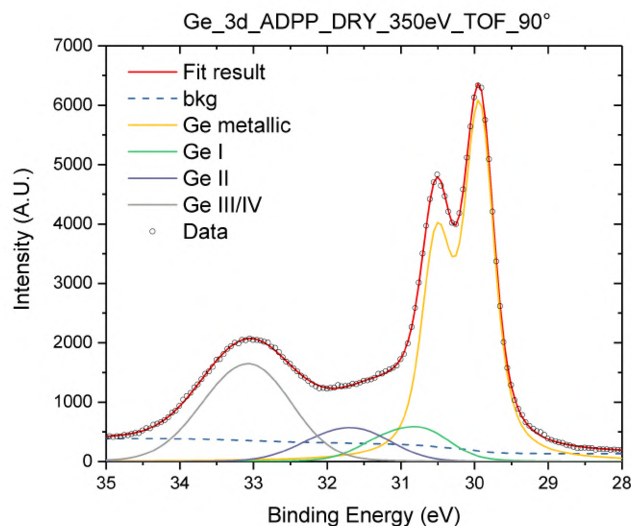

Figure 3.14. Synchrotron Ge 3d XPS spectrum of ADPP at 90° *take-off angle with a 350 eV X-Ray energy beam.*

at 29.8 eV the Ge metallic peak is present, presenting a clearly separated 5/2 and 3/2 components. Others 3 different oxidised components are necessary to correctly fit the signal. At the best of my knowledge, only one paper reported with such accuracy a Ge 3d XPS deconvolution analysis [128]. The metallic Ge 3d is reported to be at 29.8 eV, so in good agreement with our binding energy. Shifts with respect to this 0 oxidation state reference are reported in ref. [128] for other 4 components corresponding to 4 oxidation states: a Ge I at 0.7-0.8 eV chemical shifts, Ge II at 1.5-1.8 eV chemical shifts, Ge III at 2.4-2.6 eV chemical shifts and Ge IV varying between the Ge III values for thin layers (lowest reported value is 0.6 nm GeO_2 at 2.8 eV chemical shift) up to a 3.6 3.8 eV for 3.5 nm GeO_2. These literature data are in a very good agreement with the results coming from the deconvolution showed in figure 3.14, as can be noted.

In graph 3.16, a comparison between our data (blue stars) and literature data [128] is shown. Ge I and Ge II peaks can be univocally identified, presenting the same chemical shifts of Matsui and co-workers [128]: Ge III - IV peaks are not resolved in our case and we fitted them by a single signal that has a binding energy between the two (we report the value with an average 3.5 oxidation number). In our case, the amount of Ge oxide is lower than these data, according ARXPS analyses, and so Ge IV chemical shift is expected to be very similar to the Ge III one, producing overlapped Ge III and Ge IV signals. For this reason, we

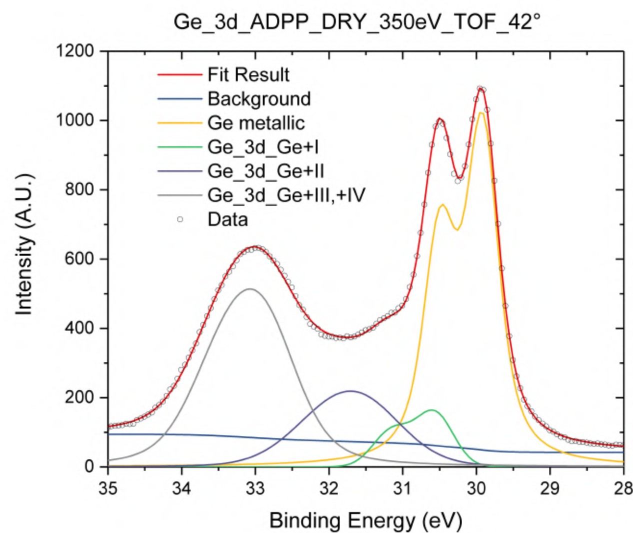

Figure 3.15. Synchrotron Ge 3d XPS spectrum of ADPP at 42° take-off angle with a 350 eV X-Ray energy beam.

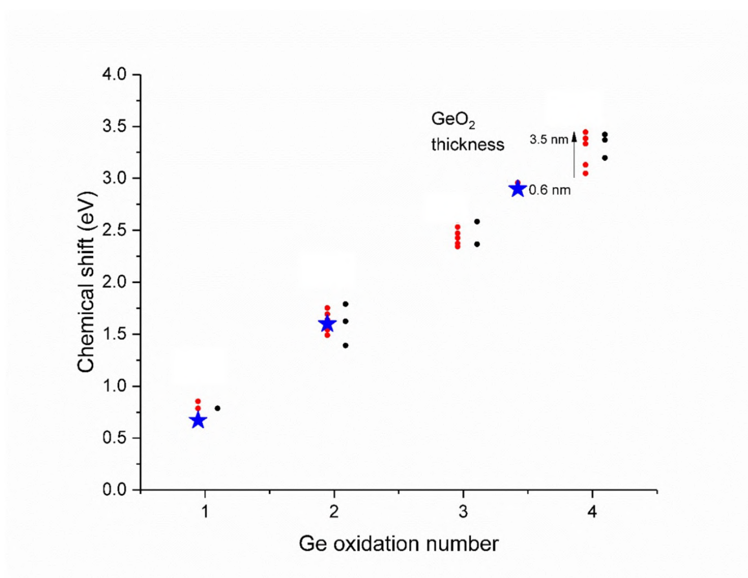

Figure 3.16. Comparison between our chemical shift data for Ge 3d XPS peak (blue stars), and literature data (Matsui and co-workers [128]). Our data for Ge III-IV peak is presented as a IV data, in order to compare this value with the germanium oxide thikness trend.

report a single star in between III and IV oxidation state, indicating a unique peak deconvolution for III and IV states.

To verify this hypothesis, in figure 3.17 we report the deconvolution of 3d spectrum for the sample that only underwent cleaning procedure but not P adsorption (see preparation paragraph for details, herafter called GeH sample).

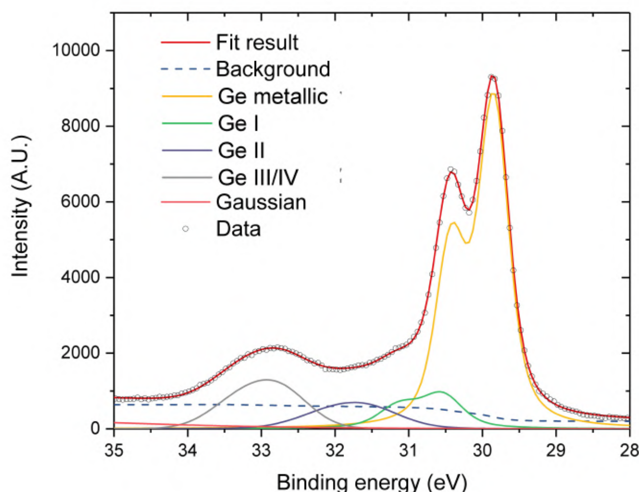

Figure 3.17. Synchrotron Ge 3d XPS spectrum of Ge after a germanium oxide removal process (as described in the experimental session) called Ge-H surface, at 90° *take-off angle with a 350 eV X-Ray energy beam.*

As can been seen in this figure, Ge-H surface presents the same germanium oxides deconvoluted binding energies of figure 3.14 within experimental errors, suggesting that an eventual chemisorption can not be detected by a simple deconvolution method. Moreover, it is important to remember that the Ge-H XPS peaks are collected 3-4 hours after the preparation, since the sample has been transported to the synchrotron facility under mesitylene: during this time, it can not be excluded that a small surface oxidation occurs.

3.2.2 Germanium oxide interlayer quantifications

In this section, an adsorbed molecule quantification analyses are presented by means of Angle Resolved XPS analysis and Nuclear Reaction analysis.

The XPS angle resolved analysis consists in the analysis of the variation of the XPS intensities by changing the take-off angle. Intensities are obtained by deconvolution as previously reported in figures 3.14 for Ge 3d peaks and 3.12 for P 2p and Ge 3p.

An example of the peaks variation by changing the take-off angle is reported in figure 3.18 for P 2p Ge 3p region. The Angle Resolved peak intensities are

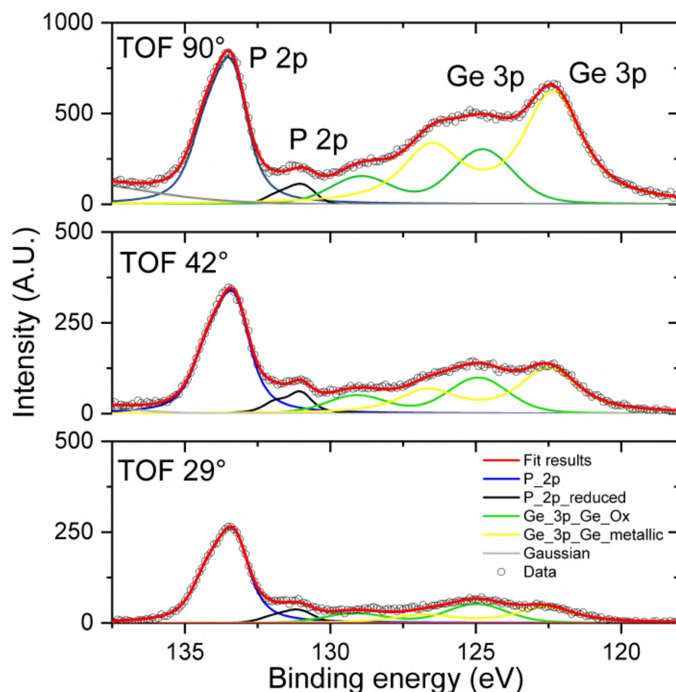

Figure 3.18. Angle Resolved XPS spectra of Ge ADPP dry sample. P 2p and Ge 3p region are reported at 90 (i.e. normal emission), 42 and 29 degree take-off angle. Data (withe points) are fitted by different components as reported in the previous section, and the global fit result is reported with a red curve, taking into account also the background (grey curve). The spectra were acquired using an X-Ray beam with a photon energy equal to 350eV.

analysed with Brixias code package, as reported in the Methods chapter 2. Different parameters are given to the simulation package such as the geometry of the experimental chamber, the polarisation and the energy of the X-Ray beam. Thanks to this software, it is possible to quantify the amount of chemical species on Ge surfaces by assuming a layer model of the surface. Each layer has a proper fixed composition and density, and the layer thickness can be set as a free fitting parameter. Each XPS angle resolved data can be assigned to a specific layer: as an example, the P 2p peak is assigned to the phosphorus monolayer input layer, or the oxidised component of Ge 3p is assigned to germanium oxide input layer. In this way, the thickness of each layer is linked to the angle resolved trend of XPS signals.

The software takes into account the different XPS cross section and calculates the DDF parameter (basically both elastic and inelastic photoelectron scattering) for

each input layer. The data fitting consists in the variation of layer thickness in order to fit the ARXPS data. The DDF parameter is recalculated iteratively, since each layer thickness variation modified the electron free path and so the more complex DDF.

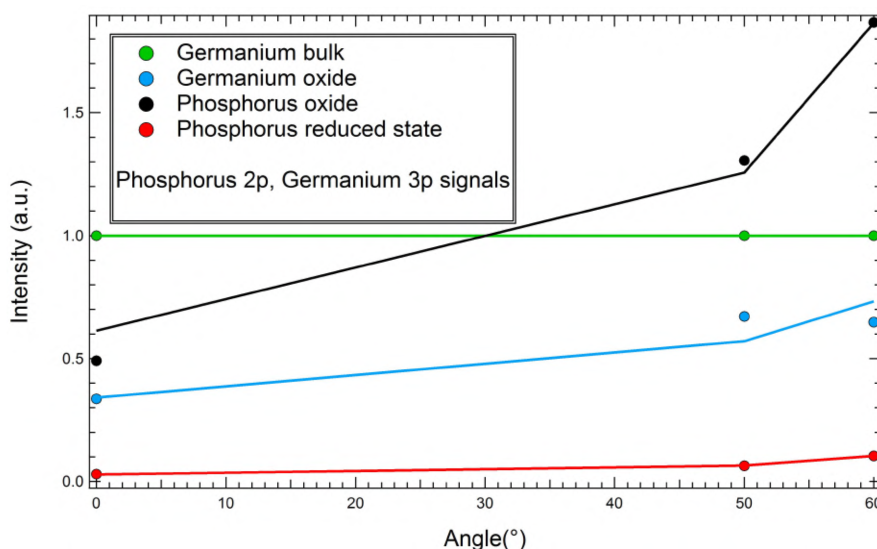

Figure 3.19. Angle Resolved XPS modelling and fitting of Ge ADPP standard sample. The reported data are peaks intensities as a function of the emission angle: the angle is the complementary of the take-off angle (90-x). The used peaks are P 2p, Ge 3p metallic and oxidised. The Ge metallic signal are used as a reference (fixed to 1) as the bulk signal. The two phosphorus components are treated separately. The model and the fitting result are reported in the inset table.

In Figure 3.19 an example of Angle Resolved modelling and fitting is reported. The data are normalised point by point to the metallic Ge intensity that therefore results equal to the unit at each angle. In this figure, the two phosphorus signals present after ADPP adsorption are reported: the less intense is referred to the peak that appears under beam irradiation. The used layer structure is reported in the in-box table. As mentioned above, the model consists of a sequence of layers. Each layer has an assigned material whose properties, described in a database, determine the mean free path of photoelectrons. Each XPS signal is assigned to come from one or more layers. Our model considers (from the depth towards the surface): a bulk of germanium, from which the Ge metal signal comes, a GeO_2 layer from which the 3p signal of the oxidised Ge comes, a P_2O_3 layer from which the main P signal comes.
We have chosen this material because it is the only one that has the same oxidation among those present in the Brixias database. We also tried with other

database materials (P_2O_5 for example) and no strong variation of P content in the layer comes from the alternative fitting, even if the fit quality is slightly better for P_2O_3.
Another layer is assigned to P 2p reduced signal, assuming the same composition: this layer is extremely thin and it shouldn't influence the fit result. The last layer on top is a carbon layer: this layer is normally inserted in all the AR-XPS analyses. It takes into account the attenuation due to some atmospherical carbon contaminant that could be adsorbed on top of samples. This layer has no XPS signal assigned but it influences the other signal intensity and trend with angle. As will be shown, the amount of atmospheric contaminants is very low; this was possible only by synthesising a sample batch specifically for synchrotron analysis and taking some precaution such as the transportation under vacuum boxes.
The best fit simulation of XPS intensities is shown with coloured lines, and the layer thicknesses are reported in the inset with the fitting error (estimated by the software).
By using these layer model, all the AR-XPS data were fitted with good fitting results: as an example, a fitting result is reported in figure 3.19.

In order to cross check the obtained results, we have also analysed the 3d signals. In figure 3.20 and 3.21, Ge 3d signals are reported together with their best fit simulations.

As can be seen in figure 3.20 and 3.21, the input layer models are a $C - P_2O_3 - GeO_2 - GeO - Ge$ layer model, in which only GeO_2, GeO, C thickness are fitted (metallic Ge 3d is also used as a reference) and P_2O_3 layer is fixed to the best fitting value obtained by P 2p analysis. The Ge I component is not inserted as a germanium oxide. We interpreted this Ge-I component as the topmost part of the crystalline Ge and added it to metal Ge signal. This probably happens also in 3p data set thanks to the lower chemical shift sensitivity. Moreover, there is a limit in the number of signals that Brixias can simulate simultaneously. On the contrary Ge II and Ge III-IV are assigned to GeO and GeO_2 layers respectively.

The germanium oxide is therefore evaluated both by P 2p - Ge 3p and Ge 3d XPS data, giving two different estimations of the germanium oxide thickness by using Ge 3p or Ge 3d signals. Thus, it is interesting to compare these results to evaluate the Brixias code analysis, the goodness of the proposed modelling and other systematic errors, such as the DDF evaluation by Montecarlo estimation.
In figure 3.22 the germanium oxides estimation with Ge 3p and Ge 3d data are showed.

The Ge 3p quantification (red bars) is related to the only oxidised component

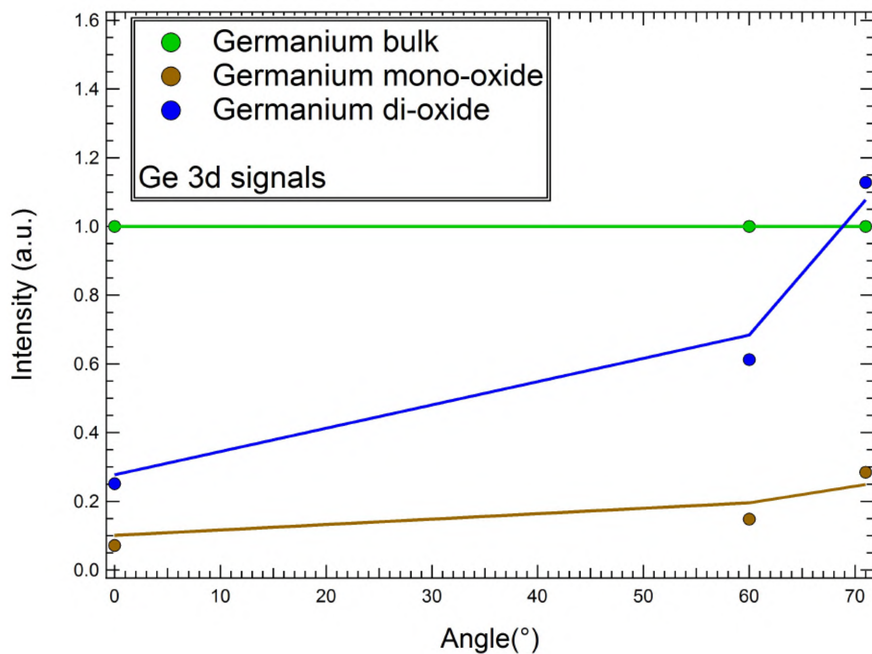

Figure 3.20. ARXPS fitting of Ge 3d region of DPP dry sample. The Ge 3d oxide signals are related to Ge II and Ge III-IV. Ge I is not included as germanium oxide.

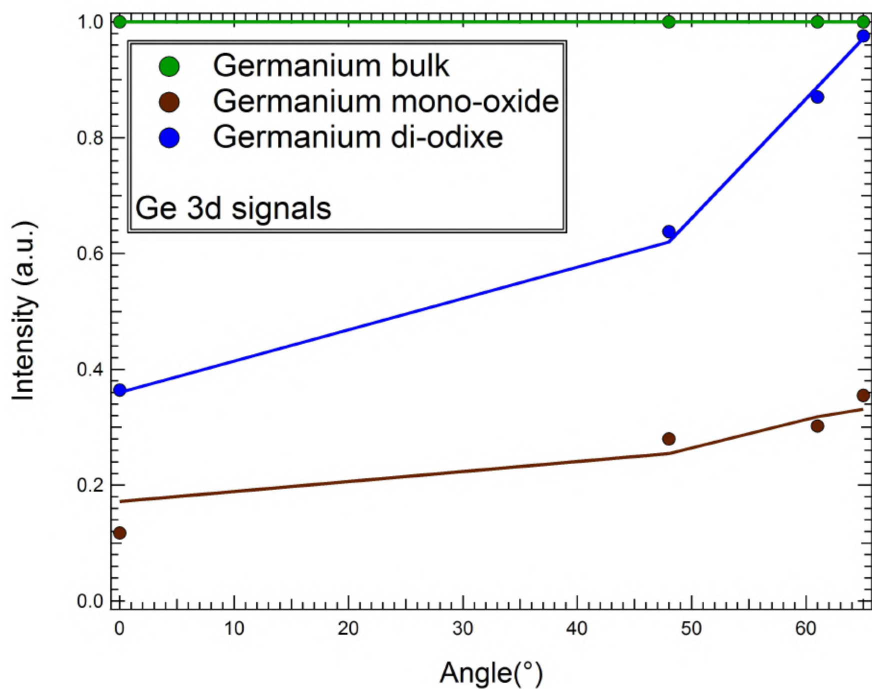

Figure 3.21. ARXPS fitting of Ge 3d region of ADPP dry. The Ge 3d oxide signals are related to Ge II and Ge III-IV. Ge I is not included as germanium oxide.

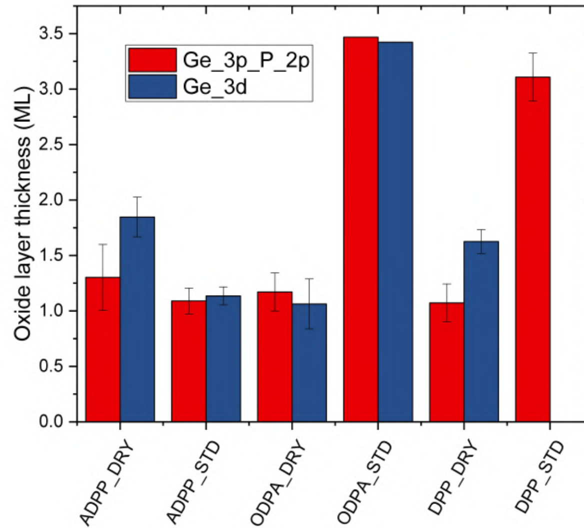

Figure 3.22. Comparison between germanium oxide quantification via ARXPS analysis. For each analysed sample, Ge 3p and Ge 3d oxide quantification is reported with the error bar given by the fitting software. The Ge 3p quantification (red bars) are related to the only one oxide component revealed in the XPS deconvolution step, while the Ge 3d quantification (blue bars) are the sum of all oxidised component Ge II and Ge II-IV.

revealed in the XPS deconvolution step (as reported in figure 3.12), while the Ge 3d quantification (blue bars) is the sum of all oxidised component Ge II and Ge II-IV, without the Ge I component. The 3d quantification is in most cases higher than the 3p one. This may be due to a systematic error, or to the fact that 3p signal is less sensitive to different oxidised Ge components, and maybe Ge-II component could be superimposed to the metallic one instead of Ge-III and IV, as implicitly assumed by our analyses. The error bars reported for ARXPS analyses are calculated by the Brixias simulation package. These error are calculated by the software as a sum of data-fitting deviations, and so they correctly reports the deviation between the model and the fitted data. It is clear that this error estimation does not takes into account the input model correctness (that contains the DDF evaluation and the material density correctness) and all the cross sections. For example, the GeO_x density is assumed to be equal to the GeO_2 bulk oxide. In the light of these considerations, and as can been seen in figure 3.22, the error bars are probably underestimated: this can be expected as previously discussed, and also considering that it do not takes into account the phosphorus over layer thickness, in this specific case. Probably, this discrepancy between the two dataset can be simply explained by considering a slightly higher statistical error with respect

to those reported by the fitting code. In fact, no clearly systematic over or under estimations are present for Ge 3p and Ge 3d data. Interesting, this type of comparison is not presented in any analysed literature work, thus no literature suggestions are available.

Some important results can be derived by this graph: the dry procedure presents the same GeO_x thickness (1-1.5 ML) regardless of the molecule precursors used. The dry procedure is therefore quite effective in limiting the Ge oxidation, especially if compared to standard one in case of ODPA and DPP where 3 ML GeO_x are produced. It's difficult to decide if the Ge oxidation in dry procedure occurs during the adsorption process or during the short air exposure or mesitylene transport of cleaned samples. As we previously said, others groups reported the formation of 0.5 ML GeO_x monolayer after a cleaning procedure like ours and a short air exposure. From this point of view, it could be that in case of ODPA and DPP, where O is present in the precursor, oxidation may occur as a consequence of the adsorption that forms P-O-Ge bonds. On the other hand, the same reasoning my not be applied to ADPP precursor that does not contain O in its starting molecule. Therefore, it is likely that a small oxidation occurs during the process and this is not so unexpected given the ML level of such phenomenon, even if it does not occur in UHV ambient. Probably, the 1ML GeO_x is the limit we can achieve with a non UHV process. A further element to this reasoning is the XPS quantification of the Ge-H surface after transport to synchrotron, which evidenced a GeO_x thickness of 2 ML, thus indicating that oxidation has took place during this stage. The lower GeO_x value in adsorbed samples under dry processes suggest that P ML coating may have instead a protective effect on the Ge surface against further oxidation.

The standard procedures show an increase of germanium oxide thickness during the molecules adsorption procedure, with the exception of ADPP std samples. The oxides increase is justified by the not perfectly dry conditions of this deposition procedure: in any case, these thickness values are quite low, underling that also the standard procedure is a efficient and effective procedure for monolayer deposition.

It is interesting to discuss the ADPP sample that presents low oxides values, comparable with dry procedures results even if this procedure is completely similar to the other std processes. This fact suggests a role of the ADPP molecule adsorption in the oxide growth quenching: as shown in the XPS binding energies analysis, the ADPP molecules is oxidised during the adsorption, and this process can be in competition with germanium oxide growth. If occurring, the oxidation

of phosphines is a fast process and thus quenching the germanium oxide growth. This hypothesis will be also discussed later, with more experimental evidences.

3.2.3 Phosphorus quantifications in adsorbed layers

In this paragraph, we will discuss the quantity of P in the adsorbed samples. The data about this quantity are obtained by the AR-XPS analyses described in the previous paragraph but also by NRA analyses as described in Methods chapter 2.

In figure 3.23, a comparison of phosphorus quantification obtained by NRA and ARXPS techniques are shown.

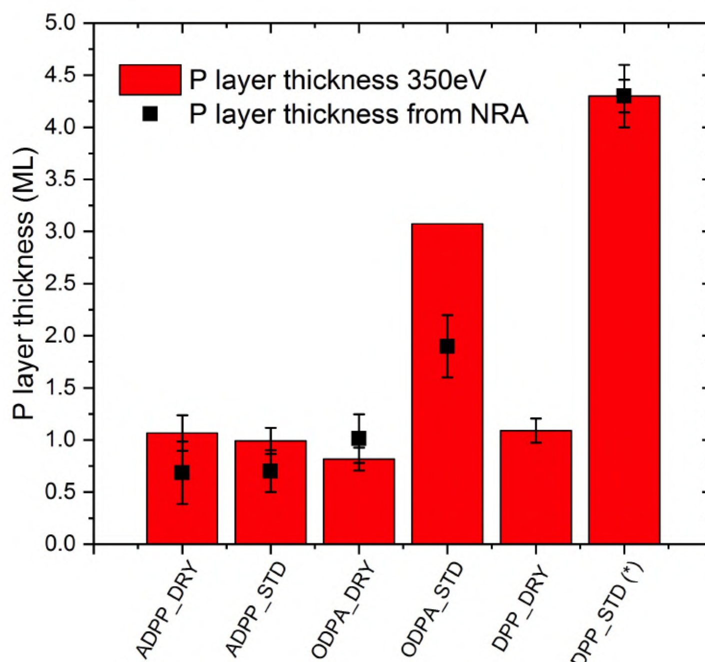

Figure 3.23. Comparison between phosphorus estimations obtained with Angle Resolved XPS analysis and Brixias code fitting (red histograms) and Nuclear Reaction Analysis data fitting (black points). Error bars are calculated form data fitting error estimation for NRA analysis, and from Brixias software package for ARXPS data. ODPA std red bar do not present any error bar since this data is not a complete Angle Resolved analysis, but it is only one XPS spectra evaluated at normal emission insted of a set of XPS spectra collected at different takeoff angle. The datum for DPP std red bar is derivates from Angle Resolved XPS from common X-Ray source; in particular, the data were collected with the Surface Science group XPS at Dept. of Chemical Sciences, Univ. of Padova.

The NRA data are reported as black points, while ARXPS data are reported with red bars. The reported error bars are evaluated by data fitting analysis and

by Brixias ARXPS code for NRA and ARXPS data respectively, as previously discussed. The NRA data are in good comparison with ARXPS data, except for ODPA std datum. As a matter of fact, the ODPA std XPS datum does not coming from a complete angle resolved analysis, but a single point evaluation (it is only one 90° XPS datum, instead of a set of XPS spectra at different takeoff angles and analysed with ARXPS modelling), this analysis does not allow us to correctly estimate an error for this datum, but only an higher error is expected for this point compared with others ARXPS data. On the other hand, it is possible that these process is not highly reproducible and this sample presents some anomaly form its synthesis. In all the other cases the good agreement demonstrates the accuracy of the adopted analytical techniques and the reproducibility of the processes that is aided by the self-limiting behaviour of the adsorption.
It is relevant to note that 4 over 6 processes bring to the formation of about 1 ML of deposited P: the ADPP both in dry and standard process, ODPA and ADPP in dry process. Because of the BE shift measured for these 4 processes with respect to the starting molecules values, these single monolayer formations are very likely to be due to a chemisorption process that bring to the modification of adsorbed molecule bonding when interacting with the Ge surface.
An interesting trend is visible for the P amount in dry and wet processes: while ADPP std and dry processes show the same P amount of about 1 ML, the DPP and ODPA molecules show a net increase of adsorbed P amount, going from 1 ML in dry conditions to 2-3 ML for ODPA and 4 ML for DPP in standard condition.
This behaviour can be correlated with the germanium oxide amount previously reported in figure 3.22. For all the processes that bring to 1 ML formation the GeOx layer is between 1 to 1.5 ML while, for DPP adsorption in standard conditions, the GeO_x is equal to 3 ML and for ODPA is 3.4 ML. A further test to understand the behaviour of DPP and ODPA deposited in standard condition was performed as suggested in literature [67]. The rinsing of sample with methanol (MeOH) is tested in order to verify the possibility to remove a physisorbed fraction: in fact, DPP and ODPA precursors are soluble in this solvent and if a molecule fraction is physisorbed on the surface, it should be removed by this process.
The same test was not performed on ADPP since MeOH is not a good solvent for ADPP, instead, the mesitylene is a very good solvent and all samples are rinsed with it at the end of any deposition process, as described in the deposition process section. In table 3.2, the P amount measured by NRA before and after MeOH

Precursors	GeH surface	MeOH rinsing
DPP	4.3 ± 0.3	2.0 ± 0.2
ODPA	1.9 ± 0.3	1.2 ± 0.2
ADPP	0.7 ± 0.2	–

Table 3.2. NRA doses expressed in monolayer units (ML) of DPP, ODPA and ADPP adsorption on GeH with standard deposition procedures. For each deposition, also a value after MeOH rinsing is reported for DPP and ODPA molecules.

rinsing is shown. As can be noted, DPP decreases from 4 to 2 ML after the rinsing, while ODPA decreases from about 2 to 1 ML. This fact strongly supports the fact that under standard mechanism both DPP and ODPA undergo physisorption. Since the rising procedure is not necessarily assuring a complete removal of the physisorbed fraction, it is impossible to demonstrate that the remaining P fraction is only ascribed to chemisorption. Indeed, this process can be considered as a comparison between the molecule solubility in MeOH and their interaction with the Ge surface, not an absolute cleaning procedure.

The correlation between the GeO_x amount and the accumulation of physisorbed DPP and ODPA in standard deposition process still remains open. GeO_x increase is clearly related to the less controlled atmosphere that promotes substrate oxidation. The increase of physisorbed fraction may be due to an increased long distance interaction between the molecules and the thicker oxide, or by a process that may stabilise the precursors to the surface in presence of oxidising agents. In the first case we can suppose that GeO_x could have a polar behaviour inducing an attraction to the incoming molecules that has baring $P = O$ polar bonds. This could be true only if the grown oxide is ordered and this should be demonstrated.

In the second case, the formation of P-O-P bridges between different precursor molecules could be invoked in the presence of oxidising agents, such as a water traces. While water should aid this process through ODPA dissociation, it should be more difficult to be foreseen in case of DPP that is not an acid.

Further investigations should be performed to understand this particular aspect of the studied depositions.

At this point some questions remain open, such as: how do the DPP and ODPA chemisorb on Ge surface under dry conditions? Which is the ADPP structure after the adsorption? Why ADPP does not change the GeO_x thickness and P monolayer formation under standard deposition conditions ? In order to answer to these questions, in the next section other surface analyses are presented.

3.2.4 Structural modification of adsorbed molecules

In this section, the structural and chemical changes of molecular precursors after the adsorption procedure are presented. Infrared spectroscopy has been performed on Ge functionalized powder to verify to verify any modification of the molecule structures through IR absorption, in particular by checking the IR absorption of the functional groups. Thanks to *Diffuse reflectance infrared Fourier transform spectroscopy* (DRIFTS), even a weak signal coming from a low amount of precursor adsorbed on Ge powder surfaces (a monolayer) is clearly acquired and analysed. This powerful and easy-access technique can not be performed on Ge (001) flat surface since a high surface area is needed to achieve a sufficiently high signal. In principle, these results have to be carefully compared to the previous ones since the adsorption occurs in a multi-faced germanium and not on a single (001) surface. In order to overcome this problem we integrated the results with EXAFS synchrotron radiation analyses of selected samples. DRIFTS was performed on the samples prepared with the std procedure, while EXFAS was performed on both standard and dry for ADPP samples.

DRIFTS analyses were conducted on Ge powder, previously prepared with a HF 10% solution, to remove the oxide and prepare Ge-H functionality, as demonstrated at the beginning of this chapter, figure 3.1. The adsorption reaction was conducted with the same procedure used for Ge (001) surface, as previously described. The spectrum of HF-treated powder was employed as a background for all the DRIFTS spectra.
The spectrum of Ge-H powder functionalized with ODPA is reported in figure 3.24, compared with the IR ODPA precursor spectrum [129]. The ODPA spectrum was obtained thanks to a ODPA and KBr tablet analysed in a standard FTIR transmission mode. The P-(O-H) group of the ODPA molecule generates two wide absorption bands at 2800 and 2300 cm^{-1} ascribed to bound and free hydroxyls P-(O-H) stretching modes. In the $3000-2700$ cm^{-1} region C-H stretching modes are visible as emerging peaks, ascribed to the octadecyl group of ODPA molecule. The same methyl and methylene groups are identified by C-H bending modes appearing with a sharp and intense peak at 1474 cm^{-1}. The 1225 cm^{-1} absorption is ascribed to the P=O group, while the peaks in the region $1100-950$ cm^{-1} are attributed to ν_{as} P-O(-H) and ν_s P-O(-H) as reported in the Luschtinez and co-workers paper [130].

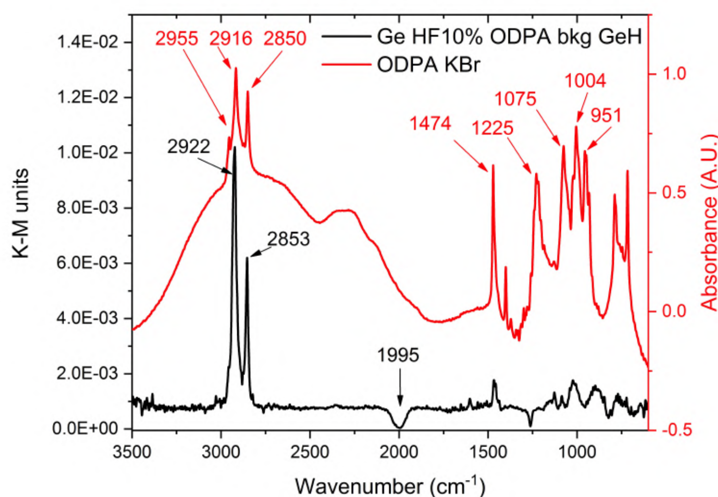

Figure 3.24. DRIFTS data of Ge powder treated with 10% HF and functionalized with ODPA precursor; background Ge-H powder. In red, transmittance FTIR spectrum of ODPA in KBr.

The spectrum of H-terminated Ge powder after treatment in mesitylene/ODPA solution via reflux reaction, as described previously, is reported in the same figure 3.24 (black line). The functionalized powder presents a negative absorption at $1995\ cm^{-1}$, indicating a Ge-H functionalization disappearance whereas the persistence of the absorption peaks in the $3000 - 2700$ region and at $1470\ cm^{-1}$ confirms the presence of the aliphatic chain of ODPA. The wide absorption band ascribed to P-O-H stretching (2800 and $2300\ cm^{-1}$) and ν_{as} P-O(-H) and ν_s P-O(-H) ($1100 - 950\ cm^{-1}$) almost disappeared, as well as the $1225\ cm^{-1}$ phosphoryl group. Only weak absorptions at around $1050\ cm^{-1}$, ascribed to P-O groups, and at around $880\ cm^{-1}$ assigned to Ge oxide are visible.
These experimental observations indicate that significant changes in the precursor structure occurred and suggest the creation of covalent bonds between the Ge surface and either the phosphoryl group or the P-OH group. This hypothesis is further supported by the consideration that ODPA chemisorption on H-terminated silicon surfaces, proposed by Longo and co-workers, show the same adsorption mechanism [69]. Others papers, related to ODPA grafting to metallic surfaces and SiO_2, show the same chemisorption mechanism [125, 130–132]: depending on the process conditions, it provides the opening of one P-OH group or both, and also the P=O functionality can be reactive with surfaces. In the light of these suggestions, in figure 3.25 mono- bi- tridentate

chemisorption suggestion are showed [129].
The DRIFTS result (shown in figure 3.24) suggest that ODPA forms a tridentate

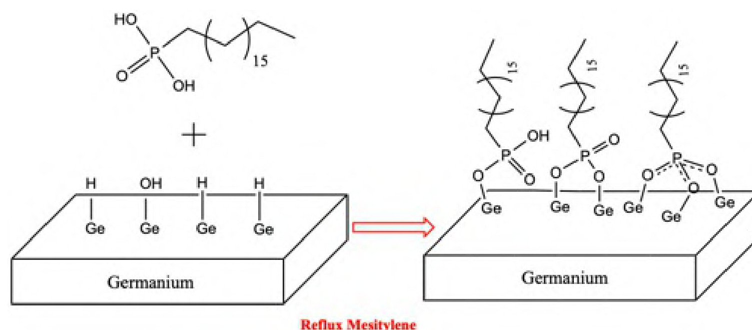

Figure 3.25. Different suggestion on ODPA chemisorption: mono- bi- tridentate.

chemisorption on Ge powder surfaces, since no P-OH and P=O functionalities are visible in DRIFT spectra after the adsorption process.
In principle, another structure can be formed during ODPA chemisorption, and it is proposed in figure 3.26. This structure is compatible with DRIFTS data

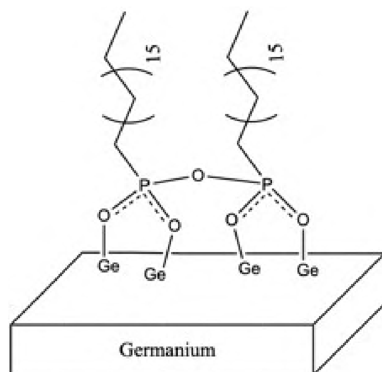

Figure 3.26. Different suggestion on ODPA chemisorption: bidentate chemisorption with P-O-P bridge.

since all the experimental evidences, such as P-O-H and P=O disappearance and the presence of aliphatic C-H stretching, are in agreement with this structure. The only difference between the previously proposed structures is the P-O-P bond, that, according with literature data [133], generates a broad band at $540 - 480\ cm^{-1}$ due to its bending, and around $770\ cm^{-1}$ a stretching absorption [133]. Only a very noisy signal is seen in the $540 - 480\ cm^{-1}$ range, while the peaks in the $770\ cm^{-1}$ region are normally assigned to germanium oxides. In the light of these discussion, this structure can not be excluded from DRIFTS data.

The DPP functionalized Ge-H powder DRIFTS spectrum is shown in figure 3.27 in black, with liquid DPP FTIR spectrum (red spectrum) and oxidised germanium powder DRIFTS data (green spectrum) [129]. According to the

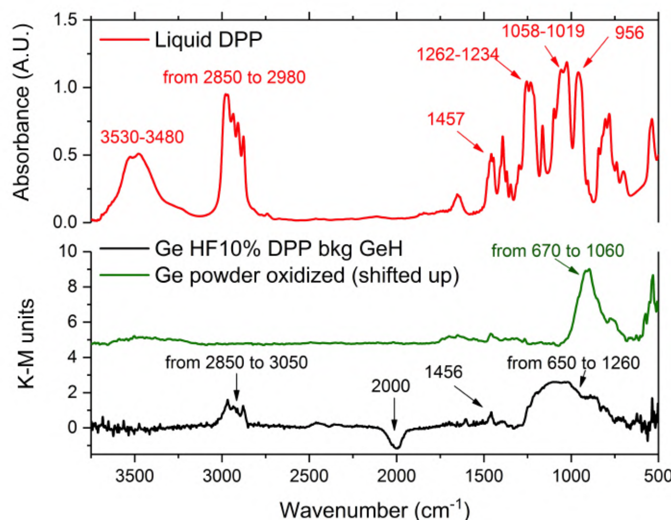

Figure 3.27. In black, DRIFTS data of Ge powder treated with 10% HF and functionalized with DPP precursor; background Ge-H powder. In red, transmittance FTIR spectrum of liquid DPP precursor. In green, Ge oxidised powder, as a comparison spectrum.

work of Daasch and co-workers [134], the most important fingerprints of DPP precursor are: the phosphoryl group that generates an intense peak in the $1260 - 1230$ cm^{-1} region; alkyl phosphate esters that generates the strong absorption in the $1060 - 1020$ cm^{-1} region (P-O ν mode) and the absorption at 960 cm^{-1} (P-O-C deformation) [134, 135]. In the $2900 - 2850$ cm^{-1} region the C-H stretching modes of ethyl and propyl groups are visible, accompanied by the corresponding bending modes in the $1480 - 1440$ cm^{-1} range. All such absorption peaks are clearly present in the DPP transmission reference spectrum (red line).

Furthermore, it is worth to note the presence of the broad -O-H absorption in the $3550 - 3450$ cm^{-1} spectrum region and the sharp peak at around 1650 cm^{-1}, which are a strong indication of the presence of adsorbed water in the liquid precursor. Since this spectrum was acquired by using pure DPP extracted directly from the bottle without any dilution, we suppose that the revealed water comes from the liquid precursor, which is present as a contaminant (DPP precursor $> 97.56\%$ of purity).

The spectrum of the functionalized Ge powder after treatment in hot

DPP/mesitylene solution is reported in the same figure (black line, figure 3.27): the negative absorption near $2000\ cm^{-1}$ indicates the disappearance of Ge-H surface functional groups, which were present in the background spectrum taken as reference (black line, figure 3.4). Other peaks, ascribable to DPP are visible, such as the C-H stretching modes and the corresponding bending ones at $2900 - 2850\ cm^{-1}$ and $1480 - 1440\ cm^{-1}$ regions, respectively. On the contrary, the peak from phosphoryl group ($1260 - 1230\ cm^{-1}$) and the P-O-R stretching and deformation modes ($1060 - 960\ cm^{-1}$) appears to be merged in a broad structured band from $1260\ cm^{-1}$ to $670\ cm^{-1}$. Among the possible reasons of these changes, the most likely seems to be the appearance of IR features ascribable to Ge oxide [80], in particular a broad peak at around $1000 - 670\ cm^{-1}$, which overlaps with the P-O-R peaks. In order to further support this assignment, the spectrum of Ge powder (green line, 3.27) after oxidation by prolonged exposure in ambient air at $50°$C is reported in green: besides the oxide peak centered at $880\ cm^{-1}$ and covering the range $1060 - 670\ cm^{-1}$ in agreement with ref. [80], the presence of traces of Ge-OH is suggested by the low intensity, broad band at around $3400 - 3200\ cm^{-1}$, ascribed to -O-H stretching mode. Therefore, it can be inferred that, during the treatment at about $160°$C, oxidation of Ge surface occurs leading to H-termination disruption.

Nevertheless, Ge surface grafting with either alkyl phosphonate or phosphoryl

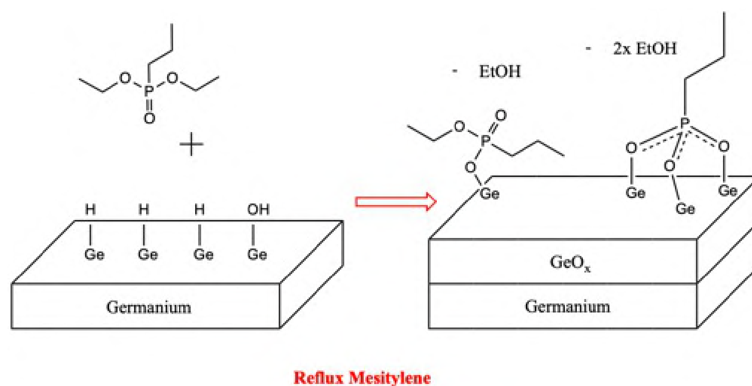

Figure 3.28. DPP chemisorption hypothesis: P-O-R moiety can react with Ge surfaces (Ge-OH group) and form a mono-dentate (shown) or bi-dentate adsorption, or also a P=O moiety can react with Ge surface, as seen with ODPA precursor, generating a possible tri-dentate adsorption (shown). These are all the possible chemisorption products.

groups, whose DRIFTS features are visible after the treatment, took place generating a chemisorbed layer (both chemisorption are shown in figure 3.28), but the evident oxidation of the Ge surface leads to the conclusion that physisorption

cannot be ruled out. The P-O-R and P=O groups can indeed interact through simple H-bonding and/or dipole-dipole interactions with Ge-OH and Ge-O surface moieties.
XPS analyses on samples produced with the standard conditions as for DRIFT samples, still demonstrated that more than 2 ML are deposited. MeOH rinsing experiment (showed in the NRA results paragraph) suggested that the second ML is strongly physisorbed (since it is not removed with MeOH rinsing) while the others are less bound to the substrate, and they can be removed by MeOH rinsing. Therefore the most probable gripping picture is for a chemisorbed of the 1 ML and a physisorption of the others via long-range interactions with polar GeO_x layer. This may also explain the absence of physisorbed layer when dry less oxidising conditions are applied, due to weaker dipole attraction of the second layer with the surface.

In figure 3.29 the ADPP adsorption with Ge powder is studied with DRIFTS and FTIR spectra. The pure ADPP spectra in reported in red, presenting a clear

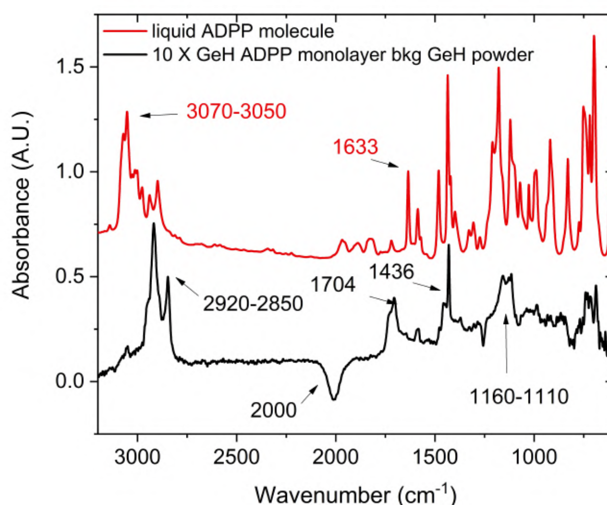

Figure 3.29. In black, DRIFTS data of Ge powder treated with 10% HF and functionalized with ADPP precursor; background Ge-H powder. In red, transmittance FTIR spectrum of liquid ADPP precursor.

signal of different C-H stretching modes related to phenyl groups present on ADPP precursor in the $3070 - 3050\ cm^{-1}$ region, and also the aliphatic C-H near $2900 - 2850\ cm^{-1}$. Also the C-H stretching of allyl group $CH_2 - CH = CH_2$ is present with a peak just above $3000\ cm^{-1}$. This group generates a stretching

of C=C bond at $1633\ cm^{-1}$ and probably also the CH_2- scissoring absorption overlapped with the previous peak [136]. Many absorption features are generated by the phenyl group, such as its out-of-plane C-H ring bending in the $675 - 900\ cm^{-1}$ region, the in-plane C-H ring bending in the $1000 - 1300\ cm^{-1}$ region and the skeletal ring C-C stretching vibration in the $1500 - 1400\ cm^{-1}$ and $1600 - 1585\ cm^{-1}$ regions.

In figure 3.29 the DRIFTS data of ADPP funzionalised Ge powder are also reported, which show a strongly different absorption with respect to ADPP molecule. As can be expected, a negative absorption near $2000\ cm^{-1}$ is present, indicating the disappearance of Ge-H surface functional groups, which were present in the background spectrum taken as reference (black line, figure 3.4). The disappearance of all peaks above $3000\ cm^{-1}$ suggests that the two ADPP phenyl groups are probably lost during functionalization, the C=C bond is not anymore present, but its chain still remains, since the aliphatic C-H in the $2900 - 2850\ cm^{-1}$ are still present. The new peak at $1704\ cm^{-1}$ suggests that the C=C bond are now oxidised in a C=O, since this peak can be related only with stretching modes of this moiety. Another confirmation of the presence of the aliphatic chain is given by the $P - CH_2-$ peak at $1440\ cm^{-1}$ [136]. The $1160 - 1110\ cm^{-1}$ region presents other absorption peaks that are in the P-O-R (that could be P-O-Ge) absorption region, as saw in the previous DRIFTS analyses.

In the light of all these results and XPS analyses, it can be concluded that ADPP chemisorbed with an oxidation process instead of a hydrogermilation reaction, since the C=C bond is probably oxidised to a C=O group: the chemisorption reaction must involves the release of phenyl groups, with a possible creation of P-O-Ge bonds. This is in agreement with XPS binding energy analyses and suggested by DRIFTS analyses, but further experimental evidences ruled out other possible interpretations.

As a matter of fact, in the $675 - 900\ cm^{-1}$ some absorption features that can be ascribed to out-of-plane C-H ring bending are present, but mesitylene solvent (used for the adsorption process) or some residual phenyl group are supposed to be present in a very small amount.

In order to clarify this major molecule changes as a result of the deposition process, further structural analyses will be present in this section, especially for ADPP precursor.

X-Ray Absorption Spectroscopy analysis Some functionalized Ge (001) sample were analysed at the Sirius beamline, SOLEIL synchrotron: the phosphorus K-edge was exploited to collect XAFS phosphorus absorption signal, containing neighbouring atom informations. To perform it, the samples were analysed in a total reflection configuration (Refl-EXAFS), with the X-Ray beam below the critical angle, in order to maximise the surface signal and minimise the bulk Ge fluorescence background. The fluorescence detection mode was used, selecting the P K-alpha signal.
The sample that will be presented here are ODPA and ADPP functionalized Ge samples, with standard and dry deposition comparison for the ADPP precursor case.
In figure 3.30, the normalised absorption spectra for dry processes are shown. In figure 3.31 k-space signals for ODPA (dry) and ADPP (std and dry) samples

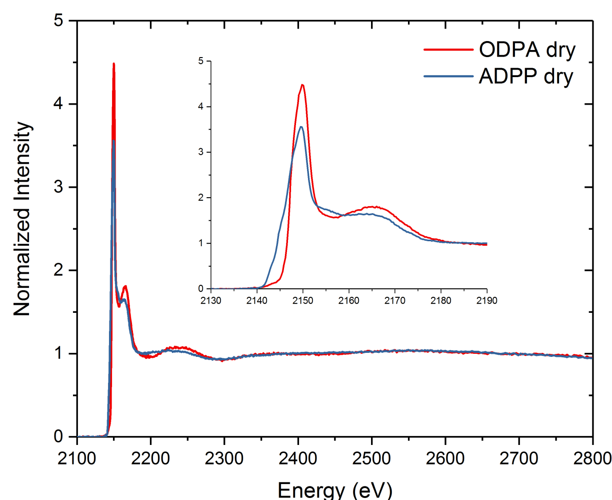

Figure 3.30. Normalised X-Ray absorption spectra of ODPA (red curve) and ADPP (blue curve) functionalized Ge (001) surfaces at phosphorus K-edge. Inset: zoom XANES region.

are shown, with a proper background subtraction. Then, the signals in the k-range from 2.5 Å^{-1} to 11.5 Å^{-1} are filtered with Fast Fourier Transform, in order to obtain the R-space signal. The low-k range is normally excluded because it includes multiple scattering paths not suitable for EXAFS analysis. High-k cut is performed to avoid noisy part of the signal. In figure 3.32, a data comparison in R-space is shown. All the presented data show only one R-space peak, revealing that the collected signal brings information only from first neighbouring atoms.

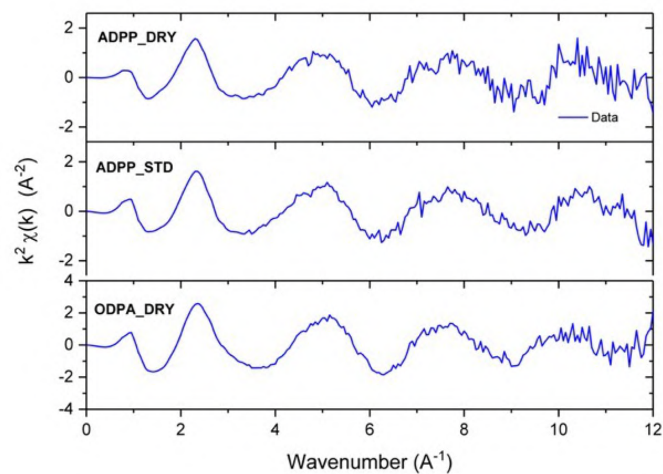

Figure 3.31. Fine structure oscillation function in k-space for ADPP dry, ADPP standard and ODPA dry samples at phosphorus K-edge after a background subtraction.

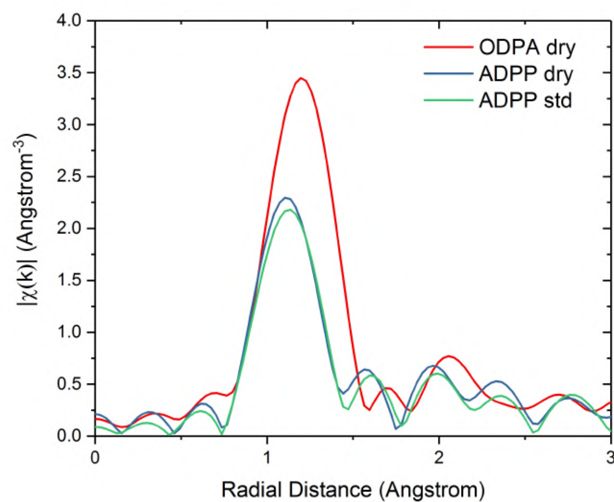

Figure 3.32. Fine structure oscillation function transformed in R-space, obtained by Filter Fourier Transform analysis. ADPP dry, ADPP standard and ODPA dry samples are shown.

This can be probably due to a larger disorder of the structure outside the first shell.
The ODPA dry sample (red curve) presents an intense peak that is at higher R and more intense than ADPP first shell peak. Moreover, it appears that dry and std APDD samples are almost identical, meaning that the nearest neighbours of P are the same for the two processes. It is worth to remember that R coordinate in figure 3.32 is not directly the interatomic distance since it has to be corrected by the phases of the path. Therefore to have reliable data a deeper analyses by simulation and fitting is necessary.
The first step of our analysis is focused on the ODPA dry spectrum. As a starting model of the P atom neighbourhood, we used the experimental X-ray structure of metylphosphonic acid (MPA) molecule, given in reference [137], that is very similar to starting ODPA structure. The P atom forms a double bond with O (1.499 Å), two single bond with O-H (1.544 Å), and a single bond with a C (1.759 Å). FEFF calculation is performed to compute the scattering properties (amplitude and phase) of P-O, P=O and P-C paths. These paths are a satisfactory set of signals that can be optimised by fitting the data via the EXAFS formula.
In principle, the 3 kind of paths should have 3 free parameters each (N, R and DW), plus the common parameter E_0, that adjusts the edge energy position, thus yielding 10 free parameters (plus the S_0^2 factor that will be discussed later). This would bring for sure to an over-parameterised fitting. As a first simplification, we decided to fix Debye Waller factors for this analysis: the Debye Waller factors were estimated with the *Einstein-correlated model* [116]. This model considers a pair of absorber and back-scatterer atoms as an independent oscillator with a frequency ω_E. Dalba and co-workers [116] (and others paper, for example ref. [138]) demonstrate that there is a satisfactory agreement between Einstein frequencies and vibrational symmetrical stretching frequency, concluding that the mean-square relative displacement is dominated by optical stretching models. The vibrational frequency can be considered as a measure of the effective bond-stretching strength constant. For this reason, the Debye Waller factors were estimated by evaluating the P=O and P-O- stretching modes and calculating the DW factors by the Einstein-correlated model. Looking at the IR spectrum shown before for ODPA adsorption, the vibration at $1050\ cm^{-1}$ was ascribed to P-O group, also according with literature data, while a larger peak in the same region was also detected for DPP (very wide due to the overlap of other peaks) and ADPP $1160 - 1100\ cm^{-1}$. Using these values, a range between $1.5 - 1.35\ 10^{-3}$ Å^2 values of DW factors was estimated for P-O- bonds in our case. It is also possible to derive

the value for a pure P=O bond, since its stretching frequency was measured for ODPA precursor: the $1225\ cm^{-1}$ peak was assigned to this vibrational mode, accordingly to literature data. This value would return a DW factor of $1.29\ 10^{-3}$ Å^2 according to this model. In the light of these discussion, a mean value of $1.4\ 10^{-3}$ Å^2 was assumed for P-O scattering path in this EXAFS analysis. The DW factors were likewise estimated also for the P-C bond, and $2.8\ 10^{-3}$ Å^2 value has been obtained.
After this first simplification, 7 free parameters in principle remains for data analysis. We decided to start with simple fits introducing the different paths when needed.
In figure 3.33, a ODPA fitting with a single scattering P-O path is shown, using as free fitting parameter dE_0 (the correction to the K-edge energy position), dR (correction to path length, and so to the bond distance), N (the multiplicity of the path). These parameters were then referred to different paths by adding a proper subscript. The R-space windows are chosen to include all possible contributions from the first shell, starting from the minimum possible R distance (0,86 Å) according to the previous background subtraction.
The fitting results are shown in the first raw of table 3.3. The number of degener-

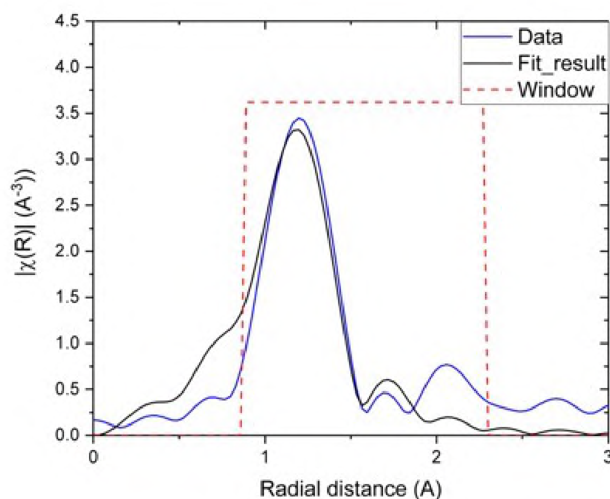

Figure 3.33. ODPA dry sample data in R-space (blue line) fitted with a P-O path with a free degeneracy and distance parameters.

acy of the path N is compatible with the ODPA structure that has 3 oxygen atoms in its surrounding. The P-O distance is in good agreement with the single P-O

N_{P-O}	$error$	N_{P-C}	$N_{P=O}$	R_{P-O}	$error$	χ^2
				Å	Å	
2.7	0.3	0 (fix)	0 (fix)	1.55	0.02	43.2
2.9	0.3	1 (fix)	0 (fix)	1.56	0.02	47.9
2.6	0.3	1 (fix)	1 (fix)	1.51	0.02	65.2

Table 3.3. EXAFS fitting results for ODPA dry sample. N_{P-O} is the multiplicity of P-O path, N_{P-C} is the P-C path multiplicity, $N_{P=O}$ is the P=O path multiplicity, R_{P-O} is the P-O path length and χ^2 is referred to the fitting.

bond of MPA model, within a few hundredth of angstrom.
Two points remain: are we sensitive to an eventual P=O bond ? and to the P-C bond?

Since DRIFTS data revealed that a carbon chain is still present during the molecule deposition on Ge powder, the fitting procedure was implemented with a P-C path, with an initial bond guess equal to 1.759 Å[137]. To avoid increasing the fitting degree of freedom, and since the P-C bond length should not be affected by chemisorption, this path was fixed to a degeneracy 1, and also the P-C distance was fixed to the initial guess. The fitting results are shown in table 3.3, second line. The χ^2 value should be comparable with the previous one, since the number of free fitting parameters was the same than the previous fitting model. The addition of a P-C path did not influence the fitting results so much, and the χ^2 is indeed comparable with the previous one.
As shown in figure 3.34, the carbon and the oxygen contributions were summed not in phase, and so also with this different model, the data were fitted with a resulting χ^2 value comparable with the previous one. If the P-C path degeneracy is fixed to higher value than 1, the χ^2 value is increased significantly.
It is worth to note that these fitting models do not presuppose the presence of P=O bond, that presents a bond length equal to 1.4993 Å[137]. Indeed, an eventual P=O path does not improve the fitting result, suggesting that the P=O is not present after the chemisorption on Ge (001) surface, as it is clearly shown in table 3.3, third line.

This EXAFS analysis on ODPA dry sample proposes a tri-dentate interpretation of data, since the three first neighbouring oxygens are placed at the same distance, within the experimental error.
But, is this the only possible interpretation of these data?
As suggested in the DRIFTS data analysis, also a different structure is in theory compatible with experimental data, as a consequence of the chemisorption

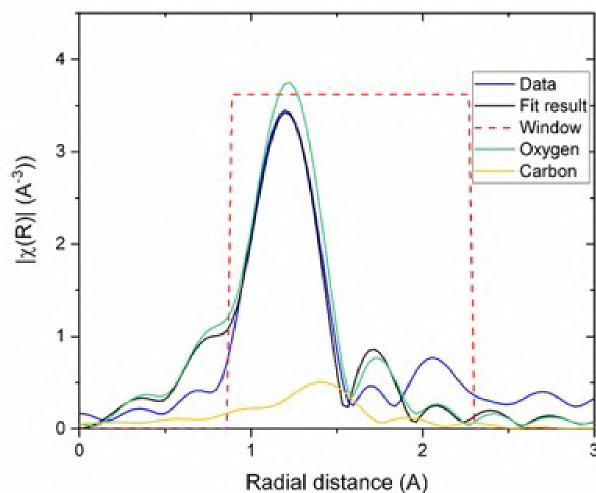

Figure 3.34. ODPA dry sample data in R-space (blue line) fitted with a P-O path and 1 fixed P-C path. The reported values are the square modulus of the signals: the green curves represent the square modulus of the oxygen path contribution, the yellow curve the carbon one and the black curve is the square modulus of their sum.

process. This structure, shown in figure 3.26, presents a P-O-P bridge in between different ODPA molecules, thus generating a bi-dentate ODPA chemisorbed layer with a P-O-P cross link. But how long is this bond? Is it compatible with EXAFS data or we can exclude this possibility?

Several P-(O-P) bond distances can be found in literature, as a typical bond present in different structures, such as P_4O_6 (a molecule formed only by P-O-P bond), P_2O_5 (or its dimer P_4O_{10} that alternates P=O and P-O-P bond). For P_2O_5 Cruickshank work [139] demonstrated by crystallographic measurements that this bond is 1.56 (± 0.015) Ålong, and for the P_4O_{10} structure the bond length was varying between 1.58 and 1.60 Å, depending on which P-(O-P) bond was taken into account [140]. Similar value was reported also by Mowrey and co workers [141], while for the P III molecule P_4O_6 (its monomer was P_2O_3) 1.64 Åwas reported. Beagley and co-workes [142] made a systematic study on P_4O_n oxides and reports different value on P-(O-P) bond length: they report 1.638 Åfor the P-(O-P) length for P_4O_6, referred to $P_{III} - OP_{III}$ bond, while for $P_{III} - OP_V$ is 1.66 Åand for $P_V - O$ bridge is 1.59 Å.

In the light of all these works, it is clear that the P-O-P bond length can significantly vary, mainly depending on P oxidation number and in general on molecular structures. Moreover, it is quite difficult to separate different EXAFS

bond distance contribution from the same scatterer atom, in the same shell, as in our case for oxygen. This means that EXAFS data suggest that the three oxygens are placed at the same distance, as shown in table 3.3, but it can not be totally excluded that a P-O-P bond is present. Also Kuper and co-workers were not able to separate the different contributions analysing similar bond (P=O and P-O 1.44 and 1.59 Å), although working with bulk material [143].

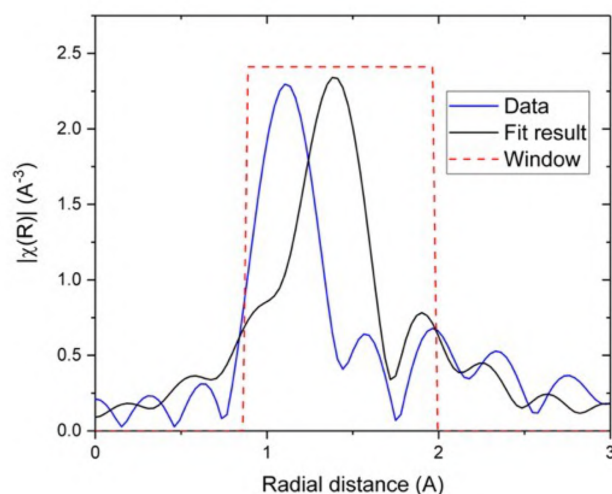

Figure 3.35. ADPP dry sample data in R-space (blue line) fitted with a P-C path with a degeneracy fixed to 3 and an input distance equal to 1.759 Å.

The first data analysis on ADPP molecule is shown in figure 3.35, in which the ADPP dry sample signal was simulated with a P-C path, imposing a degeneracy equal to 3 and using a distance equal to 1.759 Å, as suggested by literature data [137]. This should be the situation if ADPP molecule has maintained its (3x) C neighbours after absorption. It is clear that P-C single scattering signal generates a completely different R signal compared to the experimental one: this fact is in accordance with previous data, underlining that major structural changes occur during the adsorption process.

As a consequence, the ADPP functionalized Ge (001) samples were analysed, starting with an input model similar to the ODPA one: a P-O path with a 1.5443 Åinitial long bond distance was used as an initial guess distance for the FEFF path simulation. In figure 3.36 an ADPP fitting with a single scattering P-O path is shown, using as free fitting parameter dE_0 (the correction to the K-edge energy

N_{P-O}	$error$	N_{P-C}	R_{P-O}	$error$	χ^2
			Å	Å	
2.2	0.4	0 (fix)	1.50	0.02	70.4
2.3	0.3	1 (fix)	1.50	0.02	60.1
2.4	0.6	2 (fix)	1.48	0.03	138.9

Table 3.4. EXAFS fitting results for ADPP dry sample. N_{P-O} is the multiplicity of P-O path, N_{P-C} is the P-C path multiplicity, R_{P-O} is the P-O path length and χ^2 is referred to the fitting.

position), dR (correction to path length), N (the multiplicity of the path). As ex-

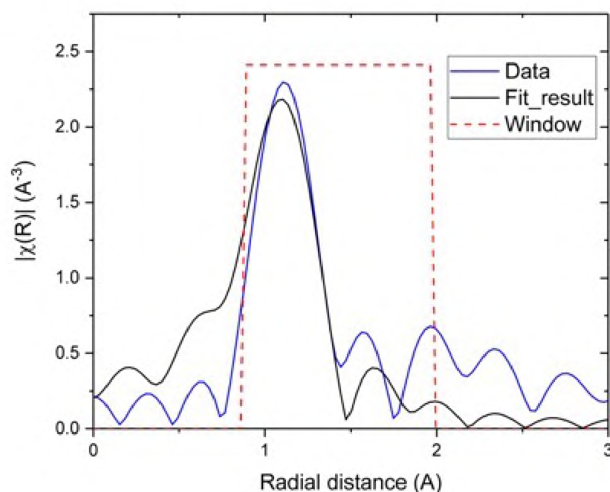

Figure 3.36. ADPP dry sample data in R-space (blue line) fitted with a P-O path. The reported values are the square modulus of the signals.

pected by the ADPP-ODPA R-space comparison, the R peak for ADPP molecule can be bitted by a P-O single scattering path, giving a lower number of first neighbouring oxygen atoms. As reported in table 3.4 first line, the fitted multiplicity is equal to 2.2, while the bond distance is equal to 1.50 Å.

Also in this case, the data were also fitted in the light of DRIFTS experimental results, that suggest the presence of a carbon atom in the first shell. The results of these fittings are reported in the second line of table 3.4, fixing the presence of 1 C atom at 1.759 Å. The fitting result (shown in figure 3.37) has a lower χ^2 with respect to the previous.

The values obtained by this fitting must be discussed, since the P-O length proposed by this model is 1.50 Å, with two oxygen atoms. In the light of what

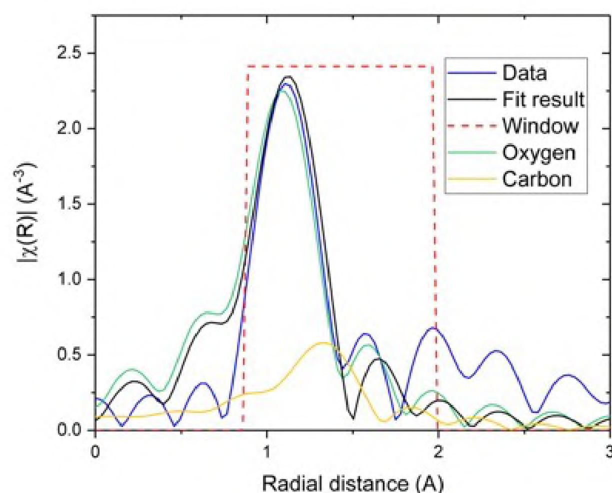

Figure 3.37. ADPP dry sample data in R-space (blue line) fitted with a P-O path and a fixed P-C path. The reported values are the square modulus of the signals.

was previously reported in this discussion, this value is similar to a double bond length (1.49 Å) and by looking at the degeneration number of this path, this molecule should have two oxygens double bonded with one phosphorus atom. This result is quite anomalous, since no molecule in literature presents a phosphorus linked to two double bonds [144, 145] and so this hypothesis must be discarded. Moreover, if a P=O bond is present on our system, why does no P=O signal is found in DRIFTS data?

In figure 3.38 two different reaction products are proposed, as a consequence of all experimental evidences. The proposed molecules present a XPS-compatible P binding energy with oxidation state equal to I, no phenyl group and a oxidised vinyl group as suggested by DRIFTS data, and two oxygens and a carbon atom as first neighbours. The two suggested chemisorption products differ in the two oxygen bonds: in the first case, a P=O bond is present and the molecule is adsorbed with a mono-dentate P-O-Ge bond, while in the second case the molecule is bi-dentate to Ge surface, with a delocalised electron in the P-O-Ge bonds. The first chemisorption product does not perfectly agree with DRIFTS data, since no P=O bond stretching has been detected, even if a different chemisorption between Ge powder and Ge(001) should be in principle possible.

Nevertheless, the second proposal should be the preferred one, since no P=O bonds is present and thanks to the delocalisation of one electron, the two bonds

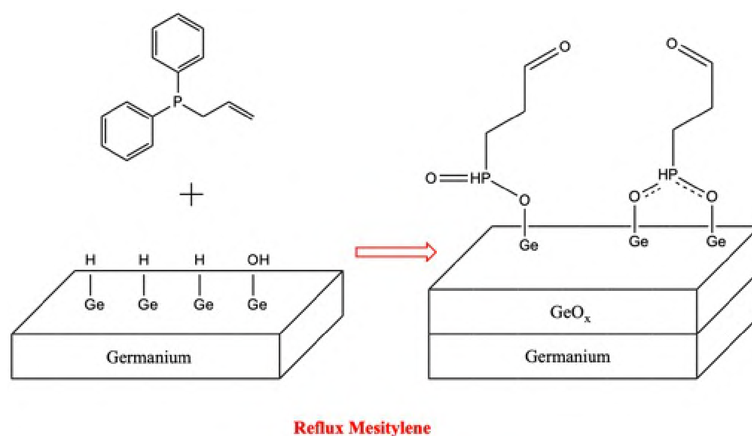

Figure 3.38. Chemisorption proposal for ADPP precursor. As discussed in the text, the right one proposal must be preferred.

N_{P-O}	$error$	N_{P-C}	R_{P-O}	$error$	χ^2
			Å	Å	
2.1	0.3	0 (fix)	1.50	0.02	20.5
2.1	0.3	1 (fix)	1.52	0.02	21.6

Table 3.5. EXAFS fitting results for ADPP stdandard sample. N_{P-O} is the multiplicity of P-O path, N_{P-C} is the P-C path multiplicity, R_{P-O} is the P-O path length and χ^2 is referred to the fitting.

are shorter than a P-O-Ge bond and the P oxidation state is compatible with XPS result. Unfortunately, we have no certain information on this bond length, but if we compare this with the ODPA bond lengths, we correctly expect shorter bond distances, as it is clearly shown by data. Indeed, a delocalisation of an electron on three different bonds is expected to generate a weaker and longer bond distance with respect to the the case with a delocalisation in two bonds.

In table 3.5, a fit result of an analogous analysis conducted on ADPP standard deposition sample is shown. As expected from R-space data comparison previously shown (figure 3.32), no significant difference from ADPP dry sample is revealed, confirming that the two samples are equal, within experimental errors. Therefore, similar considerations can be inferred for this sample, as the previously presented ones for ADPP dry sample.

Considering that, for ADPP and ODPA molecules a similar chemisorption has been evaluated, the use of $1.4\,10^{-3}$ value for the Debye - Waller factor is justified in the aftermath. Moreover, different DW factor values have been tested ($\pm\,1\,10^{-3}$), and only minor variations on the fitted degeneracy of P-O path have been noticed

(0.15 as maximum degeneracy variation), thus not strongly supporting on the chemisorption hypothesis.

Another parameter that should be considered in our analyses is S_0^2. Usually this parameter is in between 0.7 and 1. The reported fit results in this work have been calculated imposing $S_0^2 = 1$. The EXAFS analyses results are satisfactory if cross checked with the other techniques used in this work. If the opposite limit case is used, about $N_{P-O} = 4$ would result for ODPA adsorption. This should be completely rejected by considering the XPS oxidation state and more in general the phosphorus chemistry. Therefore, a S_0^2 value close to 1 is expected.

3.3 Phosphorus Diffusion Tests

The three different phosphorus precursors are tested with different thermal diffusion processes. Thanks to these processes, are thermally degraded, with consequent release of atomic P, and its diffusion into mono-crystalline Ge: indeed, only atomic P can be an electrically active donor for Ge. If a bigger fragment diffuses inside Ge, no effective electrical activation and lower diffusivities are expected . The thermal diffusion will be promoted in this section by means of standard furnace annealing, a Rapid Thermal Processing (called also Rapid Thermal Annealing) and Pulsed Laser Melting technique.

3.3.1 Thermal Diffusion

The functionalized Ge samples were tested for thermal diffusion by the use of a standard tubular furnace and a Rapid Thermal Processing machine. Before the diffusion test is conducted, the monolayer doping technique involves also a capping deposition step [75, 146]. This step is normally used in literature, since the P atomic release on surface could be not only promoting a P in-diffusion in Ge, but without a proper diffusion barrier, the dopant could be eject in the atmosphere. For instance, this phenomenon is the bases of monolayer remote doping [147]. A capping layer deposition normally prevents this, and the released dopant can diffuse inside Ge as the material with higher diffusivity coefficient, since the capping layer normally is a SiO_2 layer, presenting high diffusion coefficient for P [60]. Its deposition is made by RF sputtering technique, starting from a SiO_2 source and by fluxing a O_2 gas on chamber during the deposition, in order to obtain a stoichiometric SiO_2 layer [129, 148, 149]. The thermally processed samples are subsequently etched to remove the SiO_2 capping layer, as in the previous

Table 3.6. Tubular furnace treatments for DPP and ODPA sample.

Sample FUR num.	Max temperature	Duration	Rinsing	Molecule
–	$[^{o}C]$	$[min]$	–	–
1	664	10	Mesit. + MeOH	DPP
2	648	30	Mesit. + MeOH	DPP
3	573	30	Mesit. + MeOH	DPP
4	606	30	Mesit. + MeOH	DPP
5	680	30	Mesit.	ODPA
6	606	30	Mesit.	DPP
7	606	30	Mesit.	ODPA
8	535	30	Mesit.	ODPA

case. Finally, samples are analysed with SIMS spectrometer.

The DPP and ODPA samples are the first tested molecules, and a processing data grid for tubular furnaces is reported in table 3.6. The samples are treated inside the tubular furnace after five N_2 - vacuum cycles, that ensures an inert atmosphere inside the chamber. The thermal process is monitored by a thermocouple placed next to the sample during the annealing, as shown in figure 3.39.

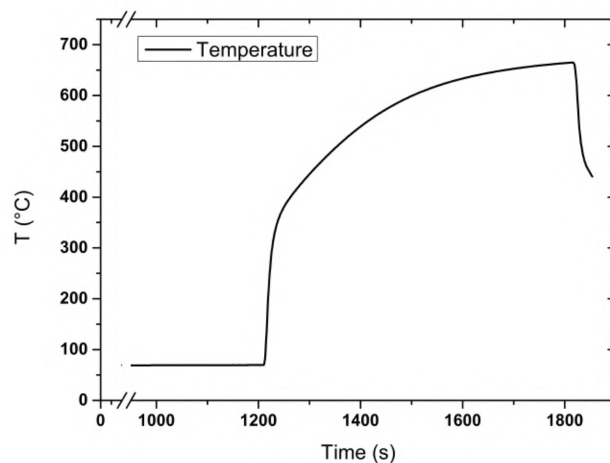

Figure 3.39. Tubular furnace thermal ramp measured by a thermocouple placed next to the sample during the annealing.

The processed samples are extracted from the furnace and the capping layer is removed from the surface by a standard chemical etching (HF 5% for 1 minute). After this step, the samples are analysed by Secondary Ion Mass Spectrometry

machine, in order to detect an eventual diffusion of P in Ge. The first results are reported in figure 3.40.

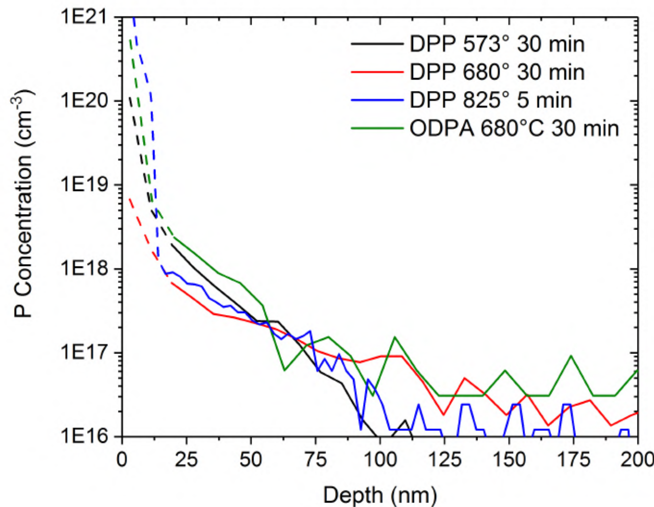

Figure 3.40. SIMS analysis after furnace processing. Phosphorus chemical profile is reported as a function of depth. Dashes lines are referred to SIMS surface peak.

As can be seen, figure 3.40 presents some different chemical profiles that clearly indicates that no diffusion occurs during this treatment. As a matter of fact, these profiles do not present a diffusion shape, but instead they are a surface morphology-induced SIMS signals.
To increase the thermal budget, the samples are treated with a Rapid Thermal Processing machine, as described in the Methods chapter. In table 3.7 the process parameters grid is shown for all the precursor.

Unfortunately, also in this case no diffusion profile is detected for all precursors. In figure 3.41, a SIMS analysis on Ge ADPP annealed at $825°$C for 5 minutes is shown as an example.

As can be clearly seen, no significant P diffusion in Ge is detected also for higher thermal budget treated sample. If a diffusion occurs, less than $1\ 10^{19}\ cm^{-3}$ P at the surface enter inside Ge, being a very low concentration for phosphorus Ge doping.

Why does no phosphorus diffusion is detected in these samples?
The process parameters summarised in table 3.7 have been chosen in order to ensure that phosphorus released from the monolayer source can diffuse in germanium, by using a well assessed P diffusion model in Ge by Bracht, Brotzmann

Table 3.7. Rapid thermal processing samples applied to DPP, ODPA and ADPP functionalized Ge samples.

Sample RTA num.	Temperature [°C]	Duration [min]
1	650	1
2	650	5
3	650	30
4	730	1
5	730	5
6	730	30
7	825	1
8	825	5
9	825	30

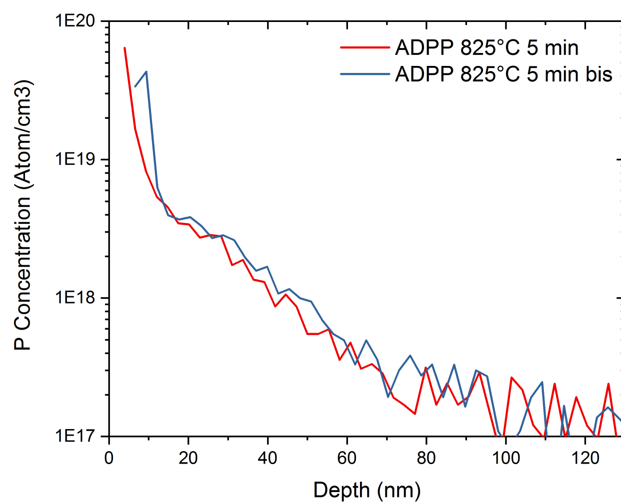

Figure 3.41. SIMS analysis after RTP annealing. Phosphorus chemical profile for ADPP precursor is reported as a function of depth.

and co-workers [50, 51]. There are two hypotheses that can explain these phenomena: the molecule does not release P atoms or the molecule releases it, but it out-diffuse. To verify which hypothesis is true, NRA was conducted on thermally treated sample, with the capping layer still on top. In figure 3.42 a NRA in depth analysis is shown.

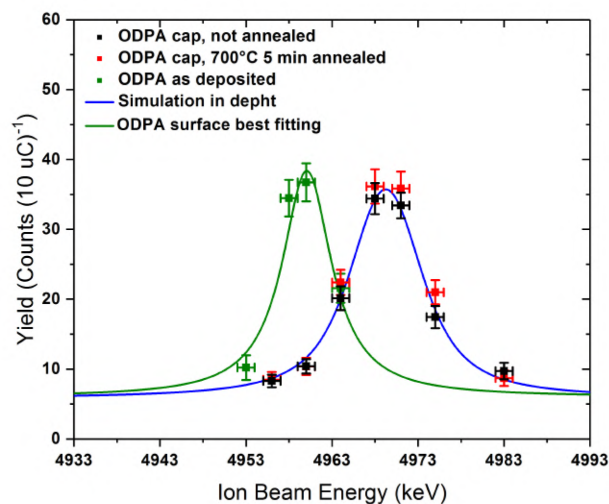

Figure 3.42. NRA in depth analysis. In this figure, experimental NRA resonance data are reported as points: green points are referred to a sample presenting a monolayer on the surface, black points are referred to a sample with a SiO_2 capping layer, and red points are NRA coming from a capped ODPA samples annealed via RTP at 700°C for 5 minutes. The green curve is a surface fitting of NRA signal coming from uncovered surface monolayer, as previously shown. Blue curve is a simulation of NRA resonance, taking into account also the energy loss phenomena and straggling phenomena due to the capping layer presence on top of phosphorus atoms.

Reaction yields are plotted against the beam energy. The green data are relative to a Ge-H ODPA treated sample without capping reported as a reference and the maximum yield occurs at resonance energy of 4.96 MeV. The black and red points are relative to the capped sample before and after annealing respectively: as can be seen, the maximum yield shifts at higher energy due to the energy loss into the cap. Continuous lines represent the optimal simulation curves for the collected data obtained by fitting the phosphorus amount at the interface. In particular, the blue curve represents the best fitting of black data: it is clearly evident that the data for the annealed sample (red points) and the data for the non-annealed sample (black points) are well fitted with the same simulation curve, confirming that the phosphorus diffused neither inside germanium nor through the SiO_2 capping. It follows that the amount of phosphorus at the cap-

ping layer/Ge interface, before and after the annealing treatment, is the same and that it did not diffuse inside the sputtered SiO_2 layer. Similar results are obtained for DPP treatment and also for treatments at much higher temperature ($825°$C, 5 min).
ADPP data is reported in figure 3.43, and similar results are obtained. All these

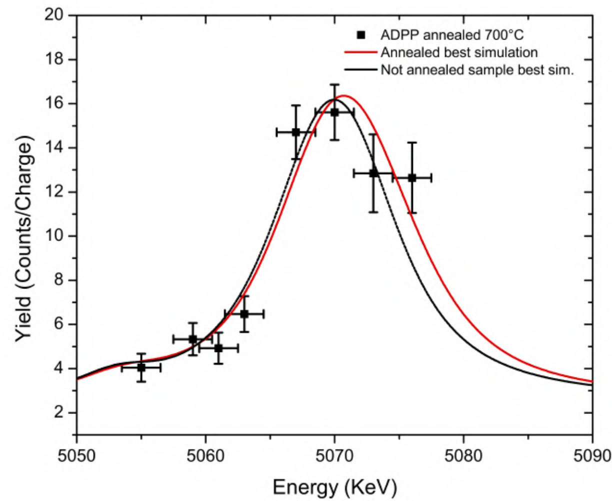

Figure 3.43. NRA analysis in depth for ADPP functionalized sample at $700°$C, using a double resonance simulations. Annealed and not annealed simulations are compared: only annealed data are reported for clarity. Energy axis not calibrated.

data confirm that phosphorus precursors do not release phosphorus able to diffuse, but the entire amount of P remains at the silicon dioxide - Ge interface.
Some hypotheses that explain this phenomenon are proposed in Sgarbossa and co-workers paper [129], and in the conclusion section of this chapter they will be resumed and updated, in the light of all experimental evidences shown in this work.
The basic fact that emerges from these results, is that the highest temperature reached in this work, $825°$C, is not sufficient to release atomic P from all three molecules, neither for 30 minutes long treatment. Moreover, it is not possible to reach higher process temperatures since the Ge material starts to degrade. On the contrary, DPP and ODPA precursors work admirably on Si substrate [56, 57, 63] since the diffusion process for Si are normally performed at higher temperature, so the thermal budget is sufficient to degrade these molecules, and without damaging the bulk material.

3.3.2 Pulsed Laser Melting

The Pulsed Laser Melting technique is used in this work as a different degradation and diffusion route for phosphorus monolayer doping. The samples are subjected to UV laser pulses that are absorbed by germanium, causing a heating, as explained in the Methods chapter. The functionalized germanium surfaces were melted by the irradiation with a Nd:YAG laser with a (single or multi-) pulse of 7 ns and a threefold frequency (wavelength equal to 355 nm) with an energy density around $400\ mJ\ cm^{-2}$.

The DPP and ODPA molecules are treated with 1 pulse at around $400\ mJ\ cm^{-2}$, generating a diffusion profile shown in figure 3.44 and 3.45. These figures demonstrate for the first time that a phosphorus molecular monolayer acts as a source of dopant for PLM technique, with a surface concentration estimated between $1-8\ 10^{19}\ cm^{-3}$ [129] . A variable P dose up to $9\ 10^{13}\ cm^{-2}$ is injected into Ge, which is a significant fraction of the deposited dose. Very interestingly, NRA analysis performed on PLM treated samples demonstrates that most of the P remains at the Ge surface after the treatment. This residual P is in principle still available to increase the injected P amount by means of further laser pulses.

As reported in figure 3.44, a comparison of different SIMS profile performed on

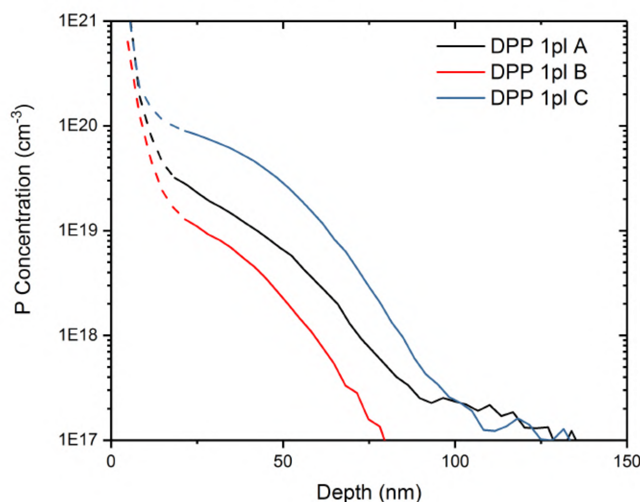

Figure 3.44. Comparison of different SIMS profile performed on the same DPP std functionalized Ge sample diffused by PLM technique (as reported in the previous image).

the same sample but in different position, highlights the inhomogeneity of the diffused chemical profile. In particular, it is possible to note that the surface con-

centration can vary of one order of magnitude. This result is revealed not only for DPP std processed sample, but also with ODPA std ML source, as reported in figure 3.45.

These variation can be related in principle to two different facts: the lateral in-

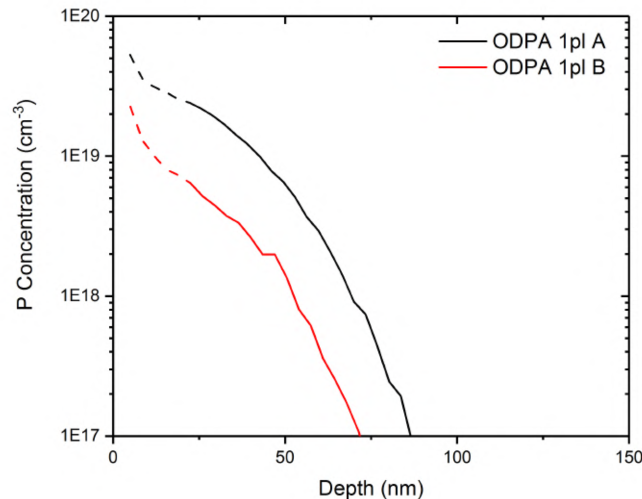

Figure 3.45. Comparison of different SIMS profile performed on the same ODPA std functionalized Ge sample diffused by PLM technique.

homogeneity of the process and of the dopant source. The former is related to a not uniform energy density among the laser pulse, that causes a melt depth variation and so a chemical profile variation. The latter directly involves the surface P amount availability, that turn into a lateral variation of concentration. This second fact is the major responsible for the shown experimental result since the collected secondary ion image during the SIMS experiment shows localised ions signal, instead of a uniform areal distribution.

By looking at figures 3.44 and 3.45, it is clear that the inhomogeneity of the laser energy density is present, but it is not affecting the concentration, since the dose of different SIMS profiles is different and the maximum melt depth is never reached by the diffusion tails (estimated to be in between 150-180 nm).

These two samples were analysed with Van der Pauw - Hall electrical measurement system, as described in the Methods chapter. Unfortunately these measures do not allow to have a precise percent of electrically active phosphorus atoms, due to the lateral doping inhomogeneities. The junction is not laterally uniform and, thanks also to the fact that the depth profile is not box-like (as can be

clearly seen by SIMS profile), both these factors contribute to obtain a completely altered electrical measurement, that is normally performed in homogeneously doped profiles (laterally and in depth). Sheet resistance measures indicate that the processed layers have some electrically active carrier, as opposed to the non processed bulk samples, both for DPP and ODPA std cases.
The PLM on ADPP precursor is shown in figure 3.46, in which the process was repeated several times, by shooting not only 1 pulse, but a sequence.

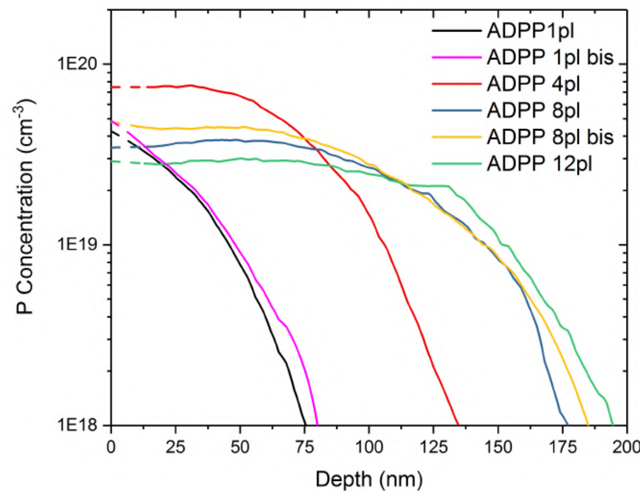

Figure 3.46. ADPP functionalized Ge samples diffused by PLM technique with 1, 4, 8 and 12 pulses (repetition rate 1 Hz) of Nd:YAG laser at 355 nm for 7 ns, with an energy density around $400\ mJ\ cm^{-2}$*. Dashes lines are mathematical extrapolation to surface. The bis spectra are SIMS profiles performed on the same sample, but in a different place, in order to test the reproducibility.*

Each pulse is uncorrelated with the previous one since the repetition rate, thus the interval between pulses, is very long compared with the whole melting-diffusion-crystal regrow process. For this reason, the n-pulse treatment can be considered equivalent to n different 1 pulse PLM treatments.
As can be seen in figure 3.46, also ADPP molecular deposition diffuses in Ge with PLM technique, presenting a 1 pulse surface concentration near $4\ 10^{19}\ cm^{-3}$. Also the diffusivity is comparable with the previous treatment, with a small difference which can be attributed to a slights energy density difference between the two different treatments. The SIMS profile are reproducible, indicating that the ADPP std process does not present the same problem showed before for DPP and ODPA std samples. The not perfect reproducibility of laser energy density is still affecting the diffusivity, but minor effect are detected as expected. As an example, it is

possible to see that the bis profiles differ from the others with a diffusion length variation in the order of 5-10 nm (max).
The phosphorus incorporated dose, calculated as the integral of the SIMS profile, increases with the number of pulses: the 1 pulse value is $1.5\ 10^{14}\ cm^{-2}$, while $5.8\ 10^{14}\ cm^{-2}$ is the 4 pulses value, 8 pulses sample shows a dose equal to $4.5\ 10^{14}\ cm^{-2}$ and 12 pulses equal to $4.0\ 10^{14}\ cm^{-2}$. This behaviour is very interesting, since with a 4-pulse treatment, all the deposited phosphorus diffuses inside Ge. At 8 pulses, the dose is decreasing, showing a lower P amount, and the same behaviour is present also with 12 pulses. These doses values have a 10-15% error attributed to SIMS areal dose calibration. A comparison of P doses must take into account also the reproducibility of deposited dose between different samples (i.e. different processes): in the light of these considerations, it must be concluded that there is no significant difference between samples with 8 and 12 pulses and the lower amount between 4, 8, 12 pulses should be related to a small variability of the deposited dose.
The ADPP sample with 12 pulses was measured with VdP apparatus: the measured sheet resistance was $52\ \Omega/sq$, with a measure error assumed to be in between 10 and 15 %. This value can be compared with an estimation that can be calculated by the chemical profile and literature data [150]. By assuming the SIMS chemical profile, a total activation of dopant and literature mobility, the expected sheet resistance should be in the order of $50\ \Omega/sq$. This result confirms the electrical activation of phosphorus.
The Ge epitaxial regrow after PLM treatment was evaluated also by HRXRD (High Resolution XRD): in the next chapter 3, a similar analysis is described for the Sb ML case after PLM.

The differences revealed by SIMS diffusion analyses can be explained and correlated with the deposition processes discussed in previous paragraph. The main difference between DPP-ODPA and ADPP standard processes are the amount of physisorbed fraction present on Ge surface. DPP and ODPA precursors form more than a single monolayer, instead of ADPP that forms a single ML, without any residual physisorbed fraction after the mesitylene rinsing procedure, normally performed in all samples. This fact suggest that the physisorbed fraction is not perfectly uniform on Ge surface, affecting the P surface amount locally present for the diffusion. On the contrary, the ADPP chemisorption seems to form a uniform layer, that clearly has repercussions on the final diffused samples.
The dimension of these phosphorus accumulation can be estimated by the SIMS

secondary ion image, by considering that the SIMS crater has a dimension 250x250 μm^2 and the ions are collected form a 100x100 μm^2 area. An eventual phosphorus accumulation should have a dimension lower than 100x100 μm^2, presumably in the range of 10x10 - 50x50 μm^2.
An AFM study has been previously presented on this chapter, in the phosphorus precursor adsorption section. The reported images has a 100 x 100 μm^2, that is in principle suitable for the detection of these physisorbed structures. Unfortunately, no evidence of these features has been revealed by these measure basically due to the fact that the used instrument and the large scale used do not permit to be sensitive to ML step, or also to some ML steps. The resolution can be improved by reducing the AFM image size, but as a consequence the investigated area becomes too small with respect to the dimension of the features that we want to investigate.
In the light of all, the most probable scenario is a physisorption variation in a tents μm^2 scale, that generates a variation of phosphorus availability: the AFM image only excludes the presence of a surface phosphorus cluster or aggregation.

Considerations on P release and diffusion In this section, the release probability of phosphorus from molecular precursors is analysed, starting from the shown experimental results and literature data, using a simple release model. The release probability will be described for thermal processes, comparing the thermal diffusion with the PLM technique.
The release probability should follow a thermally activated Arrhenius trend and the release probability (PR) is obtained multiplying the release frequency by the annealing time t, accordly to the following relationship:

$$P_r = t\, \nu_0\, exp\left(-\frac{E}{kT} \right) \tag{3.1}$$

where E is the activation energy for P release from the source, ν_0 is the release attempt frequency of the order of the typical bond oscillations ($10^{-13} s^{-1}$).

In the case of the data presented by Shimizu et al [151] on MLD on Si substrate, the release probability PR has been evaluated to be about 0.1 after a thermal treatment at $950°$C for 5 s, from the ratio between the total P amount measured in the Si bulk and the P amount in a monolayer (DPP precursor). Hence, by inverting equation 3.1, an activation energy of about 3.6 eV is obtained. This datum explains the absence of doping found after the annealing at the lower temperature

(875°C for 5 s), since it leads to an estimated value of PR of less than 0.01, thus reasonably below the lower detection limit of SIMS technique.
Supposing that DPP has the same release energy toward Ge bulk as toward the Si one, our maximum thermal budget at 825°C for 5 min would lead to PR = 0.1 and the P diffusion should be revealed by the present experiment. In other words, the low temperature of our experiment does not explain the lack of doping since it should be compensated by the long annealing time (5 min instead of 5 s). By applying equation 3.1 to derive the activation energy that accounts for less than 1% injection, as shown by the herein presented data (figures 3.41 3.40, as examples), a value higher than 3.9 eV has been calculated. Therefore, this analysis suggests that the nature of the interface influences the stability of the MLD source. In general, the activation energy for the release from ML source will be affected by two main factors: the stability of the molecule bonds and the stability of the released P species into the receiving matrix.
As a result of previous structural analyses, all the chemisorbed molecules presents a P-O-Ge bond, with electron delocalised on P-O bonds. In order to evaluate bond energy value, and so the stability of the molecule, some consideration are presented below. The dissociation of P-O delocalised bonds should involve a chain of reactions, including breaking all the phosphorus bonds with other atoms. This process requires at least an activation energy that is equal to the highest energetically bond breaking process.
Longo and co-workers estimate a degradation temperature for P-C bond near 500°C [69], estimating this temperature using a ODPA molecules as example. This value reveals that this bond breaking process should occur also in our case (normally we used higher temperatures in annealing processes), and so we can consider that the P-C break is not the most highest energetically dissociation step. A single P-O bond break, involving a delocalised electron, should have a bond breaking energy in between the P-O and P=O. After a dissociation of P-O delocalised bond, the molecular structure must reorganise, and it is extremely probable that during the dissociation chain, the P=O structure appears as an intermediate bond: in this case, the most energetically demanding step would be the P=O bond dissociation, and so its value should be used to estimate the energy barrier for the release of atomic phosphorus by molecules. The P=O bond has a bond energy of ca. 5.6 eV [152] and the dissociation of PO molecule present a dissociation energy equal to 6.0 eV [153].
These values are reduced indeed by the fact that the released P is then dissolved into the crystal lattice and not in atomic form. In particular, the energy reduction

will be higher for Si matrix than for Ge as indicated by the higher solubility of P in Si [154] with respect to Ge [155], (about tenfold in the considered temperature range). Therefore, also this fact contributes to the difference between Si and Ge MLD technique.
An eventual role of second nearest atoms in the dissociation chain process should involve the (Ge-O)-P bond. The Ge-O bond presents a dissociation energy equal to 6.7 eV [156], higher than 4.5 eV reported for Si-O dissociation energy [157]. These values underline the strong affinity between Ge - O, with respect to Si - O, that may probably contribute to the difference between Si and Ge MLD effectiveness.

The P release from either DPP, ODPA or ADPP into Ge is therefore hindered by a low effective release of P from the source under standard annealing conditions. The only possibility to overcome this limitation is to exploit out-of-equilibrium, non-conventional processes with very short times and high temperatures such as flash lamp annealing or PLM.
During PLM, the laser beam melt the Ge surface, with a maximum melt depth around 200 nm (with the used laser parameters in this work). The Ge surface retains a temperature close to the melting point ($937°C$) for a time as long as 30 ns (as evaluated by laser induced melting predictions LIMP, the Harvard simulation software package [89] based on heat flow calculation calibrated on Ge physical and optical literature properties data). This period is dominated by the heat dissipation and is longer than the laser pulse.
In this condition, PR turns out to be exceedingly small: considering an activation energy of 3.9 eV (calculated as our minimum thermal energy given by standard thermal processing), PR should be less than 10^{-10} and the amount of P diffused into Ge should be very small as well. However, the higher phosphorus solubility in liquid Ge should be considered to explain the reduction of the diffusion barrier. As a matter of fact, Fistul et al. [155] report a solubility increase of a factor 10 that is explained by a P binding energy difference of about 0.3 eV between liquid and crystalline Ge [158]. Nevertheless, even considering a lower energy barrier of about 3.6 eV for P release toward liquid Ge, we obtain a PR lower limit of 10^{-9}. Therefore, it can be deduced that molecule breaking under laser pulse does not follow a thermal equilibrium path, but it is strongly enhanced or modified by a direct interaction with the laser UV light.

3.4 Conclusions

In this chapter, a study on phosphorus precursor adsorption on Ge has been presented, focused on the use of phosphorus containing molecules as a source of dopant for *monolayer doping technique* on Ge. Three different molecules have been chosen as representatives for three different phosphorus molecule families, that were previously used in literature for Si MLD technique [57]. The diethyl 1-propylphosphonate was used as a representative for phosphonates, the octadecylphosphonic acid as a representative for phosphonic acids, and the allyldiphenylphosphine as a representative for allyl-phosphines.
During the debate on this work, it became patently clear that the oxidation chemistry of Ge surface plays a crucial role, since the germanium oxide is strongly reactive and easy to be formed: it is easily formed in the presence of air, also with a small amount of humidity and its formation is strongly enhanced by the presence of water/humidity and high temperatures [3]. Moreover, it is very difficult to totally remove the native germanium oxide using strong acid attack, and at least 0.5 ML of germanium oxide still remain on Ge surface [79]. The Ge-H surface termination has been chosen as the most reactive and easily produced germanium termination [123], since it is formed as a consequence of HF treatments, that is already needed to remove the thick native germanium oxide. The molecules used in this work are similar to the ones normally used on Si MLD [57], but a completely different behaviour was revealed in this work, shining a light on the difference between two similar semiconductor with a completely different surface behaviour.

The self-limiting adsorption of these precursors has been deeply investigated by quantitative analysis, studying the process parameters that influence the variation of phosphorus deposited amount. A standard reflux deposition method and a similar dry-box deposition process are presented and described in the first section of the chapter.
The use of synchrotron X-Ray radiation for XPS allowed to evaluate the germanium oxide amount and by a cross checking with NRA analysis, some considerations on chemisorbed vs physisorbed phosphorus amount has been made. The use of methanol rinsing helped to reveal the presence of a physisorbed fraction and underlined the particular affinity between DPP and ODPA precursor with Ge surface.
Thanks to a very precise P and Ge oxide quantification, a correlation between these values has been found: as a consequence, it has been supposed that

the oxidation of germanium increases the polarisability of Ge surfaces with the formation of thin ordered oxide structure, increasing the strength of non-covalent bond interaction between Ge surface and molecule functional groups.
The adsorption tests on Ge powder and its analysis via DRIFT spectroscopy, revealed several molecular changes during the deposition, helping us to determine which type of chemisorption occurs during this process. The adsorption of phosphonate and phosphonic acid produces stable P-O-Ge bonds with the surface, probably involving a delocalised electron on phosphorus oxygen bonds. Surprisingly, the allyldiphenylphosphine does not adsorb to Ge surface via hydrogermilation reaction [59] as expected, but phosphorus oxidation inducing chemisorption through oxygen atoms also in this case. The phosphorus presence probably influences the chemistry of the vinyl group [59, 62], putting it in competition with phosphorus oxidation reaction. Unfortunately, the residual germanium oxide present on the surface is sufficient to oxidise the P of the phosphine molecules also in dry conditions, thus generating completely different chemisorbed molecules compared with the initial one. These considerations are the result of XPS, DRIFTS and EXAFS analyses, which allowed to verify the oxidation state of phosphorus, the molecular structure changes in terms of functional group and phosphorus first neighbours.
These considerations are strengthened by the phosphorus quantification results via NRA, highlighting that ADPP residual molecules do not physisorb on Ge, or if they do it, they are easily removed from Ge surface by a mesitylene rinsing. This suggests that only chemisorbed molecules are oxidised, while other molecules at least present a phenyl group that allows molecule removal from the surface. In fact, if P=O groups (or other polar groups that can be formed as a consequence of an oxidation) are formed on ADPP, a strong physisorption of oxidised ADPP molecule must occur, as demonstrated with similar precursors in this work and in literature [67].

During the thermal diffusion tests, either DPP, ODPA and ADPP molecules did not show P in-diffusion in Ge, suggesting a similar chemisorption of the used molecules. Indeed, as suggested in our work [129], the stability of these molecules could be explained in terms of the release frequency from the ML source: it should follow a thermally activated Arrhenius trend and the release probability (PR) is obtained multiplying the release frequency by the annealing time t, according to the equation 3.1 showed before. The scenario previously shown underlines that the phosphorus in-diffusion lack is probably due to

the formation of P-O-Ge bonds that show a very high stability to thermal degradation. In particular, by considering the dissociation energy of P=O, and comparing the previous MLD on Si results, it is strongly suggested that the P-O strong affinity and the impossibility to reach higher annealing temperatures are the reasons of P diffusion lack in Ge (and the main difference between MLD technique applied to Si instead of Ge).
The eventual presence of physisorbed fraction should not contribute to release phosphorus, since the P=O bond present on ODPA and DPP molecule is extremely stable as previously discussed [129]
The use fo ADPP precursor has been decided in order to avoid a Ge-O-P bond formation, but as showed in this work, the hydrogermilation reaction do not occur as expected, and so only Ge-O-P (with delocalised P-O bonds) chemisorption is obtained, as previously shown in this work.

The use of Pulsed Laser Melting technique with these phosphorus precursors, that involves different chemical-physics phenomena whith respect to a simple thermal annealing, such as Ge melting and liquid diffusivity, has been tested in this work. The used energy density range ensures about 200 nm Ge melting as a consequence of a single laser pulse in the UV wavelength range. Thanks to this work, we demonstrate that the use of different phosphorus precursors is effective for germanium doping, since diffusion and electrical activation are detected for the formed layer.
All the phosphorus precursors tested in this work show an effective phosphorus diffusion, even if DPP and ODPA molecules show a spatial variability of P concentration after PLM, probably due to the inhomogeneity of the physisorbed fraction. On the contrary, ADPP precursor processed with PLM shows a very laterally uniform diffusion and the obtained phosphorus doping profiles fully meet our best expectations, also in terms of electrical activation. As suggested by previous evaluations, the UV laser not only acts as a heater for Ge surface local melting, but probably the UV beam interaction with molecules promotes their dissociation (or lowers their dissociation energy), since the thermal budget induced by a single PML is lower than the higher thermal budget delivered with RTP machine.
In conclusion, the PLM process described in this work is only a first proof of the successful diffusion of dopants from a surface-deposited molecular precursor: this is very promising, since the junction depth can be simply tuned by varying the energy density of the laser. In particular, it is possible to reduce the melt

depth, and in turn to reduce the junction thickness, by tuning the energy density of the laser. Unfortunately, the used Nd:YAG laser is not suitable for this purpose, but a more proper excimer laser could easily reduce the junction thickness, thus increasing the phosphorus surface concentration.

Chapter 4

Antimony Monolayer Doping

In this chapter, we study a new phenomenon: the formation of a self-limiting monolayer of antimony on Ge (001) surface. After the characterisation of the deposition process, by analysing the process window in terms of time and temperature, we perform an accurate surfaces analysis, revealing that the surface Sb layer is in an oxidise state (III,V), while a small but significant amount of metallic Sb is present in the first Ge matrix layer. In the light of all experimental observations and results, an adsorption chemical mechanism will be proposed and justified through thermodynamics considerations.
After the study of this phenomenon, the ML behaviour as a source of dopant is tested, revealing that only the small metallic Sb amount is able to diffuse inside Ge with standard thermal annealing processes. This diffusion is characterised and modelled exploiting a literature model that takes into account intrinsic or extrinsic diffusion mechanism occurring during the annealing, depending on the Sb concentration.
The pulsed laser melting technique was applied also to this system, revealing that with only one PLM laser pulse, all the Sb ML diffuse in Ge, without any loss. After diffusion, electrical characterisation reveals that all the diffused Sb is electrically active, suggesting that laser treatment induces a Sb chemical reduction from III-V in the surface oxide state, to the value of I, typical of the active doping state.

4.1 Deposition Method

The Sb self-limiting deposition on Ge (001) surface has been discovered during a study of hyper pure Ge doping via direct sputtering Sb deposition and diffusion

[159]. In this study, we were using Sb gas generated by sublimation during annealing: during this process, it was discovered that Sb is deposited in all lateral Ge faces, with a fixed amount, and even the rear part of the samples turned from undoped to n-type during the process. In ref. [159] we observed that the direct deposition of Sb over Ge is not a good doping route since it brings to the formation of surface defects on the Ge surface as shown in figure 4.1. The following

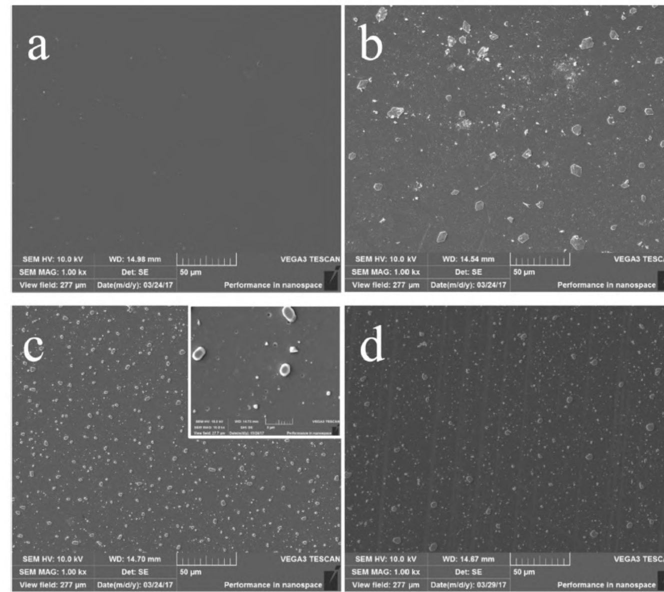

Figure 4.1. SEM images of directly deposited Sb-on-Ge samples: a) as deposited; b) fast annealed at $570°C$; c) fast annealed at $610°C$; d) fast annealed at $630°C$. Inset in figure: magnified view of the sample annealed at $610°C$ aimed at highlighting the holes on the sample surface.

step, in order to improve the surface morphology and exploit the Sb self-limiting deposition, that we will investigate in detail in the next paragraphs, was to test a remote deposition process. In this procedure Sb is sputtered over a Si substrate that is used as a Sb source when Sb sublimates under heating. A Ge target is placed in the same heating chamber, together with the Sb on Si source, and the deposition takes place.
In more detail, Ge samples are obtained from a Ge wafer (provided by Umicore, p-doped $0.04 - 0.4\ \Omega\ cm$ resistivity) that was cut into $1x1\ cm^2$ and $1x2\ cm^2$ samples.
Sb on Si sources are obtained by cutting a Si (001) wafter into $1x2\ cm^2$ samples. The sputtering equipment consists of a stainless steel vacuum chamber evacuated

by a turbo-molecular pump. [1] Pure Sb (99.999%, provided by ACI Alloys) was used as a sputtering target material. Sb deposition rate was determined and then monitored by Rutherford Backscattering Spectrometry (RBS) and the duration of each deposition run was varied in order to achieve a film thickness of 20 nm and 100 nm [159]. Each Sb source sample is analysed with c-RBS, before and after the deposition procedure.

Antimony was deposited on Ge substrates from a gas phase, exploiting Sb sublimation from the heated metallic Sb on Si source. As a matter of fact, these deposition are also called gas phase depositions. These thermal processes were conducted with two different furnaces: a standard tubular furnace equipped with a quartz tube for vacuum and gas flux treatments, and a Jipelec JetFirst Rapid Thermal Processing machine (RTP), both described in method chapter. The former had a maximum heating ramp of $3°C/s$ in fast annealing use (i.e. by rapid insertion and removal of the sample in the pre-heated furnace) and the latter heating ramp was $100°$-$150°C/s$. These two different ramps were used in order to explore different durations of the deposition process: from a duration of half an hour, down to 10 s. The sample temperature was monitored by a thermocouple connected with the sample boat in the standard furnace and by a calibrated pyrometer, which measured the temperature of a supporting Si wafer in the RTA system. Before any deposition, both the furnace and RTA were cleaned with five cycles of vacuum and N_2 refill.

In the standard furnace, the Sb-coated Si substrate was placed on two spacers over a Ge target, with the Sb-deposited face in front of Ge target at a distance of 8 mm, as schematised in figure 4.2. This distance was studied in order to avoid any Ge surface damaging, ref. [159]. The whole system (shown in figure 4.2) was placed in a quartz boat to be entered into the furnace [159]. The tubular furnace was used only for 30 minutes treatments, while RTP was used for shorter annealing, from 30 minutes down to 10 s, thanks to its performance.

As an example, in figure 4.3 are reported SEM images collected during the deposition parameter studies [159]: in particular the distance between Sb-Si and Ge sample was deeply investigated using a tubular furnace (as reported in figure 4.2). In this figure a, b images are referred to a Ge sample placed at 1.5 mm, while in

[1]The glow discharge sustaining device was a cylindrical magnetron sputtering source connected to a radio frequency power generator (600 W, 13.56 MHz). The deposition parameters used for all the films were: direct RF power 30 W; target-to- substrate distance 14 cm; working gas Ar (99.9999% purity); Ar flow 20 sccm. A mass flow controller regulated the working gas flow and the chamber was continuously pumped during the deposition in order to reduce atmosphere contamination by wall outgassing.

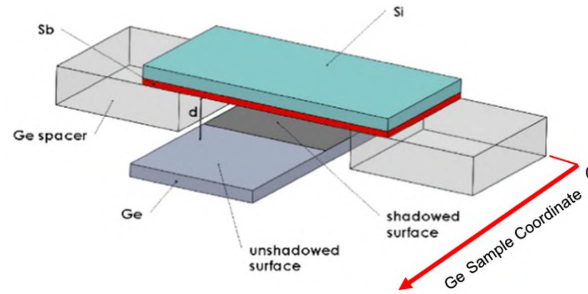

Figure 4.2. Deposition scheme of Sb ML deposition with standard tubular furnace. In figure, d is the distance between Ge surface (target) and Sb film surface (source). The Ge surface exactly below the Sb-coated Si was named shadowed surface. The scheme is not in scale.

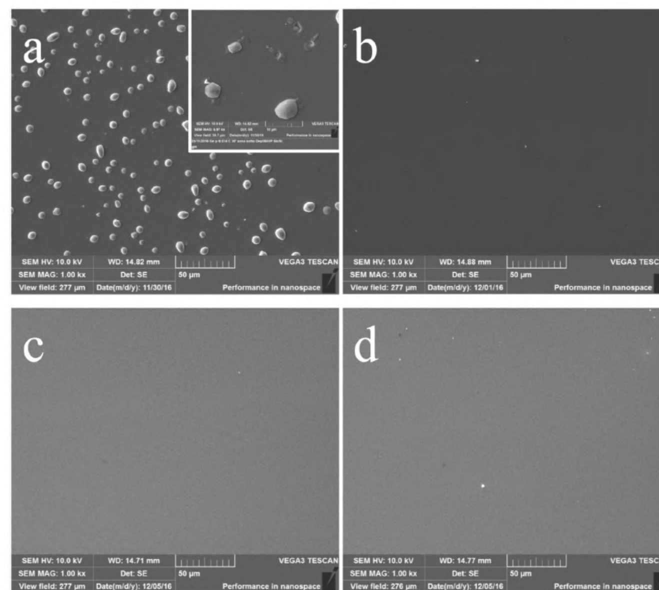

Figure 4.3. SEM images of remotely deposited Sb on Ge samples: a) Ge sample at 1.5 mm far from Sb source: image below Si sample (shadowed surface); b) the same sample in the unshadowed surface; c) Ge sample at 8.5 mm below Si sample (shadowed surface); d) the same sample in the unshadowed surface. Inset in figure: magnified view aimed at highlighting the grains and holes on the sample surface.

c, d boxes the Ge sample was placed at 8.5 mm. It is clear that at 1.5 mm some Ge surface defect is formed (a box), but looking on the same sample further from the source, the area is defect free (b box), suggesting that the defect can be avoided by setting a proper distance between them. As a matter of fact, 8.5 mm is sufficient to form a surface defect free sample, both in shadowed and unshadowed zones. In RTP, the Si source and Ge sample were placed side by side on the supporting wafer with upward sputtered Sb source and Ge depositing surface both looking at the heating lamps. Quartz spacers were added in order to confine the deposition area from the all furnace chamber, as reported in figure 4.4. This geometry is

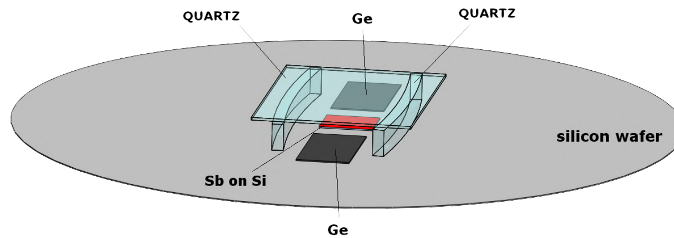

Figure 4.4. Deposition scheme of Sb ML deposition with Rapid Thermal Processing. In the scheme, the Sb source sample is reported in red and the Ge target samples are reported in grey. Some quartz spacer and windows are placed for the protection of machine main windows, and are reported as transparent materials. All the samples and the quartz are placed on top of a Si wafer. The scheme is not in scale.

functional to the cold wall furnace that guarantees heating homogeneity of samples placed on the supporting Si wafer in front of the lamps. The quartz spacers have the aim of avoiding direct emission of Sb on the cold quartz window that protect the RTP lamps. Quartz is transparent to lamps emission so it does not perturb too much the heating of the sample; moreover, they are changed after each deposition in order to avoid an eventual Sb deposition on its surfaces and so a decreasing of light transmission. The effect of the difference of Ge emissivity with respect to silicon, and the impact of quartz spacers were computed in a finite element thermal simulation of the system. Temperature differences lower than $10°$C with respect to the unperturbed system and no significant effects on the ramp were estimated. In figure 4.5, a typical RTP recipe is reported, showing a typical deposition in detail. In the first minute the last N_2-vacuum cycle is completed, followed by a pre-heating / stabilising time lapse. After that the

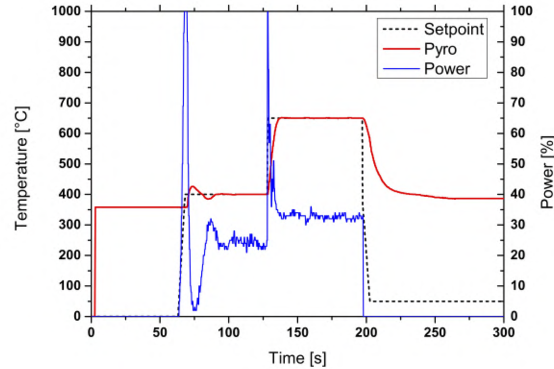

Figure 4.5. A typical RTP recipe used for Sb ML deposition. In this figure, different parameters are plotted as a function of time, i.e. the duration of the process. A 650°C for 60 s deposition is shown. The dashed black line indicates the set point of the recipe, while the red curve is the temperature reading by the pyrometer directly on Si wafer. The Blue curve is the % of the RTP lamps used during the process. It is important to underline that the minimum reading of pyrometer is 360°C.

real deposition step starts with a rapid heating to the setting temperature, during which a dry N_2 flux at 500 sccm is constantly fluxed in the locked chamber. After the deposition, the lamps are switched off and the N_2 flux is increased to 2000 sccm in order to cool the samples down.
After the monolayer deposition, the samples are stored under Ar, until the following surface analysis and processing. However, as it will be further discussed, the monolayer is perfectly stable also in air for (at least) several weeks.

4.2 Sb Monolayer Formation

The self-limiting deposition behaviour of Sb on Ge (001) is demonstrated by RBS quantification. After the discovering and demonstration of the Sb self-limiting deposition behaviour on Ge, several different deposition parameters were tested: in this section, time and temperature parameters are modified in order to verify the self-limiting deposition process windows.

4.2.1 Gas phase deposition: time and temperature deposition parameters study.

The antimony deposition on Ge (001) was first studied in a wide temperature range, from 400°C to 790°C, by using a standard tubular furnace and setting 1800 s as deposition time. A 100-nm-thick metallic Sb source deposited on Si was used

as described in the deposition section. Thanks to the c-RBS measurements, the Sb behaviour on Ge (001) surface at different temperature can be easily monitored, and the Sb areal density (i.e. dose) deposited on Ge is reported in figure 4.6.

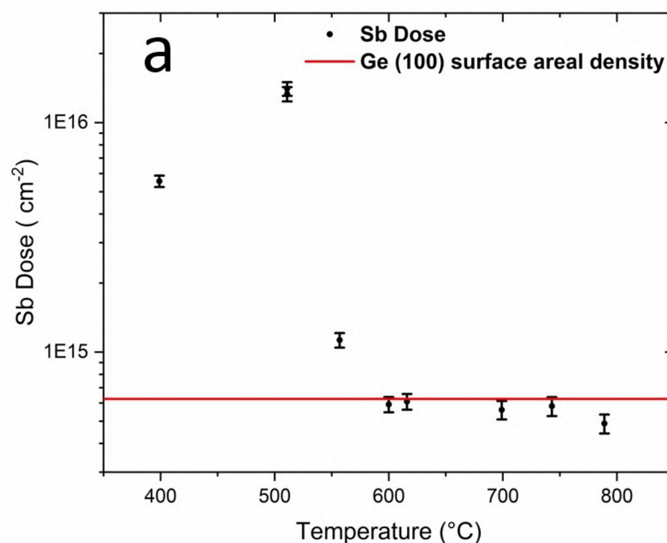

Figure 4.6. Sb quantification on different Ge samples as a function of the deposition temperature. Data are obtained via c-RBS. The red line is the Ge(001) theoretical surface density.

It can be observed in figure 4.6 that Sb areal density increases going from $400°$C to $510°$C, then decreases and remains approximately constant between $600°$C and $750°$C with a slight decrease at the highest $790°$C temperature. The plateau shown in the deposition range between $600°$C and $790°$C is extremely similar to the red line, that is the Ge (001) surface atomic density $(6.25\ 10^{14}\ at\ cm^{-2})$.

In order to explain this complex behaviour, RBS Sb quantification were performed also on Sb source samples after the deposition procedure. By the analyses of the Sb source we notice that the 100-nm-thick Sb film is only partially consumed at $400°$C while it is almost exhausted at $510°$C and no trace is found at higher temperatures. The increase of Sb on Ge going from $400°$ to $510°$ is therefore due to the increased availability of Sb that evaporates faster at higher temperature.

A different phenomenon is revealed at even higher temperature when the Sb source is exhausted: the $560°$C deposition reveals a net decrease of the Sb, meaning that the Sb deposition is not stable at higher temperature after source exhaustion. This instability does not apply to the first monolayer of the deposit that remains stable between $600°$ up to $750°$C, showing a clear self-limiting behaviour.

In order to remove all doubts, also 20 nm Sb thick sources were used, and the same behaviour has been obtained.

It is evident that the first Sb monolayer deposited on top of Ge surface displays

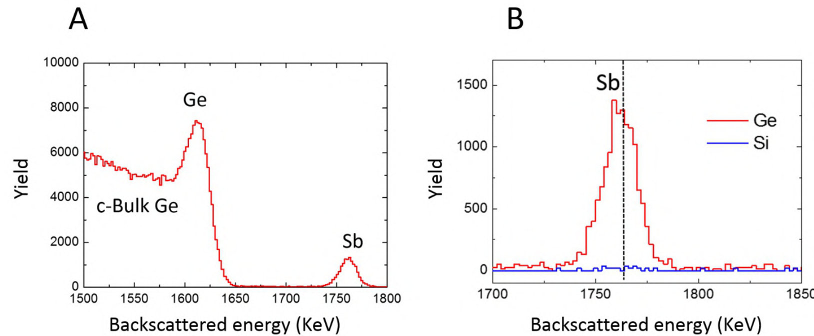

Figure 4.7. RBS spectra in axial channeling conditions. On left (A), a typical Sb ML on Ge c-RBS spectra: the Ge substrate is put in channeling conditions, thus the Ge signal, after a typical surface peak, decrease at lower particle energies (higher scattering depth). Thanks to this condition, the pile-up phenomena is reduced and consequently a low background is present at higher energies, respect to Ge peak. In this way, Sb peak can be quantified with a very good signal to noise ratio. On right (B), RBS signal in Sb region of the RBS spectrum shown on left (red histogram), compared to the signal coming from an exhausted Si source sample (blue histogram), after the Sb ML deposition process at T>600°C.

a different thermodynamic stability with respect to Sb directly bound to Ge surface. Furthermore, it is worth to note that at the same temperature Sb is not stable on the silicon surface (as reported in figure 4.7B), as proved by the complete removal of Sb from the Si surface, whereas the layer is stable on Ge surface. This indicates that a specific interaction between Sb and Ge surface occurs, as it will be investigated in depth in this chapter.

The second important deposition parameter is the duration of the process. The temperature that we decided to use for this process is the lowest temperature that ensures a self-limiting behaviour and a good uniformity (see next section) and for these reasons 600°C was chosen. Thanks to the use of RTP furnace, the duration of the process can be diminished down to a few s, allowing us to explore the minimal duration of the process. As described in the deposition section, a 20 nm-thick metallic Sb thick source has been used to scale down the treatment time, to avoid the waste of Sb and to minimise the Sb dispersed inside the chamber.

Figure 4.8 shows the Sb doses detected with c-RBS on Ge target sample after different treatment times. It is evident that the ML formation is a very fast process, which is already accomplished within the first 10 s. This result means that the sublimation of Sb on Si substrate, its diffusion/transportation on Ge sample and its adsorption on Ge occur in less than 10 s.

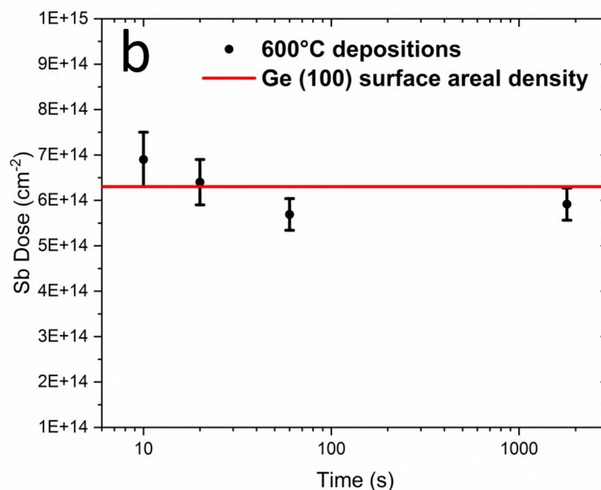

Figure 4.8. Sb quantification on different Ge samples as a function of the deposition duration. Data are obtained via c-RBS. The red line is the Ge(001) theoretical surface density.

But is this layer uniform on the whole surface of the sample? In order to answer to this question, a laterally resolved mapping is performed.

4.2.2 Monolayer areal homogeneity analysis.

Homogeneity test was performed mapping the sample surface with different RBS spectrum. The beam size is 0.5x0.5 mm^2 and the position accuracy is in the order of 0.01 mm. By looking at the deposition geometry (see figures 4.4 and 4.2), it is interesting to verify the homogeneity of Sb ML along the directions called sample coordinate because of geometrical-symmetry and because of the fact that N_2 flux (in the tubular furnace and RTP) is directed along this direction. Some additional measurements (not shown) demonstrate the homogeneity also in the orthogonal direction.
The Sb distribution on the Ge surface as a function of the position along the sample coordinate is reported in figure 4.9 that extends the single point results of figure 4.6.

The reported data point out that processes carried out at T<600°C show a Sb dose gradient toward the source. This gradient is in all likelihood due to the gas phase diffusion in N_2 flux, that cause the higher Sb concentration near the source sample, and lower Sb amount at higher distances. Above the 600°C, the self-limiting behaviour is confirmed that limits the amount of Sb to 1ML all along

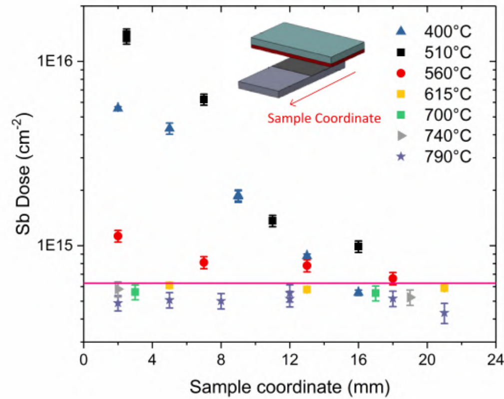

Figure 4.9. Sb quantification on different Ge samples in different position of sample. Data are obtained with c-RBS quantification. Each colour represent a different deposition temperature (so a different sample), all performed with a tubular furnace, using a 30 minutes deposition. The red line is the Ge (001) theoretical surface density.

the sample.
This behaviour is verified also with RTP deposition processes, as reported in figure 4.10. In this figure the homogeneity is verified for 1 min treatment in RTP.

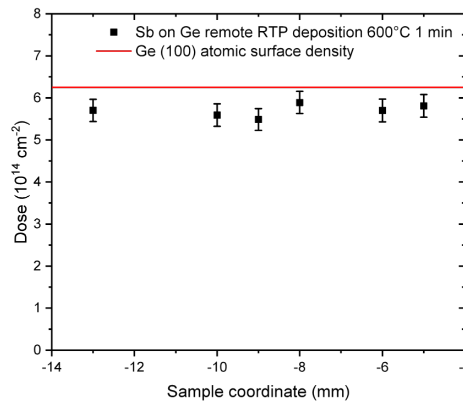

Figure 4.10. Sb quantification on RTP formed Sb ML on Ge with a 1 minute deposition at 600°C*. Data are obtained with c-RBS quantification. The red line is the Ge (001) theoretical surface density.*

Similar results are obtained also for 20 s depositions with RTP (not shown).
This finding is a crucial point in the perspective of doping applications: the self-limiting regime that is obtained in the latter thermal window guarantees a high homogeneity of the Sb distribution in a final device.

To verify the layer uniformity at lower scale, surface AFM images were acquired on untreated Ge wafer and after 1 minute at $600°$C monolayer deposition on Ge. In figure 4.11 these images is compared. These AFM images are taken over

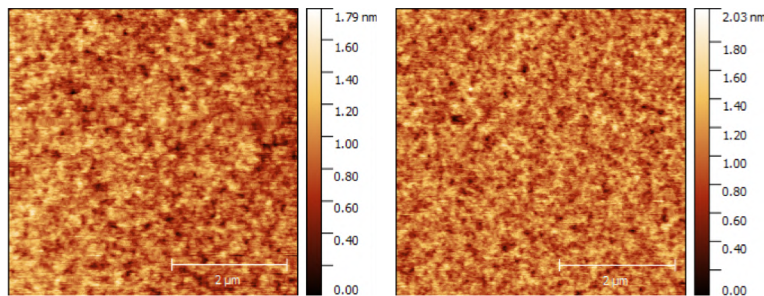

Figure 4.11. AFM images: on left, Sb ML on Ge (001) syntetised with RTP at $600°C$ for 1 minute, to be compared with an untreated Ge sample, on right.

$5x5$ μm^2 area with a DI Cp-II AFM instrument using a commercial silicon nitride cantilever. These images reveal negligible surface roughness differences, eventually caused by the deposition process. The evaluated roughness on both images reveals 1.8 $\AA$ and 1.9 $\AA$ values for functionalized and untreated sample respectively. This observation excludes any antimony oxide surface aggregation, that is not detectable by c-RBS technique and strengthens the existence of a specific surface interaction between germanium and antimony that generates the self-limiting behaviour of the process.

In the light of all these experimental evidences, a spatially uniform Sb ML has been detected, and time-temperature formation parameters have been studied showing a very rapid and uniform formation process.

4.3 Sb Monolayer Surface Characterisation

After the study on process parameters, the antimony monolayer is chemically characterised and a discussion on the surface chemistry formation will be further proposed. The self-limiting layer is analysed with XPS technique, using a synchrotron X-Ray source: the signals are collected at different take-off angles (AR-XPS) and these data are quantitatively analysed. In the light of all the experimental and literature evidences a chemisorption reaction will be proposed below.

4.3.1 AR-XPS surface analysis

In order to verify the surface composition of antimony monolayer on Ge surface, XPS analysis is conducted on RTP Sb ML, formed at $600°C$ for 60 s. In figure 4.12, the Ge 3p - Sb 4p region acquired with a photon energy of 305 eV at $90°$ take-off angle is shown.

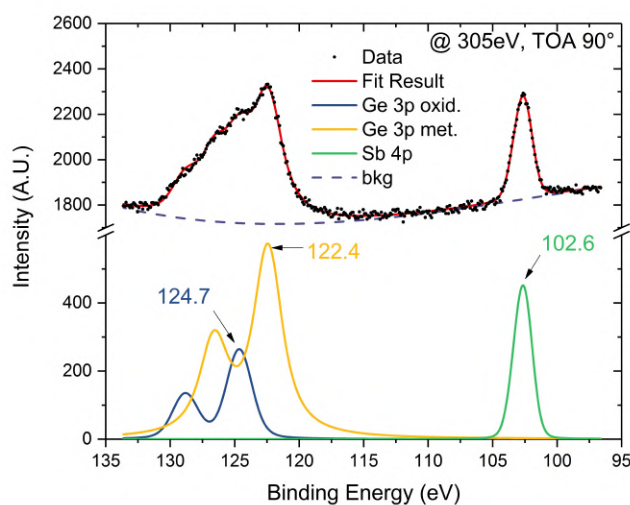

Figure 4.12. XPS signal coming from Sb ML deposited on Ge (001) sample: the Ge 3p - Sb 4p region is shown, acquired with a photon energy of 305 eV at $90°$ take-off angle. The signal (black points) are deconvolved with a single component for Sb 4p (green line), two components for Ge 3p (metallic in yellow and oxidised in blue) and a background (dashed line). The red line is the sum of all components and the background. The spectrum are acquired with a pass energy equal to 50 eV and a 0.1 eV step.

The Ge 3p region is well deconvolved by two components [126] representing metallic Ge and a Ge oxide, with the 3/2 components at 122.4 and 124.7 eV, respectively (associated peaks at lower energies are the 1/2 components, separated with a shared splitting parameter during the deconvolution). The Sb 4p 3/2 peak presents a binding energy of 102.6 eV, revealing an oxidised state ([160, 161]) of the adsorbed antimony.
The O 1s, Sb 3d XPS signals were also acquired: in figure 4.13 this region is shown.

The Sb 3d peak present in this figure shows a 3/2 component at 540.4 eV, compatible with the results of Garbassi and co-workers [160], within the experimental error, thus in agreement with Sb 4p peak. Furthermore, the assignment of Sb (V) can be correlated with the presence of a O 1s peak at 531.6 eV. As reported in the literature [160], the oxygen bonded with Sb (V), as in the Sb_2O_5, presents a binding energy equal to 531.5 eV, compatible with our data. All these data are well

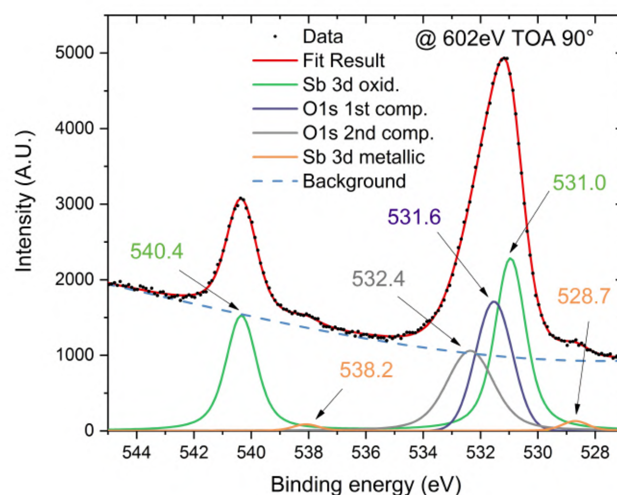

Figure 4.13. XPS signal coming from Sb ML deposited on Ge (001) sample: the O 1s - Sb 3d region is shown, acquired with a photon energy of 602 eV at 90° take-off angle. The signal (black points) are deconvolved with a single component for Sb 4p (green line) having two peaks 3/2 at 540.4 and 5/2 at 531.0 eV with a very high splitting between components of 9.4 eV. Two components for O 1s are reveal (grey and violet lines) and a background is shown with dashed line. A small component attributed to metallic Sb is visible as two splitted shoulders at 538.2 and 528.7 eV, representing 3/2 and 5/2 components. The red line is the sum of all components and the background. The spectrum are acquired with a pass energy equal to 50 eV and a 0.1 eV step.

Table 4.1. Literature XPS binding energies used for Sb analysis.

XPS peak	Sb_2O_3 eV	Sb_2O_4 eV	Sb_2O_5 eV
$Sb\ 3d_{5/2}$	530.1-530.3	530.7-531.2	531.0-531.1
$Sb3d_{3/2}$	539.5-539.7	540.0-540.5	540.4-540.6

matched with a Sb_2O_4 assignment as well, since there is not a significant difference of chemical shift between Sb_2O_5 and Sb_2O_4 in the literature [160, 161]. So, the Sb ML can be compatible with a mixture of Sb (V) and Sb (III), as the antimony in the Sb_2O_4 structure presents.
In the same binding energy region the GeO related O 1s contribution could be present, while the GeO_2 O 1s component is clearly separated and visible at 532.4 eV, in agreement with the value of 532.6 eV reported by Prabhakaran et al. [3] for the case of air oxidised Ge surface.
In this XPS region it is even possible to notice a small additional Sb 3d component: the 3/2 and the 5/2 components are clearly present and deconvolved at 538.2 eV and 528.7 eV respectively. The splitting between these two peaks corresponds to the value reported in literature (9.4 eV) [160], thus confirming the correct deconvolution.
It is worth to note that it is not possible to evaluate the Sb / O atomic ratio using O 1s and Sb XPS peaks, since we do not have a O 1s peak purely attributed to the Sb surface compound. We can only suppose the ML composition by the Sb 3d and Sb 4p binding energy. The Sb / O ratio is in between the 2:5 and 2:3 since the binding energy is compatible with Sb_2O_5 (purely Sb V atoms) and Sb_2O_4 (mixed Sb V and Sb III atoms) compound as well, and not with the Sb_2O_3 oxide (purely Sb III atoms). In table 4.1 literature binding energies for Sb oxides are reported.

The XPS Ge 3p and Sb 4p signals were collected at different take-off angles in order to study the angular dependence of the peak intensities (Angle Resolved XPS). The intensities of Ge 3p (metallic and oxidised) and Sb 4p peaks are reported in figure 4.14 as a function of the emission angle normalised to the Sb signal.

A first analysis can be done by simply looking the XPS intensities trend with the angle: it is clear that the antimony oxidised signal (blue data) is placed over the germanium oxide (yellow data) that are over the bulk germanium (red data, metallic signal), by considering the relative slope between data: the deeper is the layer the higher is the attenuation of the relative signal by increasing the take-off

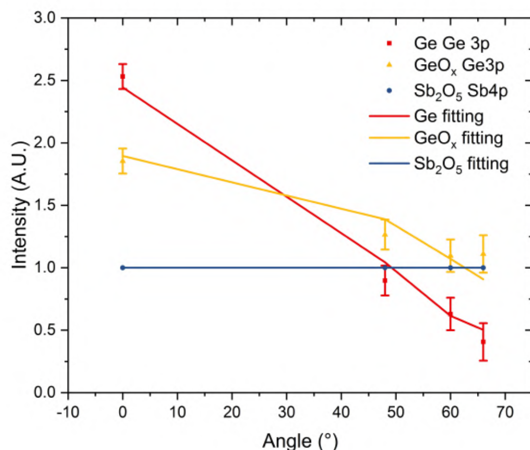

Figure 4.14. Angle Resolved XPS data normalised to Sb 4p signal as a function of the emission angle. The continuous lines are the best fitting of a multi-layer model (described in the text) made with BRIXIAS code package.

Table 4.2. Properties of layers used as input model for AR-XPS analysis on Ge 3p and Sb 4p region. The fitted thickness are reported in the last two column, with different units.

XPS peak $E_{phot} = 305eV$	Layer composition	Input Layer Density gcm^{-3}	Fitted Thickness Å	Fitted Thickness ML units
-	C	2.26	4.5	8.5
Sb 4p	Sb_2O_5	3.78	2.6	0.6
Ge 3p	GeO_x (II,IV)	4.70	3.8	1.7
Ge 3p	Ge (0)	5.32	bulk	bulk

angle. This evaluation was used as starting layer structure to fit the data.
By using the BRIXIAS code package [106, 162], these XPS signals are analysed and their intensity variation with the angle is fitted with a multi-layer model. The continuous layers are considered in the model since no island distribution is expected in the light of AFM measurements results. As a further confirmation of this, discontinuous layers with islands formation are used to model the data, obtaining only a worsening of the fit quality.
As described in the Methods chapter, the BRIXIAS code package is able to evaluate the attenuation of photoelectrons (i.e. the Depth Distribution Length DDL) by a Monte Carlo simulation by taking into account the multi-layer composition of the system: each layer is characterised by a specific material and thickness so that starting from an initial guess, whose parameters are adjusted during the fitting procedure, it is possible to estimate the DDL for the emitted photoelectrons and consequently the simulated thickness.

A set of parameters used for the calculation is reported in table 4.2.
The fitting results are reported in table 4.2. The thickness of the Sb ML is 2.6 $\AA$. In order to compare this value with the RBS one, the thickness can be expressed in areal density by multiplying the number for the layer density obtaining a surface concentration of about $4\ 10^{14}\ cm^{-2}$ Sb atoms. This value can be expressed also in terms of monolayer coverage of Ge (100) surface: remembering that Ge (100) surface atomic density is $6.25\ 10^{14}\ cm^{-2}\ =\ 1ML$ unit, obtaining a value of 0.6 ML ($4/6.25\ 10^{14}\ cm^{-2}\ =\ 0.6ML$ units).
It is worth to note that even if the density of the antimony oxide and germanium oxide layers could be quite different from the bulk one (that are the tabulated and used one), the metallic bulk germanium signals allow us to have an important reference signal to fit. Moreover, the possibility to compare the AR-XPS fit results with another technique (i.e. c-RBS) can support us to validate our fitting model results.
The 0.6 ML units value represents the total Sb ML amount, but not the total amount of Sb, since the Sb 3d region shows also a small Sb (0) component. By comparing the peak intensities, we obtain that the Sb (0) is about 4% of the total Sb amount. In figure 4.15, the quantification is shown.

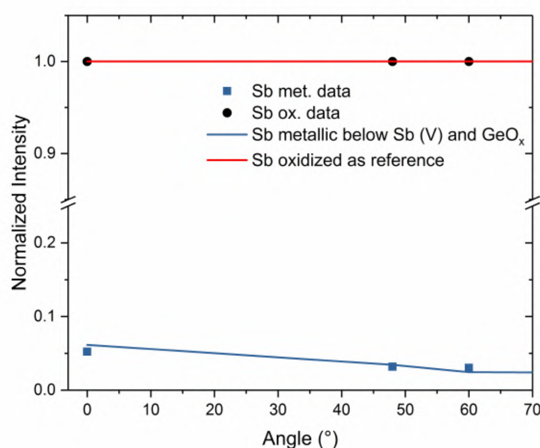

Figure 4.15. Angle Resolved XPS data normalised to Sb 3d oxidised signal as a function of the emission angle. The black points, fitted with the red curve, are Sb 3d oxidised intensities, while blue points are Sb 3d metallic intensities, fitted with blue curve.

Since the Sb ML was quantified with a c-RBS technique and since the AR-XPS quantification using the BRIXIAS code simulation, gives us a Sb amount, the total amount of antimony estimated by ARXPS technique can be directly compared

with c-RBS results. It is important to remember that the Rutherford Backscattering technique gives a dose information, while ARXPS technique is primarily chemically sensitive and the absolute amount of Sb can be estimated only through a simulation. The c-RBS analysis gives a $5.7\ 10^{14}\ cm^{-2}$ Sb surface areal density which corresponds to approximately 0.9 ML units ($(5.7/6.25)\ 10^{14}cm^{-2} = 0.9ML$ units), to be compared with the 0.6 ML units obtained by AR-XPS simulation. These two values are in reasonable agreement considering that the Sb ML layer was simulated by assuming a Sb_2O_5 density, but it could also be Sb_2O_4, as previously reported. Indeed, the Sb:O ration is not clearly determined, and it could be ranging between the maximum value 2:5 and the lower 2:3. This assumption can introduce a systematic error in the XPS dose estimation, contributing to the slight disagreement between the results of the two techniques.

Another interesting result is given by the germanium oxide quantification. According to table 4.2, less than 2ML of GeO_x are present after the ML deposition. This result is surprisingly low, since the initial sample presents a native oxide layer, that is thicker compared to this result. In figure 4.16, a comparison between an untreated Ge sample, presenting a Ge native oxide on its surface, and a Sb ML functionalized sample is shown.

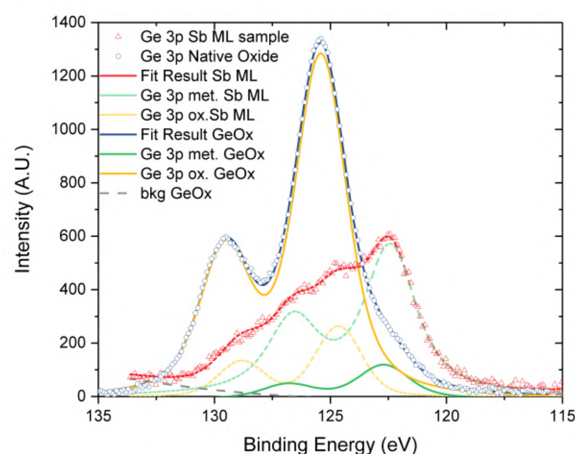

Figure 4.16. XPS Ge 3p region of an untreated Ge sample, presenting a Ge native oxide on its surface, and the Ge 3p region of a Sb ML sample. Experimental data are reported as points (circular for native oxide, triangular for Sb ML sample), while the fit results are continuous line, blue for germanium oxide sample, red for Sb ML sample. Ge metallic and Ge oxide two peaks deconvolution is also shown in figure, green curves and yellow curves respectively. The continuous are referred to germanium native oxide, while the dashed to Sb ML sample.

Thanks to this figure, it is clear that a strong decrease of germanium oxide

occurs, and it will be discussed further in this chapter. The Ge oxide thickness decreases from about 20 Åto a thickness of 3 Å.

In conclusion, XPS analysis reveals that antimony is mainly in an oxidised state (III,V), with a small metallic fraction of metallic Sb (0), estimated to be around 4%. The peak intensities trend as a function of the take-off angle indicates that an oxidised Sb layer is coating a small amount of GeO_x. ARXPS data analysis (summarised in table 4.2) and c-RBS results are in agreement within the experimental errors, confirming the layer modelling and the fitting analysis performed on the Sb ML system. Finally, the germanium oxide amount is strongly decreased as a consequence of Sb ML deposition process.

4.3.2 Chemical Adsorption suggested reaction

A particular affinity between Sb and Ge surface during the gas phase deposition treatment is suggested by experimental evidences and, as we previously saw, a relatively stable oxidised Sb surface phase is present after the monolayer formation. In this section, some considerations will be presented and a surface reactivity will be suggested.
The synthesis process of Sb ML can be divided in two different processes that occur during the deposition:

- the formation of an antimony monolayer on Ge surface
- the instability of Sb over-layers

both concurring to the self-limiting behaviour of the whole process not to form more than one layer.
These two different processes are clearly presented in the data discussed on previous sections and the instability of Sb over-layers above around $600°$C is highlighted in Figure 4.6. It is important to note that the ML is stable against back-decomposition toward the external environment up to the maximum Ge process temperature that is about $800°$C. In the light of all the experimental evidences, a possible pathway for the ML formation is inferred.
It is well known in literature that antimony releases Sb_4 gas molecules [163] as a consequence of its sublimation in an inert atmosphere not only from Sb bulk substrate [163], but also from a thin film source [164]. Moreover, the nature and the stability of the germanium surface have to be taken into account, with a particular care to germanium oxide evolution. Indeed, as reported in figure 4.16, a

strong GeO_x decrease is revealed. This evidece can be correlated to the fact that at the temperature at which the ML process occurs (more than 600°C), germanium oxides start to be unstable and GeO is released [81, 82]. This thermal activated mechanism was described in the introduction section, and it can be summarised in to $Ge + GeO_2 \longrightarrow 2GeO$ and than $GeO_{solid} \longrightarrow GeO_{gas}$, sublimation process.
From these informations, we propose that the adsorption of Sb on the Ge surface occurs through the oxidation of Sb_4 gas by the germanium oxide according to the following reaction:

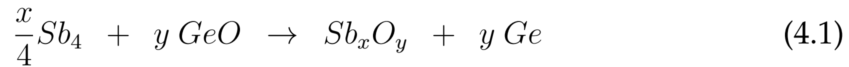

$$\frac{x}{4} Sb_4 \ + \ y\, GeO \ \rightarrow \ Sb_x O_y \ + \ y\, Ge \tag{4.1}$$

The reaction product Sb_xO_y molecule represents the Sb oxidised ML formation on Ge (001) surface, bonded with it through an oxygen atom, as suggested by AR-XPS analysis.
This reaction is consistent with different experimental evidences, first and foremost, the net decrease of Ge oxides after the deposition process, as clearly reported in figure 4.16 by comparing Ge 3p XPS regions of untreated and Sb ML functionalized germanium surface. By using the germanium oxide sublimation mechanism presented in literature[82], it is possible to evaluate that after 10 s at 600°C about $10^{15} cm^{-2}$ of GeO sublimate.
This process underline that germanium mono-oxide can act in the proposed reaction with a sufficient amount of GeO released from the surface. In particular, the GeO_2 component is eliminated from the surface owing to $Ge + GeO_2 \longrightarrow 2GeO$ disproportionation and the subsequent sublimation of GeO [82]. Taking into account that the typical GeO_x areal density we measured by AR-XPS is about $7 - 8\ 10^{15}\ cm^{-2}$, it is clear that GeO is not a limiting reagent for the proposed adsorption reaction.

The proposed adsorption reaction is also supported by thermodynamic considerations. The variation of Gibbs free energy for a given reaction ΔG_r, can be evaluated starting from the formation values ΔG_f of each reactant and product [165] at a given temperature[166].
The $\Delta G_r^{\ominus}$ is calculated from the following equation:

$$\Delta G_r^{\ominus} = \sum_{Products} \nu \Delta G_r^{\ominus} - \sum_{Reactants} \nu \Delta G_f^{\ominus} \tag{4.2}$$

or more formally:

$$\Delta G_r^{\ominus} = \sum_j \nu_j \Delta G_{f,j}^{\ominus} \tag{4.3}$$

Since the reaction occurs not in standard conditions, the ΔG_r must be evaluated at a certain T. For this reason, equation 4.3 can be expressed also at different temperature:

$$\Delta G_r(T) = \sum_j \nu_j \Delta G_{f,j}(T) \tag{4.4}$$

As discussed above, GeO and Sb_4 reactants can be reasonably considered, while, as a first approximation, we can consider thermodynamic parameters for bulk Sb_2O_4 that is the stable oxide at the treatment temperature (more than $600°$C) [167] and is compatible with the previously reported XPS analysis.
The thermodynamically evaluated reaction is:

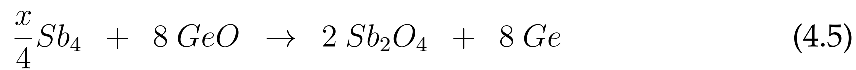

$$\frac{x}{4}Sb_4 \;+\; 8\,GeO \;\rightarrow\; 2\,Sb_2O_4 \;+\; 8\,Ge \tag{4.5}$$

The Ge is considered in its standard element state and for this reason the $\Delta G_f(Ge) = 0$ at different temperatures.
The resulting ΔG_r is negative and equal to $-364 KJ\,mol^{-1}$ at $527°$C and the values remain negative in the explored process thermal window.

A further support to the hypothesis of a GeO-induced reaction is that the Sb monolayer does not form on the Si surface as revealed by RBS analyses, as previously shown. Si native surface is characterised by a stable SiO_2 oxide. If a reaction between Sb_4 and silicon dioxide to produce Sb_2O_4 is supposed, ΔG_r turns out to be positive with a value higher than $+1700\ KJ\ mol^{-1}$ between 300-727 K, ruling out the possibility of a similar reaction on Si and explaining the peculiar behaviour of Ge native surface.
This value was obtained by calculating the ΔG_r of the supposed following reaction:

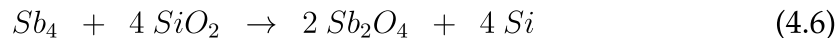

$$Sb_4 \;+\; 4\,SiO_2 \;\rightarrow\; 2\,Sb_2O_4 \;+\; 4\,Si \tag{4.6}$$

The above calculations support the feasibility of a red-ox reaction between Sb_4 and GeO, with a formation of a stable Sb oxidised surface phase, although it does not take into account the surface interaction of the final product, which is expected to play a significant role. In fact, the effective structure is a self-limiting mono-layer (not a bulk oxide) bonded to the Ge surface.
As a matter of fact, it can be argued that the limiting factor for the formation of a bulk Sb_2O_4 over-layer is the finite availability of O that comes from GeO as an oxidising agent. In more detail, considering the phase diagram of Sb-O system [168], one can see that Sb_2O_4 is stable above about $600°$C only if O molar fraction

is above 4% (or more at higher temperature). After a first transient during GeO sublimation, GeO concentration decreases and the remaining Sb, which grows as a stable metallic layer below 600°C, becomes unstable being in a liquid state [168]. This last fact is also strongly related and explain the fact that more than 1 ML accumulate below 600°C.

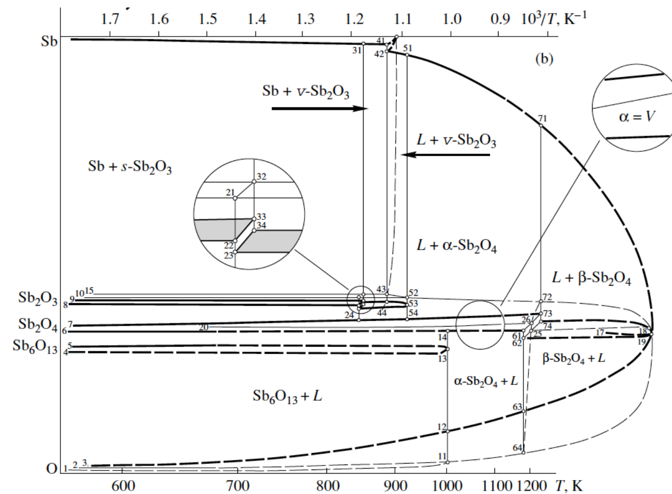

Figure 4.17. Temperature-composition (T-x) section of the p-T-x complete phase diagram of the Sb-O system. Graph reported form literature data in ref. [168]

Another question should be why the amount of Sb corresponds exactly to a Ge monolayer independently of the treatment conditions above 600°C. This can be explained only considering that a specific interaction with the finite amount of Ge surface sites plays a role. In other words, the stable phase that really forms is a surface ternary compound with Ge-O-Sb bonds linking the Sb monolayer with the Ge substrate or GeO_x interlayer. This surface phase was not previously investigated and it could deserve further investigations by theoretical approaches to confirm its stability and structure.

4.4 Sb Monolayer Diffusion

In this section, the Sb ML behaviour to act as a source of dopant is tested: after a diffusion characterisation of Sb diffusion, as a consequence of Sb ML deposition, pre-formed Sb ML are thermally treated by means of equilibrium and out-of-equilibrium diffusion techniques. Diffusion results and diffusion modelling are provided in the next pages.

4.4.1 Sb thermal diffusion

The samples with the monolayer functionalization are analysed with Secondary Ion Mass Spectrometry to verify the Sb in-diffusion in Ge during the deposition process and also after subsequent annealing. In figure 4.18 different SIMS profile are shown. Violet star points are a SIMS profiles of a 615°C 20 s Sb ML sample

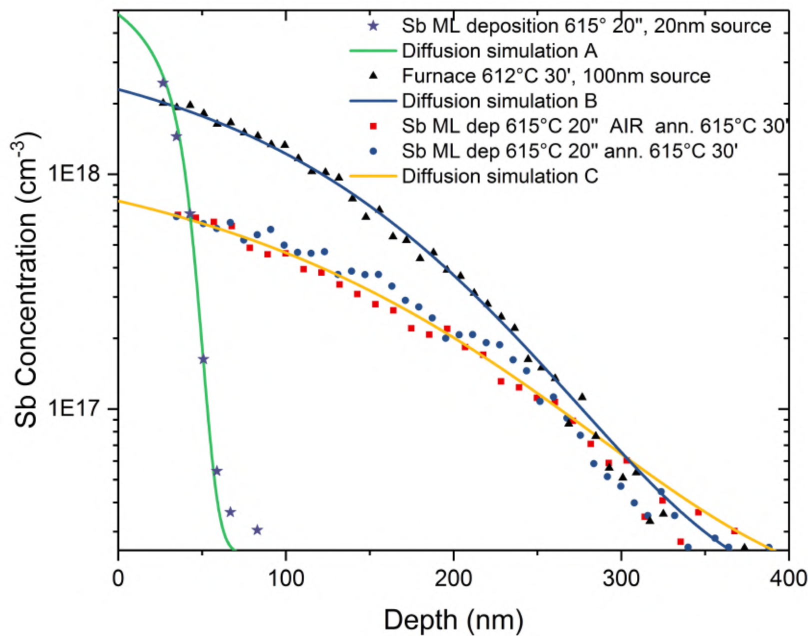

Figure 4.18. SIMS profile of Sb in Ge of different samples. Violet star points: 615°C 20 s Sb ML formed in RTA. Black triangles: Sb ML deposited with 612°C for 30 minutes by using a 100 nm Sb on Si source. Blue circles: Sb ML deposited via RTA 615°C 20 s and annealed at 615°C for 30 minutes without any air exposure between the two processes. Red squares: same as the previous sample but with an air exposure between the deposition and the diffusion annealing. All these data are simulated with a diffusion model as described in the text; continuous lines reported in the graph are the best simulation results.

formed in RTA, while black triangles are a Sb ML sample deposited with 612°C for 30 minutes by using a 100 nm Sb on Si source. This two samples highlight the Sb diffusion in Ge during the deposition processes. The other SIMS profiles, reported in blue circles and red squares are referred to samples that underwent a subsequent annealing process after the formation. Also in these cases, antimony diffused in Ge.

In order to understand more deeply the Sb diffusion process and characterise the Sb ML as a diffusion source, SIMS profiles are simulated with a diffusion model,

based on a well assessed literature model, based on extrinsic diffusivity (as previously described in methods chapter).
The time evolution of Sb concentration c in Ge can be calculated by a dilute species transport equation:

$$\frac{\partial c}{\partial t} + \nabla(-D_{eff}\nabla c) = 0 \quad (4.7)$$

where D_{eff} is the diffusion coefficient. According to the literature, the D_{eff} for n-type dopants in Ge depends on carrier concentration n [51, 52] as follow:

$$D_{eff} = D_{Sb}^{in}\left(\frac{n(x)}{n_i}\right)^2 f \quad (4.8)$$

where D_{Sb}^{in} is the Sb diffusivity for Ge intrinsic doping, and $(n/n_i)^2$ represents the effect of charge defect-mediated diffusion in extrinsic conditions, as described in the first chapter of the thesis, the $n(x)$ is the local electron concentration determined by the doping concentration, while n_i is the intrinsic carrier concentration. Intrinsic diffusion data for Sb are available in ref [50]. The f factor, accounts for the effect of the charge species drift in the junction field, as reported in literature [159]:

$$f = \frac{2n(x)}{\sqrt{c^2 + 4n_i^2}} \quad (4.9)$$

By numerically solving these set of equations, the Sb diffusion can be simulated both in intrinsic and extrinsic conditions. By applying this model to all the collected data reported in figure 4.18, all the Sb chemical profiles are properly simulated, within a T $\pm$ $10°$C temperature and t $\pm$ 2s time uncertainties, respectively.
It is worth to note that the model closely fits the data after assuming that all the Sb is electrically active, i.e. that all the Sb in the bulk contributes to the carrier concentration n. The perfect agreement between data and simulations is a clear evidence that Sb diffuses into the bulk in a reduced state, jumping from substitutional state by interaction with vacancies present in an equilibrium concentration, as assumed in the diffusion model and previously reported in literature [52, 169]. Therefore, the oxidation state of Sb inside Ge is strongly reduced with respect to the oxidised state of the Sb surface ML. This fact rules out any possible effect of O contamination on the Sb diffusion and the possibility of Sb-O co-diffusion into the bulk. A direct measurements of activation by means of electrical measurements was not possible due to the relatively small amount of activated dopant.

It is interesting to note that only a fraction of the total Sb dose at the surface diffuses into the bulk: indeed, by integrating the SIMS chemical profiles, doses of

$1.2\ 10^{13}\ cm^{-2}$ for the RTA 20 s $615°$C sample and $1.8\ 10^{13}\ cm^{-2}$ for the furnace 30 minutes $612°$C enter in the Ge bulk, while the measured surface Sb dose is about $6.0\ 10^{14}\ cm^{-2}$ for both samples, according to c-RBS measurements previously reported.
In order to understand the role played by the oxidised Sb surface ML in the bulk Sb injection, we tried to further anneal the RTA 20 s $615°$C sample with a second process for 30 minutes at $615°$C. The resulting chemical profile is also reported in figure 4.18 (red squares). The diffusion profile can be perfectly simulated by assuming that the Sb profile after 20 s (violet star points, in the same figure) further diffuses for 30 minutes at equilibrium without any Sb loss or injection through the surface. As a matter of fact, the Sb dose in this sample is $1.2\ 10^{13}\ cm^{-2}$ perfectly comparable with the first annealing step, thus demonstrating that no Sb in-diffusion contribution comes from the oxidised Sb surface monolayer, which appears to be rather a diffusion barrier to Sb out-diffusion.
We can suppose that the diffusing Sb under these standard annealing procedures is the Sb in the reduced chemical state, that appears below the surface during the formation of the monolayer and is revealed by XPS as the small metallic Sb peak shown in XPS results e analysed in figure 4.15.

In figure 4.18, it can be noticed that the single step 30 minutes annealed sample (shown with black points) has a higher Sb concentration with respect to the two steps sample (shown with red points). The differences between the two samples are the air exposure between the two annealing treatments for the two-step sample and the longer Sb gas exposure during the annealing for the single step sample (the latter was produced with a 100 nm source instead of a 20 nm used for the two steps). In order to understand the reason of this difference, the two steps annealing sample is repeated by performing the second annealing without any air exposure. This can be done by cleaning the RTP oven by N_2 flux and vacuum cycles immediately after the deposition process, keeping the oven closed from the beginning to the end of processes. Taking into account that after the first step the 20 nm source is completely exhausted (see previous RBS results), the presence of Sb gas in the chamber during the second annealing is absolutely ruled out.
The result is represented by blue circles in figure 4.18: this SIMS profile is identical to the two steps annealing with air exposure (red data). This demonstrates that air exposure does not influence the process and this is compatible with the idea that the diffusing Sb is already embedded into Ge after 20 s.
We can conclude that the differences between black data with red and blue data

are due to a different Sb gas exposure time. Indeed, the black data sample has been exposed to Sb gas for a longer time with respect to the other samples due to the higher Sb amount in the source and this stimulates the Sb injection into the bulk at a higher concentration.

The Sb fraction that diffuses inside Ge has been evaluated only at 612°C: but what did happen at higher temperature? In order to answer this question, we measured the diffusion of Sb into the bulk when the formation processes occur at higher temperature. In figure 4.19, SIMS data of samples treated for 30 minutes with a 100 nm source between 612°C and 789°C are shown.

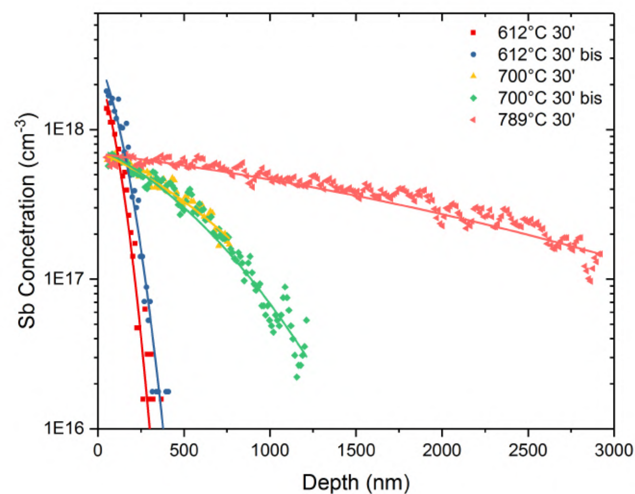

Figure 4.19. SIMS profile of Sb in Ge are reported with coloured dots: each profile is relative to a sample deposited at the indicated temperature for 30 minutes using a tubular furnace. Continuous line are the results of erfc fitting, based on literature intrinsic diffusion model, plotted as a reading guide for the reader.

Also in this case, diffusion profiles trend can be reproduced with the above described equilibrium model. SIMS allows to evaluate by integration the total dose of antimony entering the bulk that is reported as black squares in figure 4.20. In the same figure we report the surface doses as measured by RBS on the same samples. It is worth to note that the diffused Sb enters at a low concentration inside Ge, such as to be no longer detectable by RBS technique. At the same time, as we explained, the SIMS technique is completely blind to the surface one. Therefore, surface Sb doses by RBS and bulk doses by SIMS are complementary information. As can be seen, there are two clear and complementary trends of SIMS and RBS doses: at higher temperature, the Sb amount detected by RBS

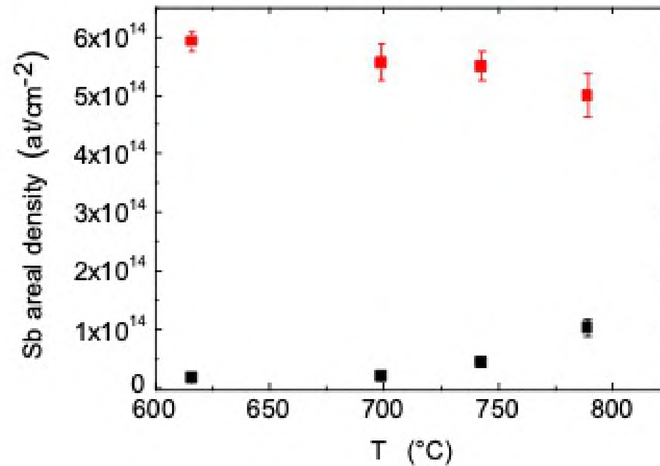

Figure 4.20. Red points are referred to RBS doses of Sb deposited on Ge (100) at different deposition process temperatures (furnace depositions, 30 minutes), while in black are reported SIMS integrals (and so the diffused doses) of the same samples at different process temperatures.

decreases, while the diffused dose increases. Thanks to this fact, it is possible to understand that at higher temperature, the fraction of mobile Sb injected in Ge is higher than 4%, as detected and estimated with XPS technique at $612°$C, emphasising that the Sb availability can slightly increase with the temperature.

In summary, standard diffusion annealing showed that only a fraction of the deposited Sb is able to diffuse into Ge. This diffusion still occurs during short ML formation processes, such as 20 s long treatments.

The diffusion data are well reproduced by equilibrium concentration diffusion of fully active Sb and the fast diffusion in a first short period can be explained by the non-linear term in diffusivity that results to be higher at the higher concentration at the beginning of the process. The diffusing Sb fraction detected and quantified by SIMS analysis, appears to be a re-distribution of the reduced Sb fraction, incorporated in Ge during the deposition. No evidence of Sb release from the oxidised monolayer was found under the investigated equilibrium thermal processes, thus suggesting its possible role as an out-diffusion barrier.

It could be interesting to further investigate very short times and higher temperatures gas exposure by a closed source, developing a special experimental set-up for this aim. This could lead to the formation of shallow junctions at higher concentration and with shorter length, possibly aided by the slight increase of Sb available for diffusion at higher temperature, even though the low total amount of injected Sb seems to be impossible to overcome simply by playing with tem-

perature.
In the following section, a different non-equilibrium diffusion technique is applied to Sb ML samples: the technique is the Pulsed Laser Melting (PLM).

4.4.2 Sb diffusion by PLM

Here we report the application of non-equilibrium annealing process to Sb ML functionalized sample, followed by the analysis of the resulting diffusion and dopant activation in Ge. As described in the methods chapter, the Pulsed Laser Melting (PLM) technique promotes impurities redistribution exploiting the high diffusion coefficient in liquid phase: a high energy density laser pulse melts the Ge surface (about 150 nm thick) and consequently Sb can diffuse in liquid Ge. After a certain delay, Ge recrystallises epitaxially from the liquid/solid interface and Sb is then embedded in Ge [83].
In our case, a Sb ML, formed with RTP 20 s $600°$C, is treated with PLM technique. In figure 4.21 the SIMS profile of Sb diffused in Ge after a PLM 1 pulse treatment is reported.

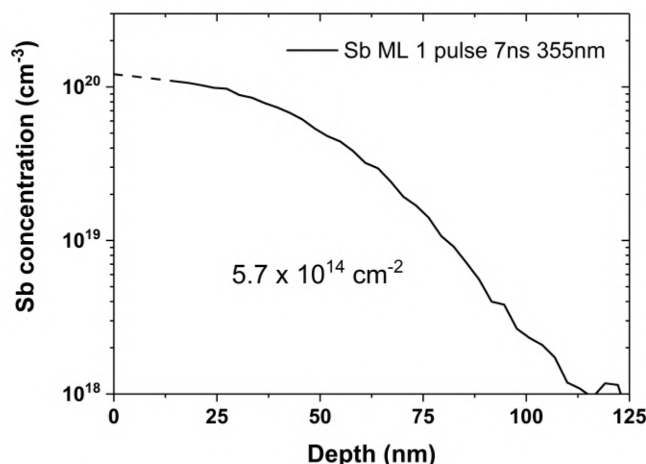

Figure 4.21. SIMS chemical profile of Sb ML diffused with PLM technique: 1 pulse of 7 ns at 355 nm photon wavelength. The line is truncated near the surface since in this region the SIMS signal can be affected by surface effect. The total dose, obtained by integrating the SIMS profile, is reported in the figure.

As can be clearly seen, only after a 1 PLM laser pulse, the Sb diffuses in Ge matrix, showing a typical diffusion profile of a PLM treated samples [41]. It is clearly evident that a high concentration of Sb in Ge is reached, with a surface concentration of $1.2\ 10^{20}\ cm^{-3}$, well above the maximum equilibrium solid

solubility ($1.3\ 10^{19}\ cm^{-3}$) of Sb in Ge [154] and previous results presented in this work (figure 4.18).
The PLM process at the energy density of ca. $400\ mJ/cm^2$ is expected to induce melting for about 30 ns and up to a depth of about 150 nm.[2] This is fully compatible with our result, since the diffused Sb profile is shallower than 150 nm and does not show any shoulder typical of diffusion limited by the maximum melt-depth. Thus, the Sb diffusion behaviour revealed by the data of this paper points to a limitation induced by the Ge liquid diffusivity rather than the maximum melt-depth.
An estimation of the Sb diffusivity can be done, by considering the calculated melting time of 30 ns and the observed profile depth at half maximum, by considering $L_{diff} = \sqrt{2Dt}$. This estimation gives an order of magnitude of $10^{-4}\ cm^2 s^{-1}$, which is in agreement with the values reported in literature for the diffusivity of dopants in liquid Ge [92].
By integrating the SIMS profile, it can be obtained that the areal density of Sb diffused in Ge is $5.7\ 10^{14}\ cm^{-2}$, that is in agreement, inside the experimental errors with the value of the surface Sb amount measured in the source by RBS, thus demonstrating that all the available Sb diffused with PLM technique. This is a crucial point: while standard annealing techniques exploit only a small fraction of the deposited Sb, being not able to break the Sb-O bond, PLM seems to succeed in chemically reducing Sb. In order to fully demonstrate this, it should be demonstrated that Sb is substitutionally bonded to Ge matrix i.e. it should be electrically active as a dopant.

The quality of the germanium crystallinity after the PLM process is evaluated by HR-XRD (High Resolution XRD) analysis. In figure 4.22, the scattering intensities are plotted in the reciprocal space area around the substrate Ge (004)symmetric reflection. Reciprocal space coordinate relative to the main peak are plotted. The map shows an elongation of the diffraction peak along the vertical direction in the reciprocal space (the truncation rod), while no significant lateral spreading is revealed. These data agree with an epitaxial regrow of the melted Ge layer, with a very low concentration of defects, that would have generated a horizontal spreading of the diffraction peak. In figure 4.23 a rocking curve of the same sample is shown; intensities are obtained by averaging the map data along omega scan directions. The hump present on the right of the main peak is

[2](based on LIMP simulation - the Harvard simulation software package based on heat flow calculation calibrated on Ge physical and optical literature data

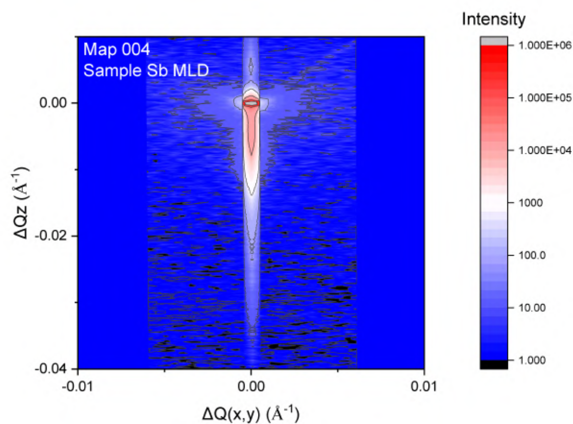

Figure 4.22. HRXDR reciprocal space maps around Ge (004) reflection of a sample Ge with a Sb ML deposition and a single pulse PLM treatment of about $400mJ/cm^2$. Reciprocal space coordinates are centered into Ge (004) substrate peak.

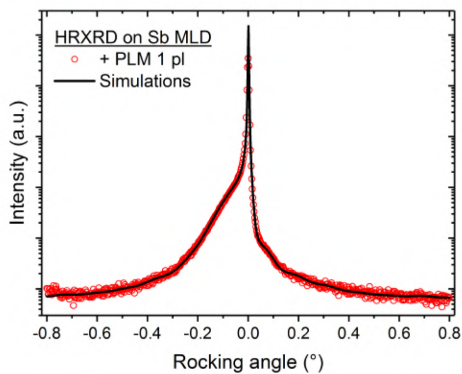

Figure 4.23. HRXRD rocking curve of Sb ML deposition and a single pulse PLM treatment around $400mJ/cm^2$. Black curve is a HRXRD simulation of fully substitutional Sb atoms in crystal Ge matrix, according to SIMS diffusion profile.

a clear sign of compressive strain into the surface doped layer, as expected for Sb doping in Ge matrix. The figure reports a dynamical HRXRD simulation in which a perfect Ge crystal is simulated as bulk material, and near the surface, fully substitutional Sb atoms are added to Ge crystal, according to SIMS chemical profile, as previously reported. More in detail, SIMS concentration profile is transformed into a lattice deformation profile according to ref. [170]. Thanks to the very good agreement of the simulation with experimental data, it is possible to conclude that the melted Ge layer epitaxially regrow, keeping a perfect Ge crystallinity and englobed Sb atoms in substitutional position.

In order to verify the electrical properties of the doped layer, van der Pauw-Hall measurements were conducted on the processed sample. This technique, as reported in the methods chapter, allows to determine the Hall Coefficient that depends on the carriers sign and areal density [117]. The Hall Coefficient measured for this sample is $-1.45\ 10^{4}\ cm^{2}C^{-1}$. Considering a full electrical activation of the diffused Sb (i.e. each Sb atom produces one electron carrier), Hall coefficient can be also calculated by exploiting the procedure reported in ref [171] and [172], thus resulting to be $-1.53\ 10^{4}\ cm^{2}C^{-1}$. On the basis of the very good agreement between measured and calculated values, we can conclude that all the Sb is fully electrically active within the experimental errors. This datum is in very good agreement with HRXRD data and simulation, since electrically active Sb is expected to be in substitutional lattice position.
These interesting results show that the PLM technique is able to promote the diffusion of the whole Sb ML, by reducing the oxidised Sb ML fraction without any Sb loss during the process. The full electrical activation of the layer demonstrates that no detrimental effect of O present in the ML structure occurs in the junction. This could be indeed expected taking into account the small O amount in the ML structure (only 3 $\AA$ thick) as compared to that in the native GeOx (in the order of 20 $\AA$).

This experiment shows that Sb ML acts as a dopant source also for PLM technique and a fully electrical layer can be easily generated, presenting a surface concentration of $1.2\ 10^{20}\ cm^{-3}$. The entire Sb ML amount diffused in Ge, thus confirming that a reduction process occurs during the treatment.

4.5 Conclusions

In this chapter, a new Ge surface phenomena, involving a Sb ML formation on Ge (001), has been described. A wide range of formation parameters has been examined such as time, temperature. Sb displays an extremely fast and self-limiting ML formation over a wide thermal window, accompanied by a very good areal uniformity. Thanks to XPS analysis, the Sb ML chemical status has been characterised, revealing an oxidised Sb surface status, with a small amount of metallic Sb probably placed in the first Ge surface layers. In the light of all experimental evidences, a chemisorption reaction has been proposed, and supported by some thermodynamic considerations. The self-limiting behaviour of the entire process is explained by considering the stability of Sb-O system under variable oxidising agent concentrations and suggesting a specific role of the surface in the formation of a Ge-O-Sb surface phase.
SIMS characterisation on functionalized Ge surfaces detected the presence of an antimony fraction able to diffuse and dope Ge under equilibrium thermal conditions. The diffusion of Sb can be modelled with the well assessed equilibrium diffusion of Sb, unveiling a Sb diffusing in a substitutional (chemically reduced) state in the Ge matrix. Thanks to these tests, it was discovered that only the reduced Sb is able to diffuse under standard diffusion process, while the surface oxidised Sb ML fraction is stable and probably acts as an out-diffusion barrier.
Finally, an out-equilibrium process exploiting the innovative Sb source was demonstrated to reach a Sb n-doping of Ge with a 100% electrical activation and a very high concentration by using all the oxidised Sb ML as a dopant source and presenting a very good Ge crystallinity by an epitaxial Ge regrowth, as showed by HRXRD analysis. This imply that the process is able to reduce the oxidised Sb fraction, conversely to standard annealing processes. A further laser parameter optimisation, such as the use of a different laser energy density, should reduce the junction thickness and consequently raise the Sb concentration in Ge. The creation of shallow junctions in germanium using PLM method was already proved in literature, thanks to the fact that by tuning the energy density of laser, the maximum melt depth can be finely modified [84]. Therefore, the result shown in this work can be improved, reducing the junction thickness (down to the as deposited one) and consequently increasing the Sb concentration.

As compared to classical ML doping techniques, this new promising deposition approach features several remarkable strengths, such as:

- eliminating of the need for complex chemical reactions, eventually required

for the synthesis of the Sb molecular precursor and its functionalization with a proper functional group;

- avoidance of the incorporation of any residual molecular fragments that can act as contaminants in germanium;
- possibility of performing a one-step process by deposition and diffusion of Sb at the same time;
- seconds-time scale Sb ML formation;
- thermal removal of the native germanium oxide by sublimation (avoiding a strong acid dissolution process) and a subsequent stabilisation of the surface by Sb itself.

Conclusions

The aim of this thesis was to exploit innovative methods for germanium doping. In recent years, germanium has been a material brought back to light by scientific research in various fields: its excellent electrical properties make Ge again suitable for nano-electronics and high-efficiency photovoltaic cells. But nowadays the Ge applications in plasmonics and laser field is also possible, thanks to recent scientific discoveries: the structure of the Ge band can be modified through the use of hyper doping and strain, and as a consequence, direct gap transitions in Ge are now possible. For all these applications, it is fundamental to achieve high levels of dopant incorporation and electrical activation. Since the use of nano-structured devices is today a reality, this requires new doping technologies to be compatible with nano-structured geometries and at the same time to be able to generate thin or shallow junctions with a good local control of the doping amount.
The development of such demanding tasks is extremely complicated and it requires to develop a new Ge doping strategies. During the last years, the Monolayer Doping technique (MLD) has been successfully tested on Si to respond to similar requests in Si research fields. In this work, we try to apply the MLD to germanium, by executing experiments focused on the understating of ML formation mechanisms and doping processes on planar surfaces. We focused on n-type doping, using phosphorus and antimony surface dopant sources, starting from three different phosphorus molecular precursors (DPP as representatives for phosphonate, ODPA for phosphonic acids, ADPP for phosphine) and using a gas phase source for the antimony ML formation. In both cases, a strong surface affinity between precursors and Ge surface was revealed, showing the formation of -O-Ge chemical bond as a consequence of the adsorption processe.

Surface quantitative analysis were performed on adsorbed precursors by the use of NRA and AR-XPS in phosphorus ML cases, showing the reproducibility of the adsorption technique and, in combination with chemical rinsing, allowed us to determine the presence of physisorbed fraction for DPP and ODPA precursors.

Moreover, thanks to the chemically sensitive AR-XPS technique, a quantification of germanium oxides was possible, and a correlation between the oxidation and the adsorbed P amount was clearly shown, thanks to the comparison between standard and dry deposition processes. By using DRIFTS and EXAFS measurements, the adsorption reactions have been deeply investigated: by crossing all the acquired data, we were able to suppose the chemisorbed molecular structures, highlighting the surface reactivity between the precursor and the germanium oxide surface. An unexpected chemisorption of ADPP via its oxidation instead of hydrogermilation reaction was revealed, and a self limiting formation of 1 ML occurs independently on the fine control of atmospheric conditions.
The antimony monolayer was characterised with c-RBS and AR-XPS analysis revealing a perfectly self-limiting behaviour to 1 ML with a deposition process with T $> 600°$C, presenting an Sb oxidised status (III-V), bonded with the surface with Sb-O-Ge functionality. Interesting, a small metallic Sb fraction (about 4% of ML) is enbadded in the Ge matrix during the deposition, and the deposition process promote a germanium surface oxide removal via GeO sublimation. A chemisorption reaction was proposed and justified with some considerations regarding thermodynamics and the Sb-O phase diagram.

The capability of dopant release for P and Sb monolayers under thermal treatment were tested. Both the oxidized MLs do not act as a source of dopant with standard thermal processes (in case of Sb only the metallic fraction acts as a dopant source). These thermal processes were ranged up to 780 - $825°$C, that is close to the maximum Ge treatment process before its surface degradation. In the light of these experimental evidences and literature results on different substrates, it was suggested that the lack of dopant release is due to P-O-Ge and Sb-O-Ge high thermal stability. The use of oxygen free and reduced phosphorus precursor (ADPP) did not avoid the formation of such stable functionality, even in dry box conditions. The high tendency of germanium to be oxidised and also its high reactivity, given by the presence of -OH terminal groups for example, make very challenging the task to obtain oxygen free germanium surface chemisorption.

The use of an out of equilibrium technique, such as the Pulsed Laser Melting (PLM) technique, has given interesting results. The PLM technique promotes the phosphorus and the antimony in-diffusion from surface monolayer sources, by promoting the release of P and Sb species that diffuse in the liquid Ge. By electrical measurements, the electrical activation of P and Sb in Ge were tested, demonstrating that the laser promotes the reduction of initial source species

from an oxide state (P in the molecules III, I and Sb in surface oxide III,V) to I form, typically the active n-type dopant in Ge.
In the P MLD case, the adsorbed DPP and ODPA molecules induce diffusion of P that is not laterally uniform after the process, probably due to the fact that their physisorbed fraction is not homogeneously distributed on the surface, while ADPP precursor (that doesn't show any physisorbed fraction after the rinsing process) forms a perfectly homogenous layer, with a total electrical activation tested after PLM. In the antimony case, the Sb ML gives a perfectly homogenous doped layer, with a 100 % activation, since also in this case only a chemisorbed layer is formed as a consequence of surface reactivity.

Some interesting perspectives can be exploited in the future starting from the results of this thesis.
First of all, we demonstrated the feasibility of a robust methodological approach to the understanding of this particular field of surface science oriented to doping. The integration of surface science techniques such as XPS and Refl-EXAFS with ion beam analyses allows to reach a deep and quantitative understanding of the absorption mechanism. This same approach can be exploited also for other precursors, for example investigating the p-type MLD on Ge or n- and p- type doping on other semiconductors.
While the application of the methods described has to be demonstrated for nanoelectronics, since the use of laser on nano-structures has to be carefully evaluated, the method is very interesting due to the high doping level reached with relatively low cost methods. The use of chemical processes and laser can overcome the low doping that can be obtained by equilibrium doping techniques or limit the cost with respect to ion implantation in case of large area production such as in photovoltaic or high purity germanium gamma detectors.
In both this last cases an interesting aspect is related not only to the doping but also to the passivation of surfaces. Further experiment are ongoing to evaluate if highly stable phosphorous monolayer can have a role in electrical passivation of Ge surface. Moreover, experiments involving the use of our new PLM ML doping joined to strain control by alloying have started, in collaboration with international institutes i.e. Tyndall Institute in Ireland. The aim of these studies are the obtainment of high doping - high strain condition to easily produce optoelectronics devices.

Bibliography

[1] H.C.A. Winkler. In: *J. Prak. Chemie* 34.177 (1886).

[2] John Bardeen and Walter Houser Brattain. “Physical principles involved in transistor action”. In: *Physical Review* 75.8 (1949), p. 1208.

[3] K Prabhakaran and T Ogino. “Oxidation of Ge (100) and Ge (111) surfaces: an UPS and XPS study”. In: *Surface Science* 325.3 (1995), pp. 263–271.

[4] Martin M Atalla, Eileen Tannenbaum, and EJ Scheibner. “Stabilization of silicon surfaces by thermally grown oxides”. In: *Bell System Technical Journal* 38.3 (1959), pp. 749–783.

[5] Cor Claeys and Eddy Simoen. *Germanium-based technologies: from materials to devices*. elsevier, 2011.

[6] Ravi Pillarisetty. “Academic and industry research progress in germanium nanodevices”. In: *Nature* 479.7373 (2011), pp. 324–328. ISSN: 0028-0836. DOI: 10.1038/nature10678. URL: http://www.nature.com/doifinder/10.1038/nature10678.

[7] Mitchell Waldrop. “More then Moore”. In: *Nature* 530.11. February (2016), p. 145. ISSN: 0028-0836. DOI: 10.1038/530144a. arXiv: Nature, 2016, 530(7589):144..

[8] Gordon E Moore et al. *Cramming more components onto integrated circuits*. 1965.

[9] T H E Irds, I S Devised, Intended For, Technology Assessment, I S Without, et al. *International Roadmap for Devices and Systems ed 2017*. Ed. by IEEE. 2017.

[10] YH Xie, Don Monroe, EA Fitzgerald, PJ Silverman, FA Thiel, et al. “Very high mobility two-dimensional hole gas in Si/Ge x Si1- x/Ge structures grown by molecular beam epitaxy”. In: *Applied physics letters* 63.16 (1993), pp. 2263–2264.

[11] Duygu Kuzum, Tejas Krishnamohan, Abhijit J Pethe, Ali K Okyay, Yasuhiro Oshima, et al. “Ge-interface engineering with ozone oxidation for low interface-state density”. In: *IEEE Electron Device Letters* 29.4 (2008), pp. 328–330.

[12] Duygu Kuzum, Abhijit J Pethe, Tejas Krishnamohan, Yasuhiro Oshima, Yun Sun, et al. "Interface-engineered Ge (100) and (111), N-and P-FETs with high mobility". In: *2007 IEEE International Electron Devices Meeting*. IEEE. 2007, pp. 723–726.

[13] Jerome Mitard, Brice De Jaeger, FE Leys, Geert Hellings, Koen Martens, et al. In: *2008 IEEE International Electron Devices Meeting*. IEEE. 2008, pp. 1–4.

[14] Gareth Nicholas, TJ Grasby, DJF Fulgoni, CS Beer, J Parsons, et al. In: *IEEE Electron Device Letters* 28.9 (2007), pp. 825–827.

[15] Moustafa El Kurdi, Guy Fishman, Bastien Sauvage, and Philippe Boucaud. "Band structure and optical gain of tensile-strained germanium based on a 30 band kp formalism". In: *Journal of Applied Physics* 107.1 (2010). ISSN: 00218979. DOI: 10.1063/1.3279307.

[16] Jose R. Sánchez-Pérez, Cicek Boztug, Feng Chen, Faisal F. Sudradjat, Deborah M. Paskiewicz, et al. "Direct-bandgap light-emitting germanium in tensilely strained nanomembranes". In: *Proceedings of the National Academy of Sciences of the United States of America* 108.47 (2011), pp. 18893–18898. ISSN: 00278424. DOI: 10.1073/pnas.1107968108.

[17] Jifeng Liu, Xiaochen Sun, Dong Pan, Xiaoxin Wang, Lionel C Kimerling, et al. "Tensile-strained , n-type Ge as a gain medium for monolithic laser integration on Si". In: *Optics Express* 15.18 (2007), pp. 2442–2444.

[18] Zhiping Zhou, Bing Yin, and Jurgen Michel. "On-chip light sources for silicon photonics". In: *Light: Science and Applications* 4.11 (2015), pp. 1–13. ISSN: 20477538. DOI: 10.1038/lsa.2015.131.

[19] S. Wirths, R. Geiger, N. Von Den Driesch, G. Mussler, T. Stoica, et al. "Lasing in direct-bandgap GeSn alloy grown on Si". In: *Nature Photonics* 9.2 (2015), pp. 88–92. ISSN: 17494893. DOI: 10.1038/nphoton.2014.321.

[20] Daniela Stange, Nils Von Den Driesch, Thomas Zabel, Francesco Armand-Pilon, Denis Rainko, et al. "GeSn/SiGeSn Heterostructure and Multi Quantum Well Lasers". In: *ACS Photonics* 5.11 (2018), pp. 4628–4636. ISSN: 23304022. DOI: 10.1021/acsphotonics.8b01116.

[21] S Biswas, J Doherty, and Justin D. Holmes. "Non-equilibrium induction of tin in germanium: towards direct bandgap Ge1-xSnx nanowires". In: *Nature Communications* 7.11405 (2015). ISSN: 13490540. DOI: 10.1038/pj.2016.37.

[22] Adrian Kitai. *Principles of Solar Cells, LEDs and Diodes: The role of the PN junction*. John Wiley & Sons, 2011.

[23] Wolfgang Guter, Jan Schöne, Simon P Philipps, Marc Steiner, Gerald Siefer, et al. "Current-matched triple-junction solar cell reaching 41.1% conversion efficiency under concentrated sunlight". In: *Applied Physics Letters* 94.22 (2009), p. 223504.

[24] RR King, DC Law, KM Edmondson, CM Fetzer, GS Kinsey, et al. "40% efficient metamorphic GaInP/ GaInAs/ Ge multijunction solar cells". In: *Applied physics letters* 90.18 (2007), p. 183516.

[25] L Barrutia, I Garcia, E Barrigón, M Ochoa, I Lombardero, et al. "Development of the Lattice Matched GaInP/GaInAs/Ge Triple Junction Solar Cell with an Efficiency Over 40%". In: *2018 Spanish Conference on Electron Devices (CDE)*. IEEE. 2018, pp. 1–4.

[26] Youngjo Kim, Nguyen Dinh Lam, Kangho Kim, Won-Kyu Park, and Jaejin Lee. "Ge nanopillar solar cells epitaxially grown by metalorganic chemical vapor deposition". In: *Scientific Reports* 7 (2017), p. 42693. ISSN: 2045-2322. DOI: 10.1038/srep42693. URL: http://www.nature.com/articles/srep42693.

[27] Martin A Green. "Thin-film solar cells: review of materials, technologies and commercial status". In: *Journal of Materials Science: Materials in Electronics* 18.1 (2007), pp. 15–19.

[28] Martin A Green, Keith Emery, Yoshihiro Hishikawa, Wilhelm Warta, and Ewan D Dunlop. "Solar cell efficiency tables (Version 45)". In: *Progress in photovoltaics: research and applications* 23.1 (2015), pp. 1–9.

[29] Niels Posthuma, Giovanni Flamand, and Jef Poortmans. *Germanium solar cell and method for the production thereof*. US Patent 7,964,789. 2011.

[30] Niels Posthuma, Giovanni Flamand, Jef Poortmans, and Johan van der Heide. *Germanium solar cell and method for the production thereof*. US Patent 8,664,525. 2014.

[31] Lewis M Fraas, Kenneth R Zanio, and Ronald C Knechtli. *Multijunction gallium aluminum arsenide-gallium arsenide-germanium solar cell and process for fabricating same*. US Patent 4,128,733. 1978.

[32] Horst Kibbel, Ulf Koenig, Johannes Konle, and Hartmut Presting. *Silicon-germanium solar cell having a high power efficiency*. US Patent 6,670,544. 2003.

[33] Lewis M Fraas. *Multilayer photovoltaic solar cell with semiconductor layer at shorting junction interface*. US Patent 4,255,211. 1981.

[34] J. van der Heide, N. E. Posthuma, G. Flamand, W. Geens, and J. Poortmans. "Cost-efficient thermophotovoltaic cells based on germanium substrates". In: *Solar Energy Materials and Solar Cells* 93.10 (2009), pp. 1810–1816. ISSN: 09270248. DOI: 10.1016/j.solmat.2009.06.017. URL: http://dx.doi.org/10.1016/j.solmat.2009.06.017.

[35] J. Van Der Heide, N. E. Posthuma, G. Flamand, and J. Poortmans. "Development of low-cost thermophotovoltaic cells using germanium substrates". In: *AIP Conference Proceedings* 890 (2007), pp. 129–138. ISSN: 0094243X. DOI: 10.1063/1.2711729.

[36] Jara Fernandez. "Development of Crystalline Germanium for Thermophotovoltaics". PhD thesis. Konstanz University, 2010, p. 152.

[37] A. Datas, C. Algora, V. Corregidor, D. Martín, A. W. Bett, et al. "Optimization of germanium cell arrays in tungsten emitter-based solar TPV systems". In: *AIP Conference Proceedings* 890.January 2014 (2007), pp. 227–237. ISSN: 0094243X. DOI: 10.1063/1.2711740.

[38] J. Eberth and J. Simpson. "From Ge(Li) detectors to gamma-ray tracking arrays-50 years of gamma spectroscopy with germanium detectors". In: *Progress in Particle and Nuclear Physics* 60.2 (2008), pp. 283–337. ISSN: 01466410. DOI: 10.1016/j.ppnp.2007.09.001.

[39] D.R. Napoli, G. Maggioni, S. Carturan, J. Eberth, V. Boldrini, et al. "New Developments in HPGe Detectors for High Resolution Detection". In: *Acta Physica Polonica B* 48.3 (2017), p. 387. ISSN: 0587-4254. DOI: 10.5506/APhysPolB.48.387. URL: http://www.actaphys.uj.edu.pl/findarticle?series=Reg{\&}vol=48{\&}page=387.

[40] Virginia Boldrini. "DEVELOPMENT AND ANALYSIS OF N-TYPE DOPING PROCESSES FOR HIGH PURITY GERMANIUM". PhD thesis. via Marzolo 8, Padova, Italy: PhD in Physics, University of Padova, 2018.

[41] G Maggioni, S Carturan, W Raniero, S Riccetto, F Sgarbossa, et al. "Pulsed laser di ff usion of thin hole-barrier contacts in high purity germanium for gamma radiation detectors". In: *European Physical Journal A* 54.34 (2018). ISSN: 1434-6001. DOI: 10.1140/epja/i2018-12471-0.

[42] Virginia Boldrini, Sara Maria Carturan, Gianluigi Maggioni, Enrico Napolitani, Daniel Ricardo Napoli, et al. "Optimal process parameters for phosphorus spin-on-doping of germanium". In: *Applied Surface Science* 392 (2016), pp. 1173–1180. ISSN: 01694332. DOI: 10.1016/j.apsusc.2016.09.134. URL: http://linkinghub.elsevier.com/retrieve/pii/S0169433216320153.

[43] V. Boldrini, G. Maggioni, S. Carturan, W. Raniero, F. Sgarbossa, et al. "Characterization and modeling of thermally-induced doping contaminants in high-purity Germanium". In: *Journal of Physics D: Applied Physics* 52.035104 (2019), p. 11. ISSN: 13616463. DOI: 10.1088/1361-6463/aae9c0. arXiv: 1807.00748.

[44] Peter Pichler. *Intrinsic Point Defects, Impurities, and Their Diffusion in Silicon*. Springer Verlag Wien, 2004.

[45] Alfred Seeger and K P Chik. "Diffusion Mechanism and Point Defects in Silicon and Germanium". In: *Physica Status Solidi* 29 (1968), p. 455. ISSN: 03701972. DOI: 10.1002/pssb.19680290202.

[46] Scotten W Jones. "Diffusion in silicon". In: *Journal of Applied Physics* 38.9 (2000), p. 3475. ISSN: 00218979. DOI: 10.1063/1.1710153. URL: http://link.aip.org/link/?JAP/38/3475/1{\&}Agg=doi.

[47] D L Beke and C E Allen. *Diffusion in Semiconductors and Non-metallic Solids*. Vol. 33. 1998. ISBN: 3540609644. URL: https://books.google.se/books?id=gO9LQAAACAAJ.

[48] Paul Martin Fahey, PB Griffin, and JD Plummer. "Point defects and dopant diffusion in silicon". In: *Reviews of modern physics* 61.2 (1989), p. 289.

[49] Hartmut Bracht and Sergej Brotzmann. "Atomic transport in germanium and the mechanism of arsenic diffusion". In: *Materials Science in Semiconductor Processing* 9.4-5 SPEC. ISS. (2006), pp. 471–476. ISSN: 13698001. DOI: 10.1016/j.mssp.2006.08.041.

[50] Sergej Brotzmann and Hartmut Bracht. "Intrinsic and extrinsic diffusion of phosphorus, arsenic, and antimony in germanium". In: *Journal of Applied Physics* 103.3 (2008), p. 033508.

[51] A Chroneos and H Bracht. "Diffusion of n-type dopants in germanium". In: *Applied Physics Reviews* 1.1 (2014), p. 011301.

[52] A Chroneos, H Bracht, RW Grimes, and BP Uberuaga. "Vacancy-mediated dopant diffusion activation enthalpies for germanium". In: *Applied Physics Letters* 92.17 (2008), p. 172103.

[53] SM Hu. "Nonequilibrium point defects and diffusion in silicon". In: *Materials Science and Engineering: R: Reports* 13.3 (1994), pp. 105–192.

[54] J. Vanhellemont and E. Simoen. "Brother Silicon, Sister Germanium". In: *Journal of The Electrochemical Society* 154.7 (2007), H572. ISSN: 00134651. DOI: 10.1149/1.2732221.

[55] S. Mirabella, D. De Salvador, E. Napolitani, E. Bruno, and F. Priolo. "Mechanisms of boron diffusion in silicon and germanium". In: *Journal of Applied Physics* 113.3 (2013). ISSN: 00218979. DOI: 10.1063/1.4763353.

[56] Johnny C Ho, Roie Yerushalmi, Zachery A Jacobson, Zhiyong Fan, Robert L Alley, et al. "Controlled nanoscale doping of semiconductors via molecular monolayers". In: *Nature Materials* 7.1 (2008), pp. 62–67.

[57] John O Connell, Subhajit Biswas, and Ray Duffy. "Chemical approaches for doping nanodevice architectures". In: *Nanotechnology* 27.342002 (2016). ISSN: 0957-4484. DOI: 10.1088/0957-4484/27/34/342002.

[58] V. Chechik, R. M. Crooks, and C J M Stirling. “Reactions and Reactivity in Self-Assembled Monolayers”. In: *Advanced Materials* 12.16 (2000), pp. 1161–1171. ISSN: 0935-9648. DOI: 10.1002/1521-4095(200008)12:16<1161::AID-ADMA1161>3.0.CO;2-C.

[59] Jillian M. Buriak. “Organometallic chemistry on silicon and germanium surfaces”. In: *Chemical Reviews* 102.5 (2002), pp. 1271–1308. ISSN: 00092665. DOI: 10.1021/cr000064s.

[60] Massimo Mastromatteo, Davide De Salvador, Enrico Napolitani, Elisa Arduca, Gabriele Seguini, et al. “Modeling of phosphorus diffusion in silicon oxide and incorporation in silicon nanocrystals”. In: *Journal of Materials Chemistry C* 4.16 (2016), pp. 3531–3539. ISSN: 20507526. DOI: 10.1039/c5tc04287a.

[61] Massimo Mastromatteo. “MECHANISM OF FLUORINE REDISTRIBUTION AND INCORPORATION DURING SOLID PHASE EPITAXIAL REGROWTH OF PRE-AMORPHIZED SILICON”. PhD thesis. Università degli Studi di Padova, Dip. Fisica e Astronomia: Scuola di Dottorato in Scienza e Ing. dei Materiali, 2010.

[62] Janneke Veerbeek and Jurriaan Huskens. “Applications of Monolayer-Functionalized H-Terminated Silicon Surfaces: A Review”. In: *Small Methods* 1.4 (2017), p. 1700072. DOI: 10.1002/smtd.201700072.

[63] Johnny C Ho, Roie Yerushalmi, Gregory Smith, Prashant Majhi, Joseph Bennett, et al. “Wafer-scale, sub-5 nm junction formation by monolayer doping and conventional spike annealing”. In: *Nano letters* 9.2 (2009), pp. 725–730.

[64] Ori Hazut, Arunava Agarwala, Iddo Amit, Thangavel Subramani, Seva Zaidiner, et al. “Contact doping of silicon wafers and nanostructures with phosphine oxide monolayers”. In: *ACS nano* 6.11 (2012), pp. 10311–10318.

[65] Liang Ye, Arántzazu González-Campo, Tibor Kudernac, Rosario Núñez, Michel De Jong, et al. “Monolayer Contact Doping from a Silicon Oxide Source Substrate”. In: *Langmuir* 33.15 (2017), pp. 3635–3638. ISSN: 15205827. DOI: 10.1021/acs.langmuir.7b00157.

[66] Janneke Veerbeek, Liang Ye, Wouter Vijselaar, Tibor Kudernac, Wilfred G. Van Der Wiel, et al. “Highly doped silicon nanowires by monolayer doping”. In: *Nanoscale* 9.8 (2017), pp. 2836–2844. ISSN: 20403372. DOI: 10.1039/c6nr07623h.

[67] Roie Yerushalmi, Johnny C Ho, Zhiyong Fan, and Ali Javey. “Phosphine oxide monolayers on SiO2 surfaces”. In: *Angewandte Chemie* 120.23 (2008), pp. 4512–4514.

[68] Elisa Arduca, Massimo Mastromatteo, Davide De Salvador, Gabriele Seguini, Cristina Lenardi, et al. "Synthesis and characterization of P δ-layer in SiO2 by monolayer doping". In: *Nanotechnology* 27.7 (2016), p. 075606.

[69] Roberto C. Longo, Kyeongjae Cho, Wolf Gero Schmidt, Yves J. Chabal, and Peter Thissen. "Monolayer doping via phosphonic acid grafting on silicon: Microscopic insight from infrared spectroscopy and density functional theory calculations". In: *Advanced Functional Materials* 23.27 (2013), pp. 3471–3477. ISSN: 1616301X. DOI: 10.1002/adfm.201202808.

[70] W. Pim Voorthuijzen, M. Deniz Yilmaz, Wouter J.M. Naber, Jurriaan Huskens, and Wilfred G. Van Der Wiel. "Local doping of silicon using nanoimprint lithography and molecular monolayers". In: *Advanced Materials* 23.11 (2011), pp. 1346–1350. ISSN: 09359648. DOI: 10.1002/adma.201003625.

[71] Liang Ye, Sidharam P. Pujari, Han Zuilhof, Tibor Kudernac, Michel P. De Jong, et al. "Controlling the dopant dose in silicon by mixed-monolayer doping". In: *ACS Applied Materials and Interfaces* 7.5 (2015), pp. 3231–3236. ISSN: 19448252. DOI: 10.1021/am5079368.

[72] Rosaria A. Puglisi, Cristina Garozzo, Corrado Bongiorno, Salvatore Di Franco, Markus Italia, et al. "Molecular doping applied to Si nanowires array based solar cells". In: *Solar Energy Materials and Solar Cells* 132 (2015), pp. 118–122. ISSN: 09270248. DOI: 10.1016/j.solmat.2014.08.040. URL: http://dx.doi.org/10.1016/j.solmat.2014.08.040.

[73] Brenda Long, Yordan M. Georgiev, Nikolay Petkov, Gerard P. McGlacken, John O'Connell, et al. "Organo-arsenic Molecular Layers on Silicon for High-Density Doping". In: *ACS Applied Materials and Interfaces* 7.28 (2015), pp. 15514–15521. ISSN: 19448252. DOI: 10.1021/acsami.5b03768.

[74] Laurent Mathey, Thibault Alphazan, Maxence Valla, Laurent Veyre, Hervé Fontaine, et al. "Functionalization of silica nanoparticles and native silicon oxide with tailored boron-molecular precursors for efficient and predictive p-doping of silicon". In: *Journal of Physical Chemistry C* 119.24 (2015), pp. 13750–13757. ISSN: 19327455. DOI: 10.1021/acs.jpcc.5b03408.

[75] Liang Ye, Michel P. de Jong, Tibor Kudernac, Wilfred G. van der Wiel, and Jurriaan Huskens. "Doping of semiconductors by molecular monolayers: monolayer formation, dopant diffusion and applications". In: *Materials Science in Semiconductor Processing* 57.January (2017), pp. 166–172. ISSN: 13698001. DOI: 10.1016/j.mssp.2016.10.015.

[76] Brenda Long, Giuseppe Alessio Verni, John O'Connell, Justin Holmes, Maryam Shayesteh, et al. "Molecular Layer Doping : Non-destructive Doping of Silicon and Germanium". In: *Ion Implantation Technology (IIT), 2014 20th International Conference on*. Cork, Ireland: IEEE, 2014. ISBN: 9781479952120. DOI: 10.1109/IIT.2014.6939995.

[77] B. Long, G. Alessio Verni, J. O'Connell, M. Shayesteh, A. Gangnaik, et al. "Doping top-down e-beam fabricated germanium nanowires using molecular monolayers". In: *Materials Science in Semiconductor Processing* October (2016). ISSN: 13698001. DOI: 10.1016/j.mssp.2016.10.038. URL: http://linkinghub.elsevier.com/retrieve/pii/S1369800116304735.

[78] Thibault Alphazan, Adrian Diaz Alvarez, Francois Martin, Helen Grampeix, Virginie Enyedi, et al. "Shallow heavily-doped n++ germanium by organo-antimony monolayer doping". In: *ACS Applied Materials & Interfaces* 9 (2017), pp. 20179–20187. ISSN: 1944-8244. DOI: 10.1021/acsami.7b02645. URL: http://pubs.acs.org/doi/abs/10.1021/acsami.7b02645.

[79] S Carturan, G Maggioni, SJ Rezvani, R Gunnella, N Pinto, et al. "Wet chemical treatments of high purity Ge crystals for γ-ray detectors: Surface structure, passivation capabilities and air stability". In: *Materials Chemistry and Physics* 161 (2015), pp. 116–122.

[80] Kibyung Park, Younghwan Lee, Jonghyuck Lee, and Sangwoo Lim. "Oxidation mechanism of hydrogen-terminated Ge (100) surface". In: *Applied Surface Science* 254.15 (2008), pp. 4828–4832.

[81] By William, L Jolly, and Wendell M Latimer. "The Equilibrium Ge + GeO2 = 2 GeO. The Heat of Formation of Germanic". In: *Journal of American Chemical Society* 74.22 (1952), pp. 5757–5758. DOI: 10.1021/ja01142a056.

[82] Yves Pauleau and Jean Claude Remy. "Kinetics of the formation and sublimation of germanium monoxide". In: *Journal of The Less-Common Metals* 42.2 (1975), pp. 199–208. ISSN: 00225088. DOI: 10.1016/0022-5088(75)90005-3.

[83] J Poate and J.W. Mayer. *Laser annealing of semiconductors*. Elsevier, 1982, p. 576. ISBN: 9780323145428.

[84] R. F. Wood, J. R. Kirkpatrick, and G. E. Giles. "Macroscopic theory of pulsed-laser annealing. II. Dopant diffusion and segregation". In: *Physical Review B* 23.10 (1981), pp. 5555–5569. ISSN: 01631829. DOI: 10.1103/PhysRevB.23.5555. arXiv: arXiv:1011.1669v3.

[85] R. F. Wood and G. E. Giles. "Macroscopic theory of pulsed-laser annealing. I. Thermal transport and melting". In: *Physical Review B* 23.6 (1981), pp. 2923–2942.

[86] C.M. Surko, L. Simons, D. H. Auston, J. A. Golovchenko, and R. E. Slusher. "Calculation of the dynamics of surface melting during laser annealing". In: *Applied Physics Letters* 34.10 (1979), pp. 635–637. ISSN: 0003-6951. DOI: 10.1063/1.90619.

[87] Michael O Thompson, GJ Galvin, JW Mayer, PS Peercy, JM Poate, et al. "Melting temperature and explosive crystallization of amorphous silicon during pulsed laser irradiation". In: *Physical Review Letters* 52.26 (1984), p. 2360.

[88] "Macroscopic theory of pulsed-laser annealing. III. Nonequilibrium segregation effects". In: *Physical Review B* 25.4 (1982), pp. 2786–2811. ISSN: 01631829. DOI: 10.1103/PhysRevB.25.2786.

[89] David E. Hoglund, Michael O. Thompson, and Michael J. Aziz. "Experimental test of morphological stability theory for a planar interface during rapid solidification". In: *Physical Review B - Condensed Matter and Materials Physics* 58.1 (1998), pp. 189–199. ISSN: 1550235X. DOI: 10.1103/PhysRevB.58.189.

[90] P. Baeri, S. U. Campisano, G. Foti, and E. Rimini. "A melting model for pulsing-laser annealing of implanted semiconductors". In: *Journal of Applied Physics* 50.2 (1979), pp. 788–797. ISSN: 00218979. DOI: 10.1063/1.326046.

[91] HW Lo and A Compaan. "Raman measurement of lattice temperature during pulsed laser heating of silicon". In: *Physical Review Letters* 44.24 (1980), p. 1604.

[92] R. Milazzo, E. Napolitani, G. Impellizzeri, G. Fisicaro, S. Boninelli, et al. "N-type doping of Ge by As implantation and excimer laser annealing". In: *Journal of Applied Physics* 115.5 (2014). ISSN: 10897550. DOI: 10.1063/1.4863779.

[93] E. Bruno, G. G. Scapellato, G. Bisognin, E. Carria, L. Romano, et al. "High-level incorporation of antimony in germanium by laser annealing". In: *Journal of Applied Physics* 108.12 (2010). ISSN: 00218979. DOI: 10.1063/1.3520671.

[94] J. Frigerio, A. Ballabio, K. Gallacher, V. Gilberti, L. Baldassarre, et al. "Optical properties of highly n-doped germanium obtained by in situ doping and laser annealing". In: *Journal of Physics D: Applied Physics* 50.46 (2017). ISSN: 13616463. DOI: 10.1088/1361-6463/aa8eca.

[95] G. Impellizzeri, E. Napolitani, S. Boninelli, G. Fisicaro, M. Cuscunà, et al. "B-doping in Ge by excimer laser annealing". In: *Journal of Applied Physics* 113.11 (2013). ISSN: 00218979. DOI: 10.1063/1.4795268.

[96] R. Milazzo, M. Linser, D. Scarpa, A. Carnera, A. Andrighetto, et al. "In-diffusion of oxygen in germanium induced by pulsed laser melting". In: *Materials Science in Semiconductor Processing* 88.July (2018), pp. 93–96. ISSN: 13698001. DOI: 10.1016/j.mssp.2018.07.036. URL: https://doi.org/10.1016/j.mssp.2018.07.036.

[97] Nicolet M.A., Chu W.K., and Mayer J.W. *Backscattering Spectometry*. 1978.

[98] Rimini E. and Mayer J.W. *Ion Beam Handbook for Material Analysis*. 1977.

[99] Mayer J.W. and Feldman L.C. *Fundamentals of Modern Surface Analysis*. 1986.

[100] Picraux S.T., Mayer J.W., and Feldman L.C. *Material Analysis by Ion Channeling*. 1982.

[101] Morgan D.V. *Channeling*. 1973.

[102] E. Bagli, D. De Salvador, L. Bacci, F. Sgarbossa, L. Bandiera, et al. "Enhancement of the Inelastic Nuclear Interaction Rate in Crystals via Antichanneling". In: *Physical Review Letters* 123.4 (2019), p. 044801. ISSN: 0031-9007. DOI: 10.1103/PhysRevLett.123.044801. URL: https://link.aps.org/doi/10.1103/PhysRevLett.123.044801.

[103] W A Schier, B K Barnes, G P Couchell, J J Egan, P Harihar, et al. "Spin and parity assignments for 35Cl levels from the 31P(α, p)34S reaction". In: *Nuclear Physics A* 254.1 (1975), pp. 80–92. ISSN: 0375-9474. DOI: https://doi.org/10.1016/0375-9474(75)90583-7.

[104] Williams J.S. and Bird J.R. *Ion Beams for Material Analysis*. 1989.

[105] Nastasi M. and Tesmer J.R. *Handbook of Modern Ion Beam Materials Analysis*. 1995.

[106] G. Drera, G. Salvinelli, J. Åhlund, P. G. Karlsson, B. Wannberg, et al. "Transmission function calibration of an angular resolved analyzer for X-ray photoemission spectroscopy: Theory vs experiment". In: *Journal of Electron Spectroscopy and Related Phenomena* 195 (2014), pp. 109–116. ISSN: 03682048. DOI: 10.1016/j.elspec.2014.06.010.

[107] IS Tilinin, A Jablonski, J Zemek, and S Hucek. "Escape probability of signal photoelectrons from non-crystalline solids: influence of anisotropy of photoemission". In: *Journal of electron spectroscopy and related phenomena* 87.2 (1997), pp. 127–140.

[108] Wolfgang SM Werner. “Electron transport in solids for quantitative surface analysis”. In: *Surface and Interface Analysis: An International Journal devoted to the development and application of techniques for the analysis of surfaces, interfaces and thin films* 31.3 (2001), pp. 141–176.

[109] M Zangrando, Marco Finazzi, G Paolucci, Giovanni Comelli, B Diviacco, et al. “BACH, the beamline for advanced dichroic and scattering experiments at ELETTRA”. In: *Review of Scientific Instruments* 72.2 (2001), pp. 1313–1319.

[110] Edward A Stern. “Theory of the extended x-ray-absorption fine structure”. In: *Physical Review B* 10.8 (1974), p. 3027.

[111] Philippe Fontaine, Gianluca Ciatto, Nicolas Aubert, and Michel Goldmann. “Soft interfaces and resonant investigation on undulator source: a surface X-ray scattering beamline to study organic molecular films at the SOLEIL synchrotron”. In: *Science of advanced materials* 6.11 (2014), pp. 2312–2316.

[112] G Ciatto, MH Chu, Pascal Fontaine, N Aubert, Hubert Renevier, et al. “SIRIUS: A new beamline for in situ X-ray diffraction and spectroscopy studies of advanced materials and nanostructures at the SOLEIL Synchrotron”. In: *Thin Solid Films* 617 (2016), pp. 48–54.

[113] Boon K Teo. *EXAFS: basic principles and data analysis*. Vol. 9. Springer Science & Business Media, 2012.

[114] M. Newville. *Fundamentals of EXAFS*. Consortium for Advanced Radiation Sources University of Chicago, 2004.

[115] Matthew Newville. “EXAFS analysis using FEFF and FEFFIT”. In: *Journal of Synchrotron Radiation* 8.2 (2001), pp. 96–100. ISSN: 09090495. DOI: 10.1107/S0909049500016290.

[116] G. Dalba and P. Fornasini. “EXAFS Debye Waller factor and thermal vibrations of crystals”. In: *Journal of Synchrotron Radiation* 4.4 (1997), pp. 243–255. ISSN: 09090495. DOI: 10.1107/S0909049597006900.

[117] Leo J van der Pauw. “A method of measuring the resistivity and Hall coefficient on lamellae of arbitrary shape”. In: *Philips technical review* 20 (1958), pp. 220–224.

[118] Leo J van der Pauw. “A method of measuring specific resistivity and Hall effect of discs of arbitrary shapes”. In: *Philips technical research reports* 13 (1958).

[119] Paul Kubelka. “Ein Beitrag zur Optik der Farbanstriche (Contribution to the optic of paint)”. In: *Zeitschrift fur technische Physik* 12 (1931), pp. 593–601.

[120] Paul Kubelka. "New contributions to the optics of intensely light-scattering materials. Part I". In: *Josa* 38.5 (1948), pp. 448–457.

[121] James H Nobbs. "Kubelka Munk theory and the prediction of reflectance". In: *Review of Progress in Coloration and Related Topics* 15.1 (1985), pp. 66–75.

[122] Jennifer S. Hovis, Robert J. Hamers, and C. Michael Greenlief. "Preparation of clean and atomically flat germanium(001) surfaces". In: *Surface Science* 440.1-2 (1999), pp. 815–819. ISSN: 00396028. DOI: 10.1016/S0039-6028(99)00866-3.

[123] Kwangwook Choi and Jillian M Buriak. "Hydrogermylation of Alkenes and Alkynes on Hydride-Terminated Ge (100) Surfaces". In: *Langmuir* 16.100 (2000), pp. 7737–7741. ISSN: 0743-7463. DOI: 10.1021/la000413d.

[124] Sandrine Rivillon, Yves J Chabalfabrice Amy, Antoine Kahn, and Yves J Chabal. "Hydrogen passivation of germanium (100) surface using wet chemical preparation Hydrogen passivation of germanium 100 . . . surface using". In: *Applied Physics Letters* 87.253101 (2005), pp. 1–4. DOI: 10.1063/1.2142084.

[125] Brittany Branch, Manish Dubey, Aaron S Anderson, Kateryna Artyushkova, J Kevin Baldwin, et al. "Investigating phosphonate monolayer stability on ALD oxide surfaces". In: *Applied Surface Science* 288 (2014), pp. 98–108.

[126] Qi Xie, Shaoren Deng, Marc Schaekers, Dennis Lin, Matty Caymax, et al. "Germanium surface passivation and atomic layer deposition of high-k dielectrics—a tutorial review on Ge-based MOS capacitors". In: *Semiconductor Science and Technology* 27.7 (2012), p. 074012.

[127] Francesco Sgarbossa, Gianluigi Maggioni, Gian Andrea Rizzi, Sara Maria Carturan, Enrico Napolitani, et al. "Self-limiting Sb monolayer as a diffusion source for Ge doping". In: *Applied Surface Science* 496.May (2019), p. 143713. ISSN: 01694332. DOI: 10.1016/j.apsusc.2019.143713. URL: https://linkinghub.elsevier.com/retrieve/pii/S0169433219325103.

[128] Masafumi Matsui, Hideki Murakami, Tomohiro Fujioka, Akio Ohta, Seiichiro Higashi, et al. "Characterization of chemical bonding features at metal/GeO2 Interfaces by X-ray photoelectron spectroscopy". In: *Microelectronic Engineering* 88.7 (2011), pp. 1549–1552. ISSN: 01679317. DOI: 10.1016/j.mee.2011.03.032.

[129] Francesco Sgarbossa, Sara Maria Carturan, Davide De Salvador, Gian Andrea Rizzi, Enrico Napolitani, et al. "Monolayer doping of germanium by phosphorus containing molecules". In: *Nanotechnology* 29.465702 (2018). ISSN: 0957-4484. DOI: 10.1088/1361-6528/aade30. URL: http://iopscience.iop.org/article/10.1088/1361-6528/aade30.

[130] Regina Luschtinetz, Gotthard Seifert, Evelin Jaehne, and Hans Jürgen P Adler. "Infrared spectra of alkylphosphonic acid bound to aluminium surfaces". In: *Macromolecular Symposia* 254 (2007), pp. 248–253. ISSN: 10221360. DOI: 10.1002/masy.200750837.

[131] Irina Gouzman, Manish Dubey, Michael D. Carolus, Jeffrey Schwartz, and Steven L. Bernasek. "Monolayer vs. multilayer self-assembled alkylphosphonate films: X-ray photoelectron spectroscopy studies". In: *Surface Science* 600.4 (2006), pp. 773–781. ISSN: 00396028. DOI: 10.1016/j.susc.2005.11.030.

[132] Abraham Vega, Peter Thissen, and Yves J Chabal. "Environment-controlled tethering by aggregation and growth of phosphonic acid monolayers on silicon oxide". In: *Langmuir* 28.21 (2012), pp. 8046–8051.

[133] C. Ivascu, A. Timar Gabor, O. Cozar, L. Daraban, and I. Ardelean. "FT-IR, Raman and thermoluminescence investigation of P2O 5-BaO-Li2O glass system". In: *Journal of Molecular Structure* 993.1-3 (2011), pp. 249–253. ISSN: 00222860. DOI: 10.1016/j.molstruc.2010.11.047.

[134] L. W. Daasch and D. C. Smith. "Infrared Spectra of Phosphorus Compounds". In: *Analytical Chemistry* 23.6 (1951), pp. 853–868. ISSN: 15206882. DOI: 10.1021/ac60054a008.

[135] N. Illy, G. Couture, R. Auvergne, S. Caillol, G. David, et al. "New prospects for the synthesis of N-alkyl phosphonate/phosphonic acid-bearing oligo-chitosan". In: *RSC Adv.* 4.46 (2014), pp. 24042–24052. ISSN: 2046-2069. DOI: 10.1039/C4RA02501F. URL: http://xlink.rsc.org/?DOI=C4RA02501F.

[136] Robert M. Silverstein, Francis X. Webster, and David J. Kiemle. *Spectrometric identification of organic compounds*. 7th. Johon Wiley and sons, inc., 2005, p. 512. ISBN: 0471393622. DOI: 10.1016/0022-2860(76)87024-X. eprint: arXiv:1011.1669v3. URL: http://linkinghub.elsevier.com/retrieve/pii/002228607687024X.

[137] Hans Reuter and Martin Reichelt. "Methylphosphonic acid, CH3PO(OH)2". In: *Acta Crystallographica Section E: Structure Reports Online* 70.3 (2014), pp. 0–7. ISSN: 16005368. DOI: 10.1107/S1600536814003572.

[138] C. Y. Yang, M. A. Paesler, and D. E. Sayers. "Determination of bond strengths of arsenic and arsenic chalcogen compounds using the temperature dependence of extended x-ray-absorption fine structure". In: *Physical Review B* 36.2 (1987), pp. 980–988. URL: http://ir.obihiro.ac.jp/dspace/handle/10322/3933.

[139] D.W.J. Cruickshank. "Refinements of structures containing bonds between Si, P, S or Cl and O or N. VI. P2O5 , form III". In: *Acta Crystallographica* 17.6 (1964), pp. 679–680. ISSN: 0365-110X. DOI: 10.1107/S0365110X64001682.

[140] D. W. J. Cruickshank. "Refinements of structures containing bonds between Si, P, S or Cl and O or N.P4O10". In: *Acta Crystallographica* 17.6 (1964), pp. 685–686. ISSN: 0365-110X. DOI: 10.1107/s0365110x64001724.

[141] Richard C. Mowrey, Bradley A. Williams, and Charles H. Douglass. " Vibrational Analysis of P 4 O 6 and P 4 O 10 ". In: *The Journal of Physical Chemistry A* 101.32 (2002), pp. 5748–5752. ISSN: 1089-5639. DOI: 10.1021/jp971072o.

[142] B Beagley, DWJ Cruickshank, TG Hewitt, and KH Jost. "Molecular structures of P 4 O 6 and P 4 O 8". In: *Transactions of the Faraday Society* 65 (1969), pp. 1219–1230.

[143] G Kuper, R Chauvistre, J Hormes, F Frick, M Jansen, et al. "Phosphorus K shell photoabsorption spectra of the oxides P406,P4010, P(C6H50)3 and PO(C6H5O)3". In: *Chemical Physics* 165 (1992), pp. 405–414.

[144] Benjamin Gamoke, Diane Neff, and Jack Simons. "Nature of PO bonds in phosphates". In: *Journal of Physical Chemistry A* 113.19 (2009), pp. 5677–5684. ISSN: 10895639. DOI: 10.1021/jp810014s.

[145] E. A. Robinson. "CHARACTERISTIC VIBRATIONAL FREQUENCIES OF OXYGEN COMPOUNDS OF PHOSPHORUS AND CHLORINE: CORRELATION OF SYMMETRIC AND ASYMMETRIC STRETCHING FREQUENCIES OF PO AND ClO BONDS". In: *Canadian Journal of Chemistry* 41.1 (2006), pp. 173–179. ISSN: 0008-4042. DOI: 10.1139/v63-022.

[146] N Ioannou, D Skarlatos, C Tsamis, CA Krontiras, SN Georga, et al. "Germanium substrate loss during low temperature annealing and its influence on ion-implanted phosphorous dose loss". In: *Applied Physics Letters* 93.10 (2008), p. 101910.

[147] Ori Hazut and Roie Yerushalmi. "Direct Dopant Patterning by a Remote Monolayer Doping Enabled by a Monolayer Fragmentation Study". In: *Langmuir* 33.22 (2017), pp. 5371–5377. ISSN: 15205827. DOI: 10.1021/acs.langmuir.7b01085.

[148] H.-U. Schreiber and E. Fröschle. "High Quality RF-Sputtered Silicon Dioxide Layers". In: *Journal of the Electrochemical Society: Solid-state Science and Technology* 123.1 (1976), pp. 30–33. ISSN: 00134651. DOI: 10.1149/1.2132759.

[149] S. Suyama, A. Okamoto, and T. Serikawa. "The Effects of Oxygen-Argon Mixing on Properties of Sputtered Silicon Dioxide Films". In: *Journal of The Electrochemical Society* 134.9 (1987), p. 2260. ISSN: 00134651. DOI: 10.1149/1.2100867. URL: http://jes.ecsdl.org/cgi/doi/10.1149/1.2100867.

[150] D.B. Cuttriss. *Relation between surface concentration and avarage conductivity in diffused layers in germanium*. 1960.

[151] Yasuo Shimizu, Hisashi Takamizawa, Koji Inoue, Fumiko Yano, Yasuyoshi Nagai, et al. "Behavior of phosphorous and contaminants from molecular doping combined with a conventional spike annealing method". In: *Nanoscale* 6.2 (2014), pp. 706–710.

[152] Darwent. *National Standard Reference Data Series*. Vol. 42. Washington DC: National Bureau of Standards, 1965.

[153] T V Ramakrishna Rao, R Ramakrishna Reddy, and P Sambasiva Rao. "POTENTIAL ENERGY CURVES AND DISSOCIATION ENERGY OF THE PO MOLECULE". In: *Physica B+C* 106.3 (1981), pp. 445–451.

[154] F. A. Trumbore. "Solid Solubilities of Impurity Elements in Germanium and Silicon". In: *Bell System Technical Journal* 39.1 (1960), pp. 205–233. ISSN: 15387305. DOI: 10.1002/j.1538-7305.1960.tb03928.x.

[155] V.I. Fistul, A.G. Yakovenko, A.A. Gvelesiani, and R.L. Tsygankov, V.N. Korchazkhina. "No Title". In: *Izv. Akad. Nauk SSSR Neorg. Mater.* 11.539 (1975).

[156] J Drowart, F Degreve, G Verhaegen, and R Colin. "Thermochemical Study of the Germanium Oxides Using a Mass Spectrometer". In: *Trans. Faraday Soc.* 61 (1965), pp. 1072–1085.

[157] Donald L. Hildenbrand and Edmond Murad. "Dissociation energy and ionization potential of silicon monoxide". In: *The Journal of Chemical Physics* 51.2 (1969), pp. 807–811. ISSN: 00219606. DOI: 10.1063/1.1672071.

[158] Kurt Weiser. "Theoretical calculation of distribution coefficients of impurities in germanium and silicon, heats of solid solution". In: *Journal of Physics and Chemistry of Solids* 7.2 (1958), pp. 118–126. ISSN: 0022-3697. DOI: https://doi.org/10.1016/0022-3697(58)90252-X. URL: http://www.sciencedirect.com/science/article/pii/002236975890252X.

[159] Gianluigi Maggioni, Francesco Sgarbossa, Enrico Napolitani, Walter Raniero, Virginia Boldrini, et al. "Diffusion doping of germanium by sputtered antimony sources". In: *Materials Science in Semiconductor Processing* 75.November 2017 (2018), pp. 118–123. ISSN: 13698001. DOI: 10.1016/j.mssp.2017.11.026. URL: https://doi.org/10.1016/j.mssp.2017.11.026.

[160] F. Garbassi. "XPS and AES study of antimony oxides". In: *Surface and Interface Analysis* 2.5 (1980), pp. 165–169. ISSN: 10969918. DOI: 10.1002/sia.740020502.

[161] R. Izquierdo, E. Sacher, and A. Yelon. "X-ray photoelectron spectra of antimony oxides". In: *Applied Surface Science* 40.1-2 (1989), pp. 175–177. ISSN: 01694332. DOI: 10.1016/0169-4332(89)90173-6.

[162] Gabriele Salvinelli, Giovanni Drera, Camilla Baratto, Antonio Braga, and Luigi Sangaletti. "Stoichiometry gradient, cation interdiffusion, and band alignment between a nanosized TiO2 blocking layer and a transparent conductive oxide in dye-sensitized solar cell front contacts". In: *ACS Applied Materials and Interfaces* 7.1 (2015), pp. 765–773. ISSN: 19448252. DOI: 10.1021/am5072018.

[163] Gerd M. Rosenblatt and Pang-Kab Lee. "Vaporization Kinetics and Thermodynamics of Antimony and the Vaporization Coefficient of Antimony Single Crystals". In: *J. Chem. Phys.* 52.1454 (1970), pp. 1454–1464. DOI: 10.1063/1.1673150.

[164] A. H. Sommer. "Characteristics of evaporated antimony films as a function of the antimony source". In: *Journal of Applied Physics* 37.7 (1966), pp. 2789–2791. ISSN: 00218979. DOI: 10.1063/1.1782124.

[165] Ihsan Barin. *Thermochemical data of pure substances*.

[166] Peter Atkins and Julio De Paula. *Physical Chemistry*. eight edit. W.H. Freeman and Company, New York, 2006, p. 1053.

[167] C. A. Cody, L. Dlcarlo, and R. K. Darlington. "Vibrational and Thermal Study of Antimony Oxides". In: *Inorganic Chemistry* 18.6 (1979), pp. 1572–1576. ISSN: 1520510X. DOI: 10.1021/ic50196a036.

[168] N. A. Asryan, A. S. Alikhanyan, and G. D. Nipan. "P-T-x phase diagram of the Sb-O system". In: *Inorganic Materials* 40.6 (2004), pp. 626–631. ISSN: 00201685. DOI: 10.1023/B:INMA.0000031997.59271.0f.

[169] S. Brotzmann, H. Bracht, J. Lundsgaard Hansen, A. Nylandsted Larsen, E. Simoen, et al. "Diffusion and defect reactions between donors, C, and vacancies in Ge. I. Experimental results". In: *Physical Review B - Condensed Matter and Materials Physics* 77.23 (2008), pp. 1–13. ISSN: 10980121. DOI: 10.1103/PhysRevB.77.235207.

[170] Chi Xu, C L Senaratne, J Kouvetakis, and J Men. "Experimental doping dependence of the lattice parameter in n -type Ge : Identifying the correct theoretical framework by comparison with Si". In: *Physical Review B* 041201 (2016), pp. 1–5. DOI: 10.1103/PhysRevB.93.041201.

[171] Richard L. Petritz. "Theory of an experiment for measuring the mobility and density of carriers in the space-charge region of a semiconductor surface". In: *Physical Review* 110.6 (1958), pp. 1254–1262. ISSN: 0031899X. DOI: 10.1103/PhysRev.110.1254.

[172] R. Baron, G. A. Shifrin, O. J. Marsh, and James W. Mayer. "Electrical behavior of group III and V implanted dopants in silicon". In: *Journal of Applied Physics* 40.9 (1969), pp. 3702–3719. ISSN: 00218979. DOI: 10.1063/1.1658260.

Acknowledgments

First and foremost I want to thank my supervisor prof. Davide De Salvador, for his great professionally, humanity. He teach me how good experimental physics is done but also how it is important to revel between one RBS spectrum an another. I appreciate all his contributions of time, ideas, suggestions, inspiring proficiency, but also for supporting my ideas. I am also thankful for the excellent example he has provided as a successful physicist and professor, opened out of his scientific area and still curios to study and learn more and more things.
I'm very thankful to dr. Gianluigi Maggioni (really, not Gigi?) and dr. Sara Maria Carturan for their guidance helped me in all the time of research and writing articles. Thanks for all your time and patience, and also for saving me all days at 12.40 from LNL chemistry lab...I appreciate that, you know why! Thanks for all the coffees you, Walter and Matteo offered me! Probably, I have to provide you a life-time stock of coffee.
I want to thank prof. Enrico Napolitani for his help in interpreting results, his willingness to answer my questions, his precision, and why not, his perfect choices of restaurants after endless conference sessions.
My sincere thanks also goes to prof. Gian Andrea Rizzi for his help on solving my (many) chemistry doubts and to teach me that oxidation numbers are an old stuff, but (sometimes) they works!
I want to thank prof. Cristina Tubaro for her disposability and help during dry-box deposition and prof. Alberto Carnera for its inspiring knowledge and his innate ability to explain physics, that perhaps led me to continue in my study in this research field.
I want to thank my office mates Ruggero Milazzo, Virginia Boldrini and Stefano Bertoldo for their friendship and their help during these years, and to help me to welcome properly Ascanio on January 8th. In particular, I want to thanks Ruggero for all the coffee he provided at the conference (but also at DFA department), and the ulcer that is going to cause to me.
A big hug also for my second office mates Walter Raniero, Matteo Campostrini

and Michela Vesco for having understood (and sometime sharing with me) my hunger, especially at Legnaro lab.
I want to thank Luca Bacci, Nicola Argiolas and Carlo Scian for their precious technical support, and Adriana Schiavon for the friendship and joy she always brings with her.
I want to thanks the entire matter physics group that has been a source of friendships as well as good advice and collaboration. I am especially grateful to Chiara, Ruggero, Luca, Nicola, Virginia, Riccardo, Annamaria, Laura, Paolo, Bazz, Stefano, Alba, Sofia, Carlo, Boris, Ionut, Alberto and all the others, thank's for having endured my boring speeches and theories during lunch time, but I hope that sometimes they were interesting also for you too.
I would like to thank my friends for accepting nothing less than excellence from me. Last but not the least, I would like to thank my family: my parents for supporting me spiritually throughout this three years and my life in general, and Giulia for her love.